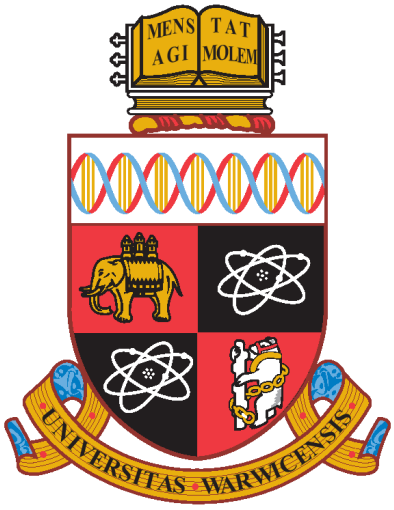

Electrical and Electrochemical Characterisation of Single Crystal Diamond

by

Bianca Barbu

Thesis

Submitted to the University of Warwick for the degree of

Doctor of Philosophy

Department of Physics

December 2009

THE UNIVERSITY OF WARWICK

In Memoriam

Ioana & Ioan Barbu

Contents

List of Figures

Chapter 1: Introduction

Chapter 2: Literature review

Chapter 3: Theoretical aspects

Chapter 4: Experimental details and methods

Chapter 5: Electrical and electrochemical characterisation of hydrogen terminated intrinsic single crystal diamond

Chapter 6: Electrical and electrochemical characterisation of oxygen and hydrogen terminated moderately boron doped single crystal semiconducting diamond

Chapter 7: Electrical and electrochemical characterisation of heavily doped (> 10^{20} cm^{-3} boron) oxygen and hydrogen terminated single crystal diamond

List of Tables

Acknowledgements

Firstly I would like to thank Dr. Mark Newton and Prof. Julie Macpherson for all their help, patience and guidance throughout my PhD, and for not giving up on me when I was tempted to do it myself. Many thanks also to Prof. Pat Unwin, for his willingness to help and for sharing his knowledge with me.

Thanks must also go to Element Six Ltd. for supplying the samples which were used for the research presented in this thesis, to Neil Wilson for showing me the nity-grity of lithography and his constant supply of biscuits, to Steve York for his guidance on FE-SEM and to all the members of the Warwick Physics and Chemistry Workshops.

Many thanks to all the members of the Warwick EPR and Diamond Group and the Electrochemistry and Interfaces Group, past and present; my PhD years wouldn't have been the same without you. Special thanks to Brad for catching everything I threw at him, to Andy for fixing everything I broke, to baby Steph for being a great ear to sound off to, to Ulrika for being a great partner to talk with about shoes, Solveig for her unusual presents, Benster for being the new face of the Diamond Group and to Robin thanks for the book, but where is my pony?!; to Ioana, Sara, Anna, Cara, Jon and Martin for being my partners in mischief on the "other side".

Many thanks to all my housemates over the years Sarah, Stu (for climbing all the stairs in all the houses where we have lived), Rob (can I still iron your face?), Lisa (who loves diamonds because they are sparkly); thanks for being such good friends.

Special thanks must go to my mother, Susana, for all her love and support, and for putting up with all her daughter's eccentric ideas. Thanks for supporting me especially over the final stages of writing up when I know I've been a pain in the neck, I appreciate it more than I could ever tell you.

Mulțumiri speciale mamei mele, Susana, pentru toată dragostea și sprijinul ei și pentru că a suportat consecințele ideilor excentrice ale fiicei sale. Mulțumesc pentru că ai fost alături de mine mai ales în ultimele etape ale doctoratului când știu că am fost o mare pacoste. Apreciez sprijinul tău mai mult decât ți-aș putea spune vreodată.

Declaration

I declare that the work presented in this thesis is my own except where stated otherwise, and was carried out at the University of Warwick, except where stated otherwise, during the period of September 2005 to February 2009, under the supervision of Dr. M. E. Newton and Prof. J. V. Macpherson. The research reported here has not been submitted, either wholly or in part, in this or any other academic institution for admission to a higher degree.

Some parts of the work reported and other work not reported in this thesis have been published, as listed below:

Conference presentations:

1. B. Barbu, M. E. Newton, and J. V. Macpherson, *Device fabrication on diamond*, Diamond Research on Interfaces for Versatile Electronics, project meeting, Krakow (Poland), oral presentation (2006).
2. B. Barbu, M. E. Newton, and J. V. Macpherson, *Device fabrication on diamond*, Nanotubes Electrochemistry Meeting, Warwick (UK), oral presentation (2006).
3. B. Barbu, M. E. Newton, and J. V. Macpherson, *Electrical characterisation of diamond: from contacts to electrochemical applications*, The 57th De Beers Diamond Conference, Cambridge (UK), poster presentation (2006).
4. B. Barbu, M. E. Newton, and J. V. Macpherson, *Device fabrication on diamond*, Diamond Research on Interfaces for Versatile Electronics, project meeting, Innsbruck (Austria), oral presentation (2006).
5. B. Barbu, M. E. Newton, and J. V. Macpherson, *Electrical characterisation of diamond: from contacts to electrochemical applications*, Diamond Research on Interfaces for Versatile Electronics, project meeting, Innsbruck (Austria), poster presentation (2006).
6. N. R. Wilson, B. Barbu, M. E. Newton, A. L. Colley, C. G. Williams, and J. V. Macpherson, *Electrical characterisation of polycrystalline boron doped diamond using scanned probe microscopy techniques*, Scanning probe microscopy conference & users meeting, Manchester (UK), poster presentation (2007).
7. B. Barbu, M. E. Newton, and J. V. Macpherson, *Electrochemical characterisation of single crystal boron doped diamond*, Diamond

Research on Interfaces for Versatile Electronics, project meeting, Hasselt (Belgium), oral presentation (2007).

8. B. Barbu, M. E. Newton, and J. V. Macpherson, *Electrical and electrochemical characterisation of single crystal boron doped diamond*, The 58th De Beers Diamond Conference, Warwick (UK), poster presentation (2007).
9. B. Barbu, N. R. Wilson, M. E. Newton, A. L. Colley, C. G. Williams, and J. V. Macpherson, *Electrical and electrochemical characterisation of polycrystalline and single crystal boron doped diamond*, Electrochem' 07, London (UK), poster presentation (2007).
10. B. Barbu, M. E. Newton, and J. V. Macpherson, *Electrochemical investigation of the surface conductivity of hydrogen terminated single crystal intrinsic diamond*, 2nd International Conference on New Diamond and Nano Carbons, Taipei (Taiwan), poster presentation (2008).
11. B. Barbu, M. E. Newton, and J. V. Macpherson, *Electrical and electrochemical investigation of the surface conductivity of hydrogen terminated single crystal intrinsic diamond*, The 59th De Beers Diamond Conference, Oxford (UK), oral presentation (2008).

B. Barbu
December 2009

Abstract

The overall aim of this thesis is to examine the electrical and electrochemical properties of single crystal intrinsic and boron doped diamond grown by chemical vapour deposition.

Techniques such as AFM, C-AFM, FE-SEM, PL imaging, in air and in solution Hall and resistivity measurements, FET, cyclic voltammetry and SECM have been employed.

The results from studying single crystal intrinsic H-terminated diamond with different surface preparations are reported. In air and in solution measurements suggest a similar behaviour for polished surfaces. Different mechanisms (for in air or in solution experiments) have to be applied in order to interpret the electrical transport data correctly. Electrochemistry of H-terminated single crystal diamond with well defined redox couples has been proven, but the electron transfer rates are relatively slow. Initial SECM experiments indicate that the surface is homogeneously active, but can be easily damaged.

Single crystal boron doped diamonds with moderate (< 10^{20} cm^{-3} boron) doping levels have been examined. PL imaging and C-AFM highlighted regions with different doping level and different conductivity even though the material is single crystal. In air electrical measurements demonstrated that the bulk mobility and carrier concentration are independent of the surface termination (O- or H-). No redox activity (or very little) was observed when the samples were O-terminated; quasi-reversible behaviour and sluggish electron transfer kinetics was observed for H-terminated surfaces.

The properties of a as-grown single crystal boron doped diamond with high (> 10^{20} cm^{-3} boron) doping levels have also been investigated. Electrical studies confirmed that the diamond behaved like a metallic conductor. Large background currents were observed when CVs were used to study the O-terminated sample in $FcTMA^{+}$, but the origin of this signal are not clear. For both $Ru(NH_3)_6^{3+}$ and $FcTMA^{+}$ the metallic boron doped single crystal diamond electrode showed quasi-reversible behaviour. The peak to peak separation is smaller for the H-termination than for the O-termination. Preliminary SECM studies showed that the electrode's surface was homogeneously active.

Abbreviations

Abbreviation	Description
AFM	Atomic Force Microscopy
BDD	Boron-doped diamond
C-AFM	Conductive Atomic Force Microscopy
CL	Cathodoluminescence
CV	Cyclic voltammetry /cyclic voltammogram
CVD	Chemical Vapour Deposition
FET	Field Effect Transistor
FE-SEM	Field-emission Scanning Electron Microscopy
HF-CVD	Hot Filament-CVD
HPHT	High Pressure High Temperature
IPI	Ideally polarisable interface
IR	Infra-red
PL	Photoluminescence
SECM	Scanning Electrochemical Microscopy
SG-TC	Substrate generation-tip collection
TG-SC	Tip generation – substrate collection
UME	Ultramicroelectrode
WLI	White-light interferometry

Glossary of Symbols

Symbol	Description
A	Area of electrode
a	Radius of disc UME
a_0	Cubic lattice parameter
B	Magnetic field
C	Concentration
d	C-C bond length
	Thickness
	UME-surface separation
D	Charge per unit area
	Diffusion coefficient
E_A	Activation energy
E_{CB}	Energy of the conduction band
E_{VB}	Energy of the valence band
E_F	Energy of the Fermi level
ε	Permitivity
F	Faraday's constant
χ	Electron afinity
hkl	Miller indices
I	Current
i_t	Current at time t
i_{lim}	Diffusion-limited current
j	Flux

μ	Mobility
n	Number of electrons
n_s	Sheet carrier density
η	Overpotential
p	Concentration of holes
q	Elementary charge
ρ	Bulk electrical resistivity
R	Resistance
	Gas constant
R_S	Sheet resistance
r_g	Radius of glass
T	Temperature
V	Voltage
V_H	Hall voltage

Chapter 1
Introduction

It has been widely recognised that, because of its unique and extraordinary properties (extreme hardness, high refractive index, high thermal conductivity, wide potential window, etc.) conducting diamond could eventually become a valuable electronic and electrode material. In all the present concepts of diamond-based electronic devices the properties of defects, interfaces and surfaces play a major role.

The investigations presented herein will be focused on the electronic and electrochemical properties of intrinsic and boron doped single crystal diamond grown by chemical vapour deposition. A variety of electrical, electrochemical and microscopic techniques have been used.

Advancement in diamond material technology and the combination of diamond with other wide bandgap semiconductors to overcome the weaknesses of each material, will favour miniaturisation, a reduction in overall system cost with improved efficiency, and the opening up of other new, high technology opportunities.

1.1. Diamond structure

Diamond, the hardest material known to human kind, has fascinated people with its beauty and its exceptional qualities even though it is just another configuration of carbon, as Antoine-Laurent Lavoisier proved in 1772 [1]. Natural diamonds are formed inside the earth, at about 200 km below the crust. Due to the high temperature (above 1300°C), high pressure and the abundance of carbon-based compounds, carbon will crystallise into the diamond

structure. The process could be slow and once formed the diamond must survive transportation to the surface in order to be accessible to man [1].

The first gem stones were discovered in India, 2700 years ago, and were used in commerce. Jewellery made with diamonds is dated a couple of centuries later than their discovery, but their true beauty was fully exposed starting with the 14th and 15th century when faceting and polishing techniques were developed [2].

In order to understand diamond, from its growth process up to its applications, basic knowledge of its structure is necessary. Tetrahedrally bonded carbon atoms, one of the most abundant elements in the universe, form diamond's lattice.

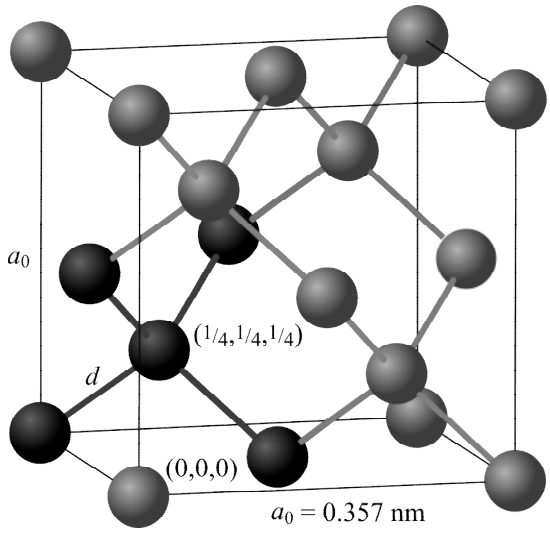

Figure 1.1 The structure of the diamond crystal: conventional unit cell of diamond, where a_0 is the cubic lattice parameter and d is the C-C bond length. The five darker spheres highlight the tetrahedral structure of diamond [3].

In pure cubic diamond, carbon atoms are bound together by single σ bonds (0.154 nm) oriented along (111) directions [4]. The diamond structure is a face-centred cubic (fcc) Bravais lattice (Figure 1.1). The unit cell is composed of two interpenetrating single fcc

lattices which are shifted with respect to each other along the cube diagonal by a quarter of its length. This is a primitive fcc basis containing two atoms at (0, 0, 0) and (¼, ¼, ¼) associated with each lattice point. The edge of the conventional cubic cell is the lattice constant and has a length of a_0= 0.357 nm (3.57 Å) at room temperature [4]. Its crystal structure is responsible for the fundamental properties of diamond. A simple method to define the lattice planes and lattice directions in a crystal like diamond is to use Miller indices (hkl) [5]. By using these indices, the orientation of a surface or a crystal plane may be considered as how the plane (or any parallel plane with it) intersects the main crystallographic axes of the solid. Schematic illustrations of the three lowest index crystallographic planes in diamond: (100), (110) and (111) are represented in Figure 1.2.

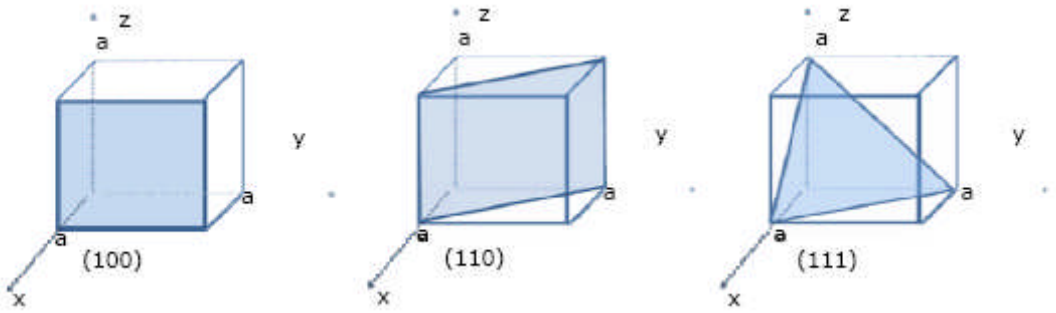

Figure 1.1 Schematic illustrations of the three lowest index crystallographic planes in diamond: (100), (110) and (111). Adapted from reference [6].

1.2. Diamond properties

A fundamental property of diamond is its ***optical transparency***. It is well known that due to its indirect bandgap (i.e. optical transition between free electrons and holes are forbidden as the minimum of the conduction band and the maximum of the valence band have different levels) of 5.47 eV, defect-free diamond absorbs electromagnetic radiation with a wavelength of ~227 nm or lower [7]. UV light or photons with higher energies will create electron-hole

pairs. The process can be accompanied by near-ultraviolet light emission, during the radiative recombination of an electron from conduction band with a hole at the top of the valence band. The indirect bandgap presence in diamond and the phonon's involvement makes the process inefficient. Therefore, diamond is transparent over a range from the near-ultraviolet, through the visible, to the far-infrared, and even at wavelengths beyond ~100 μm [7].

Many of diamond's properties, such as ***extreme hardness*** (scoring 10 on the relative Mohs scale of mineral hardness) are the result of diamond's strong covalent bonds [8]. Its ***high refractive index*** and ***moderate dispersion index***, its ***high thermal conductivity***, of about 2000 $Wm^{-1}K^{-1}$ (that is five times that of copper at room temperature) [9], are also down to its structure and the rigid covalent bonds [2].

Due to the small size of the C atoms [10] and high packing density, the C-C bonds are relatively short (0.154 nm). The large overlap of the orbitals of the C atoms involved in a C-C bond causes a large energy separation between the occupied bonding orbitals and the unoccupied antibonding orbitals. This results in a very large forbidden energy gap between the valence and conduction band states in the electronic structure of diamond. As a result, diamond is a ***wide bandgap semiconductor***, if not an insulator, with an indirect band gap of 5.47 eV at 300 K [5], as already stated.

1.3. Diamond classification

In diamond, each carbon atom is surrounded by four nearest neighbours, forming a tetrahedral structure of covalently bonded atoms with sp^3 hybridization [11]. Having a perfectly periodic lattice, all the deviations from this structure are considered imperfections. Two natural diamonds are never identical in terms of composition and properties; but it is

possible to use various schemes of classifications. For instance diamond gemstones are graded with regard to the 4C's, which is a concept from the jewellery sector that refers to the following attributes: Carat, Colour, Clarity and Cut [1].

However, synthetic and natural diamonds are classified according to the nature and amount of impurities contained within the structure. The most frequent imperfections are represented by *extrinsic substitutional impurities, intrinsic (interstitial and structural) anomalies* and *vacancies*.

A substitutional impurity refers to the presence of a different atom which would not be normally found in the diamond lattice, but which sits at the position where a carbon atom would normally be found, and replaces it. For *interstitial anomalies* the atom does not sit at a host lattice site. A *vacancy* is an empty position in the diamond lattice. Vacancies can be introduced or generated by radiation damage (natural or artificial). High-energy subatomic particles expel carbon atoms out of the structure.

Nitrogen is the most common impurity occurring in 98% of all natural diamonds. Its presence can be detected by optical absorption [10]. The material properties and the light absorption of diamond depend on nitrogen content and aggregation state [12]. Even though all composite configurations produce absorption in the infrared and ultraviolet, natural diamonds with high levels of nitrogen are usually relatively uncoloured.

Another element which is frequently observed is boron. Boron behaves like an acceptor because the boron atoms have one less electron than the carbon atoms that they substitute; every substituted boron atom accepts an electron from the valence band, if thermally excited,

or from an electron donor impurity/defect. Substitutional boron induces red light absorption, and because of the relatively low energy necessary for the electron to abandon the valence band, holes are formed in the latter even via thermal heat at room temperatures [13]. These holes can move in an electric field and make the diamond electrically conductive (p-type semiconductor).

All diamonds have crystal lattice defects and their material properties are affected by these defects and determine to which ***type*** a diamond is assigned. The classification is based on the incorporation of nitrogen and boron impurities into the diamond lattice; however this is not always precise. Many diamonds are mixed e.g. IaAB. The classification also depends on the detection limits. For example, a diamond classified as type II by infra-red (IR) absorption spectroscopy may well contain detectable concentrations of N_S^0 by Electron Paramagnetic Resonance (EPR).

Type I diamonds have significant nitrogen impurities and further sub classification according to the aggregation of the nitrogen atoms in the lattice is possible. **Type II** diamonds have low or undetectable nitrogen amounts and here the presence of boron distinguishes between the IIa and IIb subcategories. Further details of type I and II are listed below (see also Figure1.3).

Type I:

Type Ia – are the most common crystals in nature and have a nitrogen concentration up to ~ 0.3% (~ 3000 ppm). The impurity is present in aggregates of substitutional atoms, in non-paramagnetic form. It is further divided into:

- **Type IaA** - the majority of nitrogen is present in the form of A aggregates (a nearest-neighbour substitutional pair).

- **Type IaB -** the B aggregates are specific for this category (four substitutional atoms surround a vacancy) and such diamonds are rare in nature.
- **Type IaB'** – comprises diamonds with B'-defects (platelets) as well as nitrogen organized as N_3 centre (three substitutional nitrogen that surround a vacancy). In this category is also included: type IaB' regular, type IaB' irregular and type IaB without B'.

Type Ib – are rare in nature (< 0.1%) and nitrogen exists as isolated substitutional impurities with concentrations up to ~ 500 - 1000 ppm. The strong yellow colouration is due to the increased light absorption towards the blue end of the spectrum. The category includes most high pressure high temperature synthetic diamond, but only 1 in 1000 natural diamonds fit in this category.

H is also a common impurity in natural type I diamond [14].

Type II:

Type IIa – comprises diamonds which do not present optical absorption due to the presence of boron or nitrogen in the lattice and the content of nitrogen is less than ~ 10^{17} cm^{-3} (~1 ppm). This type of material can be colourless, although plastic deformation often renders such diamond brown coloured.

Type IIb – shows boron-related optical absorption; the material exhibiting significant p-type semiconductivity. Due to this factor the absorption of light happens toward the red end of the visible part of the spectrum, generating a slight blue colour of the diamond.

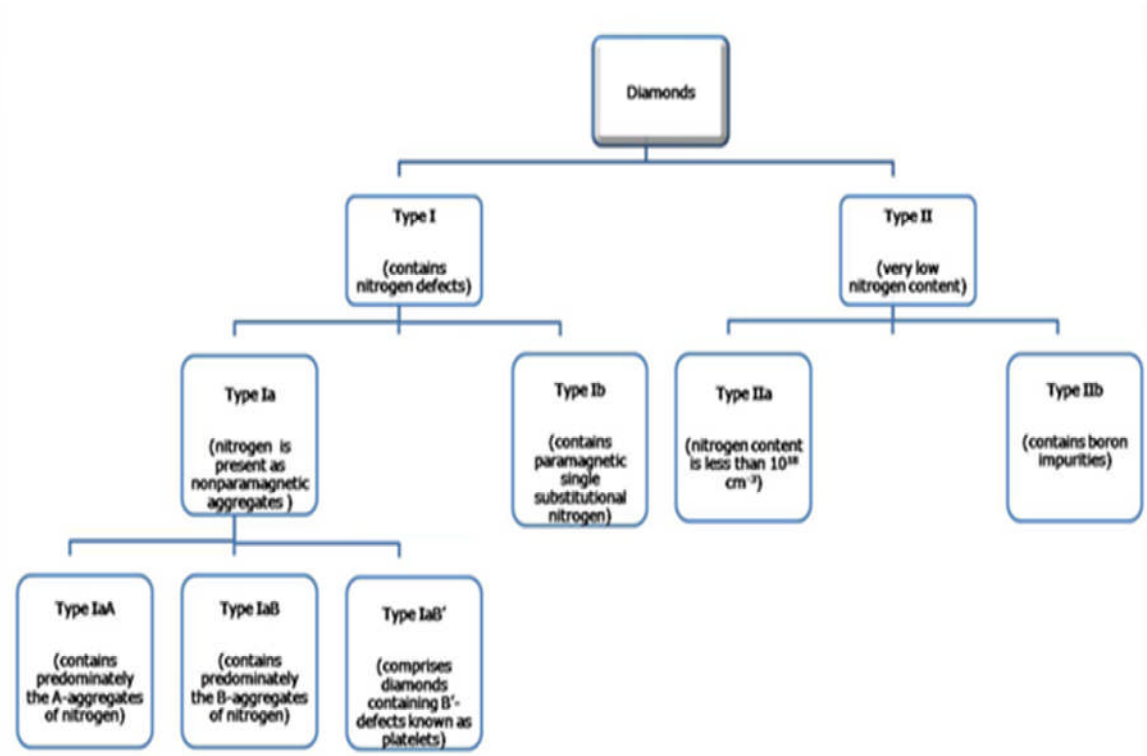

Figure 1.3 The classification of Type I and Type II diamond [15].

1.4. Diamond synthesis

Diamond's special attributes, some of which are detailed in section 1.2, have transformed it into a visionary material for various applications. However, in order for it to be exploitable for industrial purposes it has to be accessible at a lower price in large quantities and in well defined and reproducible forms (e.g. with controlled levels of impurities, structural defects, etc.), conditions that natural diamond does not fulfil.

There are two techniques that are mainly used to produce synthetic diamond. ***High Pressure High Temperature (HPHT)*** synthesis, first reported in 1959 [16, 17], produces diamond under conditions where this is the stable form of carbon; it has been used for the production of diamond for wear and abrasion applications for over 50 years. ***Chemical Vapour Deposition (CVD)***, first reported in 1958 [18], refers to the method of obtaining diamond by a low pressure vapour-phase process. In these conditions diamond is only metastable. Unless

nitrogen getters (i.e. elements that form a complex with nitrogen and lock it into solvent (e.g. Al, Ti) so it does not incorporate into diamond) are used, HPHT diamond is usually type Ib, whereas CVD diamond would usually be categorised as type IIa unless doped with boron. However there are a whole range of different types of CVD diamond and the traditional categories are not particularly useful. The focus of this thesis is on CVD diamond therefore detailed information on this process will be given in Chapter 2.

1.5. Diamond applications

For many years diamonds have been exclusively used for industrial applications such as drilling, grinding, sawing and polishing. The progress made in its synthesis has expanded the field of possible applications, while also making it a more affordable material. Its inertness to radiation established diamond as an ideal candidate for radiation detection [19, 20]. Combining its optical and thermal properties with its resistance to mechanical or chemical corrosion recommends it for optical windows [21, 22]. Furthermore its high thermal conductivity makes it suitable for high power electronic and opto-electronic devices [9], while the ability to deposit it on any substrate or shape makes it ideal for protective coatings [23].

Table 1.1 provides an overview of the actual applications of CVD diamond. This is by no means an exhaustive list; it is continuously upgraded with sophisticated new examples of applications such as biosensors, particle detectors, diamond-based acoustics devices and so on.

Application	***Examples***	***Properties of diamond***
Grinding/cutting tools	*Inserts* *Twist drills* *Whetstones* *Industrial knives* *Circuit-board drills* *Oil drilling tools* *Surgical scalpels* *Saws*	*Great hardness* *Great wear resistance* *High strength and rigidity* *Good lubricating properties* *General chemical inertness*
Wear parts	*Bearings* *Jet-nozzle coatings* *Slurry valves* *Extrusion dies* *Abrasive pump seals* *Engine parts* *Mechanical implants* *Drawing dies*	*Great hardness* *Great wear resistance* *High strength and rigidity* *Good lubricating properties* *General chemical inertness*
Diffusion/corrosion protection	*Crucibles* *Ion barriers (sodium)* *Fibre coatings* *Reaction vessels*	*General chemical inertness* *High strength and rigidity* *Good temperature resistance*
Optical coatings	*Laser protection* *Fibre optics* *X-ray windows* *UV to IR windows*	*Transparency from UV through visible into IR* *Good radiation resistance*
Photonic devices	*Radiation detectors* *Switches*	*Large bandgap*
Thermal management	*Heat-sink diodes* *Heat-sink PC boards* *Target heat-sinks*	*High thermal conductivity* *High electrical resistivity*
Semiconductor devices	*High-power transistors* *High-power microwave* *Photovoltaic elements* *Resistors* *Capacitors* *Field-effect transistors* *UV sensors* *Integrated circuits*	*High dielectric strength* *High thermal conductivity* *Good temperature resistance* *Good radiation resistance* *High power capacity* *Good high-frequency performance* *Low saturation resistance*

Table 1.1 Overview of diamond's potential applications [24].

As listed in the above table, diamond's properties have turned it into a material with a great potential for the semiconductor devices industry. Furthermore, because of its wide potential window [25], its superior chemical stability [26], and its intrinsic biocompatibility, conducting diamond could become the preferred electrode material for electrochemistry or bioelectronic applications.

Although commercial electrochemical applications e.g. for waste water treatment or amperometric sensors already exist [27, 28], a detailed study of the interface between diamond and liquids still has to be performed. This is a rapidly moving field with significant innovation potential and many research opportunities which can be explored.

1.6. Thesis outline

This thesis is laid out as follows:

- Chapter 2: A literature review of the field, involving a discussion of the electrochemical properties of diamond.
- Chapter 3: A theoretical introduction to the techniques employed.
- Chapter 4: A review of the experimental apparatus used in the studies reported.
- Chapter 5: The first experimental chapter, discussing the electrical and electrochemical characteristics of H-terminated intrinsic single crystal diamond.
- Chapter 6: Reports on the investigation into the electrical and electrochemical characteristics of moderately doped ($<10^{20}$ cm^{-3} boron) oxygen and hydrogen terminated single crystal diamond.
- Chapter 7: Reports on the investigation into the electrical and electrochemical characteristics of heavily doped ($>10^{20}$ cm^{-3} boron) oxygen and hydrogen terminated single crystal boron doped diamond.

- Chapter 8: Summarises the results presented in this thesis and highlights areas requiring further investigation.

References:

[1] R. Hazen, *The Diamond Makers* (Cambridge University Press, 1999).
[2] S. Tolansky, *The History and Use of Diamond* (Methuen & Co Ltd, London, 1962).
[3] A. M. Edmonds, *Magnetic resonance studies of point defects in single crystal diamond* (PhD thesis, 2008).
[4] C. Nebel, and J. Ristein, *Thin- film diamond I* (Elsevier Academic Press, 2003), Vol. 76.
[5] S. M. Sze, Proceedings of the IEEE **69**, 1121 (1981).
[6] S. M. Sze, *Semiconductor Devices* (John Wiley & Sons, 1985).
[7] R. Robertson, J. J. Fox, and A. E. Martin, Philosophical Transactions of the Royal Society of London Series a-Mathematical Physical and Engineering Sciences **232** (1934).
[8] P. G. Read, *Gemmology* (Butterworth-Heinemann, 2005).
[9] J. Field, *The Properties of Natural and Synthetic Diamond* (Academic Press Ltd., 1997).
[10] H. O. Pierson, *Handbook of Carbon, Graphite, Diamond and Fullerenes - Properties, Processing and applications* (Noyes Publications, 1995).
[11] M. A. Prelas, G. Popovici, and L. K. Bigelow, *Handbook of industrial diamonds and diamond films* (Marcel Dekker, INC., New York, 1998).
[12] C. Nebel, and J. Ristein, *Thin- film diamond II* (Elsevier Academic Press, 2003), Vol. 77.
[13] C. Kittel, *Introduction to Solid State Physics* (Wiley, New York, 1971).
[14] P. R. W. Hudson, and I. S. T. Tsong, Journal of Materials Science **12**, 2389 (1977).
[15] A. T. Collins, Physica B **185**, 284 (1993).
[16] H. P. Bovenkerk *et al.*, Nature **365**, 19 (1993).
[17] H. P. Bovenkerk *et al.*, Nature **184**, 1094 (1959).
[18] W. G. Eversole, and N. Y. Kenmore, (US Patent 3030187, 1958).
[19] L. Allers *et al.*, Diamond and Related Materials **6**, 353 (1997).
[20] A. Mainwood *et al.*, Journal of Physics D-Applied Physics **28**, 1279 (1995).
[21] E. Woerner *et al.*, Diamond and Related Materials **10**, 557 (2001).
[22] www.e6.com.
[23] P. Ball, New Scientist **153**, 22 (1997).
[24] H. M. Liu, and D. S. Dandy, *Diamond chemical vapour deposition - Nucleation and early growth stages* (Noyes Publications, 1995).
[25] H. B. Martin *et al.*, Journal of the Electrochemical Society **143**, L133 (1996).
[26] P. W. May, Philosophical Transactions of the Royal Society of London Series A-Mathematical Physical and Engineering Sciences **358**, 473 (2000).
[27] R. G. Compton, J. S. Foord, and F. Marken, Electroanalysis **15**, 1349 (2003).
[28] I. Troster *et al.*, Diamond and Related Materials **11**, 640 (2002).

Chapter 2
Literature review

The aim of this chapter is not to attempt to review the entire field of diamond physics and chemistry; it instead aims to review the literature of direct relevance to the results chapters that will follow. As the work outlined in this thesis was performed entirely on CVD grown samples, the CVD diamond growth process will be discussed and an overview of diamond electrochemistry will be given.

2.1. Chemical Vapour Deposition (CVD) of diamond

The term ''CVD diamond" refers to the material obtained by a low pressure vapour-phase process; as the name suggests it implies the occurrence of a chemical reaction in the gas phase above a substrate which leads to the deposition of material onto the substrate. The first attempts to implement this method were recorded in 1958 [1]. Natural diamonds heated to 900- 1100°C were used and through thermal decomposition of carbon-containing gases at low pressures synthetic diamond was grown; however only growth rates of 100 nm/ hr were accomplished. An important advancement in the field of CVD diamond growth took place in 1968 when Angus et al. [2] showed that the presence of atomic hydrogen at temperatures surpassing 1000°C led to higher growth rates. This was achieved due to the preferential removal of graphitic (sp^2) over diamond (sp^3).

Since 1968 various attempts to grow diamond through CVD have been carried out with the goal of improving the growth process, producing specifically tailored doped samples and increasing the growth rates: topics discussed in several reviews [3, 4]. The significant work performed to master the CVD growth has led to a conventional model of the CVD diamond

growth [5]. Through the dissociation of a mixture of CH_4 and H_2, carbon-containing radicals act as the source of carbon for the growing material, while the atomic hydrogen is indispensable during growth as outlined by Angus [2].

As high temperatures are necessary to accelerate the dissociation of H_2 and to form hydrocarbon free radicals, hot filament (HF) and microwave plasma (MP) CVD are the two most common techniques used to obtain them in CVD diamond growth [6]. Each technique has advantages and disadvantages.

The HF-CVD method makes use of metallic filaments (tungsten, tantalum or rhenium) at ~ 2000°C, to thermally activate the molecules of the gas mixtures and is widely used based on its simplicity. The major drawbacks are the unwanted contamination of the diamond thin film with metal impurities, which is caused by the filament deterioration and the inability to use oxygen or halogens due to the fact that these gases will even more aggressively destroy the filament [4]. By growing diamonds at relatively low substrate temperatures a step forward was made towards depositing diamond on temperature sensitive materials [7]. Moreover, HF-CVD is suitable for 3D coatings which makes this technique especially wide spread in tool applications or protective coatings [4].

Another frequently employed technique is microwave plasma CVD (MP-CVD). In a standard setup microwaves are emitted from a magnetron at 2.45 GHz; it was first reported in 1983 [8]. The specific setup of the chamber varies; nevertheless comprehensive reviews are available [4]. Its great advantage is the possibility of providing a much cleaner growth environment, due to the well controlled shape of the plasma ball and high purity surge gases. The quality of the materials prepared this way can be outstanding. Another advantage is the

possibility to use oxygen and halogens in the gas mixture; one of its few weaknesses refers to the role of chamber geometry in defining the plasma shape and location. Figure 2.1 illustrates a microwave CVD reactor used for diamond growth.

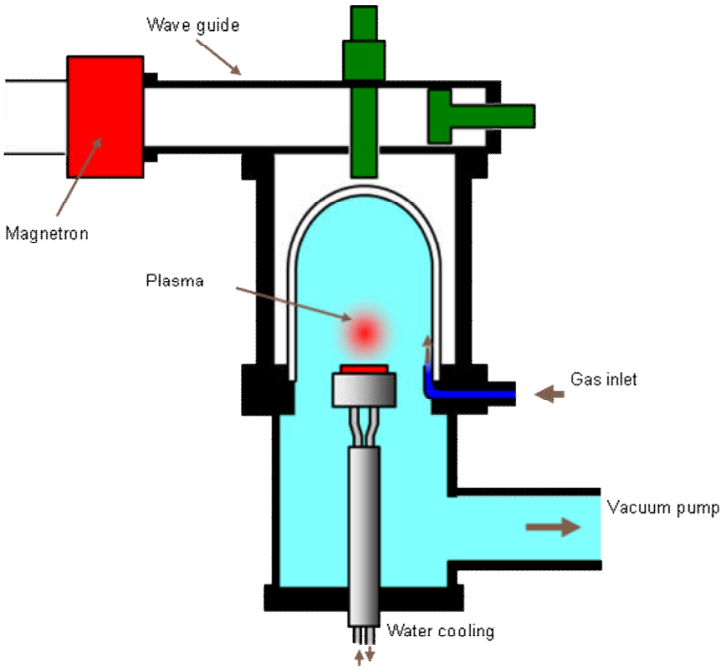

Figure 2.1 Schematic of a microwave CVD reactor used for diamond growth, capable of running at 2.45 GHz, depicting the magnetron, the gas chamber, the plasma ball, the vacuum pump and the water cooling system.

Looking at the chemical processes taking place during growth, the microwave's power, the substrate's temperature, the gases ratio, the presence of impurities are all matters that cannot be ignored. When growing high quality single crystal diamond, controlling the growth conditions and the levels of dopant present in the reactor's chamber is of the utmost importance.

In addition to the gas mixture introduced into the CVD chamber additional aspects have to be taken into consideration while aiming to grow high quality samples. It has been shown that the orientation and the preparation of the substrate, along with the temperature and pressure

can have a significant impact on the sample's morphology. Various groups have proved that it is easier to grow high quality films on a (100) substrate rather than on (111) or (110) [9, 10]. Even if important, the orientation of the substrate is not the only aspect to be taken into account. The manner in which the substrate was prepared, by chemical etching, for example [11, 12], can significantly minimize the lattice defects (polishing lines, dislocations, various other secondary nucleation sites) and so improve the step flow growth [13].

In order to understand the effect of the surface pre-treatment of (100) sectors on the quality of the deposited films, theoretical studies were conducted [12, 14] and the appearance of (110) and (113) faces on the edges and the corners of the crystal was reported. The main model parameters are α, β, γ, the relative displacement speeds of the (111), (110) and (113) planes normalised to that of the (100) planes [15, 16]. Experimental studies have confirmed the theoretical predictions of the expected morphology for the single crystal diamonds. Figure 2.2 depicts images of the experimentally obtained and theoretically predicted shape of the single crystal diamond sample.

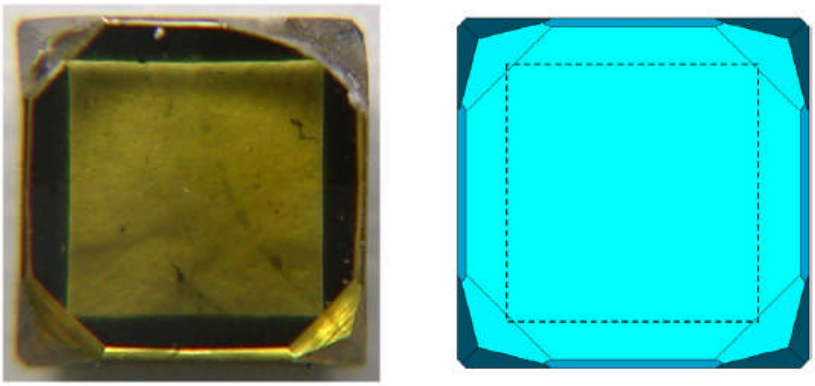

Figure 2.2 Images of (a) the experimentally grown homoepitaxial film under high purity conditions and (b) the theoretical predicted shape of a crystal grown using the model described in [16] with the parameters α=1.8, β=1.1 and γ=4 [15].

The model also has limitations, as it does not take into account the real-life constraints coming from the physico-chemistry of the growth process, the substrate availability or the growth specificities of different crystalline planes such as twinning for (111) or micro-faceting on (110) faces [15, 17].

By optimising these features, the properties of the CVD material are also better controlled. Techniques such as X-ray topography illustrated that bundles of dislocations can have their origin at the interface [18], while EPR and photoluminescence (PL) showed that the electronic properties of high quality samples thought to be identical, still vary [19].

Overall, the MP-CVD method proved to be perfect for obtaining diamond at lower cost than natural, especially because of its efficiency in controlling the properties of the produced material. Element Six (E6) Ltd. has patented methods of growing thick single crystal (sc) CVD samples as well as methods of growing very high purity samples without adding nitrogen [20].

However, as it was already pointed out, diamond is never defect or/ and impurity free. They can appear as volume lattice defects (voids and inclusions), planar lattice defects (grain boundaries, microtwins, stackling faults), line lattice defects (dislocations) or point lattice defects (interstitial and substitutional defects and vacancies) [21]. Diamond View (see Chapter 4, section 4.3) images exemplifying characteristic linear and bubble-like features seen in CVD diamond which can be related to the growth surface steps, growth sectors boundaries and pits are presented in Figure 2.3.

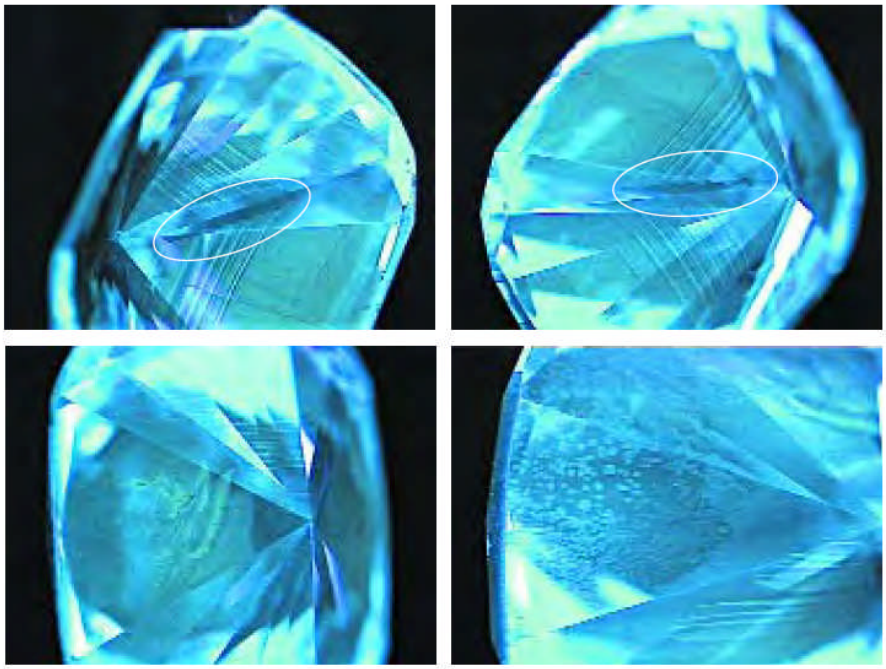

Figure 2.3 Diamond View images depicting characteristic linear and bubble-like features seen in CVD diamond which can be related to the growth surface steps, growth sector boundaries and pits. Other features can also be observed [18].

Generally these defects are detrimental to the overall electronic, mechanical, optical and thermal performance of the material, but advantageous effects have also been noticed, such as doping. Through this process a carbon atom is replaced by a foreign element which incorporates in the diamond's lattice. The most common impurities present in today's CVD diamond are nitrogen, boron and hydrogen.

2.2. Doped diamond

Diamond's excellent properties, see Chapter 1, section 1.2, the width of its bandgap, etc reinforce its great potential as a semiconductor. Currently intrinsic diamond homoepitaxial grown by CVD can yield mobilities higher than the best natural diamonds, thus values beyond 2500 cm^2/Vs at room temperature can be regularly obtained using this growing technique [22]. Even if it is an intrinsic material, diamond can be turned from an intrinsic to

an extrinsic semiconductor at room temperature by introducing different impurities in its lattice. The extremely compact diamond lattice will not allow substitutional doping for many elements. Nevertheless dopant species like B and N (neighbours next to C in the periodic table) are readily incorporated into substitutional sites; larger impurities like Si, P and Ni have also been shown to incorporate substitutionally but with relatively low solubilities compared to B and N [23].

To date, boron is the only dopant element that can cause p-type conductance and is well characterised. Natural type IIb diamonds are p-type semiconducting diamonds due to the presence of boron discovered inside their crystal structure [24]. They are very rare, and are typically only doped with 1- 5 ppm of boron. Initially, by comparing acceptor concentrations as obtained from Hall data and aluminium concentration as determined by neutron activation analysis [25], the role of the acceptor was attributed to aluminium, but detailed studies uncovered the nature of the acceptor as being substitutional boron [24, 26].

Attempts to obtain synthetic boron doped CVD diamonds were conducted and the activation energy was reported to be close to the value for natural IIb diamonds [27]. The necessary atom concentrations are achieved by introducing high purity diborane (B_2H_6) [22] or trimethylboron ($B(CH_3)_3$) [28] to the source gas during the plasma growth process. Almost at the same time with the successful incorporation of B in diamond by the CVD synthesis, p-type doping was also achieved by HPHT, using ion implantation and annealing techniques [29].

When acceptor impurities are introduced in the diamond lattice, p-type semiconducting diamond is obtained and thus discrete acceptor energy levels are formed above the valence

band. The boron acceptor is considered shallow because its activation energy is only 0.37 eV [26, 30], but even with such a low activation energy, the necessary energy is still too large compared with k_BT at room temperature (~25 meV). Consequently, thermal excitation of holes in the valence band is hindered, and only 4- 5% activation of the acceptor levels (even at 500 K) is possible in the low doping regime. This explains why high concentrations of boron atoms, as high as 10^{19} - 10^{20} cm^{-3}, are necessary for reasonable electrical conductivity [22].

The process of growing boron doped diamond is very sensitive, the incorporation of B being growth substrate and growth sector dependent. Various studies presented details about B incorporation in diamond films depending on the substrate type (obtaining single or polycrystalline diamonds) [31], the gas concentrations or the changes induced by substrate temperature variations [15, 23, 32]. The B uptake was also found to be growth sector dependent, with an order of magnitude increase in incorporation probability in (111) sectors compared with (100) sectors [33] and although the average boron concentration might be uniform on a scale larger than the grain size, at the same scale as the grain size the local boron concentration can vary greatly [28, 34].

There is considerable interest to exploit boron doped samples for a great range of applications such as field effect transistors, high-power transistors, electrochemical sensors, etc. The conduction mechanism of boron doped diamonds was investigated and for this material the conduction is believed to be of a semiconducting nature, but metallic conduction can be obtained when B acceptor concentrations exceeds 2 x 10^{21} cm^{-3} [23]. The superconducting properties of super heavily B-doped synthetic diamond layers were also explored [35, 36].

Regarding other potential dopants, substitutional nitrogen is not a practical n- type dopant as the activation energy is E_A= 1.7 eV [37]. Phosphorus is somewhat more shallow, E_A= 0.6 eV, and has been discussed [38]. Despite some research successes, practical phosphorus doped devices are far from commercial use as the material grown is extremely defected, abundant in twin sites, cracks, dislocations, etc.

There are still problems that must be overcome and many basic questions that require further investigation. For example, why the substrate on which the diamond is grown influences the quality of the final diamond sample [39]. The diamond's fabrication cost are high, but because of its amazing properties the range of possible diamond applications has expanded dramatically: radiation detector device [40, 41], hard or protective coating [42], optical windows [43], useful electrode because of its complete chemical inertness [44], potential semiconductor [45, 46] if doped with boron or phosphorus. However, for high quality electronic application, single-crystal diamond is required.

2.3. Electrical properties of diamond

Research into the electrical properties of diamonds has been carried out since it was discovered that the material was a reasonable conductive solid. The transport properties of the samples depend on their intrinsic defects and extrinsic contaminations or dopants (nitrogen, phosphorous or boron) and on their structural morphologies such as dislocations and polycrystallinity (different grains, different orientations, varying doping levels, etc). The main techniques employed for these studies are time of flight and spectrally resolved photoconductivity, temperature dependent dark conductivity and Hall effect measurements [47-50].

Investigations into the carrier mobility have been conducted as far back as the 1970s [51]. Diamond's widely quoted large band gap and its relative permittivity suggest a breakdown field of 1000 V μm^{-1}. Measurements to indentify this were conducted using Schottky diodes. Twitchen and al. [49] have reported a breakdown of 2.5 kV for an 18 µm thick intrinsic film. Values of the same magnitude have been also obtained by other groups [52, 53].

To date, the highest carrier mobilities in high purity intrinsic CVD diamonds were reported in 2002 [50]. Using Hall effect measurement and the sign of the Hall voltage it was established that in intrinsic diamond the carriers are holes. At room temperature values as high as 3800 (± 400) $cm^2V^{-1}s^{-1}$ for the hole mobility have been reported. Even at 400 K the mobility is still higher than 2000 $cm^2V^{-1}s^{-1}$. For the electron mobility values of 4500 $cm^2V^{-1}s^{-1}$ have been recorded [50].

As discussed in section 2.2 several dopants have been considered to transform intrinsic diamond from an insulator into a semiconductor or even a metallic-like material. Both phosphorous and boron have been investigated [54, 55], however most of the research has been focused on boron. The electronic properties of doped diamond are governed by a combination of bulk and grain boundary effects. To achieve practical conduction the dopant level has to be > 10^{20} cm^{-3}. By increasing the concentration the conduction mechanism is altered; the band type conduction changes into hopping conduction and then to metallic-like conduction [56]. Figure 2.4 shows the variation of the resistivity of boron doped single crystal diamond at 300 K with boron doping levels. Below about 2 x 10^{19} cm^{-3}, the decrease is inversely proportional to the acceptor density. In the range 2 x 10^{19} to 3 x 10^{20} cm^{-3} hopping conduction becomes dominant [37].

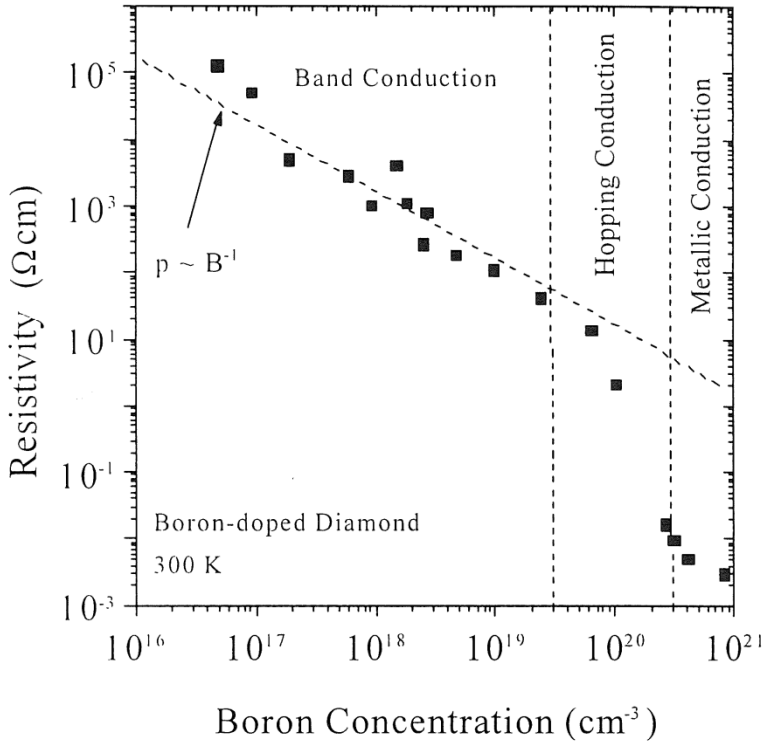

Figure 2.4 Variation of the resistivity of single crystal boron doped diamond at 300 K with boron doping levels. Below about 2 x 10^{19} cm^{-3}, the decrease is inversely proportional to the acceptor density. In the range 2 x 10^{19} to 3 x 10^{20} cm^{-3} hopping conduction becomes dominant [37].

Through a combination of conductivity and Hall effect experiments the carrier mobilities for boron doped samples have been determined. As expected the mobility's value in polycrystalline material is much smaller than in a single crystal. For polycrystalline diamonds, values in the range 1- 30 $cm^2V^{-1}s^{-1}$ have been registered [57], whereas in a single crystal the values were as high as 229 $cm^2V^{-1}s^{-1}$ [58]. By increasing the boron concentration the mobility will eventually fall to zero.

Figure 2.5 summarises results measured at room temperature on boron doped natural and synthetic [59], homoepitaxially grown single crystal CVD diamond [60], heteroepitaxially grown diamond (HOD) [61] and polycrystalline diamond films [57]. The scattering data are

attributed to residual impurities in these films, such as Fe and Mo. This collection of data clearly proves that the mobilities of the homoepitaxially grown films are 10- 50 times higher than the mobilities of the heteroepitaxially grown ones [62].

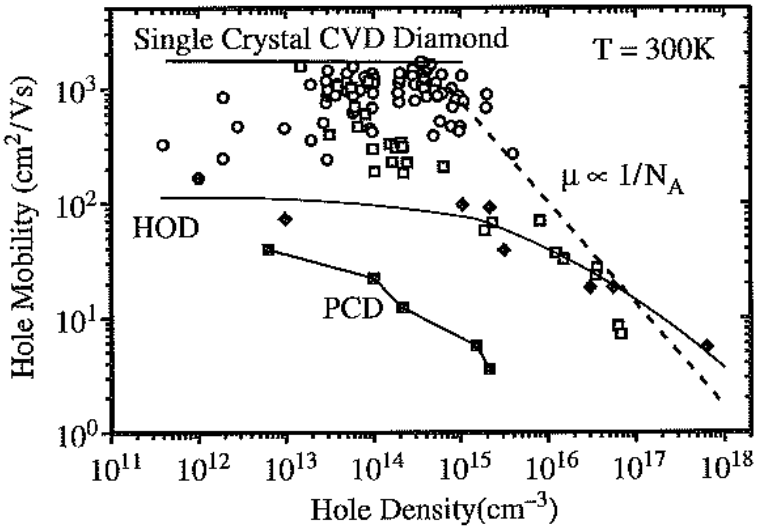

Figure 2.5 Hole mobilities measured as a function of hole densities at room temperature on natural and synthetic (□ [59]), on homoepitaxially grown single crystal (○[60]), on polycrystalline CVD diamond grown heteroepitaxially on silicon either highly (HOD)(♦ [63], ●[61]), or randomly oriented (PCD) (■[57]). The full lines are guide to the eyes and the dashed line shows the expected variation assuming scattering at ionized impurities [62].

2.4. Electrochemistry with diamond electrodes

2.4.1. H terminated intrinsic diamond

As-grown CVD diamonds are hydrogen terminated. The surface of the sample is hydrophobic [64]. However, by oxygen plasma treatments or by anodic polarization the surface changes from hydrophobic to hydrophilic [65-71] for both polycrystalline and single crystal diamond. With a band gap of ~5.5 eV, intrinsic diamond is an insulator; in 1989 Landstrass and Ravi found that H-terminated intrinsic diamond possesses significant surface conductivity [72, 73]. Since it was identified, this phenomenon provoked strong discussion as to the origin of this observation. The initial discovery of hydrogen surface conductivity on as-grown diamond led to the suggestion of many models such as passivation of deep defects, the formation of

shallow acceptor states and an adsorbate based transfer doping mechanism [64, 73-75]. Several groups have since confirmed the surface conductivity of H-terminated diamonds. It is now know that the surface conductivity of H-terminated diamonds is between 10^{-4} - 10^{-5} $\Omega^{-1}m^{-1}$ (at room temperature), the surface density of the p-type carriers responsible for the conductivity is $\rho_s = 10^{13}$ cm^{-2}, it is not temperature dependent between room temperature and 150 K and that the reported Hall mobility varies between 1 $cm^2 V^{-1} s^{-1}$ and a maximum of 70 $cm^2 V^{-1} s^{-1}$ for a carrier density of 1.2 x 10^{12} cm^{-2} [76-79].

The sign of the Hall coefficient suggests that the carriers are holes present in an accumulation layer at the surface. Opinions regarding the ''thickness" of this accumulation layer are divided extending from species at the surface to 10 nm into the diamond [80]. It has also been implied that it might be a layer buried 30 nm under the surface [81].

As already stated a clean diamond surface can be terminated by chemisorption. To promote an efficient electron transfer the lowest unoccupied orbital of the adsorbate has to be lower in energy than the diamond's highest occupied one, which is the valence band maximum. The difference in electronegativity between the diamond's surface carbon atoms and the atoms which terminate the surface, determine the dipole's sign and magnitude. This is equivalent with stating that electron affinity of the surface acceptors has to be larger than the ionization energy of the diamond [82]. Since carbon is more electronegative than hydrogen, through hydrogenation the electron affinity (χ) of diamond surfaces can give negative values; through oxygenation the electron affinity of diamond surfaces increases as a result of the large electronegativity of O [82]. Schematics of the modification of electron affinity (χ) and ionization potential (I) of diamond surfaces by hydrogen and oxygen termination and band

diagrams for the clean and fully H- and O-terminated diamond surfaces are presented in figure 2.6 [82].

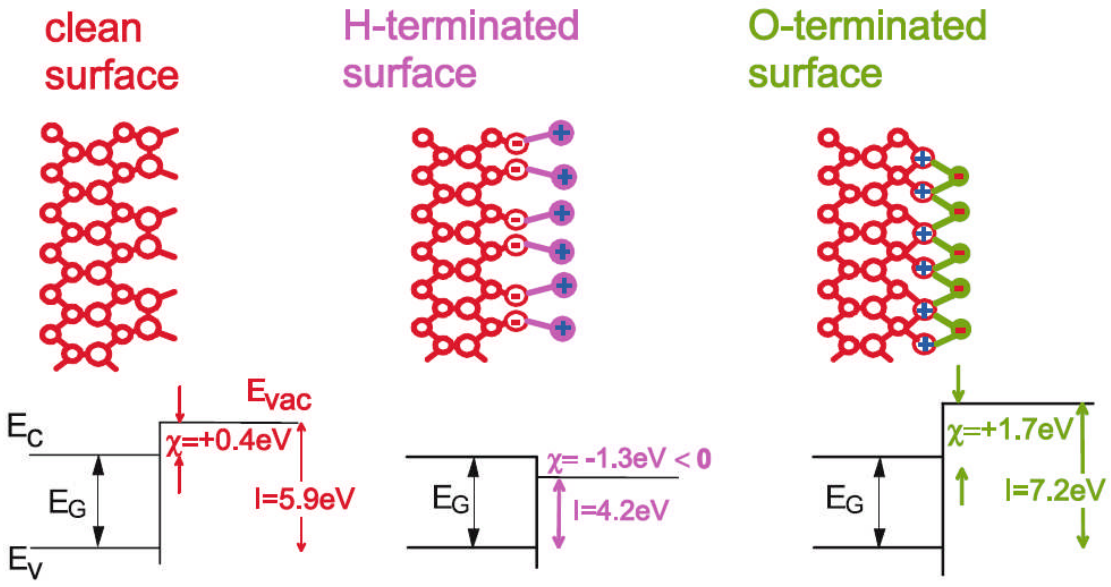

Figure 2.6 Schematics of the modification of electron affinity (χ) and ionization potential (I) of diamond surfaces by hydrogen and oxygen termination and band diagrams for the clean and fully H- and O-terminated diamond surfaces [82].

As the surface conductivity has been noticed only for H-terminated surfaces and vanishes when the samples are oxygenated it was believed that H was directly responsible for the hole accumulation layer (by creating some sort of unidentified defects that act as acceptors) [74].

Ley, Maier et al. [74] have proved that the H termination is necessary but it is not a sufficient condition for surface conductivity to be observed. It has been shown by various in situ measurements that conductivity does not appear after hydrogenation until the sample is exposed to air; so the H alone cannot be the cause for the shallow acceptors needed to create the hole accumulation layer. These acceptors must be supplied by atmospheric adsorbates. An electrochemical surface transfer doping model was suggested in which solvated ions in a thin, aqueous, atmospheric layer were responsible for the extraction of electrons from intrinsic

diamond, leaving behind holes as mobile charge carriers and so creating the surface conductivity [74]. A schematic of the surface transfer doping of diamond surfaces by hydronium ions acting as surface acceptors is presented in Figure 2.7. The chemical potential μ_e of the electrons in the electrolytic adsorbate layer on the surface is determined by the redox couple H_30^+/ H_2. Electron transfer from the diamond to the hydronium ions drives the indicated redox reaction towards the hydrogen side, leaving holes and uncompensated anions on the surface behind. As a consequence of this space-charge separation, the holes are confined to the surface by an upward band bending potential [82].

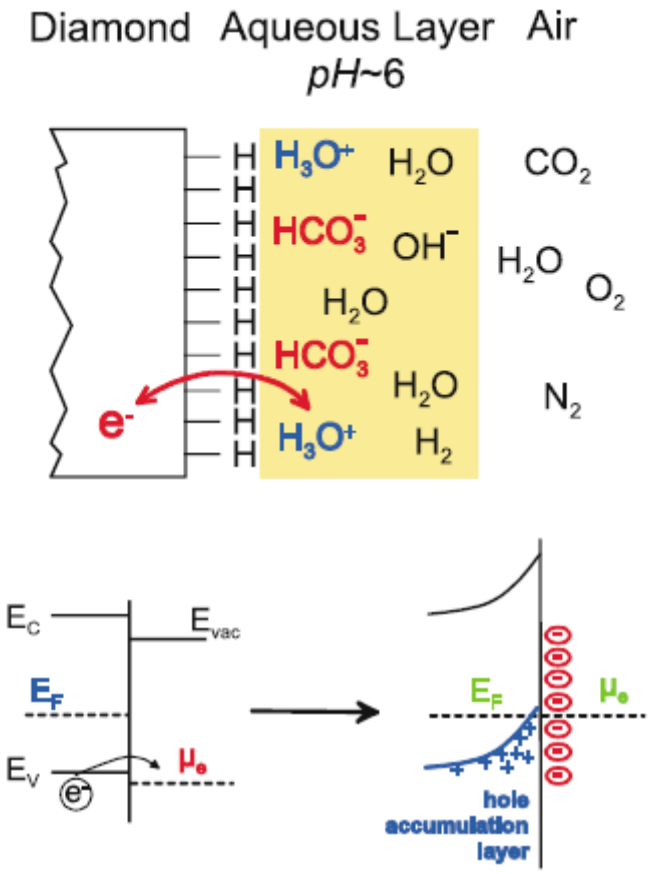

Figure 2.7 Schematics of the surface transfer doping of diamond surfaces by hydronium ions acting as surface acceptors. The chemical potential μ_e of the electrons in the electrolytic adsorbate layer on the surface is determined by the redox couple H_30^+/H_2. Electron transfer from the diamond to the hydronium ions drives the indicated redox reaction towards the hydrogen side, leaving holes and uncompensated anions on the surface behind. As a consequence of this space-charge separation, the holes are confined to the surface by an upward band bending potential [82].

The driving force behind the charge transfer was thought to be the electrochemical potential of the redox couple H_30^+/ H_2 in the aqueous layer and the charge transfer was accompanied by a redox reaction transforming hydronium ions to hydrogen. After reaching equilibrium between the diamond and the adsorbte system, the positive space charge of the holes and an equal amount of negative sheet charge of anions cause an upward bending that restrains the holes close to surface. The termination of the surface by chemisorbed hydrogen was thought to be indirectly responsible for the charge transfer by reducing the ionization potential [74, 82, 83].

Fullerene molecules were investigated as alternative surface acceptors on diamond. p-type transfer doping of hydrogenated diamond was also established using these neutral species [84, 85]. However, fullerene molecules lack thermal stability on diamond surfaces, so that encapsulation and passivation of fullerene doping layers are mandatory for electronic application in field-effect devices [64, 82].

Many studies conducted by Garrido et al. [86], Foord et al. [87] and Ristein et al. [83] have confirmed the model, being now widely accepted. H termination of diamond does not only lead to a negative electron affinity of the surface, but also to the lowest ionization potential of all semiconductors, even if it has a very large band gap. This characteristic is indirectly responsible for the unique type of doping that can be achieved on an H-terminated diamond.

Hydrogen terminated intrinsic diamond have been employed in electrochemistry, but the results suggest that on these surfaces electron transfer kinetics are rate limiting [88].

2.4.2. Boron doped polycrystalline diamond

The rarity of natural boron doped diamond prevented their exploitation for any type of technical applications. The advancements made towards its synthesis in larger, higher quality quantities using CVD, see section 1.2, laid the basis for its exploitation as an electronic and electrochemical material. As polycrystalline material was more readily available (easier to grow as it can be grown on a non diamond substrate, larger samples, etc.) almost all electrochemical studies have been carried out using polycrystalline boron doped diamond.

Intrinsic diamond is an insulator; however if boron doped, diamond exhibits bulk electrical conductivity, a property analysed in a few reviews [89, 90]. By increasing the boron concentration, the diamonds properties can vary from an insulator, to a semiconductor (10^{18} < [B] < 10^{20} cm^{-3}), to a quasi-metal ([B] > 2 x 10^{20} cm^{-3}). This material has been shown to be a complex electrode surface, with metal like properties under steady state conditions boding well for analytical applications. Some of the properties with relevance to electrochemistry such as low background current density, high resistance against chemical and electrochemical corrosion, wide potential window, stability in aqueous and non-aqueous media [91, 92] have been extensively reviewed [89, 90, 93]. However, polycrystalline diamond has different grains with different orientations, different boron uptake, different electrochemical response and possible non–diamond intergranular material. For example the boron incorporation on the (111) face is approximately ten times higher than on (100) face [94-96]. Moving away from the steady-state conditions highlights these heterogeneities. The relevance of studying the correlation between the macroscopic electrochemical properties of boron doped diamond electrodes and their properties at a microscopic level was also emphasised [90, 97] as the highlighted heterogeneities can distort their electrochemical properties.

Having a wide potential window in aqueous [67, 91, 98, 99] and non aqueous [100-102] environments, very low capacitance [103-105], fast electron transfer for representative redox systems [106] boron doped diamond (BDD) generated great interest. It is well known and understood that for classical electrodes such as platinum [107] or silver [108, 109] the exposed face has an impact on the electrochemical behaviour. For example using Fourier Transform Infrared spectroscopy (FTIR) and Cyclic Voltammetry (CV) it has been shown that the electrochemical behaviour and electrocatalytic activity of adsorbed cyanide is strongly dependent on the electrode structure Pt(111), Pt(100) or Pt(110) [107]. Ag (100) and Ag (111) single crystal surfaces gave different responses for CVs recorded in aqueous NaOH solution [108]. Diamond's electrochemical properties for different crystal faces can be evaluated using similar approaches. The electron transfer kinetics of different grains will be different and, as mentioned before, since boron tends to incorporate more readily into the (111) plane it is obvious that the electron transfer rates could be higher for the (111) faces electrodes rather than for the (100) ones. At a polycrystalline electrode's surface various faces are exposed so the electrochemical activity is not homogeneous. These relations between the diamond's structure and its electrochemical properties have been investigated using a combination of high- resolution imaging techniques such as cathodoluminescence (CL), conducting atomic force microscopy (C-AFM) and scanning electrochemical microscopy (SECM) [110]. The study has shown that the local electrochemical activity is linked to the underlying conductivity of individual grains, which at its turn is governed by the uptake of boron [110]. Figure 2.8 shows C-AFM images recorded in air of (a) height and (b) conductivity of a polycrystalline BDD sample. The conductivity image was taken at a tip potential of -5 V with a 10 MΩ current-limiting resistor in series. Two types of regions are clearly present: (i) "high'' conductivity regions (white) where the current is ~ 500nA and (ii)

"lower'' conductivity regions (black) where the current is ~ 250 nA. Even the same kind of regions still present conductivity variations [110].

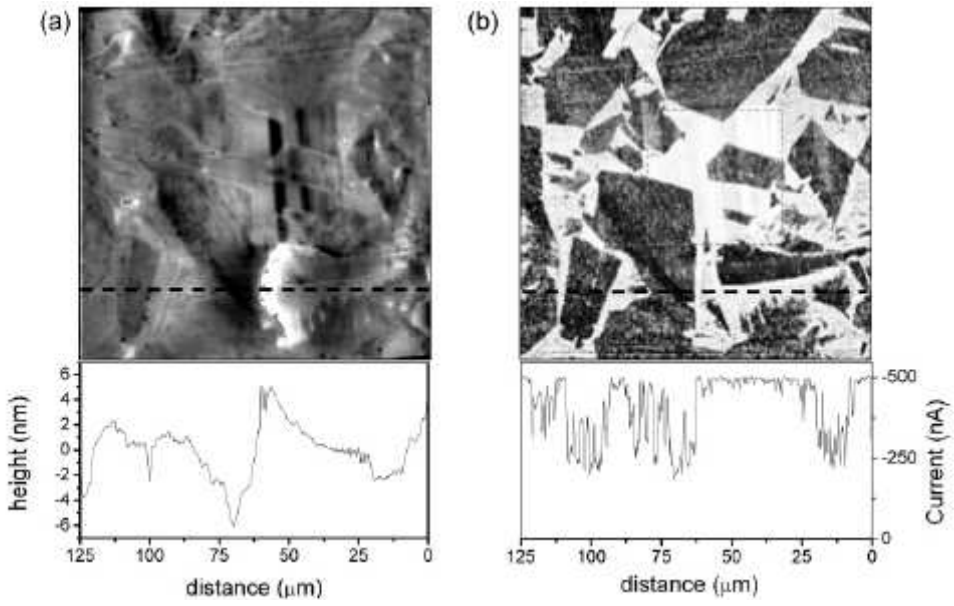

Figure 2.8 Simultaneously recorded C-AFM images (125 x 125 μm) of (a) height and (b) conductivity of the polycrystalline BDD sample recorded in air. The conductivity image in (b) was taken at a tip potential of -5 V (i.e., substrate potential +5 V) with a 10 MΩ current-limiting resistor in series. White represents regions of higher current [110].

It is known that in addition to the carrier concentration effects, the modification and the density of surface functional groups created by various surface treatments affect the electrochemical properties [106]. The as-grown surfaces, which were highly hydrophobic, become hydrophilic after the oxygen plasma treatment. The apparent surface conductivity was not significantly changed after the oxygen plasma treatment. However, the electrochemical responses to several redox systems became remarkably different. For example, the cyclic voltammetric anodic–cathodic peak separations for the oxygen-terminated diamond electrodes became extremely large compared to those for the as-grown electrodes [106].

2.4.3. Boron doped single crystal diamond

Much of the research published so far on boron doped diamond, at a fundamental level or related to industrial applications, has been conducted on polycrystalline material. Its wide availability and the continuous increase in the quality of diamond synthesised have boosted scientific work. In spite of all this, in order to understand fundamental aspects relating the diamond's structure to its electronic and electrochemical properties, strategic research needs to be conducted on single crystal diamond. Single crystal CVD diamond promises to be a good material for electrical and electrochemical application because the boron dopant density should be more homogeneous (although dependent on defect density) and it should also present metallic properties if highly doped.

Theoretical and experimental investigations have been carried out into the growth mechanisms of single crystal diamond [15, 94]. It was noted that during the CVD growth, on average, higher growth rates lead to lower crystal quality, causing the development of e.g. twins, pits, and dislocations. These defects are assimilated easier into the (111) growth sector than into the (100) one [18]. Even if identical gas chemistry and conditions are employed, the (111) sector seems more prone to defects (twins, kinks, vacancies) formation, while the (100) sector presents no defects or additional structures formation. This also explains the readiness of boron to incorporate to a greater extent into the (111) sector [28, 34]. The growth of high quality single crystal diamonds on the (111) sector, has not been addressed to the extent of the growth on (100), however theoretical studies emphasised many difficulties that might be encountered while trying to obtain a high quality sample onto this sector [15]. As discussed in section 2.1., the substrate's temperature, the gas mixture, etc., are parameters difficult to manipulate, important during growth and which will influence the quality of the end product.

Broadly speaking, for CVD diamonds, the size of the diamond that can be grown depends on the efficiency of the CVD reactor and on the size of the substrate. For polycrystalline diamonds, as large wafers (which do not need to be diamond) can be used as substrate, large samples can be obtained. For single crystal diamonds, as the sample area depends on the substrate area, one disadvantage would be that the substrate, a single crystal of diamond, is small (a few mm^2), expensive and poses problems at a practical level. The growth conditions need to be more rigorous than for polycrystalline material and by increasing the size of the substrate their boundaries are pushed; the substrate needs to be atomically flat so the crystal structure can be harmonised. This also increases the production cost, if especially polishing is taken into consideration. In order to obtain high quality material, carbon should be incorporated slowly, which means a slow growth rate and high production costs. Regardless of the challenges encountered, such as reducing the dislocations content and the differential incorporation in steps or striations [18], growing CVD synthetic high quality single crystal boron doped diamond has been achieved [22].

Researchers have looked into employing single crystal boron doped diamond as an electrode, but the lack of samples' availability (due to the difficulties encountered during the growth process) represented a major drawback. Therefore, the literature available on their electrochemistry is somewhat limited [68, 111-116].

These studies reported that single crystal diamond has a lower background current [111, 115], a wider working potential window [114], decreased interference from adsorption [115] and it is more analytically sensitive than polycrystalline diamond [68, 115]. The redox kinetics of ferri-ferrocyanide at the boron doped single crystal diamond was investigated and slow electron transfer kinetics at the O-terminated diamond/solution interface was observed, while

it exhibited fast electron transfer at H-terminated surfaces [111]; outer-sphere redox systems showed reversible redox-kinetics around the equilibrium potential, as with a metal electrode [113]. When the films were grown under different boron concentration in the feeding gas, chosen in such a way that the acceptor concentration in the different diamond films is the same, no significant difference in the kinetic behaviour was found between (equally doped) (111)- and (100)-faces [117]. A different study showed that (100) and (110) have different flat band potentials, while the doping density is comparable to that found using IR absorption and Hall- measurements [113].

Kondo [116] analysed the electrochemical properties of anodically treated homoepitaxial single crystal diamond. From the impedance behaviour it was found that an additional film capacitance element was generated by the anodic treatment. The characteristics of this sub-circuit exhibited a very slight dependence on the applied potential, suggesting that it is due to a passivation layer on the diamond surface. The capacitative character of the hydrogen-terminated surface was greatly dependent upon the potential and indicated the presence of a high concentration of acceptors, higher than expected from the boron doping level alone, suggestive of a surface region containing hydrogen acting as an acceptor. It was concluded that, the anodic treatment of BDD electrodes can cause significant changes in the electrochemical properties of these electrodes, due to changes in both the doping of the near – surface region, as well the termination of the surface itself.

2.4.4. Diamond functionalisation

By oxidising the diamonds' surface, the surface conductivity and the surface groups can be altered [71, 118]. The type of crystal surface (111 versus 100), as already stated can create different functional groups [119]. Ethers and carbonyls will to a large extent form on the

(100) surface, while hydroxyls will form on the (111) face, but will bond also to the (100) surface as they are hydrogen bonded to each other [120-131]. For these studies techniques such as high-resolution electron energy loss spectroscopy (HREELS), Auger electron spectroscopy (AES), electron loss spectroscopy (ELS) and low energy electron diffraction (LEED) have been used. In terms of functionalisation, stability and reactivity, they are comparable to other organic compounds and so make it possible for diamond's surface to be modified with DNA or various enzymes [132-134].

The effect of diamond functionalisation with various chemical groups has already been described and investigated in various laboratories [120-134]. Research was also conducted into the influence of surface morphology on to the electrochemical behaviour by using both H- and O-terminated diamond electrodes [135]. The smooth surface (average roughness 30 nm) presented a lower background current than the initial rough surface (average roughness 238 nm). Electrochemical investigations employing several redox couples showed that there are no drastic changes in the case of the H-terminated electrode regardless of the sample's morphology. The results altered for some redox couple when the sample was O-terminated. Smaller peak to peak separations are obtained for the smooth surface; therefore, it is believed that this is due to an increase in the heterogeneous electron transfer rate constant at the electrode with the smoothed surface compared to the electrode with the rough surface.

Overall, more work needs to be carried out into the growth of high quality single crystal diamond. Making significant advancements in this field will enable fundamental research into their electrical and electrochemical behaviour.

References:

[1] W. G. Eversole, and N. Y. Kenmore, (US Patent 3030187, 1958).
[2] J. C. Angus, Will, H. A., *et al*, Journal of Applied Physics **39**, 2915 (1968).
[3] J. E. Butler, and R. L. Woodin, Philosophical Transactions of the Royal Society of London Series A-Mathematical Physical and Engineering Sciences **342**, 209 (1993).
[4] M. A. Prelas, G. Popovici, and L. K. Bigelow, *Handbook of industrial diamonds and diamond films* (Marcel Dekker, INC., New York, 1998).
[5] J. Ma *et al.*, Journal of Applied Physics **106** (2009).
[6] M. Werner, Locher, R., Reports on Progress in Physics **61**, 1665 (1998).
[7] F. Piazza *et al.*, Diamond and Related Materials **15**, 109 (2006).
[8] M. Kamo *et al.*, Journal of Crystal Growth **62**, 642 (1983).
[9] C. Findelingdufour, A. Vignes, and A. Gicquel, Diamond and Related Materials **4**, 429 (1995).
[10] L. F. Sutcu *et al.*, Journal of Applied Physics **71**, 5930 (1992).
[11] G. Bogdan *et al.*, Physica Status Solidi A-Applications and Materials Science **202**, 2066 (2005).
[12] A. Tallaire *et al.*, Physica Status Solidi A-Applications and Materials Science **201**, 2419 (2004).
[13] N. S. Lee, and A. Badzian, Diamond and Related Materials **6**, 130 (1997).
[14] F. Silva *et al.*, Physica Status Solidi A-Applications and Materials Science **203**, 3049 (2006).
[15] F. Silva *et al.*, Diamond and Related Materials **17**, 1067 (2008).
[16] F. Silva *et al.*, Journal of Crystal Growth **310**, 187 (2008).
[17] G. Janssen *et al.*, Journal of Crystal Growth **125**, 42 (1992).
[18] P. M. Martineau *et al.*, Gems & Gemology **40**, 2 (2004).
[19] A. Secroun *et al.*, Diamond and Related Materials **16**, 953 (2007).
[20] G. A. Scarsbrook *et al.*, (Patent WO 0196633 A1, 2001).
[21] H. M. Liu, and D. S. Dandy, Diamond and Related Materials **4**, 1173 (1995).
[22] G. A. Scarsbrook *et al.*, (Patent WO 03052174A2, 2003).
[23] S. Koizumi, Nebel C., Nesladek M., *Physics and applications of CVD diamond* (Wiley-VCH, 2008).
[24] R. M. Chrenko, Physical Review B **7**, 4560 (1973).
[25] P. J. Dean, E. C. Lightowlers, and D. R. Wight, Physics Review **140**, A352 (1965).
[26] A. T. Collins, Lightowlers, E. C. , Physical Review **171** (1968).
[27] N. Fujimori, H. Nakahata, and T. Imai, Japanese Journal of Applied Physics Part 1-Regular Papers Short Notes & Review Papers **29**, 824 (1990).
[28] R. Samlenski *et al.*, Diamond and Related Materials **5**, 947 (1996).
[29] G. Braunstein, and R. Kalish, Journal of Applied Physics **54**, 2106 (1983).
[30] A. T. Collins, and A. W. Williams, Journal of Physics Part C Solid State Physics **4**, 1789 (1971).
[31] E. Gheeraert, A. Deneuville, and J. Mambou, Carbon **37**, 107 (1999).
[32] C. Nebel, and J. Ristein, *Thin- film diamond II* (Elsevier Academic Press, 2003), Vol. 77.
[33] K. Ushizawa *et al.*, Diamond and Related Materials **7**, 1719 (1998).
[34] R. Locher *et al.*, Diamond and Related Materials **4**, 678 (1995).
[35] E. Bustarret, Kacmarcik, J. et al. , Physical Review Letters **93**, 237005_1 (2004).
[36] E. A. Ekimov *et al.*, Nature **428**, 542 (2004).

[37] M. H. Nazare, and A. J. Neves, *Properties, Growth and Applications of Diamond* (INSPEC, London, 2001), Vol. 26.
[38] S. Koizumi *et al.*, Applied Physics Letters **71**, 1065 (1997).
[39] A. R. Krauss *et al.*, Diamond and Related Materials **10**, 1952 (2001).
[40] L. Allers *et al.*, Diamond and Related Materials **6**, 353 (1997).
[41] A. Mainwood *et al.*, Journal of Physics D-Applied Physics **28**, 1279 (1995).
[42] P. Ball, New Scientist **153**, 22 (1997).
[43] www.e6.com.
[44] Y. V. Pleskov *et al.*, Russian Journal of Electrochemistry **38**, 620 (2002).
[45] E. Bustarret, E. Gheeraert, and K. Watanabe, Physica Status Solidi A-Applied Research **199**, 9 (2003).
[46] T. Yokoya *et al.*, Nature **438**, 647 (2005).
[47] E. Kohn, and A. Denisenko, Thin Solid Films **515**, 4333 (2007).
[48] A. Vescan *et al.*, Diamond and Related Materials **5**, 747 (1996).
[49] D. J. Twitchen *et al.*, IEEE Transactions on Electron Devices **51**, 826 (2004).
[50] J. Isberg *et al.*, Science **297**, 1670 (2002).
[51] A. W. Williams, Lightowl.Ec, and A. T. Collins, Journal of Physics Part C Solid State Physics **3**, 1727 (1970).
[52] R. Kumaresan *et al.*, Diamond and Related Materials **18**, 299 (2009).
[53] W. Huang *et al.*, Proceedings of the 17th International Symposium on Power Semiconductor Devices & ICS, 319 (2005).
[54] A. Kubovic *et al.*, Diamond and Related Materials **13**, 755 (2004).
[55] S. Koizumi *et al.*, Science **292**, 1899 (2001).
[56] J. P. Lagrange, A. Deneuville, and E. Gheeraert, Diamond and Related Materials **7**, 1390 (1998).
[57] J. T. Huang *et al.*, Applied Physics Letters **68**, 3784 (1996).
[58] B. A. Fox *et al.*, Diamond for Electronic Applications **416**, 319 (1996).
[59] S. A. Grot *et al.*, Applied Physics Letters **58**, 1542 (1991).
[60] D. Takeuchi *et al.*, Physica Status Solidi A-Applied Research **186**, 269 (2001).
[61] B. R. Stoner *et al.*, Applied Physics Letters **62**, 2347 (1993).
[62] C. Nebel, and J. Ristein, *Thin- film diamond I* (Elsevier Academic Press, 2003), Vol. 76.
[63] E. Boettger, *Polykristalline Diamantschichten fur electronische Anwendungen* (PhD thesis, 1995).
[64] H. Kawarada, Surface Science Reports **26**, 205 (1996).
[65] D. A. Tryk *et al.*, Diamond and Related Materials **10**, 1804 (2001).
[66] Y. V. Pleskov *et al.*, Journal of Electroanalytical Chemistry **228**, 19 (1987).
[67] H. B. Martin *et al.*, Journal of the Electrochemical Society **143**, L133 (1996).
[68] H. B. Martin *et al.*, Journal of the Electrochemical Society **146**, 2959 (1999).
[69] T. N. Rao *et al.*, Journal of the Electrochemical Society **146**, 680 (1999).
[70] H. Notsu *et al.*, Electrochemical and Solid State Letters **2**, 522 (1999).
[71] H. Notsu *et al.*, Journal of Electroanalytical Chemistry **492**, 31 (2000).
[72] M. I. Landstrass, and K. V. Ravi, Applied Physics Letters **55**, 1391 (1989).
[73] M. I. Landstrass, and K. V. Ravi, Applied Physics Letters **55**, 975 (1989).
[74] F. Maier *et al.*, Physical Review Letters **85**, 3472 (2000).
[75] R. S. Gi *et al.*, Japanese Journal of Applied Physics Part 1-Regular Papers Short Notes & Review Papers **34**, 5550 (1995).
[76] G. Piantanida *et al.*, Journal of Applied Physics **89**, 8259 (2001).
[77] K. Tsugawa *et al.*, Diamond and Related Materials **8**, 927 (1999).

[78] A. Aleksov *et al.*, Diamond and Related Materials **11**, 382 (2002).
[79] H. Ishizaka *et al.*, Diamond and Related Materials **11**, 378 (2002).
[80] K. Hayashi *et al.*, Journal of Applied Physics **81**, 744 (1997).
[81] A. Denisenko *et al.*, Diamond and Related Materials **9**, 1138 (2000).
[82] J. Ristein, Applied Physics a-Materials Science & Processing **82**, 377 (2006).
[83] J. Ristein, M. Riedel, and L. Ley, Journal of the Electrochemical Society **151**, E315 (2004).
[84] P. Strobel *et al.*, Nature **430**, 439 (2004).
[85] P. Strobel *et al.*, Diamond and Related Materials **14**, 451 (2005).
[86] J. A. Garrido *et al.*, Applied Physics Letters **81**, 637 (2002).
[87] J. S. Foord *et al.*, Diamond and Related Materials **11**, 856 (2002).
[88] C. E. Nebel *et al.*, Diamond and Related Materials **15**, 264 (2006).
[89] J. C. Angus *et al.*, New Diamond and Frontier Carbon Technology **9**, 175 (1999).
[90] C. Levy-Clement *et al.*, New Diamond and Frontier Carbon Technology **9**, 189 (1999).
[91] G. M. Swain, A. B. Anderson, and J. C. Angus, Mrs Bulletin **23**, 16 (1998).
[92] Y. V. Pleskov, Uspekhi Khimii **68**, 416 (1999).
[93] T. Inushima *et al.*, Diamond and Related Materials **9**, 1066 (2000).
[94] B. V. Spitsyn, L. L. Bouilov, and B. V. Derjaguin, Journal of Crystal Growth **52**, 219 (1981).
[95] G. Janssen *et al.*, Journal of Crystal Growth **104**, 752 (1990).
[96] K. Ushizawa, T. Ueda, and M. Tsuboi, Biopolymers **45**, 135 (1998).
[97] J. Wang *et al.*, New Diamond and Frontier Carbon Technology **9**, 317 (1999).
[98] N. Vinokur *et al.*, Journal of the Electrochemical Society **143**, L238 (1996).
[99] P. Bouamrane *et al.*, Journal of Electroanalytical Chemistry **405**, 95 (1996).
[100] Z. Y. Wu *et al.*, Chemistry Letters, **503** (1998).
[101] L. F. Li *et al.*, Journal of the American Chemical Society **119**, 7875 (1997).
[102] M. Yoshimura *et al.*, Diamond and Related Materials **11**, 67 (2002).
[103] J. S. Xu, Q. Y. Chen, and G. M. Swain, Analytical Chemistry **70**, 3146 (1998).
[104] R. Tenne, and C. Levy-Clement, Israel Journal of Chemistry **38**, 57 (1998).
[105] G. M. Swain, Journal of the Electrochemical Society **141**, 3382 (1994).
[106] I. Yagi *et al.*, Journal of Electroanalytical Chemistry **473**, 173 (1999).
[107] F. J. Huerta *et al.*, Surface Science **396**, 400 (1998).
[108] B. M. Jovic, V. D. Jovic, and G. R. Stafford, Electrochemistry Communications **1**, 247 (1999).
[109] N. Hoshi, M. Kato, and Y. Hori, Journal of Electroanalytical Chemistry **440**, 283 (1997).
[110] N. R. Wilson *et al.*, Journal of Physical Chemistry B **110**, 5639 (2006).
[111] R. Ramesham, Sensors and Actuators B-Chemical **50**, 131 (1998).
[112] Y. V. Pleskov *et al.*, Journal of Electroanalytical Chemistry **455**, 139 (1998).
[113] J. van de Lagemaat, D. Vanmaekelbergh, and J. J. Kelly, Journal of Electroanalytical Chemistry **475**, 139 (1999).
[114] M. Yanagisawa *et al.*, Diamond and Related Materials **8**, 2059 (1999).
[115] T. Kondo *et al.*, Journal of the Electrochemical Society **149**, E179 (2002).
[116] T. Kondo *et al.*, Electrochimica Acta **48**, 2739 (2003).
[117] Y. V. Pleskov *et al.*, Journal of Electroanalytical Chemistry **595**, 168 (2006).
[118] H. Notsu *et al.*, Electrochemical and Solid State Letters **4**, H1 (2001).
[119] T. Kondo *et al.*, Journal of the Electrochemical Society **152**, E18 (2005).

[120] R. E. Thomas, R. A. Rudder, and R. J. Markunas, Journal of Vacuum Science & Technology A-Vacuum Surfaces and Films **10**, 2451 (1992).
[121] T. Ando *et al.*, Journal of the Chemical Society-Faraday Transactions **89**, 1783 (1993).
[122] J. Vanderweide, and R. J. Nemanich, Physical Review B **49**, 13629 (1994).
[123] J. L. Whitten *et al.*, Applied Surface Science **75**, 45 (1994).
[124] S. Skokov, B. Weiner, and M. Frenklach, Physical Review B **55**, 1895 (1997).
[125] M. Z. Hossain *et al.*, Surface Science **436**, 63 (1999).
[126] P. E. Pehrsson, and T. W. Mercer, Surface Science **460**, 49 (2000).
[127] P. E. Pehrsson, and T. W. Mercer, Surface Science **460**, 74 (2000).
[128] H. Tamura *et al.*, Physical Review B **61**, 11025 (2000).
[129] K. P. Loh *et al.*, Journal of Physical Chemistry B **106**, 5230 (2002).
[130] P. John *et al.*, Journal of the American Chemical Society **125**, 6600 (2003).
[131] A. Laikhtman *et al.*, Journal of Chemical Physics **119**, 1794 (2003).
[132] K. Ushizawa *et al.*, Chemical Physics Letters **351**, 105 (2002).
[133] S. Wenmackers *et al.*, Physica Status Solidi A-Applied Research **199**, 44 (2003).
[134] P. Krysinski *et al.*, Journal of the American Chemical Society **125**, 12726 (2003).
[135] R. Sato *et al.*, Chemistry Letters **32**, 972 (2003).

Chapter 3
Theoretical aspects

A short review of the theory underpinning the techniques used throughout the entire thesis is introduced in this chapter in order to allow the results presented later to be understood and linked to the underlying theoretical aspects of each technique.

3.1. Diamond Polishing

Research on the polishing of diamond has been carried out for more than 80 years. Reviews on this topic exist, although some of them are now outdated given that the technology has moved on [1, 2]. The polishing of diamonds is different from most polishing operations; wear and polish are carried out simultaneously. There are many techniques used to process diamonds and Malshe [3] provides a comprehensive review on some of the newer approaches such as: mechanical, thermo-chemical, chemo-mechanical processing techniques, laser polishing, ion beam polishing, abrasive jet polishing and reactive ion etching. Each of these techniques induces some degree of surface contamination or surface damage; however, there is a lack of systematic research into the influence that surface damage/contamination has on the electrical and electrochemical performance of samples.

Since the samples discussed in this thesis have been polished on a standard cast iron scaife this technique shall be discussed in detail. This is the method generally employed for polishing single crystal diamonds.

Cast irons are alloys of iron, carbon, silicon and phosphorous. They can be divided into two categories white or grey, determined by the concentration of silicon and carbon [4]. The

carbon equivalent in a grey cast iron is greater by about 4% by weight; silicon is added in concentrations of around 2.5 %. In contrast white cast irons have a carbon content of less than 4%. The grey cast irons present cracks which lead to poor toughness, good damping characteristics and porosity free castings. The material can be, in this case, easily machined. The white cast irons have high compressive strength and excellent resistance to wear and abrasion, but they are hard, brittle, cannot be machined and are generally used for grinding [4].

A cast iron scaife is a rotating cast iron disc (approximately 0.3 m in diameter, 20 mm thick), which can be loaded with diamond grit in pre-machined radial grooves or in pores formed in the cast iron during sand-blasting [2]. Prior to use the scaife must be prepared. After being cleaned with alcohol, a thin layer of olive oil is worked into the scaife's surface. 1-2 carats diamond power is rubbed into pre-machined grooves, until a uniform grey colour is obtained. The choice of diamond grit size is the polisher's preference and is generally in the range of 1 – 20 μm, but grit size less than 1 μm is also available. Diamond of inferior quality (boart) is used to work the diamond powder into the scaife. Through this process the diamond powder, on scaife, turns from grey to a shiny dark grey/ black colour. When the ''black layer'' appears, it is an indication that the scaife is ready to be used. The diamonds are pressed onto this surface. The wear rate is strongly dependent on the crystal orientation. The stones can be polished into two directions, soft or hard. Polishing in the ''soft'' directions can achieve acceptably quick wear rates, a good surface finish (generally) and little damage to the scaife surface [2]. All the other directions are known as ''hard'' directions. In these directions polishing is very difficult or almost impossible and observable and irreversible damage to the scaife's surface is often noted [2]. Good polishing requires skills and a lot of practice. Well

polished diamond surfaces, show ''smooth'' grooving down to the nanoscale (40- 100 nm wide). The process is not abrasive in the ''soft'' directions [5].

Though outstanding for many reasons, there is a major drawback that this technique is considered as having. Cast iron scaife polishing depends on the free standing diamond powder embedded in the scaife. However, as the diamond particles are not fixed in any way there is a big waste of diamond powder, waste which increases overall polishing costs. In order to solve these issues, various methods have been investigated through which the diamond in powder is fixed in place; phenol resins, polyimide resins, ceramics, etc. have been used [6]. The scaifes prepared like this have the advantage of avoiding the waste of diamond grit.

Depending on the desired outcome or on the time constrains, a cast iron scaife or a resin/ ceramic bonded scaife can be used. Using a resin/ ceramic bonded scaife, the samples can be processed quickly, but a high mass of the sample will be lost and a high density of defects will be induced through polishing. Cast iron scaifes, require longer processing times, but the quality of the diamond's surface finish is net superior to the one that could be obtained using a resin/ceramic bonded scaife.

Analyses of the impact of different types of polishing on the single crystal diamonds performance are presented in the Chapters 5 and 6.

3.2. Lithography

An essential step in the fabrication of devices for microelectronics is the patterning of geometries. The technical achievements in this field have experienced huge improvements since their first introduction [7]. The process through which a pattern from a mask is transferred to a radiation-sensitive resist is called lithography [7], and was discovered in 1796 by Aloys Senefelder. The method is extensively used in various domains such as opto-electronics, nanoelectronics, biotechnology, etc. [8-15]. 30-35% of the costs of manufacturing integrated circuits are represented by lithography processes [16]. The ability to control the device's scaling, the circuit's performance and the magnitude of integration, turned lithography into an invaluable technique for semiconductor processing, influencing the size, weight, cost, capability and reliability of electronic systems [7].

There are various types of lithography but by far the most popular is photo (optical) lithography.

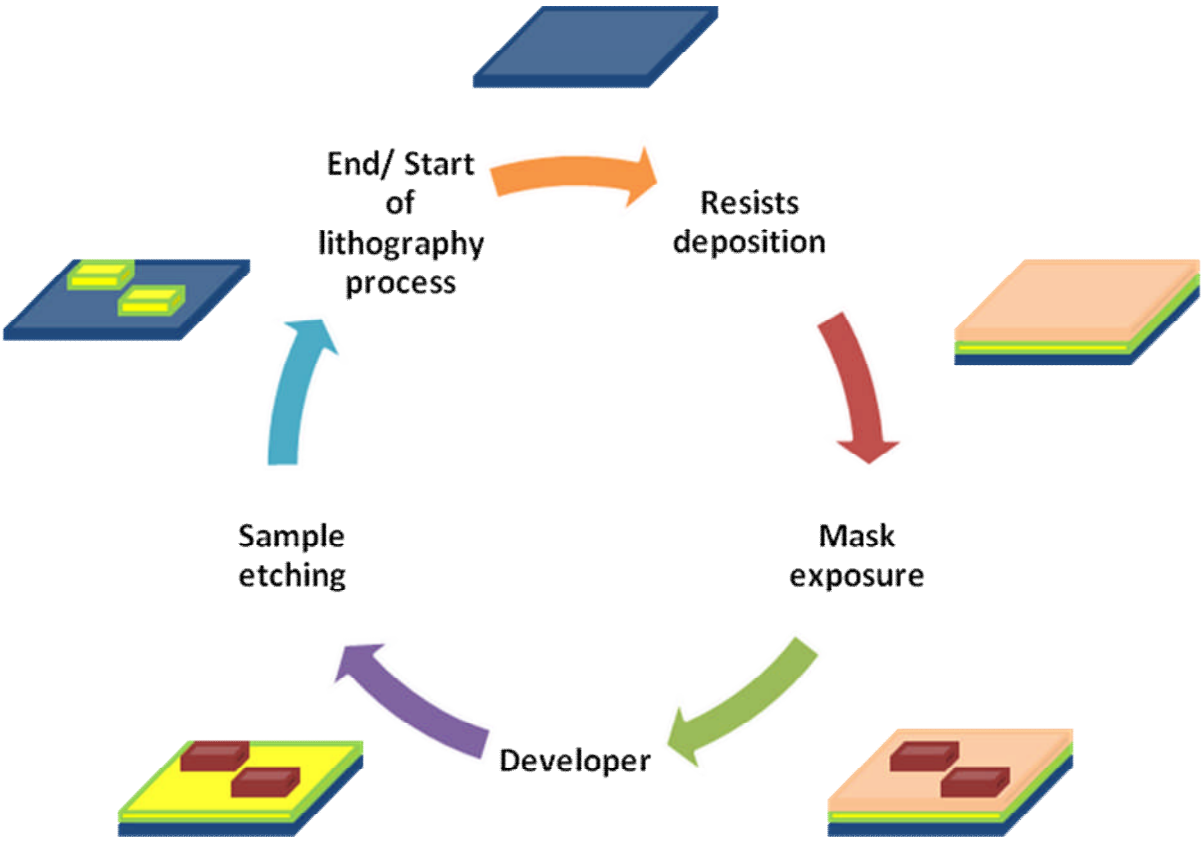

Figure 3.1 Lithography process cycle containing the main steps: resist deposition, mask exposure, developing and sample etching.

Either subtractive or additive approaches can be used to define features after transferring the pattern (see Figure 3.1). The appropriate resists are spin-coated onto the sample, which is then irradiated with the desired mask placed on top of it. Depending on the resist employed, the solubility of the exposed regions is altered, either positively (more soluble) or negatively (less soluble) [7]. The resist is used to protect areas that do not need to be etched (subtractive) or to protect areas that should not be deposited on (additive). The etching step, wet or dry, is essential for bulk processing of the devices. Each mode has specific parameters such as the etch rate, the etch selectivity and the etch uniformity. Wet etching is performed by dipping the substrate into an etchant bath or spraying it with etchant. After etching or depositing, the resist is removed by dissolving it in suitable chemicals. Sample contamination, corrosion,

reproducibility, sidewall profile and loss of critical dimensions should be taken into account while fabricating devices.

3.3. Ohmic and Schottky contacts onto CVD diamond

3.3.1. Ohmic contacts

With the advancements in diamond synthesis (today films can achieve [B] concentrations from < 10^{12}- 10^{20} and mobility around 2000 $cm^2V^{-1}s^{-1}$ [17-19]) in order to investigate their electrical and electrochemical properties metallic contacts are required. However, the preparation of metallic contacts has not changed much since the work of Moazed and Tachibana [20-22]. The Ohmic contacts are based on the carburisation reaction of a carbide forming metal. The most widespread contacts are Ti/Pt/Au, Mo/Au or Mo/Ni/Au. Ti (or Mo, etc) is carburised by annealing at around 400°C (or higher, depending on the metal) in an argon or nitrogen atmosphere for a minimum of 30 minutes, leading to a carbide based tunnelling contact with thicknesses between 50- 200 Å [20-22]. The technique leading to a Ti contact formation has been investigated [20-22] and it was explained through the generation of electronic defects states in the constrained TiC layer and at the diamond/ TiC interface allowing the tunnelling of the carriers through the contact and minimising the contact resistance. The Pt layer is used as a diffusion blocking film, while the Au coating serves as an antioxidant to which wires can be directly bonded. Using this method contact resistivities of about 10^{-3}- 10^{-4} Ωcm can be achieved, but minimising the contact resistivity depends entirely on the exact procedure followed [20-22]. A further reduction of the resistivity's value can be achieved by ion implantation which has the same result [23-27]; other attempts have employed laser scribing or a local laser graphitisation [24-26, 28-30] and Si-based contacts, Si: Si-C: C, in combination with heavily doped films [31-33].

H-terminated diamond surfaces can exhibit p-type conductivity, see Chapter 2, section 2.4.1, [34-40]; Ti/Pt/Au or just pure Au make Ohmic contacts on hydrogenated diamond surfaces [41]. Typical current-voltage characteristics of Au (dashed) and Pt (solid line) Ohmic contacts on undoped diamond (001)- 2 x1: H [2, 41] can be seen in Figure 3.2.

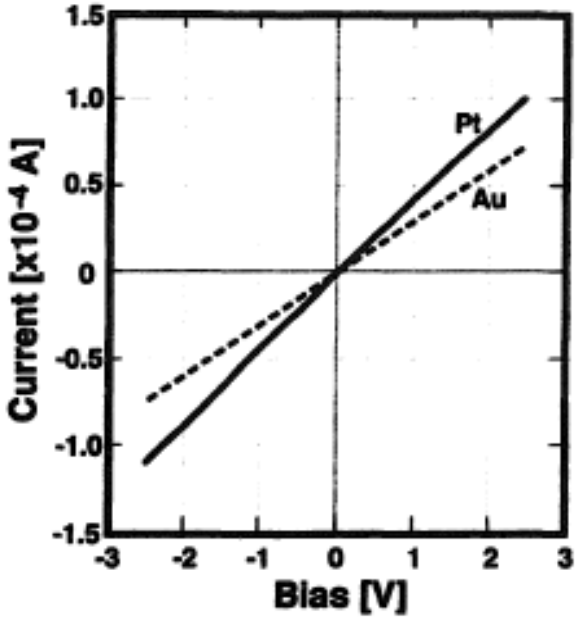

Figure 3.2 Example of typical current-voltage characteristics for an Ohmic contact. Current-voltage characteristics of Au (dashed) and Pt (solid line) point contacts on undoped diamond (001)- 2 x1: H [2, 41].

3.3.2. Schottky contacts

Practically, all metal contacts deposited on O-terminated diamond surfaces give a Schottky junction if they are not annealed or carburised [17, 32, 42-44]. Data from reference [18] is summarised in the table below.

Metal	*Work function (eV)*	*Electronegativity*	*Ideality factor*	*Forr/reverse current (1.5 V)*	*Schottky height (eV)*
Al	4.28	1.5	1.1	10^{-7}	1.23
Cr	4.5	1.6	1.1	10^{-6}	1.24
Au	5.1	2.4	1.1	10^{-7}	1.25
Ni	5.15	1.8	1	10^{-7}	1.7
Pt	5.65	2.2	1.1	10^{-6}	1.31

Table 3.1 Difference in electronegativity, ideality factor and Schottky barrier height for various metals used for contacts [18].

The information given in the Table 3.1 suggests that the Fermi level is pinned at ~1.3 eV above the top of the valence band maximum regardless of the work function of the metal. Other investigations using Al and Au contacts yielded height barriers of 1.6 eV and 1.7 eV respectively, with very low diode factors (1.06/ 1.1, nearly ideal Schottky diode junction) [45] or Ag contacts [46]. However, since Au, Al, Ag, etc. do not react with the diamond surface, they cannot lead to a tunnelling effect as a result of the generation of defect states, similar to TiC forming Ohmic contacts [41]. Figure 3.3 shows an example of typical Schottky junction characteristics of Al and Au/ B-doped junction at 298 K. The reverse *I–V* characteristic could not be measured because the current level was lower than the detection limit. An ideality factor of ~1.06 and Schottky barrier height of ~1.2– 1.3 eV was obtained with the fitted solid lines [45].

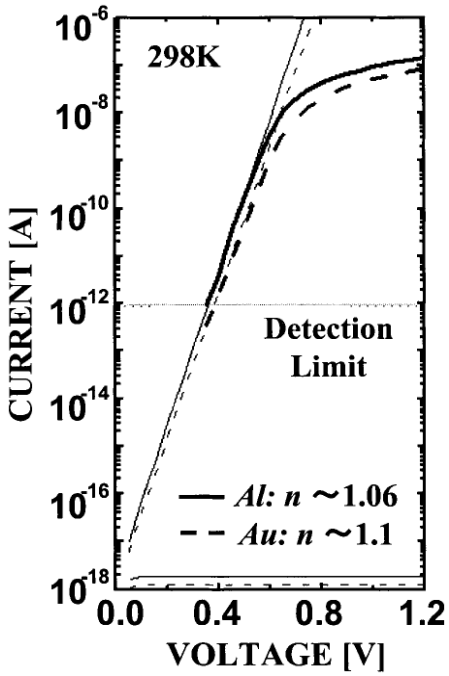

Figure 3.3 Example of typical current-voltage characteristics for a Schottky contact. *I–V* characteristics of Al and Au/ B-doped junction at 298 K. The reverse *I–V* characteristic could not be measured because the current level was lower than the detection limit. An ideality factor of ~1.06 and Schottky barrier height of ~1.2– 1.3 eV was obtained with the fitted solid lines [45].

3.4. The Van der Pauw method

In order to determine the sheet resistance of a thin layer and the mobility of the charged carriers, a combination of conductivity and Hall effect measurements is needed. The method used for this purpose has been originally addressed by van der Pauw [47, 48]. The technique is extremely sensitive, therefore sample preparation is crucial. The sample has to be symmetric, without inclusions, holes, nonconducting islands and the thickness of the conductive layer must be much less than the length and width of the sample. Four very small Ohmic contacts must be placed on the boundaries of the sample (or as close to it as physically possible), connected as simply as possible, with the contacts and the contact leads made in the same way to minimise thermoelectric effects. Potential contact configurations are shown in Figure 3.4.

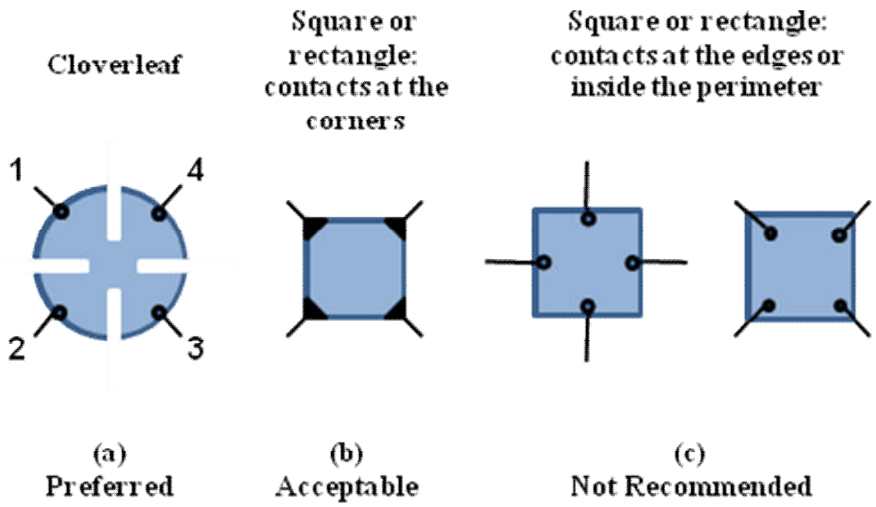

Figure 3.4 Possible contact configurations for Van der Pauw measurements, counted from 1 to 4 in an anti-clockwise order starting at the top left. Adapted from [49].

While performing an experiment the current flows for example between *1* and *2*, I_{12}, and the voltage is measured between *4* and *3*, V_{43}. Using Ohm's law the resistance can be extracted:

$$R_{12,43} = V_{43} / I_{12} \tag{3.1}$$

A schematic representation of a van der Pauw configuration can be found in Figure 3.5.

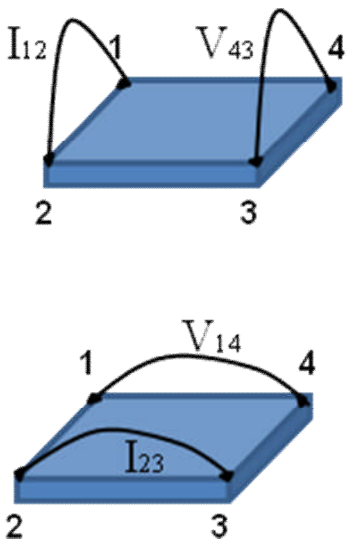

Figure 3.5 Schematic representation of the van der Pauw configuration for the resistance measurements.

Van der Pauw proved [47, 48] that there are two resistances $R_{12,\,43}$ and $R_{23,\,14}$ associated with each corresponding terminals and the sheet resistance, R_S, can be extracted numerically from the van der Pauw formula [47, 48]:

$$exp(-\pi R_{12,43}/R_S) + exp(-\pi R_{23,14}/R_S) = 1 \quad (3.2)$$

More accurate values of the two resistances, $R_{12,\,34}$ and $R_{23,\,41}$, can be obtained by taking measurements of their reciprocal resistances, $R_{34,\,12}$ and $R_{41,\,23}$, and averaging the values:

$$R_{vertical} = (R_{12,\,43} + R_{43,\,12})/2 \quad (3.3)$$

$$R_{horizontal} = (R_{23,\,14} + R_{14,\,23})/2 \quad (3.4)$$

which will transform the van der Pauw formula into:

$$exp(-\pi R_{vertical}/R_s) + exp(-\pi R_{horizontal}/R_s) = 1 \quad (3.5)$$

Reciprocal measurements are not the only way to improve the accuracy of the results. By reversing the polarities of the current and voltage sources $R_{vertical}$ and $R_{horizontal}$ can be calculated in the same manner, for the same portion of the sample, just in opposite directions. The main advantage of this process is that any offset voltages will be nulified. Through this method any error sources are the identified as the procedure checks thoroughly the reproducibility of the measurements.

Subsequently, knowing d, the thickness of the conductive layer of the investigated sample, where d « samples' width and length, the bulk electrical resistivity ρ can be calculated [47, 48]:

$$\rho = R_S d \quad (3.6)$$

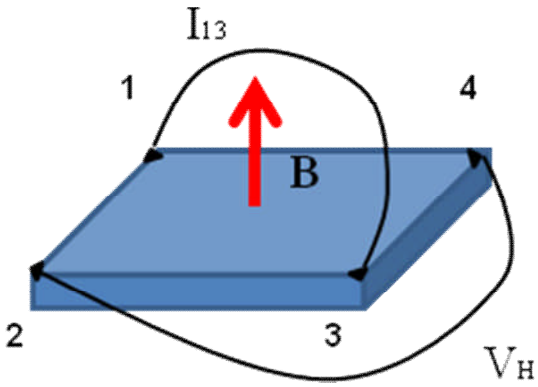

Figure 3.6 Schematic representation of the Hall measurement.

During a Hall measurement (see a schematic representation in Figure 3.6) the aim is to determine the sheet carrier density n_s by measuring the Hall voltage V_H, under a constant current I and with a constant magnetic field B applied perpendicular to the plane of the sample. Whilst measuring the Hall voltage V_H, a current I is passed through the contacts *1* and *3* and the Hall voltage V_H *(=* V_{24}*)* is measured across the remaining pair of contacts *2* and *4*.

Minimising the errors induced through sample preparation and connection can be achieved by always taking two sets of measurements: once while applying a positive magnetic field and once while applying a negative magnetic field. In a similar manner to the conductivity measurements, when the current is applied to one branch of the circuit two values will be obtained for the potential (positive and negative), by simply reversing the direction of the current. The average Hall voltage will be given by:

$$V_H = (V_{13,P}-V_{13,N}+V_{24,P}- V_{24,N} +V_{31,P}- V_{31,N} +V_{42,P}- V_{42,N})/8 \qquad (3.7)$$

The sign of the Hall voltage gives an indication of the type of material that we are dealing with and if the carriers are electrons or holes. If the potential's value is positive the material is p-type, while if it is negative the material is n-type.

With the Hall voltage V_H acquired, the sheet carrier density n_s can be calculated:

$$n_s = IB/q|V_H| \quad (3.8)$$

using the known values of *I*, *B*, and *q (*where *I* is the current, *B* the magnetic field, and *q* the elementary charge).

If the sheet carrier density n_s is determined, the carrier density *n* and then the mobility μ can also be calculated:

$$n = n_S/d \quad (3.9)$$

$$\mu = 1/qn_SR_S \quad (3.10)$$

When carrying out Hall and resistivity measurements there are, of course, a series of practical aspects which must be considered, such as the quality and size of the ohmic contact, the sample uniformity and accurate thickness determination, the thermomagnetic effects due to nonuniform temperature, and the photoconductive and photovoltaic effects which can be minimized by measuring in a dark environment [50-52]. Also, the lateral sample dimensions must be large compared to the size of the contacts and the sample thickness.

3.5. Field effect transistors

Even with research on these devices being conducted from the early 20s [53, 54] and 30s [55] it was only in 1952 [56] that Shockley proposed the first operational device. However, at this time, their production in large quantities was not possible as the semiconductor techniques were not sufficiently advanced.

The fundamental step that lead to the advancement of transistor research was better comprehension of the electron mobility in semiconductors [57]. Field effect transistors (FET) are unipolar devices, meaning that the current through the device is carried by one single type

of charge carrier, either holes or electrons, depending on the type of semiconductor employed. Each FET device has a source, a gate and a drain. The names are directly linked with their attributions.

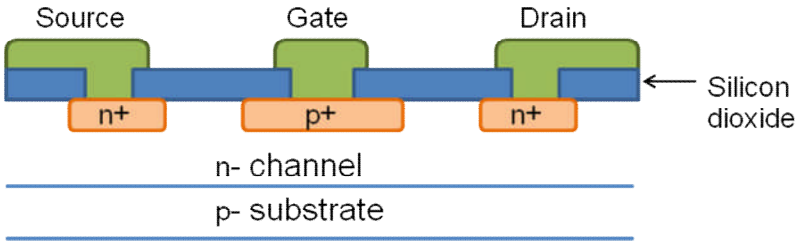

Figure 3.7 Diagram of a typical junction- gate field effect transistor consisting of an n-type silicon substrate with Ohmic contacts at each end (the source and the drain respectively). Adapted from [57].

The gate controls the transfer of carriers from the source and the drain or hinders their connection depending on the applied voltage. The conductivity of the FET depends, at any moment in time, on the electrical path. A small change in gate voltage can cause a large variation in the current from the source to the drain. The current flowing through the channel of an FET rises sharply with increasing drain-source voltage, but only to a certain point called the pinch off voltage. When this point is reached, further increase of the drain-source voltage will cause almost no increase in the current, this being the saturation region, see Figure 3.8 [58]. The family of drain characteristics and transconductance characteristic curves obtained prove that when no potential is applied to the gate source junction the FET conducts fully. Increasing the gate-source voltage causes a decrease of the drain current.

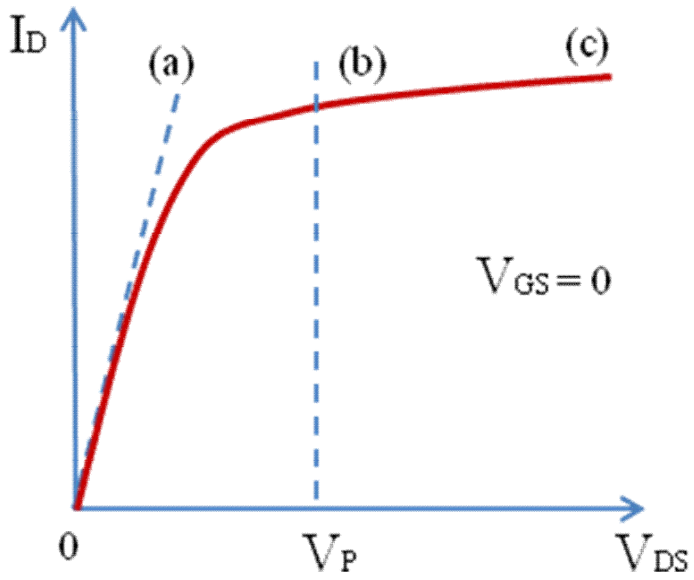

Figure 3.8 Typical drain- current/ voltage characteristic of a field- effect transistor where (a) Ohmic region, (b) pinch-off point and (c) saturation region. Adapted from [57].

3.6. Semiconductor electrochemistry

Typically, the electronic properties of solids are portrayed using the band model [59]. When a solid is formed, isolated atom combine creating new molecular orbitals. The conduction band (CB) is formed of vacant antibonding orbitals, while the valence band (VB) is formed of filled orbitals. The electrical properties of the materials are controlled by the separation between these two bands, known as bandgap and characterised by the bandgap energy. The generation of bands in solids from atomic orbitals of isolated atoms is depicted in Figure 3.9

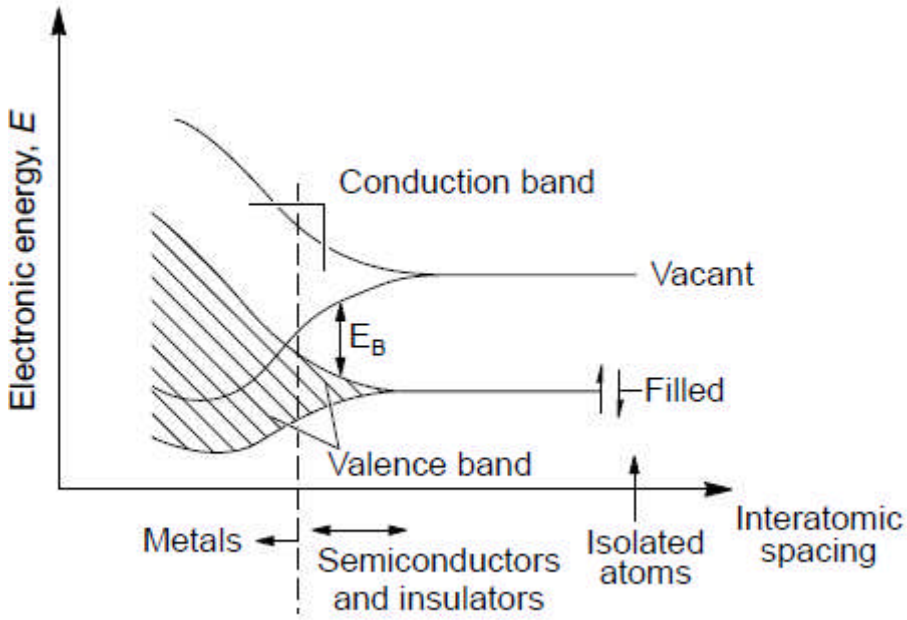

Figure 3.9 Generation of bands in solids from atomic orbitals of isolated atoms [59].

For a good conductor the empty and filled energy levels coexist typically at the same energy level. This is the reason why only a very small activation energy needs to be used so that the electrons can be transferred from one level to another.

A model of the structure of the double layer at the metal/solution interface is presented in Figure 3.10. The solution side of the double layer is believed to be formed of a number of layers. The layer closest to the electrode, called the inner Helmholtz layer or plane (IHP), is formed of solvent molecules and other species specifically absorbed (unsolvated). The centre of the electrical charge is at a distance x_1, while solvated ions can approach the electrode only to a distance x_2. The centre of this charge is called the outer Helmholtz plane (OHP). The interactions of the ions with the electrode are independent of their chemical properties, involving only long range electrostatic forces. Due to the thermal agitation, these ions (solvated and unsolvated) are dispersed across in a three-dimensional region named the diffuse layer, which extends from the OHP into the bulk of the solution. The thickness of the

diffuse layer depends on the concentration of ions in solution and its structure can affect the rates of the electrode processes [60].

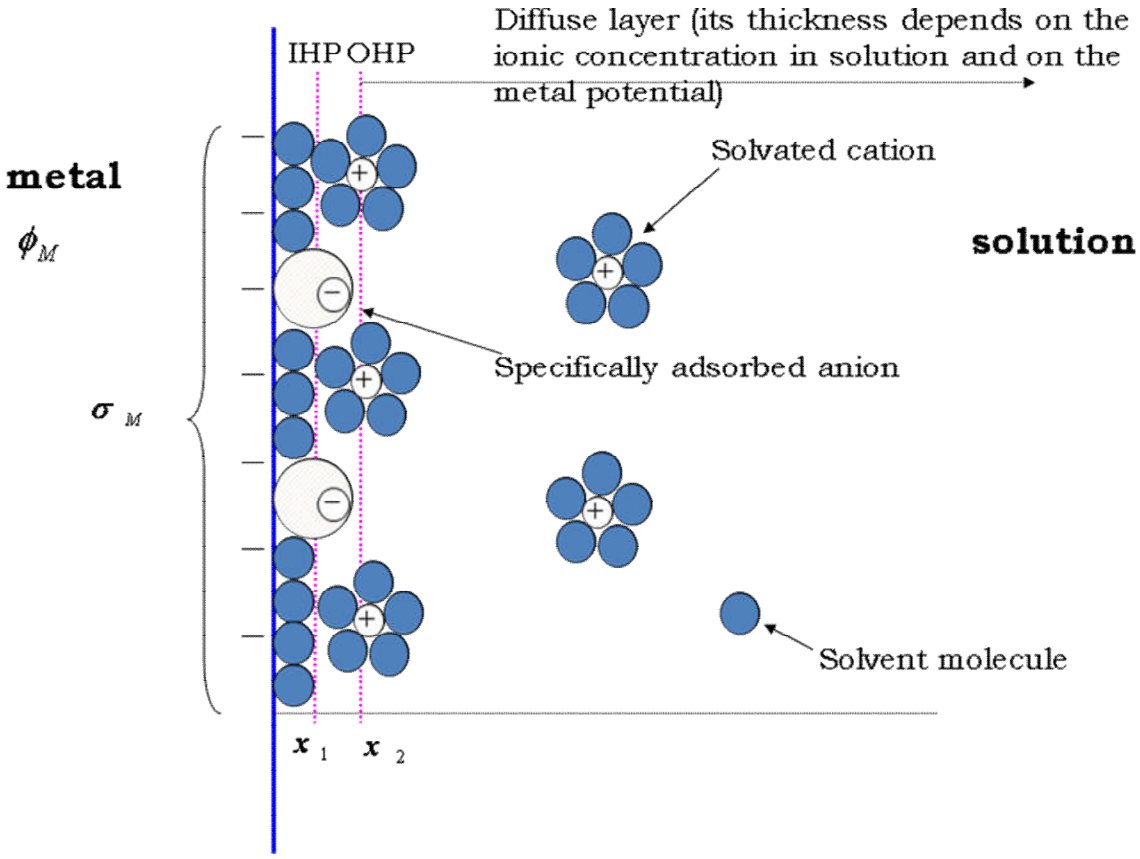

Figure 3.10 Double layer region at the metal- electrolyte interface IHP, inner Helmholtz plane; OHP, outer Helmholtz plane [60].

In the case of intrinsic diamond, the 5.5 eV bandgap ensures that the valence band (VB) is almost completely filled up, while the conduction band (CB) is almost vacant at room temperature. The thermal excitation of electrons from the VB to the conduction band makes conduction in solids possible by creating electrons in the CB and holes in the valence band with a specific electrical mobility. Intrinsic semiconductors are typically characterised by this behaviour (see Figure 3.11).

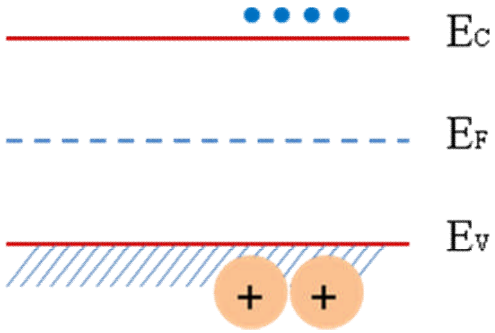

Figure 3.11 Energy bands of an intrinsic semiconductor.

Doping a diamond with boron (> 10^{17} cm^{-3}), transforms the material from an insulator to a semiconductor (see Chapter 2, section 2.2). Because boron has a deficiency of electrons in its outer shell (compared to carbon) it will act as an acceptor. An energy level, E_A, is introduced just above the valence band. Through thermal excitation the electrons move from the valence band into these acceptor sites. This behaviour confers diamond p-type semiconductivity as a result of the free electrons in the acceptor site and mobile holes in the valence band (Figure 3.12) [61]. For higher boron doping levels (10^{19}- 10^{20} atoms cm^{-3}) a mutual interaction between the boron centres forces the impurity band to broaden and shift towards the valence band and the diamond becomes metallic.

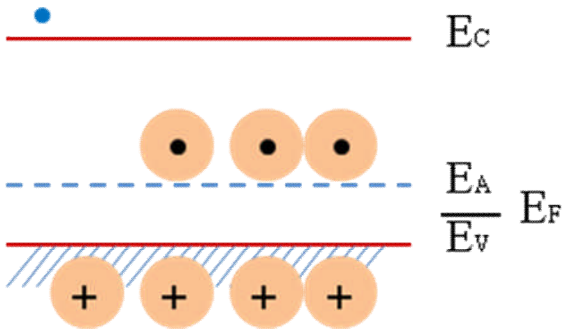

Figure 3.12 Energy bands of a p-type semiconductor.

At the interface between a semiconductor electrode and any kind of electrolyte solution, if their potentials are not situated at the same level, an exchange of charge between the solution and the semiconductor will be necessary so that equilibrium can be reached. In the case of a metallic electrode, the charges are located just below the surface, but semiconductors behave differently. For semiconductors, since the carrier density is much smaller than in a metal electrode, the charges can be distributed on a significant distance, 100- 10000 Å, below the interface. A space charge layer is formed, similar to that in pure solid devices [59]. So, for semiconductor electrochemistry, the interfaces of interest are the electrode/electrolyte double layer and the space charge double layer.

The redox potential is higher than the level of the Fermi layer for a p-type semiconductor, and hence electron transfer must occur from the solution to the electrode to attain equilibrium. This generates a negative charge in the space charge region, which causes a downward bending in the band edges. Since the holes in the space charge region are removed by this process, this region is a depletion layer.

In a similar manner to metallic electrodes, modifying the potential applied to the semiconductor electrode changes the position of the Fermi level. The band edges in the interior of the semiconductor (*i.e.* away from the depletion region) also vary with the applied potential in the same way as the Fermi level. Nevertheless, the energies of the band edges at the interface are not affected by changes in the applied potential. Therefore, the change in the energies of the band edges on going from the interior of the semiconductor to the interface, and hence the magnitude and direction of band bending, varies with the applied potential [60]. Figure 3.13 shows a schematic representation of an energy diagram for a semiconductor-electrolyte interface for a standard potential.

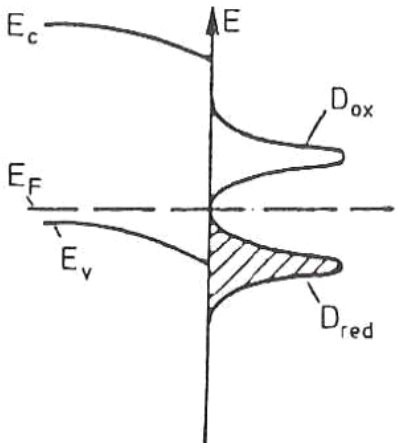

Figure 3.13 Energy diagram for a semiconductor- electrolyte interface for a standard redox potential [59]

The situations that can appear are:

a) **Flatband potential (E_{fb})**

The Fermi energy lies at the same energy as the redox potential of the electroactive species of interest**.** As there is no charge transfer, there is no band bending.

b) **Depletion region**

For p-type semiconductors, depletion occurs as the electrode potential is poised negative of the flatband potential.

c) Accumulation region

For p-type semiconductors, accumulation occurs at electrode potentials more positive than the flatband potential.

The charge transfer abilities of a semiconductor electrode depend on whether there is an accumulation layer or a depletion layer. If there is an accumulation layer, the behaviour of a semiconductor electrode is similar to that of a metallic electrode, since there is an excess of the majority charge carrier available for charge transfer. In contrast, if there is a depletion

layer, then there are few charge carriers available for charge transfer, and electron transfer reactions occur slowly, if at all.

3.7. Dynamic Electrochemistry

Dynamic electrochemistry addresses the topic of electron transfer between an electrode (usually metallic) and the chemically active species in the solution under non-equilibrium conditions. It is concerned with the development and application of techniques that probe the rate and mechanisms of electron transfer reactions. There are a series of parameters that can influence these reactions, amongst them the electrode potential, the kinetics of electron transfer and the rate of mass transport of reactants and products to and from the electrode surface [60, 62]. A schematic representation of a typical electrode reaction can be seen in the Figure 3.14.

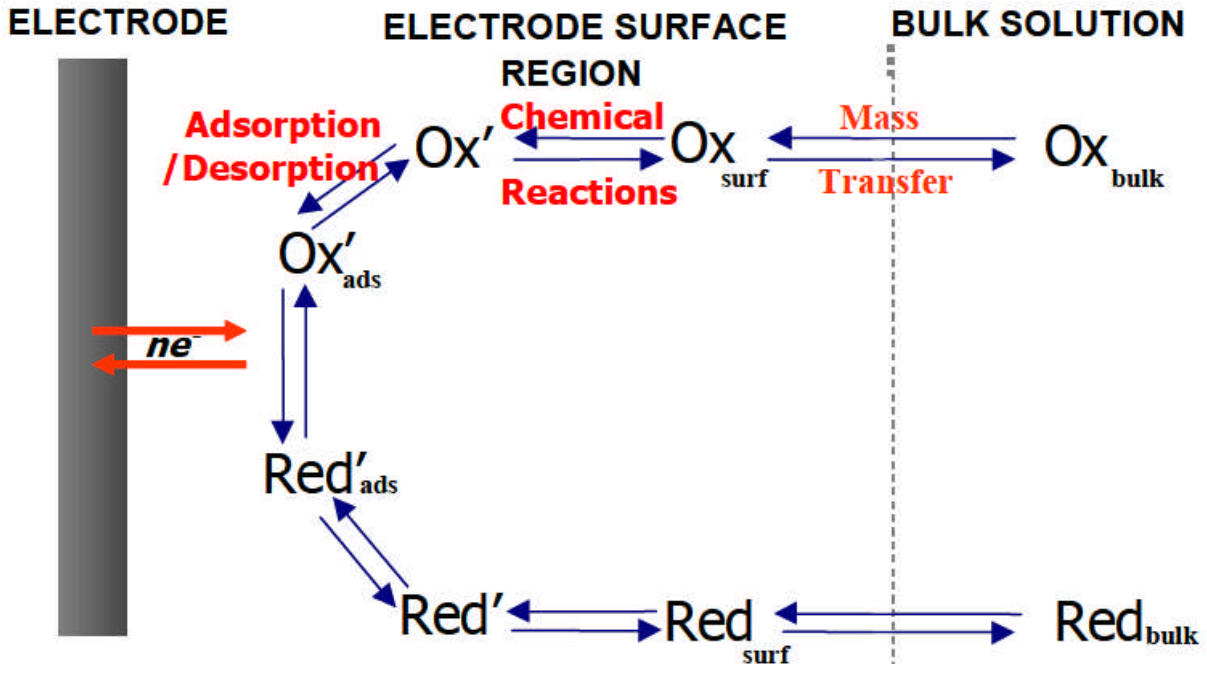

Figure 3.14 Schematical representation of a typical electrode reaction [60].

The most basic electron transfer reactions involve the mass transport of the electroactive species to/from the electrode and electron transfer at the electrode. More complex reactions may involve the reactivity of the surface and various chemical reactions before or after electron transfer [63].

The Nernst- Planck equation:

$$J_j = -D_j \nabla c_j + c_j \mathbf{V} - \frac{z_j F}{RT} D_j c_j \nabla \phi \qquad (3.11)$$

governs the movement of species from one location to another. J_j is the flux (i.e. the number of moles passing through a given area per unit time) of species j to/from the electrode, D_j is the diffusion coefficient of species j, c_j is the concentration of species j, $\mathbf{V}$ is the velocity vector, z_j is the charge on species j, F is Faraday's constant, R is the gas constant, T is temperature and Φ is the electrostatic potential [60].

Mass transport can occur through diffusion, convection and migration, processes described mathematically on the right hand side of Nernst- Planck's equation, respectively. Diffusion describes the movement of species through a solvent; it is always present in a dynamic electrode process and is a result of the difference in concentration (activity) of the species at the electrode surface and the bulk solution. Diffusion is characterised as the movement of species down this concentration gradient and has an impact on both neutral and charged species. Mathematically, this process was defined in 1855 by Fick [64]. His first law (3.12) relates the concentration gradient to the diffusive flux J_j, while the second law assesses the variation with time of the concentration species (3.13).

$$J_j = -D_j \frac{\partial c_j}{\partial x} \quad (3.12)$$

$$\frac{\partial c_j}{\partial t} = D_j \nabla^2 c_j \quad (3.13)$$

Migration is the movement of charged species in solution under the influence of an external electric field. It is often removed (as far as electroactive species are concerned) by adding inert supporting electrolyte in excess, typically at least 100 times more than the electrochemically active species [62]. This action also has another benefit: it reduces the effect of uncompensated (Ohmic) resistance [65] and condenses the size of the electrical double layer, such that the current will pass through the solution easily without being limited by the solutions conductivity.

Convection is the result of mechanical external forces acting on the solution. It can be natural or forced. Natural convection can be encountered in any solution and is a result of the differences between the density and/or thermal gradients in the solution [62]. Forced convection can be introduced into the system through stirring, bubbling or pumping, to conceal any contribution from natural convection. In this context reproducible experiments can be performed under well defined hydrodynamic conditions such as turbulent or laminar flow and stagnation conditions, with mass transport being increased over a diffusion only process [62].

Most experiments are carried out under diffusion controlled only conditions, as for the work in Chapter 5, 6 and 7.

3.8. Cyclic Voltammetry (CV)

One of the simplest electrochemical techniques used to gain knowledge on the electrode/electrolyte interface is cyclic voltammetry (CV). The technique provides a response based on the reactivity of the entire area exposed to electrolyte. The use of complementary techniques is strongly recommended if the samples under investigation are suspected to have a heterogeneous surface. This would allow a correct interpretation of the sample's voltammetric response.

In the case of a simple electron transfer ($O + ne^- \rightarrow R$) cyclic voltammogram, the potential of the working electrode is swept linearly with time, from an initial potential, E_1, which in the case of a reduction is where the species of interest in its oxidised form (O) cannot undergo reduction, to a potential, E_2, where electron transfer is driven rapidly to form the reduced species (R). The sweep direction is then reversed and the potential scanned back to E_1. Therefore the observed current depends on both the kinetics of electron transfer and mass transport of the electroactive species [62]. In the case of a reduction, as the potential is swept to more negative values the rate of electron transfer, k_r, at the electrode surface increases and a current starts to pass. For a macroelectrode (area in the mm^2 range), the radial contribution of diffusion of the electroactive species to the electrode surface is minimal compared to linear diffusion, hence the rate of mass transport, k_t, to the electrode is low, compared to a microelectrode [62, 66]. A potential is reached where the electroactive species cannot diffuse fast enough to replace material remained at the electrode surface; continuing to sweep the potential beyond this value results in the current decreasing. Thus a characteristic peak current, i_p, is obtained for diffusion controlled electrolysis at a macroelectrode [62, 66].

$$i_p = -2.69 \times 10^5 n^{3/2} A D^{1/2} c^* \upsilon^{1/2} \quad (3.14)$$

where n is the number of electrons transferred, A is the area of the electrode, D is the diffusion coefficient of the electroactive species, c^* is the bulk concentration of the electroactive species and υ is the voltage scan rate.

The shape of the CV gives an indication of the nature of electron transfer process at the electrode surface. For a reversible system, where k_r is fast, the CV recorded will exhibit the following characteristics [66]:

i) The peak separation $\Delta Ep = E_p^a - E_p^c = 56.6/n\ mV$ and is independent of υ (E_p^c- oxidative peak potential; E_p^a- reductive peak potential).

ii) $|E_{p3/4} - E_{p1/4}| = 56.6/n\ mV$ ($E_{p3/4}$ and $E_{p1/4}$ are the potentials that correspond to three quarters and one quarter of i_∞ respectively).

iii) $i_p^a / i_p^c = 1$ (i_p^a - reductive peak current; i_p^c - oxidative peak current).

iv) i_p is linearly proportional to $\upsilon^{1/2}$.

A typical CV for a reversible system can be seen in Figure 3.15.

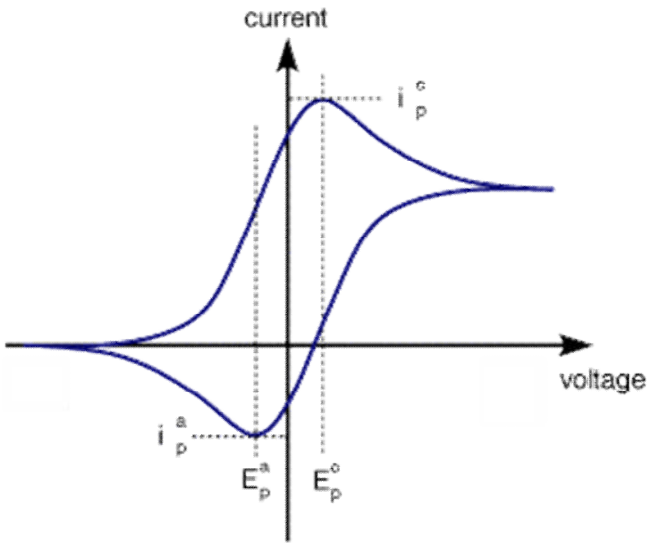

Figure 3.15 Typical cyclic voltammogram for a reversible electron transfer system (k_t limited).

When k_r is slower and hence rate limiting, a quasi- reversible system can be observed. Since equilibrium at the surface between k_r and k_t is not established as rapidly, in the case of a reduction, i_p is shifted to a more negative potential. In this case there will be a build- up of electroactive species at the surface. ΔE_p is no longer fixed and varies as a function of υ. Increasing υ reduces the time for equilibrium to be established at the electrode surface, hence reactions will appear reversible with a slow υ and not at faster υ. There will also be a decrease in the peak current relative to the reversible case. For an irreversible system, electron transfer is rate limiting, no peak occurs on reversing the scan direction, instead a continuation of current decay is observed [62, 66]. Typical CVs for an irreversible electron transfer system, showing the reduction in peak size and the increase in separation, ΔEp, are presented in Figure 3.16.

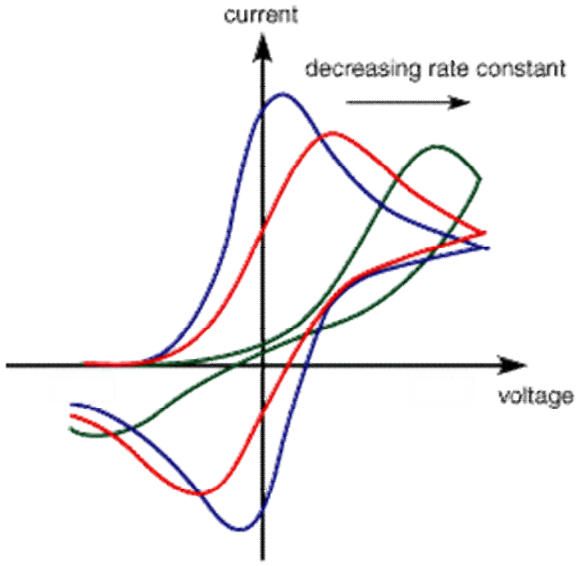

Figure 3.16 Typical cyclic voltammograms for an irreversible electron transfer system, showing the reduction in peak size and the increase in separation, *ΔEp*.

3.9. Ultramicroelectrodes versus Macroelectrodes

There are various types of electrodes employed and the critical factor determining their behaviour is the interplay between mass transport to the electrode and the electron transfer kinetics. The former is directly linked to their size. Macroelectrodes have dimensions of the order of centimetres or millimetres; when one of the critical dimensions of the electrode is in the micrometer range the electrode behaves as an ultramicroelectrode (UME) [67-71]. Diffusion to a UME is much faster than to a macroelectrode. There are many types of microelectrodes such as: array [72-74], band [75, 76], hemisphere, cylinder, ring [70, 77-79], but by far the most widely used is the disc electrode since its fabrication it is relatively straight forward, the sensing area can be polished mechanically and it is easily modellable [71, 80-84]. Various materials have been used for their fabrication such as gold, platinum, silver, mercury, nickel, carbon fibers and superconductive ceramics [67, 85].

For macroelectrodes semi-infinite planar (linear) diffusion dominates and peak- shaped CVs are recorded whilst for disc UMEs a distinctive hemispherical 3D diffusion profile is achieved, resulting in steady state, time- independent bulk-current, I_{ss}. Figure 3.17 shows the diffusion profiles and the voltammetric responses (under diffusion controlled electrolyses) for a macroelectrode (a) and for a UME (b). Under steady-state diffusion limited conditions, the time-independent bulk current, I_{ss}, flowing at the tip of the UME is defined by (3.15):

$$I_{ss}=4naFDc^* \qquad (3.15)$$

where a is the radius of the micro-disc electrode, n is the number of electrons transferred per redox event, F is Faraday's constant, D is the diffusion coefficient of the electroactive species A, and c^* is the bulk concentration of A.

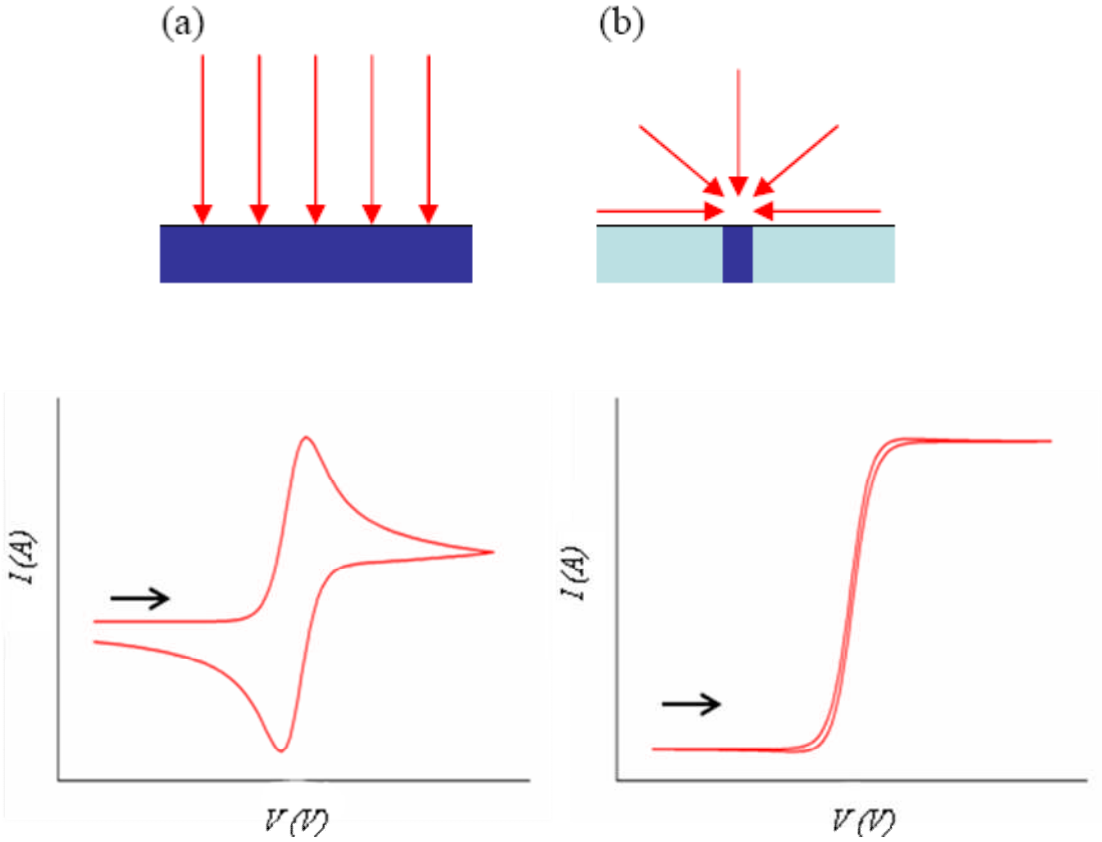

Figure 3.17 Diffusion behaviour and voltammetric responses for a) macroelectrodes and b) UMEs.

The current registered for UMEs is generally in the 10^{-12} A to 10^{-9} A region for typical concentrations in the µM- mM range. Their properties: quicker establishment of the steady-state signal, greater signal to noise ratio, higher current density compared to a macroelectrode and decreased ohmic drop due to the current passing through the finite resistance of the solution arose great interest. After 1980, the availability of sensitive instrumentation and a wider selection of microscopic wires and fibers has increased the possible applications of UMEs. They were used to investigate electrochemical reactions in high resistive media, such as solids, gases, organic solvents, low ionic strength aqueous and non-aqueous solutions, and to carry out measurements at low temperatures [86-91]. Applications for in vivo and in vitro usage [67, 92-95] have also been achieved. They were also employed to study high speed electron transfer reactions [84, 96].

3.10. Scanning electrochemical microscopy

Scanning electrochemical microscopy is a variety of the scanned probe techniques which offers a great wealth of information on the localised surface reactivity with high spatial resolution [97-102]. A UME, with the typical diameter dimensions 0.1 to 25 µm, characterised by the *RG*, where $RG = r_g/a$, (r_g-radius of the glass sheath plus the electrode; a-radius of the electrode, see Figure 3.18), positioned in a precise piezoelectric system, is scanned close to the surface of interest in the x, y, z directions.

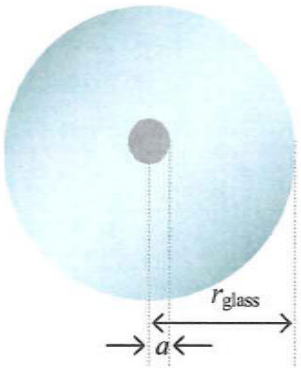

Figure 3.18 Schematic representation of a top view of an UME where r_g- radius of the glass sheath plus the electrode and a- radius of the electrode.

The response, the tip current as a function of the tip position, is directly linked to the chemical reactions and mass transport processes occurring between the tip and the sample. This results in quantitative electrochemical images of the substrate's reactivity [103, 104].

The resolution of the images obtained, depends on the size of the UME [105]. Regarding the sample, itself, there are no restrictions. It can be a single crystal [106-108], liquid-liquid interface [109-113], liquid-gas interface [114-118], porous membranes [119-121] and single living cells [122-124].

SECM measurements are typically performed in the amperometric mode, where the tip is employed as the working electrode in a standard electrochemical cell having a reference electrode and if necessary an auxiliary electrode. When the substrate of interest is a conductor or semiconductor, this can also be connected as an electrode. Insulating samples are simply placed underneath the tip.

In most cases the UME is held at a potential that causes the diffusion-controlled electrolysis of the mediator. This results in the flow of the corresponding current *i*. When the tip is situated far away from the sample (i.e. around 10 electrode radii [125]) it behaves like a

typical UME and hemispherical diffusion is observed. As it is moved closer, in the *z* direction, to a redox inert sample, the steady-state current decreases and it is less than i_{lim}. This happens due to the substrate obstructing the diffusion of the electroactive species to the tip; a phenomenon known as negative feedback (Figure 3.19 (i)) [98]. Contrary, when the tip is approaching a conducting sample the reactant present in solution is continuously regenerated between the tip and the active surface of the sample, and an enhancement of the tip current, namely a positive feedback, will be observed (Figure 3.19 (ii)). If employed in this manner the SECM is performing in the so known "feedback mode" [126].

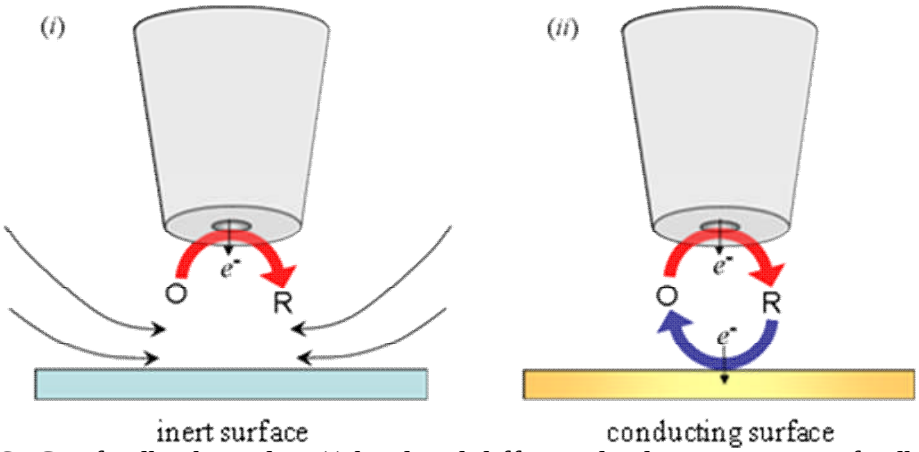

Figure 3.19 SECM feedback modes. (i) hindered diffusion leading to negative feedback; (ii) regeneration of the redox mediator, leading to positive feedback.

Curves of the variation of current, *i* normalised to i_{lim}, with respect to tip-substrate separation, *d*, provide the means to distinguish between a conducting and insulating surface and are known as approach curves (positive and negative feedback), see Figure 3.20.

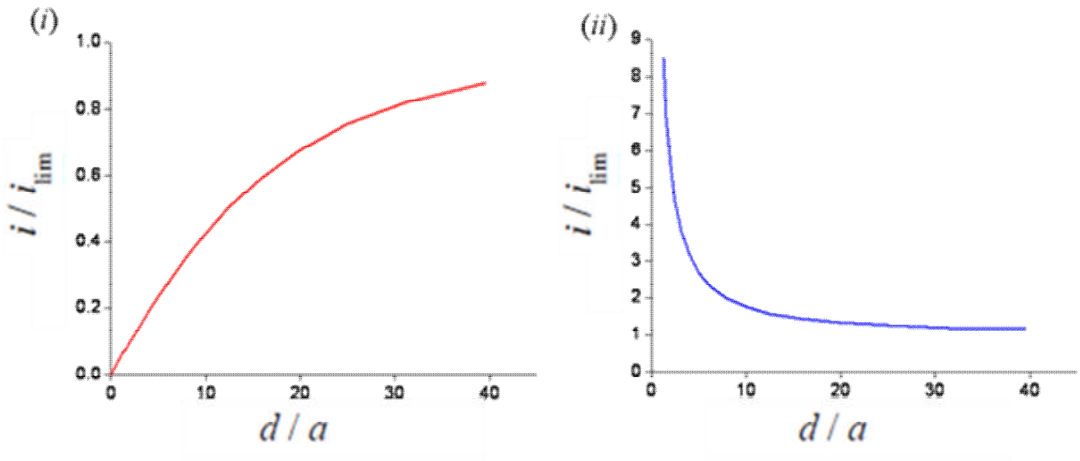

Figure 3.20 Approach curves demonstrating theoretical normalised (i) positive and (ii) negative feedback [125].

Another manner in which SECM can be exploited is the "generation-collection mode". The sample requires an electrical connection. The UME is held at an appropriate potential and used to detect and monitor the flux of electroactive species which have been generated at a much larger substrate positioned directly under the tip [127, 128]. The other way around, tip generation–substrate collection is also possible. This method is less employed due to the possibility of the presence of the tip hindering diffusion to the substrate or consuming species and so altering the response [63].

Most SECM studies assume a substrate feature size that is much larger than the tip diameter [125, 129, 130]. However, substrates can be heterogeneously active, exhibiting both conducting and insulating behaviour and while imaging with SECM the size of the UME determines the resolution of the features of the electroactivity map. For efficient maping small cone-shaped electrodes, with minimal insulating sheaths are preferred. Due to their dimensions and shape they are less likely to perturb the diffusion profiles during tip movement. Overlapping diffusion fields of neighbouring sites and edge diffusion to the tip can lead to loss of lateral resolution in all SECM measurements. Most popular UMEs have 25, 10, 5 and 2 μm diameters [131-136].

Positive and negative feedback represent two extremes of fast (diffusion controlled) and slow (effectively zero) electron transfer at the substrate [97]. Intermediate cases are also possible if electron transfer at the substrate is slow. Enhanced diffusion in the feedback mode compared to bulk, can also control electron transfer by controlling electrode potential. Approach curves can be analysed to give quantitative information about the kinetics of the electrode reaction and solution reactions which remove the electroactive species so that it cannot be regenerated [63, 105]. Experimental studies of the reduction of Fe (III) in 1 M H_2SO_4 at a Pt tip over a biased glassy carbon substrate were conducted. For very fast and very slow electrode kinetics, the feedback current was identical to the theoretical response for conducting and insulating substrates. At intermediate rates the feedback response depended on the rate and the tip insulator dimensions. At very close tip-to-substrate spacings, heterogeneous rate constants greater than 1 cm s^{-1} could be distinguished [137]. A family of feedback curves recorded for different substrate potentials at 25 mV increments between 0.8 V and 0.0 V is presented in Figure 3. 21.

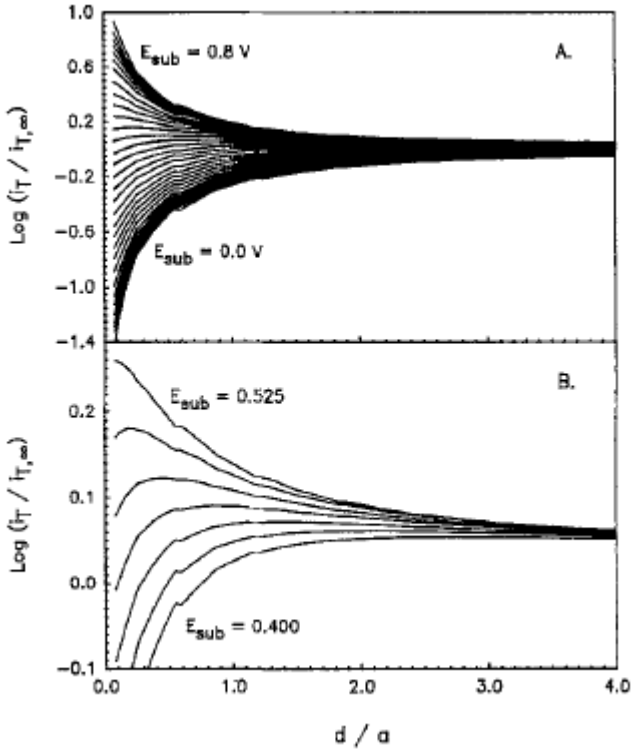

Figure 3.21 SECM log current-distance curves for a 2.1 mM Fe(III) solution in 1M H2SO4/water. Tip electrode is 11µm carbon fiber at a potential of -0.6 V; substrate electrode is glassy-carbon. (A) Curves for different substrate potentials at 25mV increments between 0.8 and 0.0V. (B) Region of Fig. A between 0.525 and 0.400 V [137].

References:

[1] J. Field, *The Properties of Natural and Synthetic Diamond* (Academic Press Ltd., 1997).
[2] E. M. Wilks, and J. Wilks, *Properties and Applications of Diamond* (Butterworth-Heinemann, 1991).
[3] A. P. Malshe *et al.*, Diamond and Related Materials **8**, 1198 (1999).
[4] H. Chandler, *Metallurgy for the non metallurgist* (ASM International, 1998).
[5] J. Hird, *The polishing of diamond* (PhD thesis, 2002).
[6] www.coborn.com.
[7] V. K. Varadan, Vinoy, K. J., Gopalakrishnan, S. , *Smart material systems and MEMS: design and development methodologies* (Wiley, 2006).
[8] K. Gamo, Materials Science and Engineering B-Solid State Materials for Advanced Technology **9**, 307 (1991).
[9] [Anon], Laser Focus-Electro-Optics **22**, 54 (1986).
[10] J. Mcinerney, M. J. Fice, and H. Ahmed, Journal of Lightwave Technology **4**, 1494 (1986).
[11] M. Vanrossum, Materials Science and Engineering B-Solid State Materials for Advanced Technology **20**, 128 (1993).
[12] H. L. Hartnagel, R. Richter, and A. Grub, Electronics & Communication Engineering Journal **3**, 119 (1991).
[13] G. Timp, Physics of Nanostructures **38**, 101 (1992).
[14] S. Britland *et al.*, Biotechnology Progress **8**, 155 (1992).
[15] K. Reimer *et al.*, Sensors and Actuators A-Physical **46**, 66 (1995).
[16] W. K. Ho *et al.*, IECON 2005: Thirty-First Annual Conference of the IEEE Industrial Electronics Society, Vols 1-3, 2278 (2005).
[17] S. Yamanaka *et al.*, Japanese Journal of Applied Physics Part 2-Letters **37**, L1129 (1998).
[18] S. Yamanaka *et al.*, Diamond and Related Materials **9**, 956 (2000).
[19] E. Bustarret, E. Gheeraert, and K. Watanabe, Physica Status Solidi a-Applied Research **199**, 9 (2003).
[20] K. L. Moazed, J. R. Zeidler, and M. J. Taylor, Journal of Applied Physics **68**, 2246 (1990).
[21] T. Tachibana, B. E. Williams, and J. T. Glass, Physical Review B **45**, 11968 (1992).
[22] T. Tachibana, B. E. Williams, and J. T. Glass, Physical Review B **45**, 11975 (1992).
[23] G. R. Brandes *et al.*, Diamond and Related Materials **8**, 1936 (1999).
[24] C. Uzansaguy *et al.*, Applied Physics Letters **67**, 1194 (1995).
[25] R. Kalish *et al.*, Diamond and Related Materials **8**, 877 (1999).
[26] R. Kalish *et al.*, Physica Status Solidi a-Applied Research **174**, 83 (1999).
[27] T. Sekiguchi, and S. Koizumi, Applied Physics Letters **81**, 1987 (2002).
[28] M. W. Geis *et al.*, Applied Physics Letters **55**, 2295 (1989).
[29] L. Nistor *et al.*, Physica Status Solidi A-Applied Research **186**, 207 (2001).
[30] Y. G. Chen *et al.*, Diamond and Related Materials **11**, 451 (2002).
[31] A. Aleksov *et al.*, Semiconductor Science and Technology **18**, S59 (2003).
[32] A. Vescan *et al.*, Diamond and Related Materials **7**, 581 (1998).
[33] A. Vescan *et al.*, Diamond and Related Materials **5**, 747 (1996).
[34] M. I. Landstrass, and K. V. Ravi, Applied Physics Letters **55**, 975 (1989).
[35] K. Hayashi *et al.*, Applied Physics Letters **68**, 376 (1996).
[36] H. J. Looi, R. B. Jackman, and J. S. Foord, Applied Physics Letters **72**, 353 (1998).

[37] H. J. Looi *et al.*, Diamond and Related Materials **8**, 966 (1999).
[38] F. Maier *et al.*, Physical Review Letters **85**, 3472 (2000).
[39] K. Bobrov *et al.*, Physical Review B **63** (2001).
[40] K. Kimura *et al.*, Applied Physics Letters **78**, 1679 (2001).
[41] H. Kawarada, Surface Science Reports **26**, 205 (1996).
[42] H. Shiomi *et al.*, Japanese Journal of Applied Physics Part 1-Regular Papers Short Notes & Review Papers **28**, 758 (1989).
[43] W. Ebert *et al.*, Diamond and Related Materials **6**, 329 (1997).
[44] K. Hayashi *et al.*, Journal of Applied Physics **81**, 744 (1997).
[45] D. Takeuchi, S. Yamanaka, and H. Okushi, Diamond and Related Materials **11**, 355 (2002).
[46] R. Zeisel, C. E. Nebel, and M. Stutzmann, Diamond and Related Materials **9**, 413 (2000).
[47] L. J. van der Pauw, Philips Research Reports **13**, 1 (1958).
[48] L. J. van der Pauw, Philips Technical Review **20**, 220 (1958).
[49] P. Y. Yu, and M. Cardona, *Fundamentals of semiconductors : physics and materials properties* (Springer, New York, 2001).
[50] L. S. Pan *et al.*, Surface & Coatings Technology **47**, 356 (1991).
[51] D. G. Jeng *et al.*, Applied Physics Letters **58**, 1271 (1991).
[52] L. S. Pan *et al.*, Applications of Diamond Films and Related Materials **73**, 341 (1991).
[53] J. E. Lilienfeld, (US patent 1745175 1925).
[54] J. E. Lilienfeld, (US patent 1900018, 1928).
[55] O. Heil, (GB patent 439457 1934).
[56] W. Shockley, (US patent 2569347, 1948).
[57] J. Seymour, *Electronic Devices and Components* (Longman Scientific and Technical, 1986).
[58] R. R. Spencer, Ghausi, M. S., *Microelectronic circuits* (Prentice Hall/Pearson Education, Inc, 2001).
[59] R. Memming, *Semiconductor Electrochemistry* (Wiley - VCH, 2001).
[60] A. J. Bard, and L. R. Faulkner, *Electrochemical methods: Fundamentals and Applications* (John Wiley & Sons, INC., 2001).
[61] Y. V. Pleskov, Russian Journal of Electrochemistry **38**, 1275 (2002).
[62] A. C. Fisher, *Electrode Dynamics* (Oxford University Press, 2003).
[63] A. J. Bard, and M. E. Stratmann, *Encyclopedia of Electrochemistry* (Springer Berlin / Heidelberg, 2003), Vol. 3.
[64] A. Fick, Journal of Membrane Science **100**, 33 (1995).
[65] J. Newman, Thomas-Alyea, K. E. , *Electrochemical Systems* (John Wiley & Sons, New York, 2004).
[66] C. M. A. Brett, and A. M. O.-. Brett, *Electrochemistry principles,methods, and applications* (Oxford University Press, 2005).
[67] J. Heinze, Angewandte Chemie-International Edition in English **32**, 1268 (1993).
[68] R. M. Wightman, Science **240**, 415 (1988).
[69] K. Stulik *et al.*, Pure and Applied Chemistry **72**, 1483 (2000).
[70] M. Fleischmann, and S. Pons, Journal of Electroanalytical Chemistry **222**, 107 (1987).
[71] C. G. Zoski, Electroanalysis **14**, 1041 (2002).
[72] T. Gueshi, K. Tokuda, and H. Matsuda, Journal of Electroanalytical Chemistry **89**, 247 (1978).
[73] F. Belal, and J. L. Anderson, Analyst **110**, 1493 (1985).

[74] M. Ciszkowska, and Z. Stojek, Journal of Electroanalytical Chemistry **191**, 101 (1985).
[75] K. R. Wehmeyer, M. R. Deakin, and R. M. Wightman, Analytical Chemistry **57**, 1913 (1985).
[76] T. V. Shea, and A. J. Bard, Analytical Chemistry **59**, 2101 (1987).
[77] M. Fleischmann, S. Bandyopadhyay, and S. Pons, Journal of Physical Chemistry **89**, 5537 (1985).
[78] A. Russell *et al.*, Analytical Chemistry **58**, 2961 (1986).
[79] D. R. Macfarlane, and D. K. Y. Wong, Journal of Electroanalytical Chemistry **185**, 197 (1985).
[80] A. M. Bond, M. Fleischmann, and J. Robinson, Journal of Electroanalytical Chemistry **168**, 299 (1984).
[81] A. J. Bard, *Electroanalytical Chemistry* (Marcel Dekker, INC., New York, 1989), Vol. 15.
[82] A. J. Bard, Mirkin, M. V., Fan, R. F., *Electroanalytical Chemistry* (Marcel Dekker, 1994).
[83] M. A. Dayton *et al.*, Analytical Chemistry **52**, 946 (1980).
[84] J. O. Howell, and R. M. Wightman, Analytical Chemistry **56**, 524 (1984).
[85] R. J. Forster, Chemical Society Reviews **23**, 289 (1994).
[86] M. L. Longmire *et al.*, Analytical Chemistry **62**, 747 (1990).
[87] P. J. Kulesza, and L. R. Faulkner, Journal of the American Chemical Society **115**, 11878 (1993).
[88] J. T. Mcdevitt *et al.*, Journal of the American Chemical Society **111**, 4528 (1989).
[89] J. Ghoroghchian, S. Pons, and M. Fleischmann, Journal of Electroanalytical Chemistry **317**, 101 (1991).
[90] J. B. Cooper, and A. M. Bond, Journal of Electroanalytical Chemistry **315**, 143 (1991).
[91] J. D. Norton *et al.*, Analytical Chemistry **63**, 1909 (1991).
[92] A. Schulte, and R. H. Chow, Analytical Chemistry **68**, 3054 (1996).
[93] D. K. Y. Wong, and L. Y. F. Xu, Analytical Chemistry **67**, 4086 (1995).
[94] B. D. Pendley, and H. D. Abruna, Analytical Chemistry **62**, 782 (1990).
[95] R. M. Penner *et al.*, Science **250**, 1118 (1990).
[96] R. J. Forster, and T. E. Keyes, Journal of Physical Chemistry B **102**, 10004 (1998).
[97] A. J. Bard *et al.*, Science **254**, 68 (1991).
[98] A. J. Bard *et al.*, Analytical Chemistry **61**, 132 (1989).
[99] A. J. Bard *et al.*, Scanned Probe Microscopy **241**, 235 (1992).
[100] A. J. Bard *et al.*, Accounts of Chemical Research **23**, 357 (1990).
[101] P. R. Unwin, and J. V. Macpherson, Chemistry & Industry, 874 (1995).
[102] M. V. Mirkin, Analytical Chemistry **68**, A177 (1996).
[103] N. R. Wilson *et al.*, Journal of Physical Chemistry B **110**, 5639 (2006).
[104] A. L. Colley *et al.*, Analytical Chemistry **78**, 2539 (2006).
[105] A. J. Bard, and M. V. Mirkin, *Scanning Electrochemical Microscopy* (Marcel Dekker, INC., 2001).
[106] P. R. Unwin, and J. V. Macpherson, Chemical Society Reviews **24**, 109 (1995).
[107] J. V. Macpherson, and P. R. Unwin, Journal of Physical Chemistry **99**, 14824 (1995).
[108] J. V. Macpherson, and P. R. Unwin, Journal of Physical Chemistry **98**, 11764 (1994).
[109] J. Strutwolf *et al.*, Physical Chemistry Chemical Physics **3**, 5553 (2001).
[110] H. Yamada, T. Matsue, and I. Uchida, Biochemical and Biophysical Research Communications **180**, 1330 (1991).

[111] A. L. Barker *et al.*, Analytica Chimica Acta **385**, 223 (1999).
[112] J. Zhang, and P. R. Unwin, Langmuir **18**, 2313 (2002).
[113] S. Cannan *et al.*, Langmuir **20**, 701 (2004).
[114] C. J. Slevin *et al.*, Langmuir **14**, 5331 (1998).
[115] J. Zhang, and P. R. Unwin, Langmuir **18**, 1218 (2002).
[116] J. Zhang, and P. R. Unwin, Physical Chemistry Chemical Physics **5**, 3979 (2003).
[117] M. A. Borden, and M. L. Longo, Journal of Physical Chemistry B **108**, 6009 (2004).
[118] G. Pu, M. L. Longo, and M. A. Borden, Journal of the American Chemical Society **127**, 6524 (2005).
[119] E. R. Scott, H. S. White, and J. B. Phipps, Journal of Membrane Science **58**, 71 (1991).
[120] E. R. Scott, H. S. White, and J. B. Phipps, Analytical Chemistry **65**, 1537 (1993).
[121] B. D. Bath *et al.*, Analytical Chemistry **70**, 1047 (1998).
[122] T. Yasukawa, T. Kaya, and T. Matsue, Electroanalysis **12**, 653 (2000).
[123] S. Amemiya *et al.*, Analytical and Bioanalytical Chemistry **386**, 458 (2006).
[124] A. J. Bard, X. Li, and W. Zhan, Biosensors & Bioelectronics **22**, 461 (2006).
[125] J. Kwak, and A. J. Bard, Analytical Chemistry **61**, 1221 (1989).
[126] R. C. Engstrom, and C. M. Pharr, Analytical Chemistry **61**, A1099 (1989).
[127] R. C. Engstrom *et al.*, Analytical Chemistry **58**, 844 (1986).
[128] R. C. Engstrom *et al.*, Analytical Chemistry **59**, 2005 (1987).
[129] P. R. Unwin, and A. J. Bard, Journal of Physical Chemistry **95**, 7814 (1991).
[130] A. J. Bard *et al.*, Analytical Chemistry **63**, 1282 (1991).
[131] C. M. Lee, J. Y. Kwak, and A. J. Bard, Proceedings of the National Academy of Sciences of the United States of America **87**, 1740 (1990).
[132] S. M. Fonseca *et al.*, Physical Chemistry Chemical Physics **6**, 5218 (2004).
[133] C. Amatore *et al.*, Journal of Electroanalytical Chemistry **484**, 1 (2000).
[134] N. J. Gray, and P. R. Unwin, Analyst **125**, 889 (2000).
[135] M. V. Mirkin, F. R. F. Fan, and A. J. Bard, Journal of Electroanalytical Chemistry **328**, 47 (1992).
[136] B. B. Katemann, and T. Schuhmann, Electroanalysis **14**, 22 (2002).
[137] D. O. Wipf, and A. J. Bard, Journal of the Electrochemical Society **138**, 469 (1991).

Chapter 4
Experimental details and methods

This chapter describes the experimental methods used in this thesis, together with the apparatus and reagents.

4.1. Samples

In Chapter 5 investigations into the electrical and electrochemical properties of H-terminated intrinsic single crystal diamonds are presented. For this study commercially available E6 CVD grown single crystal diamonds were employed. The samples, plates of 3.0 x 3.0 mm, 0.5 mm thick, have the following specifications and standard tolerances:

+0.2 /- 0.0 mm on lateral dimensions, +/- 0.05 mm on thickness,

+/-3° crystallographic orientation,

Surface finish: 1 side polished Ra (average roughness) < 10 nm,

1 side lapped Ra < 250 nm,

Laser Kerf < 3°, Dimensions to smaller side,

Typically 100% single sector (100), [N] < 1 ppm, [B] < 0.05 ppm,

Orientation (100) faces, <100> edges,

Laser cut edges, edge features < 200 µm [1].

The samples were supplied with one side polished, using a standard cast iron scaife, and with one side lapped. Some samples were repolished at Warwick on the lapped side using a standard cast iron scaife.

In Chapter 6 investigations into the electrical and electrochemical characteristics of moderately doped (<10^{20} cm^{-3} boron) O- and H-terminated single crystal diamond are presented. The samples employed, are denoted with the sample numbers 0372211- E(i) and 0372211- D(i), and contain a boron dopant density of 6 x 10^{18} – 6 x 10^{19} atoms cm^{-3}. They were grown on similar substrates in the same run. 0372211- D(i) was polished using a standard cast iron scaife. 0372211- E(i) was polished using a standard cast iron scaife, an experimental method by E6 (precise details not revealed) and finally repolished using a standard cast iron scaife.

In Chapter 7 investigations into the electrical and electrochemical characteristics of heavily doped (>10^{20} cm^{-3} boron) O- and H-terminated single crystal boron doped diamond are presented. The sample employed is 0572389/1, a single crystal boron doped diamond with a boron dopant density of ~3.4 x 10^{20} atoms cm^{-3}. The sample was employed as grown, without being polished.

All samples were grown on the (100) growth sector.

4.2. Diamond Polishing

As outlined in Chapter 3, section 3.1, single crystal diamond polishing involves the use of a scaife, which can be a cast iron scaife or a resin/ceramic bonded scaife. The samples are placed in the tang's jaws and pressed against the surface of the scaife. In many respects polishing is an intuitive technique, with the quality of the surface finish depending on the skills of the polisher. Figure 4.1 illustrates the equipment used to polish the samples at Warwick: a Colburn cast iron scaife and a tang.

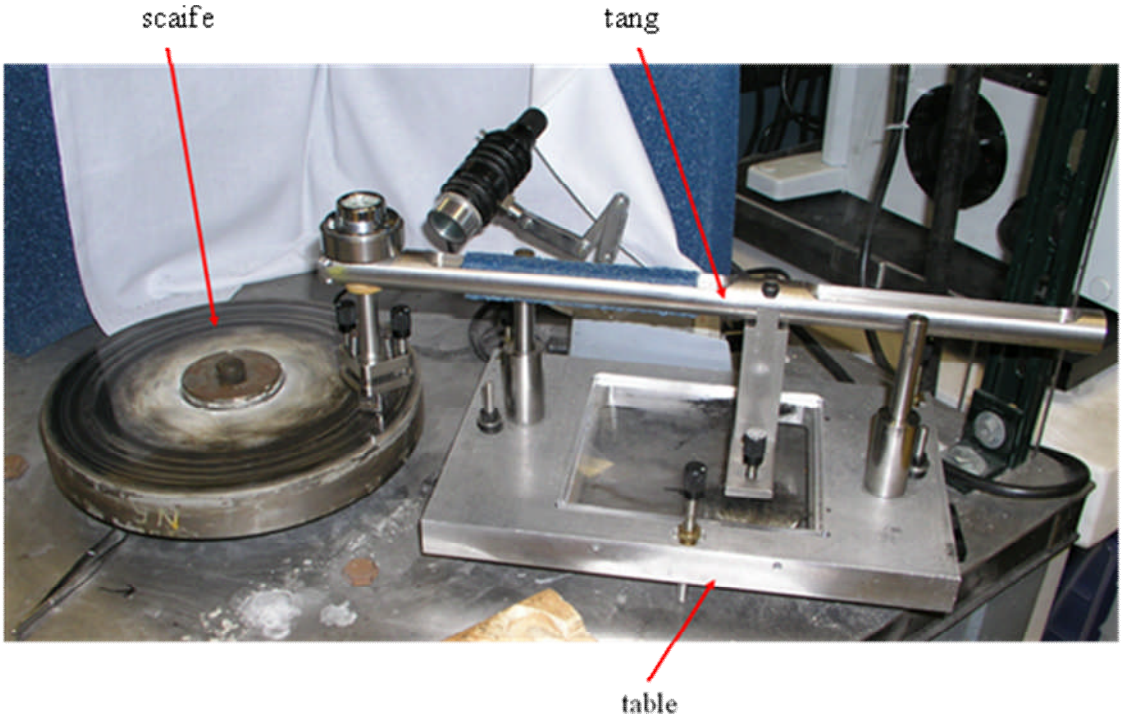

Figure 4.1 Polishing bench depicting a Colburn cast iron scaife and the tang used to hold the samples in place.

Information on the technical specifications, grit size, speed and polishing direction used while polishing the samples with a standard cast iron scaife and with a resin/ceramic bonded scaife can be found in Table 4.1.

Scaife type	***Grit size***	***Speed***	***Polishing direction***
Cast iron scaife	*2- 6 µm*	*3000 rpm*	*110*
Resin/ceramic bonded scaife	*2- 20 µm*	*3000 rpm*	*110*

Table 4.1 Technical details of the types of scaifes used and their specifications. Extensive information on diamond polishing can be found in Chapter 3, section 3.1.

4.3. Photoluminescence mapping

Scientists at De Beers Diamond Trading Company (DTC) Research Centre, Maidenhead, have developed an apparatus which allows them to positively identify a natural diamond from a synthetic one. The apparatus is known as Diamond-View^{TM} and can produce a fluorescence image of the surface of a polished diamond. This can give an indication of the sample's growth structure and impurities incorporated. On the basis of the ultraviolet (UV) excited fluorescence pattern, produced by differential impurity concentrations between growth sectors and growth bands, trained operators can positively identify whether a diamond is natural or synthetic [2]. The reason why the fluorescence patterns can be used to identify synthetic diamond is that the basic growth structure of synthetic diamonds its different from the natural ones, and details of these growth structures can be deduced from the fluorescence patterns. Synthetic diamonds grow generally as cubo-octaheral, while for natural diamonds the basic form of growth is octahedral. Small natural cubo-octahedral diamonds have been found but they are extremely rare. For most natural diamonds, as the conditions in which they grew fluctuated over time, different types and levels of impurities were incorporated at different stages of growth. This leads to differences in fluorescence behaviour between growth bands in the crystal.

For many years cathodoluminescence methods have been used to image growth-dependent patterns in minerals (including diamond) [3-6], but as this technique requires a vacuum it is not considered satisfactory when a large number of samples need to be analysed rapidly. This was the motivation that encouraged the development of ultraviolet-excited fluorescence imaging as a technique for the survey of diamonds.

Under the term *luminescence* various luminous emissions are included. Depending on the source of the excitation of the luminescent material the phenomenon can be classified in *photoluminescence* (photon excitation), produced by adsorption of light or usually ultra-violet radiation, *cathodoluminescence,* produced by excited energetic electrons or cathode rays, *chemiluminescence,* where the energy is supplied by a chemical reaction and *electroluminescence*, produced through the application of an electric field. Another distinction is frequently made between *fluorescence* and *phosphorescence*; they are differentiated through the time delay before the emission of photons. The duration of the emission (after the excitation is stopped) is determined by the lifetime of the electron transition from one energy level to another. When the emission of photons is due to a direct transition from the excited to the ground state within ~10^{-8} s, the luminescence is called *fluorescence*. Luminescence that persists after the excitation stops is called *phosphorescence*.

The Diamond-View^{TM} instrument has a camera and a fluorescence imaging unit connected to a purposely configured computer. The sample to be examined is placed in the jaws of a stone holder. The sample can be rotated while under examination. Visible light is initially shone onto the sample and the camera is focused. Subsequently the sample is illuminated with UV light, specially filtered such that almost all the light reaching the sample is of wavelengths shorter than 230 nm. The energy of this UV light is equal to or greater than the intrinsic energy band-gap of diamonds; radiation of this energy will excite fluorescence in all types of diamond regardless if they fluoresce to the standard long- and short-wave UV radiation (365 nm and 254 nm) generally used by gemmologists. Additionally at wavelengths shorter than 230 nm, all types of diamond absorb light very strongly. In these conditions fluorescence is generated very close to the surface of the diamond and so a clear two-dimensional pattern can be observed. The fluorescence emitted is viewed by a solid-state CCD (charge-coupled

device) video camera and the image is recorded. The sample can be rotated, without opening the chamber, so that other areas of interest can also be investigated it. Diamond-View^{TM} is a very useful instrument for assessing diamond's purity and quality.

Using Diamond-View^{TM} maps of the BDD single crystal samples were recorded. The substrate was held at room temperature, the luminescence excited by above band gap UV excitation, and the emitted light image recorded with a video camera.

4.4. Preparation of oxygen and hydrogen terminated diamond surfaces

4.4.1. Oxygen terminated diamond surfaces

The preparation of the oxygen terminated diamond surfaces involved two approaches: acid cleaning or plasma asher cleaning.

In the acid cleaning procedure the samples were boiled on a hot plate in a saturated solution of potassium nitrate, KNO_3 (Fisher) in concentrated sulphuric acid, H_2SO_4, (98%, Aldrich). This solution gives brown fumes which are very poisonous. The samples were boiled for at least 30 minutes or until the brown fumes turned white, which means that the KNO_3 (Fisher) is exhausted. When the solution cooled the samples were rinsed with doubly deionised water, then placed again in concentrated sulphuric acid (98%, Aldrich) and put into an ultrasonic bath for 20 minutes [7]. They were rinsed with doubly deionised water, dried with air and stored between lint free paper (V&P Scientific, Inc.) in sample pots or in antistatic sample containers (Lane Packaging Ltd.).

For the plasma asher cleaning stage, an Emitech K1050X plasma asher was used. The samples were carefully placed into the plasma asher, the gas was set for oxygen at a pressure of about 0.6 mbar (100 W) for 20 minutes. The colour of the plasma was purple/blue.

4.4.2. Hydrogen terminated diamond surfaces

The preparation of the hydrogen terminated diamond surfaces started with the samples' oxygenation, as described in section 4.4.1. Subsequently they were placed in a 2 kW microwave plasma CVD reactor, see Figure 4.2, (Bristol CVD Diamond Group), powered up under a constant flow of hydrogen at a rate of 500 sccm (standard cubic centimetres per minute). When the pressure reached *ca.* 60 torr, the diamond samples were left in this environment for 2 minutes. The substrates' temperature was measured using a single colour optical pyrometer and it was established to be ~700° C.

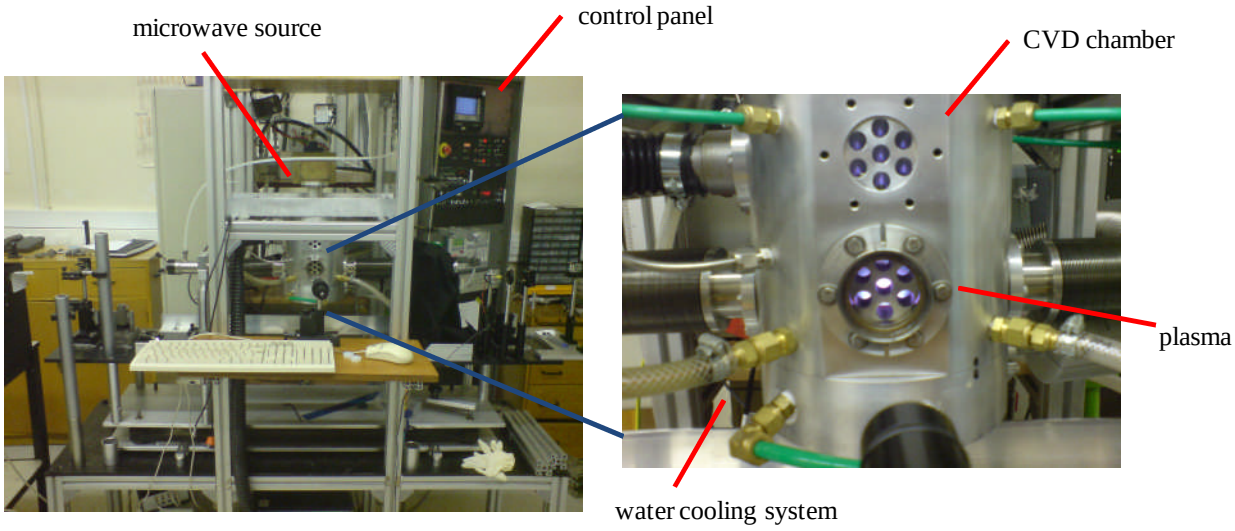

Figure 4.2 The 2kW CVD reactor and the reactor's chamber (Bristol CVD Diamond Group).

The CVD reactor was powered down at the same rate of 500 sccm under a constant flow of hydrogen. The samples were left to cool under a constant flow of hydrogen for 4 minutes.

The hydrophobicity of the samples was quickly tested through contact angles measurements of a droplet of water. In all cases, contact angles of around 90° were observed [8]; see a typical example in Figure 4.3.

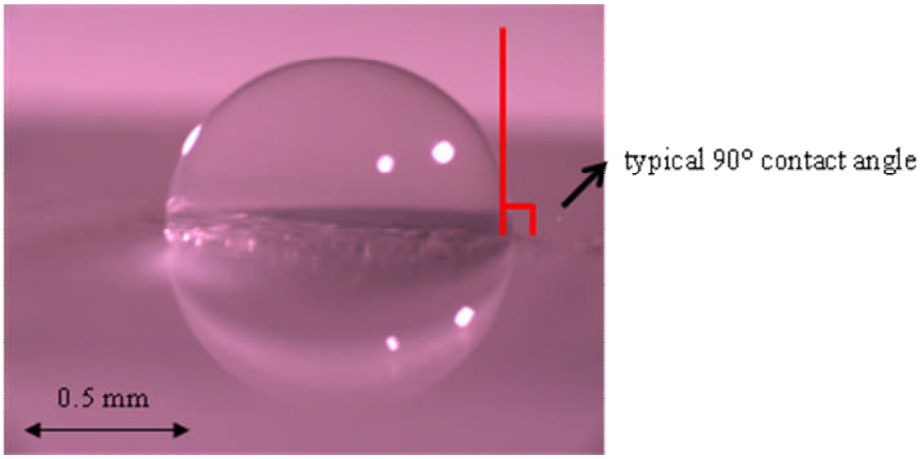

Figure 4.3 Typical contact angle on an H-terminated diamond surface (droplet of water).

The samples were stored between lint free paper (V&P Scientific, Inc.) in sample pots or in antistatic sample containers (Lane Packaging, Ltd.). The H-terminated samples proved to be easier to keep clean and dust free, compared with the O-terminated samples. The H-terminated samples exhibited a high degree of stability over time. For example, the same degree of hydrophobicity (contact angles of around 90°) was observed for the hydrogenated samples after time intervals as long as 3 months since their original hydrogenation.

4.5. Contact fabrication

In order to use the diamond samples as electrodes and to explore their electrical and electrochemical properties, a good Ohmic contact had to be formed. An Ohmic contact is regarded as one that does not change the equilibrium carrier concentration within the semiconductor, does not affect the device characteristics and does not introduce a parasitic resistance while performing the experiments [9]. Even if there are a large number of publications on the electrochemical properties of diamond samples, very few of them take into account the effects of a good/bad Ohmic contact.

Considerable practical effort was devoted to contact fabrication in order to master the techniques of diamond surface preparation, lithography and metal deposition.

Lithography (see Chapter 3, section 3.2) is a technique commonly used to imprint patterns on semiconductors that will be used as integrated circuits. It uses photoresist materials to conceal sectors on the wafer that will not be required for material deposition or removal.

There are two types of photoresist material: negative and positive. Negative resists become less soluble in the developer when exposed to light, creating negative images of the mask patterns on the wafer. Positive resists become more soluble in the developer when exposed to light, creating positive images of the mask patterns on the wafer [10]. In order to achieve maximum process reliability, substrate should be clean and dry prior to starting. Therefore it is very important to clean the samples. This was done using the method described above.

The resist thickness was obtained by spincoating the sample, varying between 15 nm and 1 μm, depending on the resist and on the spinning rate used. In the first few seconds of spin

coating the resist surplus falls off and a uniformly coated surface is obtained. One of the practical problems encountered was the size of the diamond samples. A typical spin coater is designed to be used for wafers > 1 cm^2. The diamond samples employed were < 16 mm^2. In order to overcome this obstacle and to prevent constant blocking of the spin coater with resist, the diamond samples were secured onto > 1 cm^2 silicon dioxide (SiO_2) plates (IDB Technologies) using gel pack (SPI Semicon Europe).

Standard lithography involves the use of a mask-aligner. A CA-800 mask aligner, see Figure 4.4, was employed for sample patterning herein.

Figure 4.4 The CA-800 mask aligner, using a 200 Watt UV mercury short-arc exposure system (exposure uniformity ~5% over $4^1/_2$- inch diameter area) used for sample patterning.

In order to obtain the desired patterns specific masks have been designed for each envisaged application. Several types of masks have been employed: standard Cr imprinted glass masks,

gel pack and steel masks. Each type of mask and the technique used shall be described later in section **a)**, **b)**, **c)** and **d)**.

Metal deposition was carried out using a Moorfield sputter/evaporator, see Figure 4.5. Cr/Au or Ti/Au contacts were evaporated/sputtered with thickness varying between 10 nm- 20 nm (for Cr or Ti) and 210 nm to 1 µm (for Au).

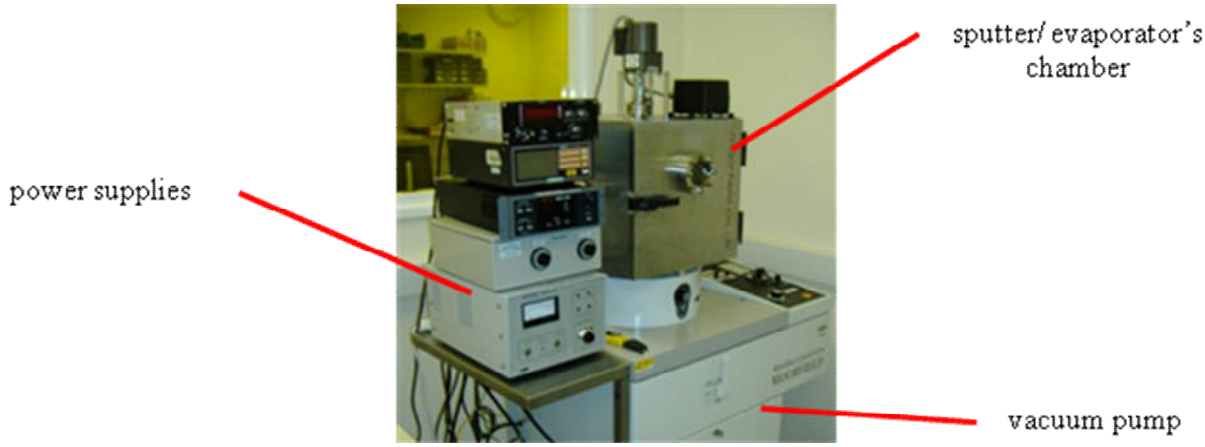

Figure 4.5 The Moorfield sputter/evaporator used for metal deposition applications without breaking the vacuum.

During evaporation the sample is placed inside a vacuum chamber where the metals to be evaporated are also located, placed in tungsten boats. The boats are heated with a high enough current so that the metal can be brought to its boiling point and the metal starts evaporating. As not all metals can be brought to their boiling point using this method, not all metals can be deposited onto the sample of interest. However, this method is preferred for flat surfaces due to its uniform coating coverage.

During sputtering the sample is also placed in a vacuum chamber with the metals of interest while argon is slowly introduced at low pressure. Using a radio frequency (RF) power source,

plasma is ignited and as the ions are ionised they are accelerated towards the metal target. Through this process atoms from the metal source leave the target in vapour form and condense on all surfaces in the chamber including the diamond samples. In contrast to evaporation, all metals used in this thesis could be sputtered.

a) First attempts to create the metal patterned surfaces were made on O-terminated surfaces (prepared as described in section 4.4.1), using the ***negative photoresist*** SU-8 (MicroChem Corp.). Briefly the following process was employed:

1. spin OmniCoat^{TM} (MicroChem Corp.), layer added to improve adhesion and allow easy stripping of the photoresist

2. soft bake at 200°C for 1 minute to drive off some of the solvent in the resist; this may result in a significant loss of mass of resist (and thickness)

3. spin SU-8 (MicroChem Corp.) negative photoresist

4. soft bake at 65°C for 1 minute to drive off some of the solvent in the resist

5. soft bake at 95°C for 3 minutes to drive off additional solvent in the resist

6. expose for 15 s to cause selective chemical properties of the photoresist to change

7. hard bake at 65°C for 1 minute to drive off most of the remaining solvent from the resist

8. hard bake at 95°C for 1 minute to drive off the remaining solvent from the resist

9. wet develop SU-8 (MicroChem Corp.) in SU-8 Remover PG (MicroChem Corp.) for 1 minute and rinse in deionised water

10. wet develop OmniCoat^{TM} in Microposit MF-319 Developer (Shipley Europe Ltd.) for 30 s and rinse in deionised water

11. deposit metal films (20 nm Cr or Ti and 120 nm Au)

12. lift off unwanted metal in Microposit MF-319 Developer (Shipley Europe Ltd.)

Figure 4.6 shows a schematic representation of the lithographic process employing the negative resist SU-8 (MicroChem Corp.).

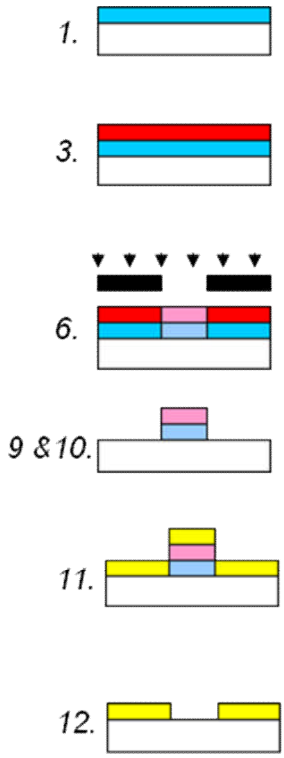

Figure 4.6 Schematic representation of the lithographic process involving the negative photoresist. OmniCoat^{TM} (MicroChem Corp.) and SU-8 (MicroChem Corp.) are spun, steps ***1*** and ***3*** respectively. The photoresist is exposed, step ***6***, and the unwanted material is removed using SU-8 Remover PG (MicroChem Corp.) and Microposit MF-319 Developer (Shipley Europe Ltd.), steps ***9 & 10***. Metal is deposited, step ***11***; subsequently Microposit MF-319 Developer (Shipley Europe Ltd.) is employed to remove the unwanted metal.

During the numerous attempts, when removing the photoresist, lifting off the gold posed problematic. Different solutions were tried: acetone (> 99%, Fisher), Stripper SUC-175 (MicroChem Corp.) and Microposit MF-319 (MicroChem Corp). The best results were obtained using Microposit MF-319 (MicroChem Corp.). Atomic force microscopy (AFM) was used to characterise the topography of the surface after each step and it emphasised the fact that the OmniCoat^{TM} (MicroChem Corp.) layer was too thin, only ±20 nm. A thicker layer (> 300 nm) would have made it easier for the photoresist remover to operate and effectively remove the unwanted material. Additionally, as a result of the thin OmniCoat^{TM}

(MicroChem Corp.) layer its undercut, the portion of the layer etched away under the photoresist, was too shallow and that is why the final step was very difficult, not allowing a clean lift off. Examples of diamond samples patterned using SU-8 (MicroChem Corp.) are presented in Figure 4. 7.

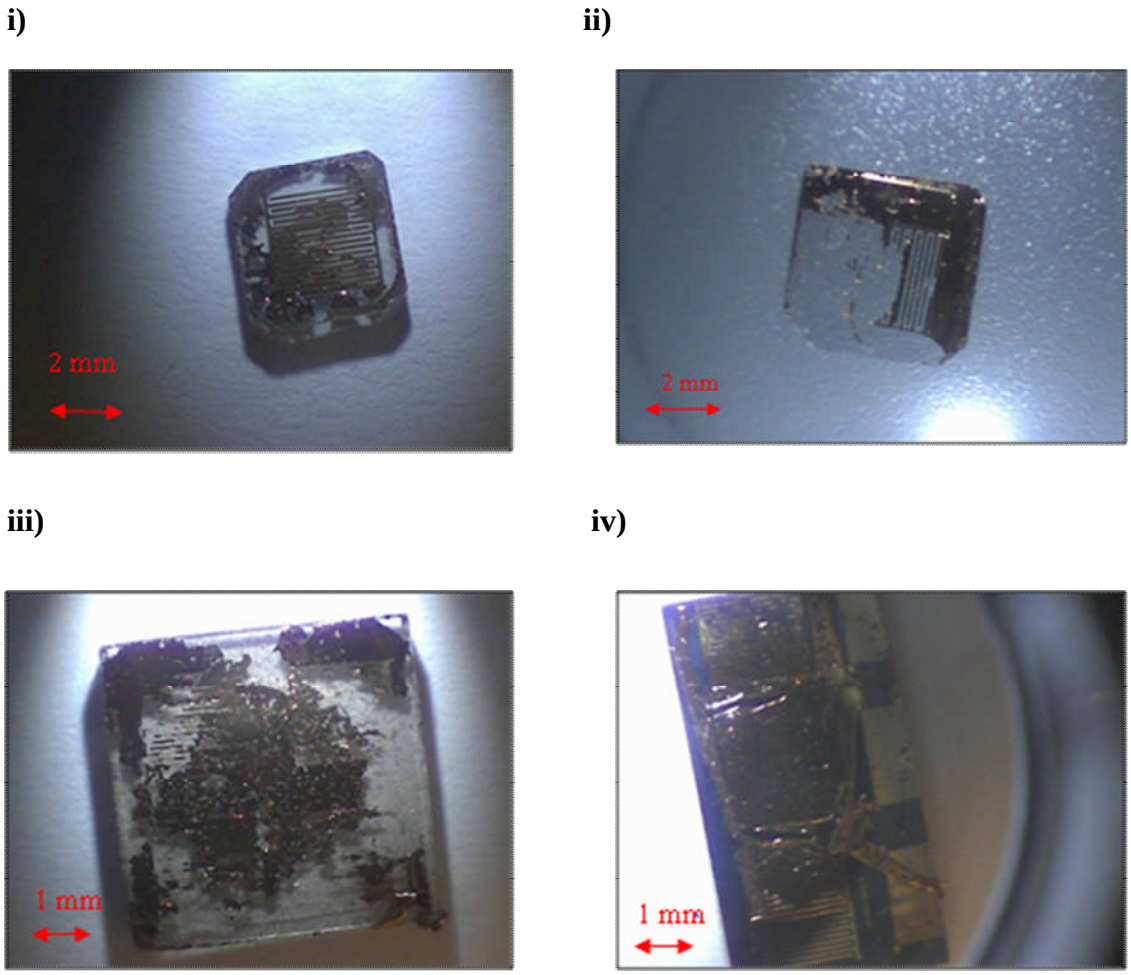

Figure 4.7 Intrinsic single crystal (i & ii), polycrystalline intrinsic (iii) and polycrystalline boron doped (iv) diamond samples, O-terminated, patterned using negative resist as described in the text and in Figure 4.6.

In most cases the lithography process failed, however, an unexpected success was obtained on two diamond samples, see Figure 4.8. The size of these two diamonds was small (2 x 3 mm) compared with the ones used before (i.e. 4 x 4 mm, 6 x 4 mm) and we suspect that the OmniCoat^{TM} (MicroChem Corp.) did not spin well, resulting in a thicker layer of OmniCoat^{TM} (MicroChem Corp.) forming, which allowed the final lift off step. Unfortunately this process was not reproducible. On other diamond samples the entire metal pattern started to lift off or it did not lift off at all.

i) **ii)**

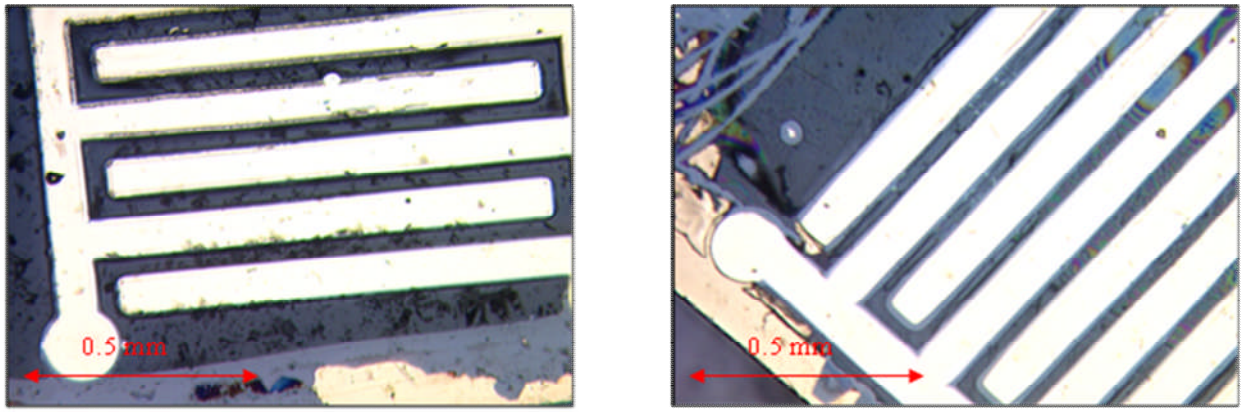

Figure 4.8 Boron doped single crystal diamonds (i & ii), O-terminated, patterned using negative resist, as described in text and Figure 4.6.

This technique was never used for H-terminated diamond surfaces, as exposing the H-terminated diamond surface to aggressive chemicals destroys the H layer, turning the samples back to O-termination.

b) Attempts were also made using the ***positive photoresist*** S1818 (MicroChem Corp.), varying the exposure time. Briefly the following process was employed:

1. spin Primer (MicroChem Corp.), layer added to improve adhesion

2. spin LOR (MicroChem Corp), layer added to allow easy stripping of the photoresist

3. soft bake at 150°C for 3 minute to drive off some of the solvent in the resist; this may result in a significant loss of mass of resist (and thickness)

4. spin S1818 (MicroChem Corp.) positive photoresist

5. soft bake at 115°C for 1 minute to drive off some of the solvent in the resist

6. expose for 20 s to cause selective chemical properties of the photoresist to change

7. wet develop in Microposit MF-319 Developer (Shipley Europe Ltd.) for 1 minute and rinse in deionised water

8. deposit metal films (20 nm Cr or Ti and 120 nm Au)

9. lift off unwanted metal in acetone (> 99 %, Fisher)

Figure 4.9 shows a schematic representation of the lithographic process employing the positive resist S1818 (MicroChem Corp.).

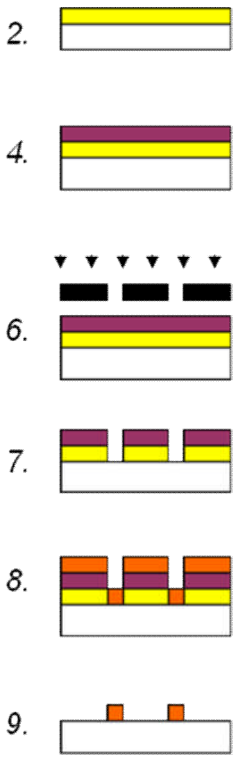

Figure 4.9 Schematic representation of the lithographic process involving the positive photoresist. LOR (MicroChem Corp.) and S1818 (MicroChem Corp.) are spun, steps ***2*** and ***4*** respectively. The photoresist is exposed, step ***6***, and the unwanted material is removed using Microposit MF-319 Developer (Shipley Europe Ltd.), step ***7***. Metal is deposited, step ***8***; subsequently acetone (> 99 %, Fisher) is employed to remove the unwanted metal.

Figure 4.10 shows SEM images of SiO_2 samples patterned using the positive resist S1818 (MicroChem Corp.) as described in text and in Figure 4.9. The images were recorded once the steps 1 to 7 were completed and before the metal deposition. The images show the LOR (MicroChem Corp.) and S1818 (MicroChem Corp.) layers and their thicknesses (~ 1 µm for LOR (MicroChem Corp.)), while also highlighting the undercut obtained through this process. Using this method, removing the photoresist and lifting off the unwanted metal posed no problems, but AFM experiments confirmed that resist residue still remained on the sample's surface. A clean, resist free surface, was never achieved. Figure 4.11 shows images of O-terminated intrinsic polycrystalline diamonds patterned using the positive resist S1818 (MicroChem Corp.).

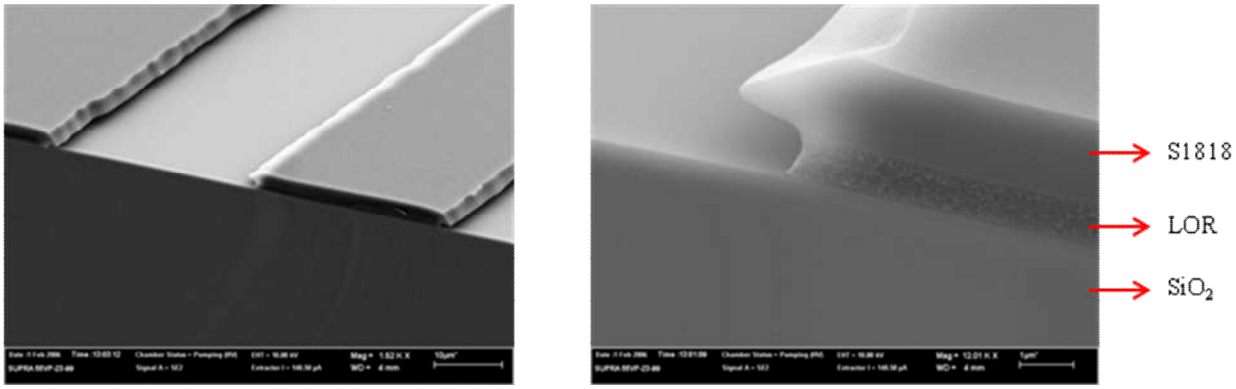

Figure 4.10 SiO_2 samples patterned using the positive resist S1818 (MicroChem Corp.) as described in text and in Figure 4.9.

i) **ii)**

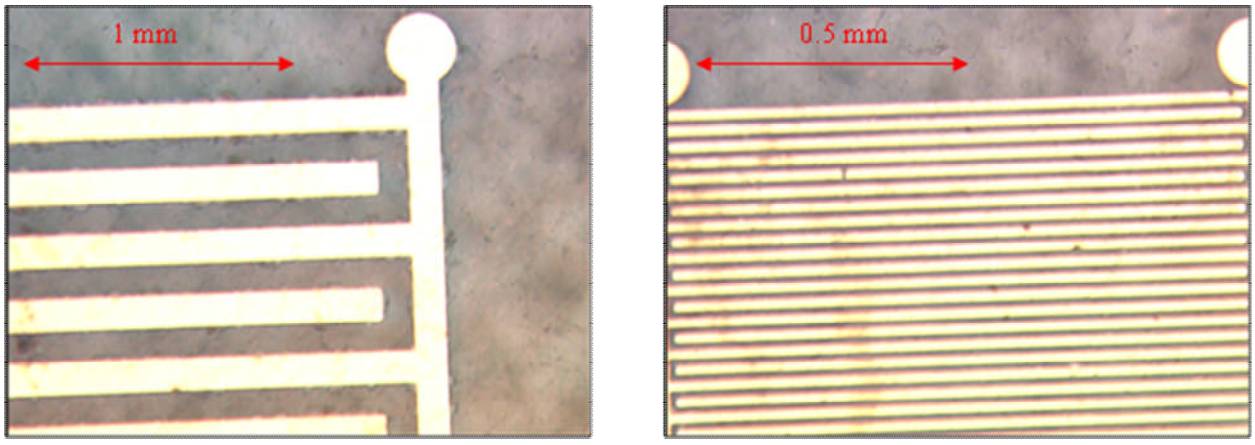

Figure 4.11 Intrinsic polycrystalline (i & ii) diamonds, O-terminated, patterned using the positive resist S1818 (MicroChem Corp.), as described in text and in Figure 4.9.

Since this process also involved harsh chemicals, H-terminated samples were never patterned in this manner as the technique would destroy the H layer.

For both lithographic approaches, described at ***a)*** and ***b)***, a big disadvantage is the fact that the surface of the diamond is directly exposed to the photoresist and obtaining a clean surface after removal of the photoresist is extremely difficult to achieve.

c) A third method employed ***etching*** of unwanted material: the metals (Ti/Au) were sputtered onto the clean diamond surface which was then patterned using positive or negative resists. The unwanted metallic material was removed using etchants, 0.28 g KI + 0.2 g I_2 + 8 ml H_2O for Au and 20% H_2SO_4 (98 % Fisher) for Ti. Using this approach the surface of the diamond was not directly exposed to the resist. The results obtained for pattering of the surface were reproducible (yield of 80%), but again the working side of the sample was found to be contaminated by the etchant. Figure 4.12 shows images of O-terminated intrinsic single crystal diamonds using etching of unwanted material as described in the text.

i) **ii)**

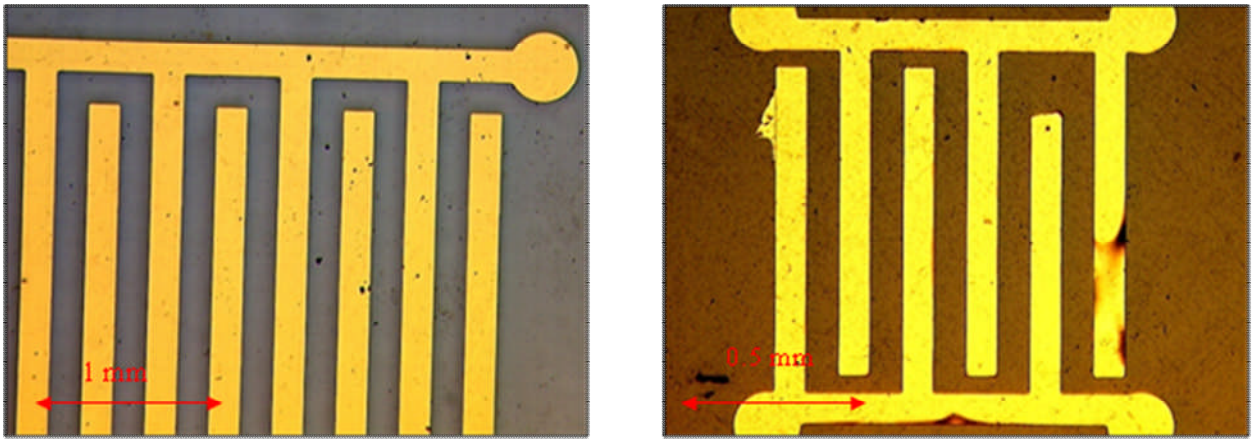

iii) **iv)**

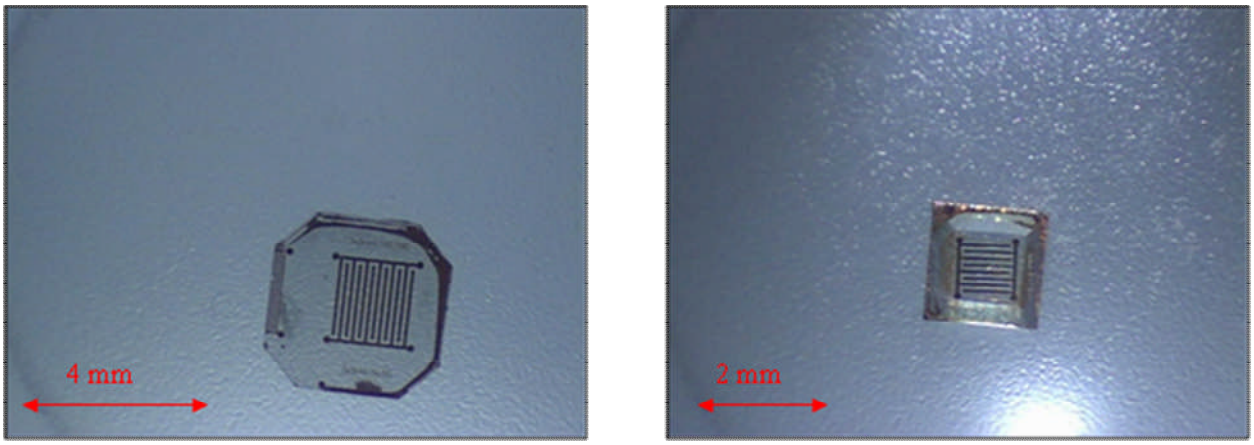

Figure 4.12 Intrinsic single crystal diamonds, O-terminated, patterned using etching of unwanted material, as described in the text.

Only O-terminated diamond samples were processed using this technique, because the exposure of H-terminated diamond samples to the chemicals used for etching the metals would have destroyed the H layer and so compromise the sample.

As the results obtained using classical methods have not been considered satisfactory, due to resist or etchant contaminated surfaces which are likely to affect the electrical and electrochemical results, a new approach was used.

d) Employing an Oxford Lasers class 4 diode-pumped solid-state Nd:YAG laser operating at 355 nm, enclosed to give a class 1 operating system, shadow masks were cut from plates of steel (thickness of 0.2 mm) (Goodfellow, UK) of the desired dimensions and etched to remove any redeposited material in 10% HCl for 15 minutes. The samples were cleaned and O- or H-terminated as described in section 4.4; the masks were placed on top of the samples. The samples with the shadow masks on top were placed in purposely designed sample holders. Images of the shadow masks can be found in Figure 4.13 and images of the sample holders can be found in Figure 4.14.

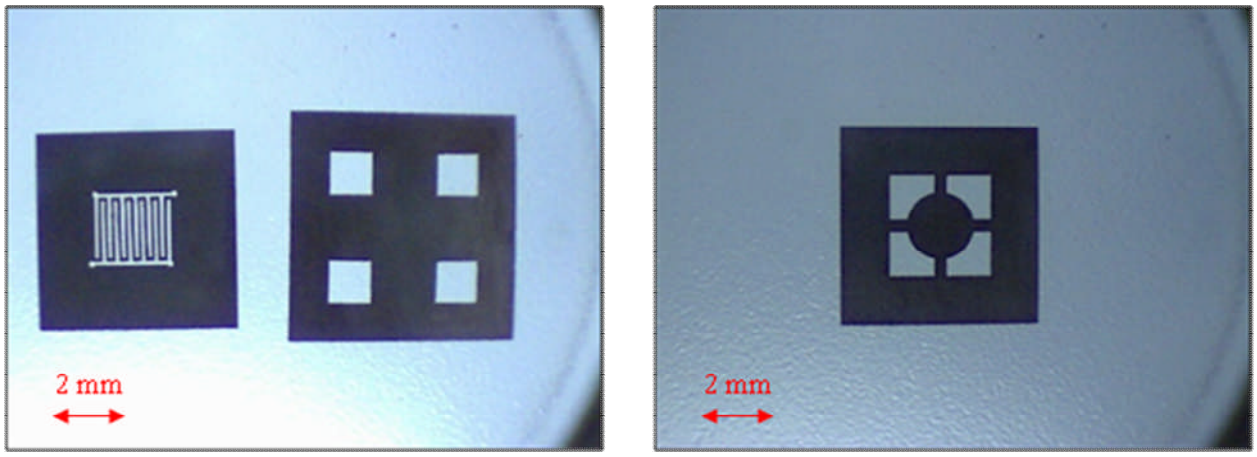

Figure 4.13 Steel shadow masks produced by laser machining them in plates of steel (0.2 mm) (Goodfellow, UK) and etching with diluted 10% HCl for 15 minutes.

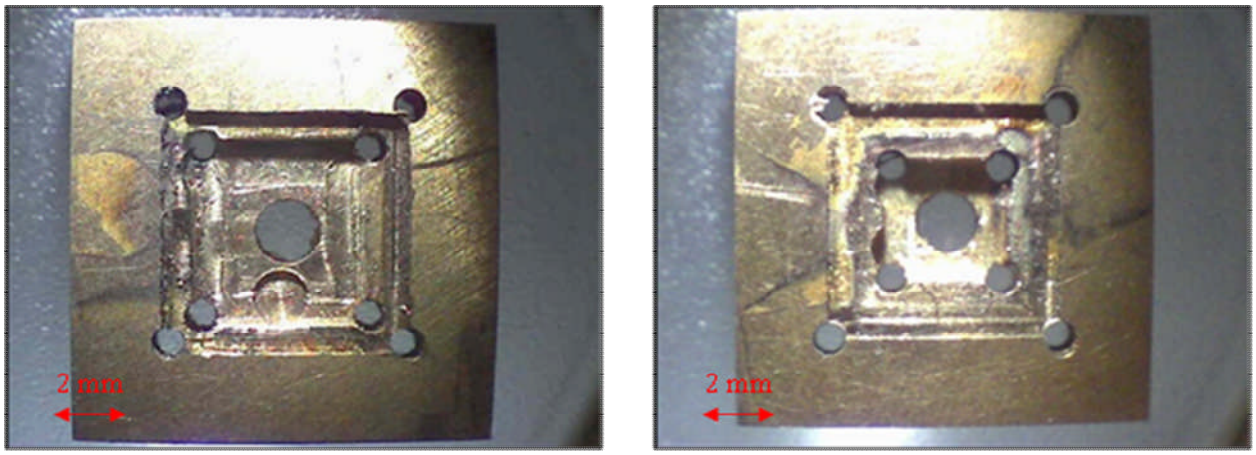

Figure 4.14 Sample holders machined by the Physics Department Workshop.

Through the method described above features' resolution of ~ 20 µm have been obtained. The size of the features depends on the resolution limit of the laser cut.

The Moorfield sputter/evaporator was used to deposit the required metals. In this case none of the previously described issues appeared and the results were found to be reproducible.

While exploring the properties of O-terminated surfaces, ± 20 nm Ti and ± 210 nm / 420 nm Au were sputtered for the top/ bottom contacts. The samples were placed in an oven (Carbolite) and annealed at 500° C for 4 h in order to form titanium carbide and so an Ohmic contact [11].

In the case of the H-terminated samples ± 210 nm Au were sputtered. The Ti layer was not necessary, as Au on an H-terminated surface directly forms on Ohmic contact [9]. Subsequently the contacts and the area between them was covered with a layer of S1818 (MicroChem Corp.) leaving only the edges of the sample exposed. The resist was allowed to dry naturally over night. The edges of the samples were thereafter oxygenated using a plasma

asher, to inhibit their parasitic contribution to the samples electrical or electrochemical characterisation. The photoresist was removed in acetone (> 99 %, Fisher). The samples' hydrophobicity was tested; contact angles typical for an H-terminated surface (around 90°) were observed.

To provide an electrical connection a 150 mm length of wire from RS Components was contacted to the gold with silver electrodag (1415M, Agar Scientific, Essex, UK). This was allowed to dry over night before all the remaining gold was covered in Araldite (Bostik Ltd., Leicester, UK), to ensure that the contact was not exposed to the solution. Schematic representations and images of the in-house built diamond electrode for electrochemical and Hall measurements are presented in Figure 4.15 and Figure 4.16.

a)

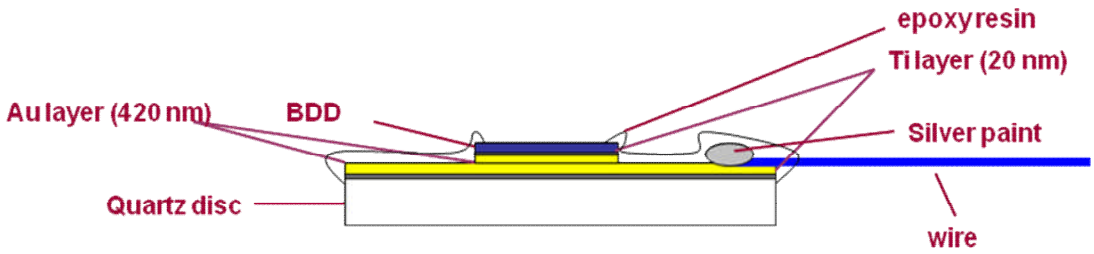

b)

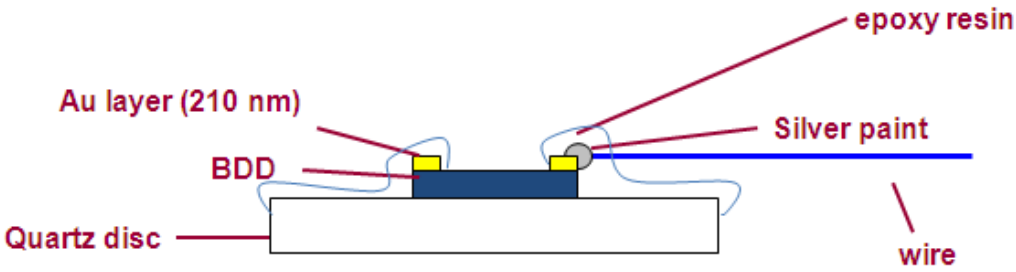

Figure 4.15 Schematic representation of the in-house built diamond electrodes. The design shown in (a) was used for oxygen terminated boron doped samples. If the samples were hydrogen terminated, regardless if boron doped or intrinsic, they were top contacted as shown in (b).

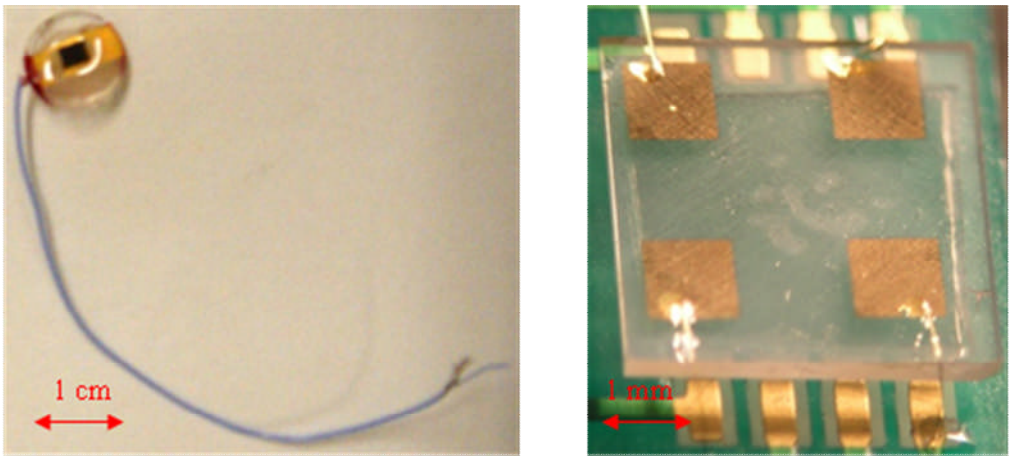

Figure 4.16 Samples of in house built diamond electrodes for electrochemical and Hall measurements.

4.6. Solution preparation

All solutions were prepared using Milli-Q water (Millipore Corp, resistivity ≥18 MΩ□cm), with the mass of material added determined with a four-figure analytical balance (Sartorius A2008). The grades and suppliers of all the chemicals used are listed in Table 4.2.

CHEMICAL	GRADE	SUPPLIER
Acetone	>99%	Fisher
Argon	Pureshield	BOC
Nitrogen	Pureshield	BOC
Potassium Nitrate (KNO_3)	>99.5%	Fisher
Potassium Chloride (KCl)	A.R.	Fisher
Sulfuric Acid (H_2SO_4)	98%	Fisher
Potassium Hexachloroiridate (K_2IrCl_6)	99%	Strem Chemicals
Potassium iodide (KI)	99%	Fisher
Hydrochloric Acid (HCl)	A.R.	Fisher
I_2	95%	Fisher
Hexaammineruthenium chloride (III) ($Ru(NH_3)_6Cl_3$)	99%	Strem Chemicals
Ferrocenylmethyltrimethylammonium iodide ($C_5H_5FeC_5H_4CH_2N(CH_3)_3]^+I^-$)	99%	Strem Chemicals
Silver hexafluorophosphate (AgF_6P)	99%	Strem Chemicals
Phosphoric Acid (H_3PO_4)	85%	Fisher
Potassium Hydroxide (KOH)	85%	Strem Chemicals

Table 4.2 Grades and suppliers of all chemicals used in the studies described within this thesis.

4.7. Ultramicroelectrode fabrication

The scanning electrochemical microscopy experiments presented herein were performed using a 25 µm platinum ultramicroelectrode (UME). The details of the fabrication procedure are described elsewhere [12-14]. In brief, a borosilicate glass capillary (2.0 mm outer diameter and 1.16 mm inner diameter, Harvard Apparatus, Kent) was pulled to a fine point using a pipette puller (model PB-7, Narishige Co. Ltd, Japan). A small piece of platinum wire

(25 µm in diameter, Goodfellow, UK) was positioned inside the capillary and then placed under vacuum for 20 minutes. To ensure perfect sealing of the Pt wire, the capillary was closed by heating the glass in a flame, turning slowly, and then examining it under an optical microscope (Olympus BH2-UMA light microscope with Nomarski differential-contrast interference objectives, magnification range: ×50 to ×1000) to make sure no bubbles were present. A thin cooper wire was connected to the Pt wire using solder to establish an electrical contact. Araldite (Bostik Ltd, Leicester) was used to close the open end of the capillary. By polishing the sealed end on a coarse Carbimet paper disc (240 grit, Buehler, Coventry) the Pt wire was exposed. The capillary was coned by hand using silicon carbide paper to obtain the required *RG*, i.e. *RG* = 10, discussed in Chapter 3, section 3.10. To obtain a flat and smoothly polished electrode surface impregnated diamond polishing pads (Buehler, Coventry) of sequentially finer grades (from 9 µm to 0.1 µm) were used to polish the tip on a polishing wheel. The polishing wheel was constructed from a PC hard-drive unit to provide a flat rotating surface. Finally, 0.05 µm alumina on a polishing cloth (Buehler, Coventry, UK) was used to give a fine finish. Dimensions of the finished UME were determined using an optical microscope (Olympus BH2, Japan). A typical UME after coning and polishing is shown in Figure 4.17.

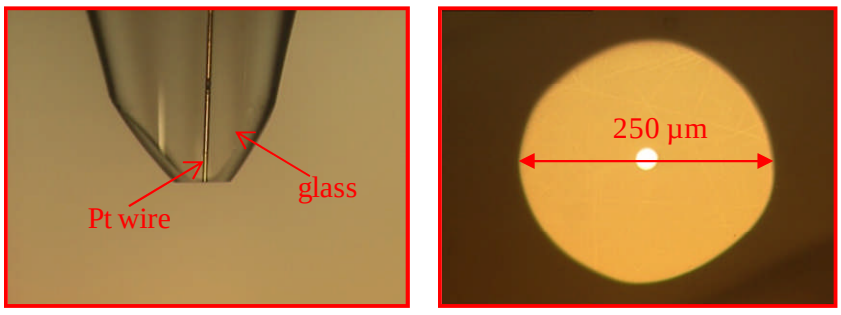

Figure 4.17 Ultramicroelectrodes after polishing and coning with the desired *RG*, i.e. *RG*=10 (*RG*= r_g/a, r_g-radius of the glass sheath plus the electrode; *a*- radius of the electrode). See also Chapter 3, section 3.10.

4.8. Electrochemical experiments

A potentiostat (model CHI 730A, CH Instruments Inc. USA) was used to record the cyclic voltammograms. The electrochemical experiments employing UMEs were performed in a two electrode set up, using a silver/silver chloride electrode as a reference electrode. If a macroelectrode was used, then a platinum gauze served as a counter electrode.

4.9. Cyclic voltammetry

Cyclic voltamograms were employed to assess the quality of the in-house fabricated UMEs and to find out the appropriate voltage at which the UME had to be held in order to maintain a steady-state current for SECM experiments. CVs were recorded at the start and at the end of each experiment in order to make sure that the performance of the UME had not deteriorated during the course of the experiment.

The electrochemical response of the diamond electrodes were tested using CVs at different sweep rates and in different mediators. The aim was to establish to what extent the samples showed characteristics typical for a reversible electrode, see Chapter 3, section 3.8.

4.10. Scanning electrochemical microscopy

The experiments were performed in an electrochemical cell, which consisted of a cylindrical glass body and a teflon base. A chemically inert O-ring (James Walker & Co. Ltd., Cumbria) was inserted into the groove on the base, enabling a water tight seal to be established between the cell and the glass body.

To ensure that the samples attached to the SECM cell were as flat as possible, they were secured to the electrochemical cell's teflon base using double sided adhesive tape. The SECM set-up utilised (see a schematic representation in Figure 4.18), consisted of three TSE-75 piezo-driven stages from Burleigh Instruments (Fischer, New Jersey, USA) in an x,y, z arrangement. The tip, a UME, was mounted onto the z axis position and connected to a computer running a home written scanning programme (Quick Basic). The stages were controlled through a 6000 controller (Burleigh) interfaced to a 486 DX 66-MHz PC and a 6003 joystick (Burleigh). The whole set-up was placed in a home-built Faraday cage and mounted on a breadboard (MSG-22-2, Newport, California, USA). The board was installed on a granite block upon vibration isolation units (pneumatic mounts, RS Components). The potentials were applied using a potentiostat (CH Instruments Inc.) interfaced to a laptop computer with the appropriate software employed (CHI Electroanalyzer, V2.06).

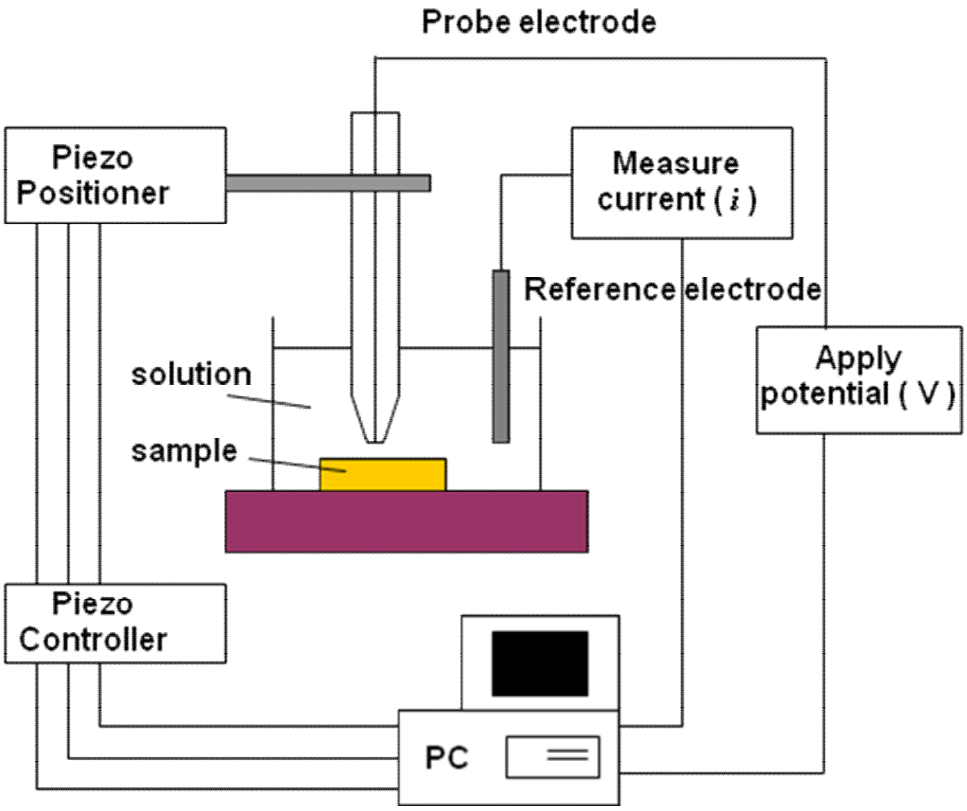

Figure 4.18 Representation of the SECM set- up (see text for more details).

4.11. Conductivity and Hall Effect measurements

The experiments were performed in a standard configuration [15, 16], using a Bruker electromagnet with a maximum field of 1.8 T (cryostat Oxford Instruments), a Keithley 236 Source Measurement Unit, a Keithley 2000 Multimeter, a Keithley 700 and a Keithley 7065. Everything was connected to a computer running an in house written LabView program. The experiments were performed at Walter Schottky Institute, Technical University, Munich, Germany (Jose Garrido's group).

For the in solution measurements, a standard electrochemical cell was placed between the magnets and connected to a potentiostat, see Figure 4.19. The solution was prepared from Milli-Q reagent water (Millipore Corp.), 0.2 M KCl, 0.1 M H_3PO_4 and 0.2 M KOH with pH 7. The surface conductivity of the H-terminated samples, prepared and contacted as described in section 4.1., was studied when the diamonds were submerged in solution and a gate electrode (Ag/AgCl) was used to control the potential at the diamond/electrolyte interface. The electrochemically active area of these samples was defined by oxidising the edges in an oxygen plasma asher leaving just the area of interest H-terminated and conductive; see section 4.5 ***d)*** for details. By using this approach the ideal configuration for conductivity and Hall measurements was achieved, see Chapter 3, section 3.4. Silicon glue (Scrintec, RTV-1K) was used to mask the metal, leaving only the electrochemically active area exposed to the solution. The diamond was used as a working electrode in a standard three electrode electrochemical cell (Ag/AgCl used as a reference and Pt as counter).

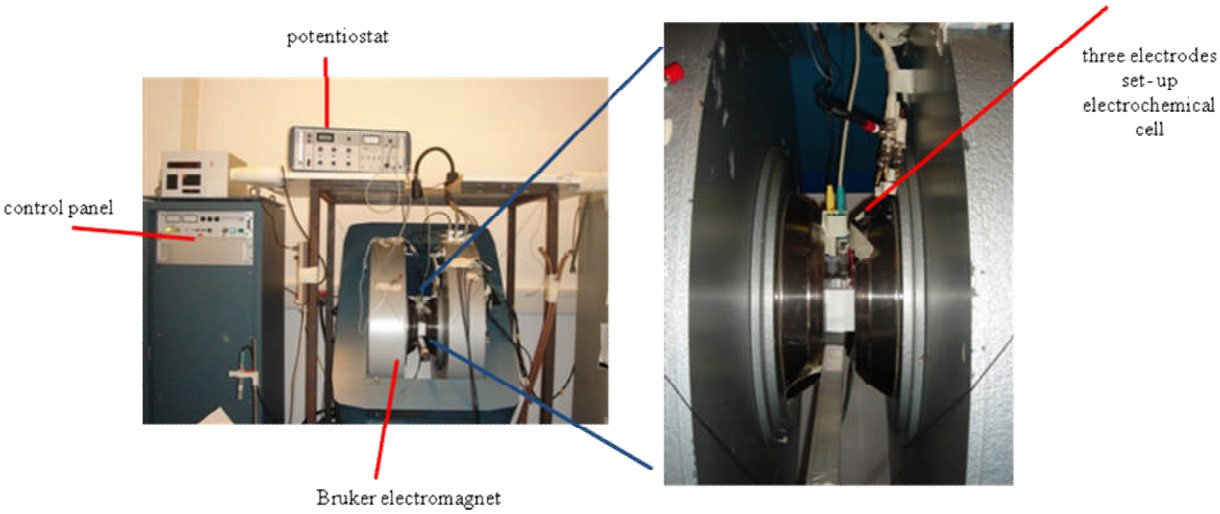

Figure 4.19 The Hall Effect set-up, using a Bruker electromagnet with a maximum field of 1.8 T (cryostat Oxford Instruments) and a standard three electrode electrochemical cell where the diamond was employed as a working electrode, Ag/AgCl as reference and Pt as counter. (Walter Schottky Institute, Technical University, Munich, Germany).

4.12. Wet-gate measurements

The wet gate experiments employed a droplet cell setup, see Figure 4.20. A drop of electrolyte solution was placed over the diamond's exposed area, and the Ag/AgCl reference electrode (RE) and Pt counter electrode (C) were positioned inside the drop. Current-voltage curves were recorded using a DAQ card (DT9800, Data Translations) for both analog output and input, controlled by purpose-written LabVIEW software. For wet gate measurements, a constant bias was applied at the source electrode (V_{SD}) while sweeping the gate potential (V_{wg}) applied to the RE, in the range of -0.7 to 0.7 V. Source-drain current (I_{SD}) as function of (V_{wg}) was converted to a voltage by an Ithaco 1211 virtual earth current preamplifier connected to the drain electrode and recorded using the DAQ card.

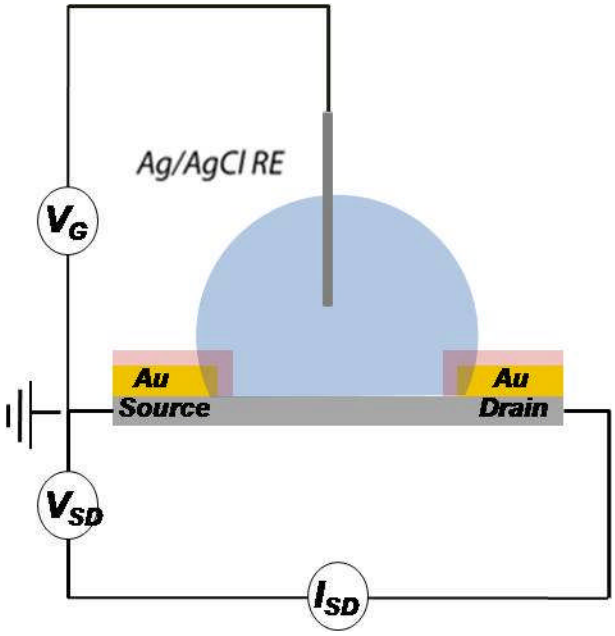

Figure 4.20 Schematic representation of the set-up used for wet gate measurements (see text for detail).

4.13. Field Emission-Scanning Electron Microscope (FE-SEM)

FE-SEM [17] reveals information about the sample's topography, morphology, etc. by scanning a small sized beam of electrons (in the range of 10 nm) across the sample's surface, while the electron-sample interactions are analysed by several detectors.

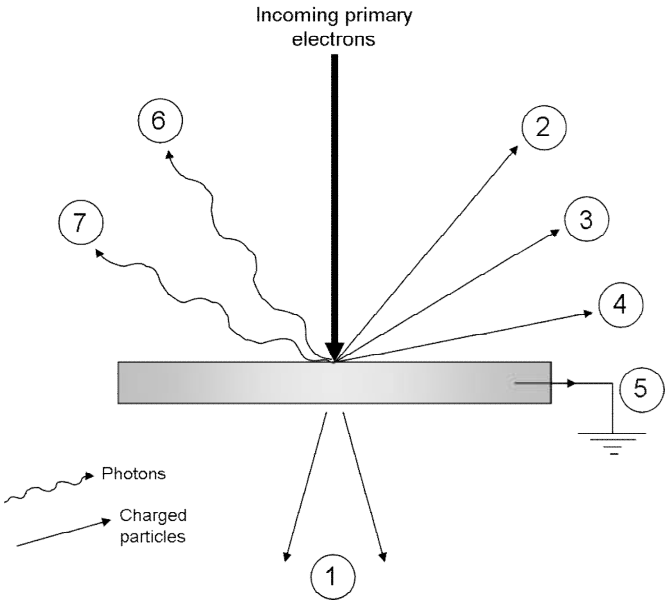

Figure 4.21 Schematic showing photon and charged particle emission from a surface following electron bombardment. 1 = transmitted electrons, 2 = secondary electrons, 3 = backscattered electrons, 4 = Auger electrons, 5 = absorbed current, 6 = X-rays, and 7 = cathodoluminescence [17].

The electrons are generated by a tungsten filament or a field emission gun. Once generated, the electrons are focused onto the sample by a set of electromagnetic lenses and accelerated to an energy which is in the range of 1-30 keV. Their penetration depth is dependent on the energy of the impinging electrons. Of particular relevance to SEM are secondary electrons and backscattered electrons. Secondary electrons produce basic topographic images, while backscattered electrons can give information on the elementary composition of the specimen.

The diamond samples examined using FE-SEM were prepared by coating in a thin layer of gold using a sputter coater (Moorfield, UK). The FE-SEM instrument Zeiss Supra 55VP FE-SEM.) was set at an acceleration speed of 10.0 kV with a working distance of 15 mm.

4.14. Atomic Force Microscopy

In contact mode AFM [18-20] a sharp Si_3N_4 tip attached to the end of a cantilever is held close to the surface of the sample which is scanned underneath the tip in a raster *x*, *y* pattern. The attractive or repulsive forces that the tip experiences result in a deflection of the cantilever, deflection which can be used to produce a topographical map of the surface. A schematic representation of the technique can be found in the Figure 4.22.

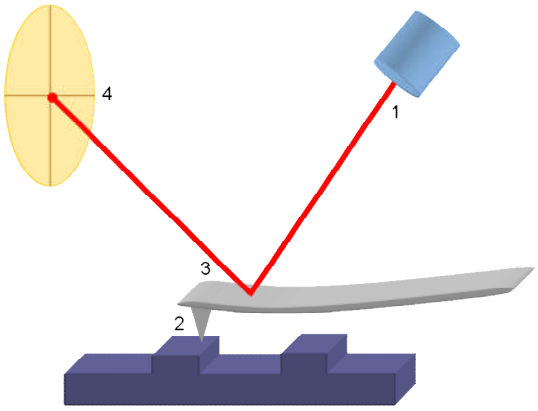

Figure 4.22 Schematic representation of the atomic force microscope (AFM). A laser beam (1) is shone onto the cantilever as the tip (2) scans across the surface of the sample. The laser reflects off the back of the cantilever (3) into a photodiode detector (4).

The surface morphology was imaged using a Nanoscope E AFM (Digital Instruments, Santa Barbara, California) used in conjunction with a Nanoscope IIIa controller. For these measurements, the apparatus was employed in contact mode and contact mode tips made of silicon nitride (Nanoprobes, Digital Intruments, California) were used. While recording the conductive AFM images in house made Pt tips were employed [7].

References:

[1] www.e6.com.
[2] C. M. Welbourn, M. A. Cooper, and P. M. Spear, Gems & Gemology, 156 (1996).
[3] G. S. Woods, and A. R. Lang, Journal of Crystal Growth **28**, 215 (1975).
[4] P. L. Hanley, I. Kiflawi, and A. R. Lang, Philosophical Transactions of the Royal Society of London Series a-Mathematical Physical and Engineering Sciences **284**, 330 (1977).
[5] D. J. Marshall, *Cathodoluminescence of Geological Materials* (Unwin Hyman Ltd., London, 1988).
[6] J. Ponahlo, R. Haubner, and B. Lux, Mikrochimica Acta **116**, 143 (1994).
[7] A. L. Colley *et al.*, Analytical Chemistry **78**, 2539 (2006).
[8] Y. Kaibara *et al.*, Diamond and Related Materials **12**, 560 (2003).
[9] H. Kawarada, Surface Science Reports **26**, 205 (1996).
[10] V. K. Varadan, Vinoy, K. J., Gopalakrishnan, S. , *Smart material systems and MEMS: design and development methodologies* (Wiley, 2006).
[11] N. R. Wilson *et al.*, Journal of Physical Chemistry B **110**, 5639 (2006).
[12] R. M. Wightman, D. O., Wipf, *Electroanalytical Chemistry* New York, 1989).
[13] C. Lee, C. J. Miller, and A. J. Bard, Analytical Chemistry **63**, 78 (1991).
[14] A. J. Bard, and M. V. Mirkin, *Scanning Electrochemical Microscopy* (Marcel Dekker, INC., 2001).
[15] L. J. van der Pauw, Philips Research Reports **13**, 1 (1958).
[16] L. J. van der Pauw, Philips Technical Review **20**, 220 (1958).
[17] I. M. Watt, *The Principles and Practice of Electron Microscopy* (Cambridge University Press, 1997).
[18] G. Binnig, C. F. Quate, and C. Gerber, Physical Review Letters **56**, 930 (1986).
[19] C. F. Quate, Surface Science **300**, 980 (1994).
[20] D. Rugar, and P. Hansma, Physics Today **43**, 23 (1990).

Chapter 5
Electrical and electrochemical characterisation of hydrogen terminated intrinsic single crystal diamond

This chapter investigates the electrical and electrochemical behaviour of hydrogen terminated intrinsic single crystal diamond. The samples were grown using Chemical Vapour Deposition (CVD), and were hydrogen terminated in an identical way. The influence of different surface finishes on the electrical and electrochemical performance was studied. Techniques including AFM, FE-SEM, Hall Effect measurements, FET, bulk electrochemistry and SECM were used.

5.1. Introduction

As outlined in Chapter 2, CVD can be used to produce intrinsic and doped single and polycrystalline diamond, which if as grown is H-terminated. Landstrass and Ravi have investigated the surface conductivity of H-terminated diamond and since its discovery [1, 2] the p-type conductivity observed for H-terminated samples has been a controversial topic of discussion. To date, the explanation proposed by Maier et al. (transfer doping) [3], and described in detail in section 2.4.1 of Chapter 2, has been widely accepted and confirmed by other groups [4-6].

The research presented hereafter aims to determine if the surface damage/contamination induced through various types of polishes influence the electrical and electrochemical performance of H-terminated intrinsic single crystal diamond and if so, how.

5.2. Samples

The samples under investigation are commercially available single crystal CVD diamonds with [N] < 1 ppm and [B] < 0.05 ppm grown by Element Six Ltd. (E6) [7]. The samples are grown on a (100) substrate which is removed after growth to produce free standing layers with lateral dimensions between 2- 8 mm and thicknesses between 0.5- 1.5 mm. The specific details of the samples employed for this study can be found in Chapter 4, section 4.1.

All samples have one side polished by E6 using a cast iron scaife and one side lapped as standard supplied, see Chapter 4, section 4.1. Some samples have been polished at Warwick on the lapped side using a cast iron scaife. Details regarding polishing can be found in Chapter 4, section 4.2.

The surfaces analysed will be denoted with **A**, **B** and **C** as follows:

- **A**: surface polished by E6 using a cast iron scaife as standard supplied
- **B**: surface polished at Warwick using a cast iron scaife
- **C**: the lapped surface as standard supplied (Ra < 250 nm)

5.3. Atomic force microscopy

Atomic force microscopy (AFM), see Chapter 4, section 4.14 was employed to map the topography of the samples polished using a cast iron scaife. A Nanoscope E AFM (Digital Instruments, Santa Barbara, California) in conjunction with a Nanoscope IIIa controller was employed in contact mode. For these measurements, contact mode tips made of silicon nitride (Nanoprobes, Digital Intruments, California) were used.

The samples were cleaned and oxygen terminated, see Chapter 4, section 4.4.1. No topographic differences were observed between surfaces **A** and **B**. Considering that the roughness of surface **C** was Ra < 250 nm this technique was not used to image it. A typical AFM image recorded in contact mode for surface **A** is presented in Figure 5.1. Various defects, cracks and chips, in the sample's surface can be observed.

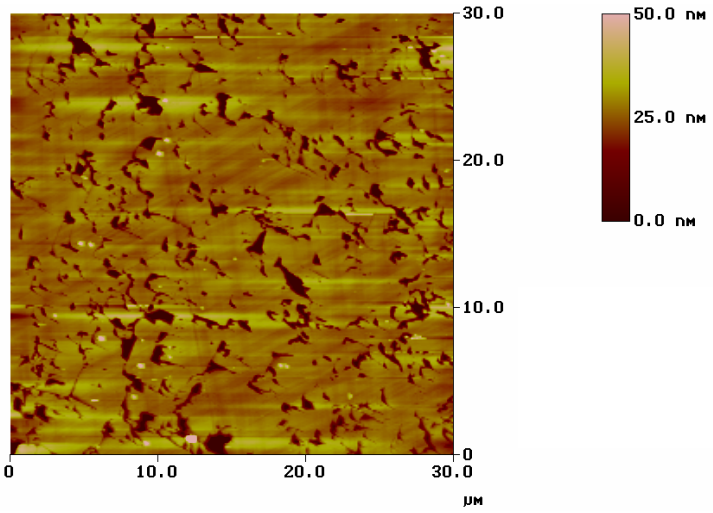

Figure 5.1 Typical AFM image recorded in contact mode for surface **A**.

5.4. Field Emission - Scanning Electron Microscopy

FE-SEM, see Chapter 4, section 4.13, is routinely used to generate low to high-resolution images with magnifications ranging between x 30 and x 10^6. This instrument is widely used to precisely image features less than 10 nm in size [8]. The information depth is in the order of several microns for diamond when 20 kV beams are used. Figure 5.2 presents a typical FE-SEM image recorded for surface **A**. The same features evident in AFM can be seen in the FE-SEM image.

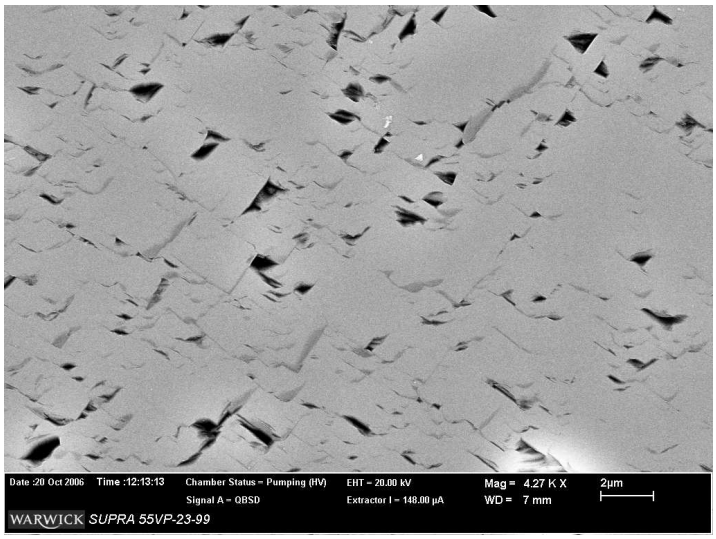

Figure 5.2 Typical FE-SEM image recorded for the surface **A.** The features evident in AFM (Figure 5.1) can also be seen using this technique.

5.5. Electrical characterisation

The carrier transport properties are important parameters of intrinsic diamond. Research in this field has been conducted for many years and recent reports have stated values of 3800 (±400) $cm^2V^{-1}s^{-1}$ for the hole mobility and 4500 $cm^2V^{-1}s^{-1}$ for the electron mobility for high quality single crystal CVD diamond [9].

In order to measure the carrier concentration, mobility, etc. the van der Pauw method was used, see Chapter 3, section 3.4. The samples were H-terminated as detailed in Chapter 4, section 4.4.2. Subsequently contacts were deposited as described in Chapter 4, section 4.5 **d)**. The gold contacts are squares of 0.5 mm x 0.5 mm wide with a 1 mm separation between them. Considerable attention was paid to the electrical connectivity as unreliable contacts would invalidate the results. In Chapter 4, Figure 4.14 shows a typical sample prepared for the electrical characterisation. For these measurements the set-up presented in Chapter 4, section 4.11 was employed.

To begin with, conductivity and Hall measurements were performed in air on all surfaces (**A**, **B** and **C**) and the values obtained for the hole sheet density, mobility and sheet resistance (calculated using the formulas (3.8) and (3.10), Chapter 3, section 3.4) are summarised below in Table 5.1.

Surface	Hole sheet density ($1/cm^2$)	Sheet resistance (kΩ)	Mobility (cm^2/Vs)
A	**2.1 (± 0.5) x 10^{13}**	**7** ± 2	**42 ± 8**
B	**1.9 (± 0.5) x 10^{13}**	**10 ± 2**	**34 ± 7**
C	**4.9 (± 1) x 10^{13}**	**40 ± 8**	**3 ± 1**

Table 5.1 Values of the hole sheet density, sheet resistivity and mobility obtained for the H-terminated intrinsic single crystal samples with different surface preparation, **A**, **B** and **C**, through in air conductivity and Hall measurements.

In the literature typical values reported for in air sheet resistance (R_S) of H-terminated diamond are in the range ~10^4- > 10^5 Ω [10-13]. The large range is due to incomplete H-termination, partial oxidation, and differing bulk diamond properties etc.

The results reported in this work are R_S ~ 7- 10 kΩ ± 2 kΩ for scaife polished surfaces, **A** and **B**, and 40 kΩ ± 8 kΩ for the lapped surface, **C**. As these measurements were made on single crystal samples with [B] and [N] levels less than 0.05 ppm and 1 ppm, respectively, the bulk impurity contribution to electrical conductivity is negligible.

Hall effect experiments reveal the p-type nature of the surface conductivity [14, 15], hole sheet densities have been reported in the range 10^{10}- < $10^{14}cm^{-2}$ and mobilities between 5 and 100 $cm^2V^{-1}s^{-1}$ [10-13]. Hall effect measurements in air at room temperature on the polished surfaces, **A** and **B**, studied here, gave results which were at the upper end of these ranges for carrier densities and in the middle of the range for mobility.

Nebel et al. [16] summarised the widely varying literature data on mobilities in diamond. The data on the polished samples studied here are typical of that reported. However, compared to the polished H-terminated surfaces, **A** and **B**, on the lapped surface **C**, the hole sheet density is higher (factor of ~2.5) and the mobility lower (factor of ~11-14). This is not surprising since this surface is rougher than the polished surfaces, see Chapter 4, section 4.1, and we have undoubtedly underestimated the effective area by taking the macroscopic sample's dimensions. Increased ionised impurity scattering (inversely proportional to the density of ionised impurities) would be expected to reduce the mobility by only a factor of ~2.5 compared to the polished sample, see Table 5.1. Here we assume the density of ions in the termination layer (ionised impurity content) is exactly equal to the number of holes in the accumulation layer.

Prepared as mentioned above, in exactly the same experimental set-up the hole sheet density and mobility of all surfaces (**A**, **B** and **C**) were also examined in a solution set at pH 7, see Chapter 4, section 4.11. Figure 5.3 shows the influence of the gate potential on the inverse sheet resistance. The inverse sheet resistance varies with the gate potential in a similar manner for both **A** and **B** surfaces and it is lower for the **C** surface. Figure 5.4 shows the influence of the gate potential on the hole sheet density. The hole sheet density increases with gate potential for both **A** and **B** surfaces, which are also very similar, but varies widely for the **C** surface. Figure 5.5 shows the influence of the gate potential on the mobility. The mobility varies with the gate potential for both **A** and **B** surfaces and is very low for the **C** surface. Discussion of the results obtained correlated with the FET measurements, is found in section 5.6.

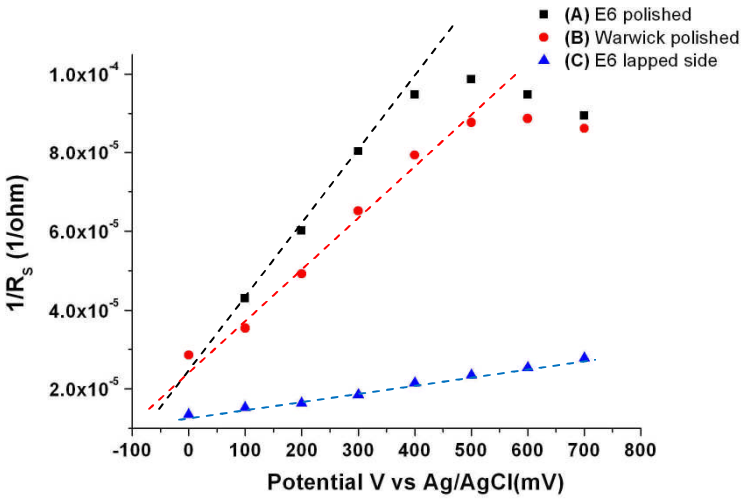

Figure 5.3 Influence of the gate potential on the inverse sheet resistance. The experiments were performed on H-terminated single crystal diamond with the surface **A**, polished by E6 (black),**B** polished at Warwick (red) and **C**, on the E6 lapped side (blue), in a solution of pH 7(H_3PO_4, KCl, KOH, H_2O); 0.1M. The inverse sheet resistance varies with the gate potential in a similar manner for both **A** and **B** surfaces. The inverse sheet resistance is low for the **C** surface.

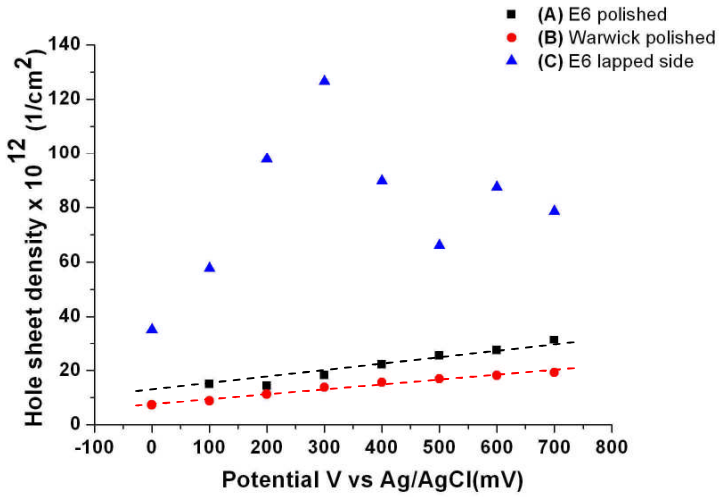

Figure 5.4 Influence of the gate potential on the hole sheet density. The experiments were performed on H-terminated single crystal diamond with the surface **A**, polished by E6 (black),**B** polished at Warwick (red) and **C**, on the E6 lapped side (blue), in a solution of pH 7; 0.1M. The hole sheet density increases with gate potential for both **A** and **B** surfaces, which are also very similar. The hole sheet density varies widely for the **C** surface.

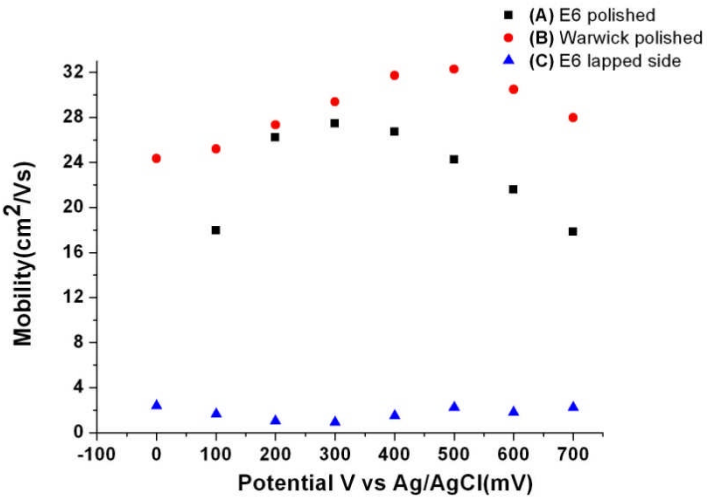

Figure 5.5 Influence of the gate potential on the mobility. The experiments were performed on H-terminated single crystal diamond on the surfaces **A**, polished by E6 (black), **B**, polished at Warwick (red) and **C**, on the E6 lapped side (blue), in a solution of pH 7; 0.1M. The mobility varies with the gate potential for both **A** and **B** surfaces. The mobility is very low for the **C** surface.

5.6. Wet gate measurements

Due to its high mobility, high break-down voltage, high thermal conductivity, etc. diamond could potentially lead to the manufacture of specifically tailored field effect transistor (FET) devices for high power/ high frequency applications. In the current market precise gaps in technology and design need to be addressed. To date only a small number of groups have reported work on diamond based FET devices [17-21] and the results are still at the proof of concept stage. In these circumstances general conclusions cannot be drawn.

The samples surfaces, **A**, **B** and **C**, were hydrogenated as described in Chapter 4, section 4.4.2 and the contacts were prepared as described in Chapter 4, section 4.5 **d)**. The contacts were squares of ~0.5 mm x 0.5 mm with a ~1 mm separation between them. The set-up used is detailed in Chapter 4, section 4.12. The solution was prepared using Milli-Q reagent water

(Millipore Corp.) and 0.1 M KNO_3. A potentiostat was used to control the voltage applied to the sample which was acting as a working electrode in a standard electrochemical cell. Figure 5.6 illustrates typical transistor like characteristics of solution gate field effect transistors based on H-terminated surface conductive intrinsic single crystal diamond on the surface **A**, while the drain current is swept versus the drain voltage for different gate potentials. Figure 5.7 shows the behaviour of gate current V_G while it was varied with respect to the reference electrode Ag/AgCl. The source drain voltage was kept constant, V_{SD} = -0.8V.

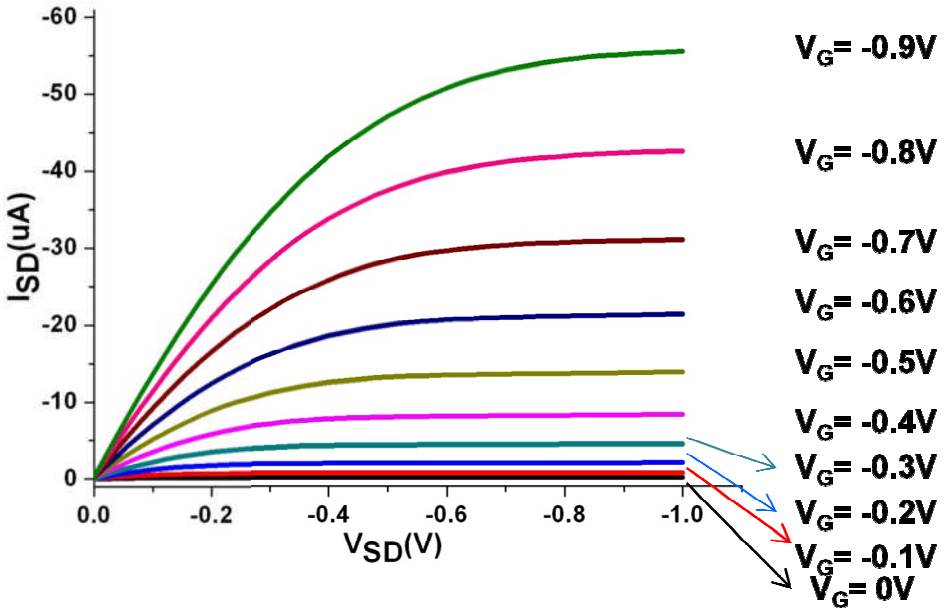

Figure 5.6 Device characterisation of solution gate field effect transistors based on H-terminated surface- conductive intrinsic single crystal diamond, for surface **A**. Transistor characteristics showing the source drain current versus the source drain voltage for different gate potentials.

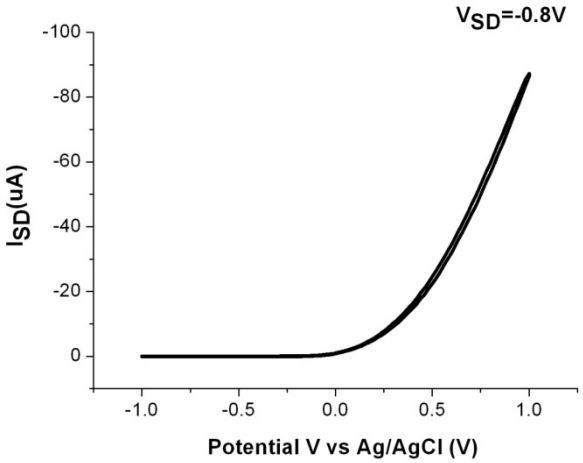

Figure 5.7 Device characterisation of solution gate field effect transistors based on H-terminated surface- conductive intrinsic single crystal diamond, for surface **A**. The source drain voltage was kept constant, V_{SD} = -0.8V, while the gate current V_G was varied with respect to the reference electrode Ag/AgCl.

The transfer doping model, in which a redox reaction in the adsorbed layer, present at any surface in air provides the electron acceptor level necessary for the accumulation of subsurface holes, as stated above, is now widely accepted as the explanation of ''in air surface conductivity''. However, many experimental results of surface conductive diamond in aqueous solution are in clear disagreement with the transfer doping model [21-25]. This important observation has not been fully appreciated to date. Even studies which claim to resolve the controversy related to the pH sensitivity of H-terminated diamond electrode, state that the pH sensitivity of the H-terminated diamond surface conductivity does not follow the prediction of the transfer doping model [26]. However, such predictions do not exist and the ion sensitivity of the electrode yields no arguments with respect to the transfer doping model, neither pro, nor con [22]. Moreover, the use of inappropriate experimental set-ups (e.g. using

pH sensitive Pt gate electrode) [27] has led to the incorrect interpretation of many experimental results.

Importantly, Garrido et al. [21] demonstrated that in contrast to the in air situation, charge transfer across the diamond interface does not govern the surface conductivity in aqueous electrolyte when a gate electrode controls the diamond/electrode interfacial potential. Instead this almost ideally polarisable interface (IPI) allows the capacitive charging of the surface [21]. The solution gate FET behaviour can be satisfactorily explained using the analogy with an IPI [21].

An electrode at which no charge transfer can occur across the electrode-solution interface, regardless of the potential imposed by the external source of voltage is called an ideal polarisable electrode (IPI) [28]. The electrode-solution interface is analogous to that of a capacitor for a H-terminated diamond. This should be a reasonable approximation so long as the potential window is not exceeded. At a given potential there will be a charge (holes) in a thin layer on the diamond surface and the charge in solution is made up of an excess of anions in the vicinity of the diamond surface. The array of charged species and oriented dipoles at the electrode-solution interface is called the electrical double layer. Unlike solid state capacitors, whose capacitances are independent of the voltage across them, the capacitance of the double layers is often a function of potential [28].

We assume the interface looks like the schematic presented in Figure 5.8:

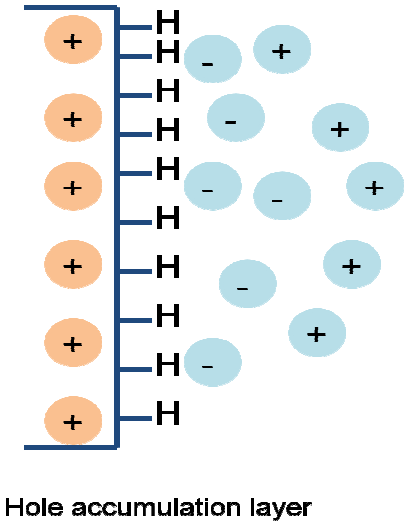

Figure 5.8 Schematic representation of the interface between an H-terminated diamond and the electrolyte solution.

The analogy with a metal-insulator-semiconductor field effect transistor can be made, where the metal is replaced by the solution and the insulator by the solution-diamond interface double layer [29]. The reference (gate) electrode in this work was Ag/AgCl.

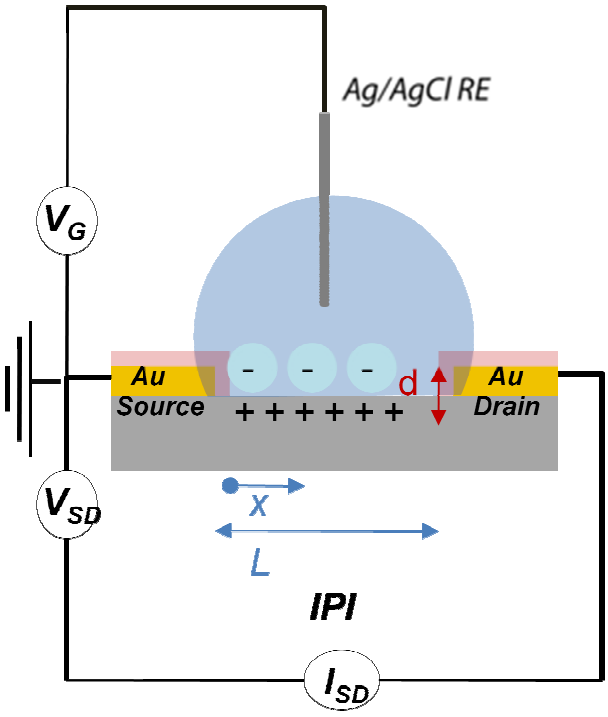

Figure 5.9 Schematic representation of the set-up of an ideally polarisable interface between an H-terminated diamond and the electrolyte solution.

The electric field (E_z) across the ideally polarisable diamond/solution interface is given by Gauss's law [29]:

$$E_z = \frac{D}{\varepsilon_{IPI}\varepsilon_0} \tag{5.1}$$

where D is the charge per unit area and ε_{IPI} the relative permittivity. If the thickness of the interface is d and the potential of the channel with respect to the source is V_x, at a distance x from the source:

$$D = \frac{\varepsilon_{IPI}\varepsilon_0(V_{GS}-V_x-V_T)}{d} \tag{5.2}$$

where V_T is a constant included to take into account the threshold voltage and the effect of possible adsorbed surface charge.

We know:

$$I_{DS} = pe\mu_h E_x S \tag{5.3}$$

where p is the concentration of holes, e the electron charge, μ_h the hole mobility in the accumulation layer, E_x the electric field and S the area of the channel which is equal to width times height, therefore:

$$I_{DS} = Dw\,\mu_h \frac{dV_x}{dx} \tag{5.4}$$

$$\frac{dV_x}{dx} = \frac{I_{DS}d}{\varepsilon_{IPI}\varepsilon_0 w\mu_h(V_{GS}-V_x-V_T)} \tag{5.5}$$

Inserting the limits $V_x = 0$ at $x = 0$ and $V_x = V_{GS}$ at $x = L$:

$$\int_0^{V_{GS}}(V_{GS}-V_x-V_T)dV_x = \int_0^L \frac{I_{DS}d}{\varepsilon_{IPI}\varepsilon_0 w\mu_h}dx \tag{5.6}$$

which leads to:

$$I_{DS} = \frac{\varepsilon_{IPI}\varepsilon_0 w\mu_h}{Ld}\,V_{DS}\left(V_{GS}-\frac{V_{DS}}{2}-V_T\right) \tag{5.7}$$

The capacitance of the ideally polarisable layer, C_{IPI}, is:

$$C_{IPI} = \frac{\varepsilon_{IPI}\varepsilon_0 wL}{d} \quad (5.8)$$

As such:

$$I_{DS} = \frac{C_{IPI}\mu_h}{L^2}[(V_{GS} - V_T)V_{DS} - \frac{{V_{DS}}^2}{2})] \quad (5.9)$$

and

$$\frac{dI_{DS}}{dV_{DS}} = \frac{C_{IPI}\mu_h}{L^2}[V_{GS} - (V_T + V_{DS})] \quad (5.10)$$

$\frac{dI_{DS}}{dV_{DS}}$ is the source drain resistance which should, at constant V_{DS}, be linearly dependent on the V_{GS}, so long as C_{IPI} and μ_h do not vary with V_{GS}.

In section 5.5, the inverse sheet resistance is plotted against the gate potential in Figure 5.3. For the lapped surface, **C**, the inverse sheet resistance behaves as predicted by equation (5.10). The data in Figure 5.5 confirm that the mobility is gate potential independent suggesting that C_{IPI} is also approximately gate (reference) voltage independent. There is a large scatter on the measured value of the sheet carrier concentration (8 ± 4) x 10^{13} cm^{-2} which may relate to a non uniform surface potential. For the polished surfaces, **A** and **B**, the carrier sheet density increases linearly with gate potential as predicted by this simple model, however for values of V_{GS} higher than about ~450 mV the inverse sheet resistance departs from the predicted linear dependence on V_{GS}. The data in Figure 5.5 show that the mobility depends strongly on the gate potential decreasing above ~450 mV, therefore the assumption of constant mobility is no longer valid.

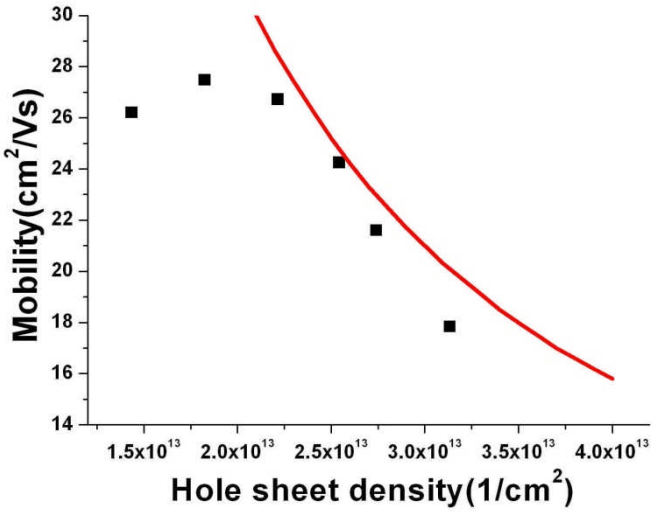

Figure 5.10 The mobility data plotted against the sheet carrier concentration for the surface A (E6 polished).

Figure 5.10 shows the mobility data plotted against the sheet carrier concentration for surface **A** (E6 polished). Above a carrier concentration of 2 x 10^{13} cm^{-2} the mobility decreases with increasing carrier concentration.

In 3D materials at low temperatures where ionised impurity scattering dominates, the mobility is inversely proportional to the concentration of ionised impurities. In the diamond samples used the bulk mobilities of holes introduced by above band gap excitation is approximately two orders of magnitude higher than measured for the near surface holes. This scattering by near surface defects or the near surface charge ions is a likely cause of the low measured mobilities. In Figure 5.10 the solid line shows the expected dependence for ionised impurity scattering originating from the near surface ions in solution.

Finally, the characteristics of a solution gate field effect transistor fabricated on the **A** surface, an H-terminated surface conductive diamond polished by E6, are shown in Figure 5.6 and Figure 5.7. The I_{DS}-V_{DS} characteristics are those that are expected for a solution gate FET. The I_{DS}-V_{DS} characteristics are obtained in the potential window of the H-terminated diamond. The drain current can be pinched off and distinct linear and saturation regions have been observed. We have not studied the pH dependence of this device, but expect similar results to Garrido et al. [21]. Saturation of the solution FET occurs at the drain voltage for which the electric field *E*, equals zero at the drain end of the gate.

Since $E = \frac{D}{\varepsilon_{IPI}\varepsilon_0}$ (5.1) and $D = \frac{\varepsilon_{IPI}\varepsilon_0(V_{GS}-V_x-V_T)}{d}$ (5.2), with $V_x = V_{DS}$, saturation occurs when $V_{DS} = V_{GS}-V_T$. Using equation (5.10)

$$I_{DS} = (V_{GS}-V_T)2\frac{C_{IPI}\mu}{L^2} \qquad (5.11)$$

As long as $V_{GS}>V_T$:

$$I_{DS} = C\mu(\frac{\omega}{L})(V_{GS}-V_T)^2 \qquad (5.12)$$

If we take a value for μ = 30 $cm^2V^{-1}s^{-1}$ then fitting (5.12) to the data in Figure 5.7 gives us a value of *C* =2 .7 μFCm^{-2} which is in good accord with other measurements on H-terminated surfaces [16].

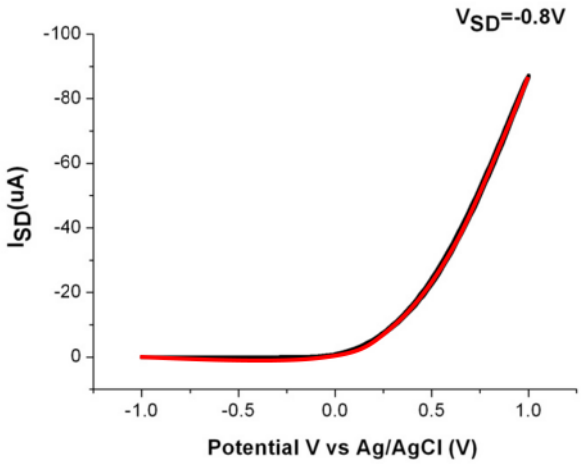

Figure 5.11 Device characterisation of solution gate field effect transistors based on H-terminated surface- conductive intrinsic single crystal diamond, for surface **A** (black). The source drain voltage was kept constant, V_{SD} = -0.8V, while the gate current V_G was varied with respect to the reference electrode Ag/AgCl. The red line represent the theoretical fit while using (5.12) and a mobility of μ = 30 $cm^2V^{-1}s^{-1}$.

In conclusion, this simple model for the aqueous solution diamond interface as an IPI follows the assumption detailed by Garrido et al. [21]. It is shown here that the surface conductivity of the H-terminated diamond in aqueous solution can be fully explained without resort to transfer doping which works so well in air. It is also shown that the low mobility of the holes in the accumulation layer is probably due to surface defects (sensitive to surface preparation) and scattering with near surface ions.

5. 7. Cyclic voltammetry

Cyclic voltammetry was used to investigate the nature of the electron transfer at the H-terminated single crystal diamond electrodes. The CVs look at the electrochemical behaviour of the sc diamond and therefore give an indication of the average electron transfer surface activity. The measurements were taken at room temperature using a three-electrode setup (CHI730A potentiostat, CH Instruments Inc.) controlled by a laptop computer, in a deaerated stationary solution in the presence of a high concentration of an inert electrolyte (KNO_3),

therefore only the rate of diffusion of the electroactive species to the electrode surface needed to be considered as a possible mass transport mechanism. A platinum gauze counter electrode was employed, with a chloridised Ag wire (Ag/AgCl) as a reference electrode.

The sample's surface, O- and H-terminated, was prepared as detailed in Chapter 4, section 4.4 and the contacts were prepared as detailed in Chapter 4, section 4.5 **d)**. The electrochemical response of the diamond samples was investigated using CVs at different sweep rates and in different mediators, to establish to what extent the samples showed characteristics of reversible electrochemistry. The electrolyte solution contained both $Ru(NH_3)_6^{3+}$ ($E_{1/2}$~ -0.3 V) and $FcTMA^+$ ($E_{1/2}$~ 0.25 V) at equal concentrations. Scans of the single crystal H-terminated samples were recorded in the scan range of 0.5 to 0.005 Vs^{-1} and with different redox mediator concentrations (in the range of 0.1 mM to 5 mM). The potential applied to the samples with respect to a Ag/AgCl reference electrode was cycled between 0 V and a maximum of - 0.8 V/ (0 V and a maximum of + 0.6 V) causing the reduction (oxidation) of $Ru(NH_3)_6^{3+}$ / ($FcTMA^+$), and back to 0 V allowing the redox active species to be oxidised (reduced) back to the original oxidation (reduction) state.

In the work on H-terminated diamond solution-gate (SG) FET structures reported here in section 5.6, the device's response can be explained by the IPI model, using the data from the electrical characterisation of H-terminated diamond in aqueous solution, data reported and discussed in section 5.5. However, Zhang et al. [22] discussed that outside the slope of the IPI approximation, there is the opportunity for charge transfer across the diamond electrode solution interface. In the aqueous SG-FET architecture this is manifested as a small gate current (typically < 10^{-9}A) but is usually ignored [22]. This charge exchange results in the

open circuit voltage (OCV) of the diamond electrode in an electrolytic cell versus the reference electrode. Zhang et al.[22] measured the OCV as a function of pH of the electrolyte. They found a mixed (or corrosion) potential that is consistent with the simultaneous equilibration of the electrode versus both the hydrogen-hydronium and the oxygen-hydroxyl redox couple [22]. Their data showed extremely long-time constants for establishing the redox equilibrium and very low exchange current densities.

Electrochemical experiments with well defined outer sphere electron transfer couples on intrinsic hydrogen terminated diamond have been reported by several workers [16, 30], but the literature is somewhat confusing and it is difficult to form a clear picture of the electrochemical properties. Most of the diamond electrochemistry studies have employed highly boron doped diamond; nanocrystalline material has also been used [31, 32]. H-terminated intrinsic single crystal diamond is a material with potential electrochemical applications, but its properties are largely uncharacterised. Ramesham et al.[33] have shown that the material demonstrated increased electrochemical stability when deposited on other substrates. The major difference between the H-terminated diamond and boron doped diamond electrodes was found to be in terms of reproducibility and stability [30]. The boron doped diamond electrodes demonstrated a high degree of stability and reproducibility over time. This was not found to be true for the H-terminated diamond electrodes [30]. This is not a surprising result, as it is known that the properties of H-terminated diamonds depend largely on the H surface coverage and can show a significant dependence on past history and electrode usage [30]. For potentials greater than of order + 1.6 V vs. SCE [16] the H-terminated diamond surface can be oxidised, which removes hydrogen from the surface and destroys the surface conductivity. We note that for good quality heavily boron doped oxygen

terminated diamond electrodes the oxidation reaction e.g. oxygen evolution is pushed out to ~ + 2.5 V vs. SCE [34, 35]. However, claims that the potential window of hydrogen terminated intrinsic diamond extends to large negative potentials with low background currents [16] are misleading. As the SG-FET measurements show (see section 5.6) when such negative potentials are applied to the H-terminated intrinsic diamond electrode no surface conductivity is observed [21], thus the H-terminated diamond is no longer functioning as an electrode and no reduction reactions *eg*. hydrogen evolution are expected or observed.

For the studies reported here redox couples were chosen with chemical potentials that are close to the energy level of the valence band (VB) maximum, see Figure 5.12. In such a calculation it has been assumed that the negative electron affinity of the diamond is ~ -1.0 ± 0.2 eV [21]. The uncertainty in the electron affinity and $\mu_{Ag/AgCl}$ mean that all we can say is that $\mu_{Ru(NH_3)_6^{3+}}$ is close to (possibly slightly above or below) the VB_{max}, whereas μ_{FcTMA^+} is certainly below the VB_{max}.

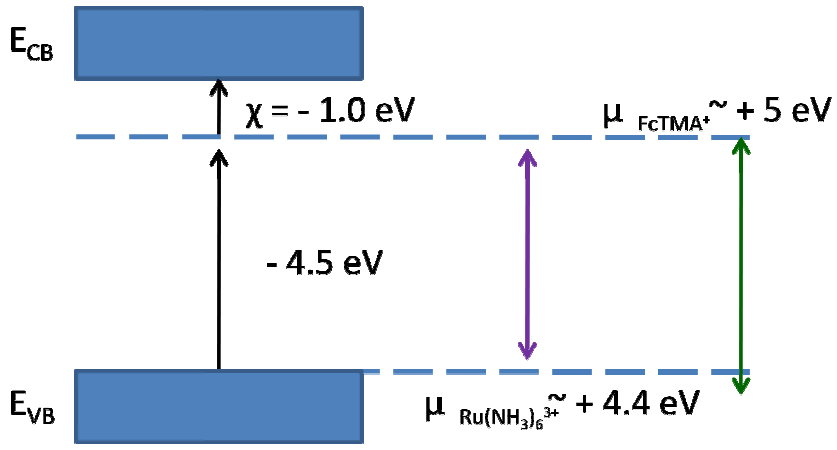

Figure 5.12 Chemical potentials estimated assuming $\mu_{Ag/AgCl}$ ~ 4.7 ± 0.1 eV for H-terminated intrinsic single crystal diamond [28].

Figures 5.13 and 5.14 show that CVs can be recorded on H-terminated intrinsic diamond. Great care was taken during the surface hydrogenation to ensure uniform high quality H coverage. It should be noted that data are only presented for the polished diamond surface, denoted with **A** (sample polished by E6 using a cast iron scaife as standard supplied) that has been H-terminated. It was shown in section 5.5 that the near surface carrier mobility is adversely affected by polishing damage. The surface of the lapped sample was very rough (Ra < 250 nm) and the electrochemical results were not reproducible; leaks to the gold contact were a continuous problem.

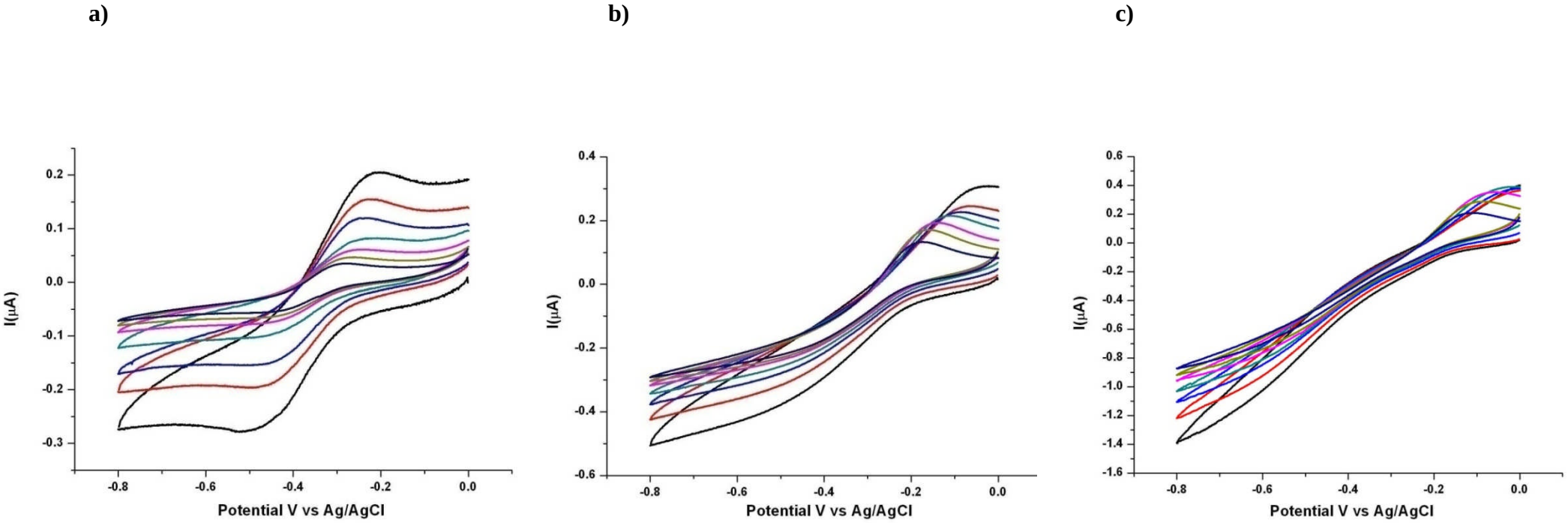

Figure 5.13 CVs in the scan rate range of 0.5 to 0.005 Vs^{-1} recorded in (a) 0.1 mM, (b)1 mM and (c) 5 mM $\mathbf{Ru(NH_3)_6^{3+}}$ (in the presence of $FcTMA^+$ of equal concentration) in 0.1 M (a & b) or 0.2 M (c) KNO_3 on the H-terminated surface **A** (surface polished by E6 using a cast iron scaife as standard supplied) (145-500-0045 – intrinsic single crystal diamond).

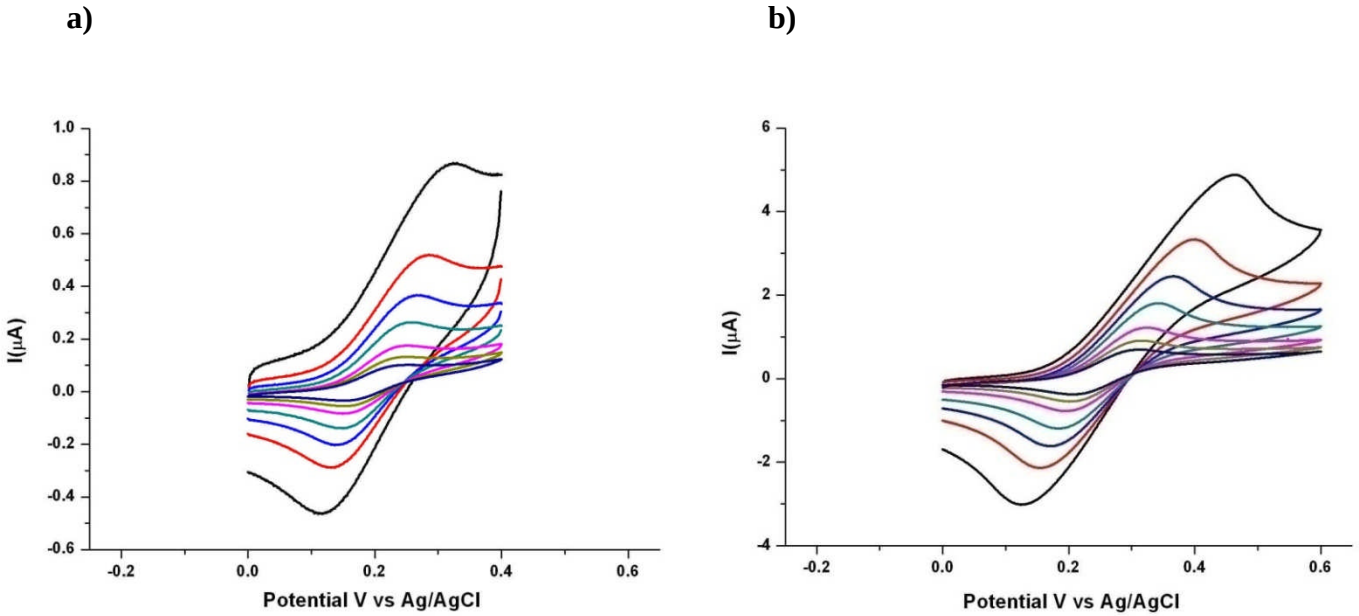

Figure 5.14 CVs in the scan rate range of 0.5 to 0.005 Vs^{-1} recorded in (a) 0.1 mM and (b) 1 mM **FcTMA**$^{+}$ (in the presence of $Ru(NH_3)_6^{3+}$ of equal concentration) in 0.1 M KNO_3 on the H-terminated surface **A** (surface polished by E6 using a cast iron scaife as standard supplied) (145-500-0045 – intrinsic single crystal diamond).

Concentration/ mediator/area exposed	Scan Rate (mVs^{-1})	i_p(µA) theoretical	i_p(µA) experimental E6 polished	ΔEp E6 polished
0.1 mM $Ru(NH_3)_6^{3+}$ Area: 1 mm^2 145-500-0045	500	0.56	0.27	296
	200	0.35	0.19	258
	100	0.25	0.15	239
	50	0.17	0.1	240
	20	0.11	0.07	211
	10	0.07	0.06	193
	5	0.05	0.05	172

Table 5.2 Summary of the current and peak separation for the 145-500-0045 single crystal intrinsic sample, H-terminated surface **A** (surface polished by E6 using a cast iron scaife as standard supplied), in 0.1 mM $Ru(NH_3)_6^{3+}$ in 0.1 M KNO_3 at different scan rates.

Concentration/ mediator/area exposed	Scan Rate (mVs^{-1})	i_p(µA) theoretical	i_p(µA) experimental E6 polished	ΔEp E6 polished
0.1 mM $FcTMA^+$ Area: 1 mm^2 145-500-0045	500	0.48	0.5	210
	200	0.3	0.38	152
	100	0.21	0.28	127
	50	0.15	0.2	108
	20	0.09	0.1	103
	10	0.06	0.09	96
	5	0.04	0.08	86

Table 5.3 Summary of the current and peak separation for the 145-500-0045 single crystal intrinsic sample, H-terminated surface **A** (surface polished by E6 using a cast iron scaife as standard supplied), in 0.1 mM $FcTMA^+$ in 0.1 M KNO_3 at different scan rates.

Concentration/ mediator/area exposed	Scan Rate (mVs^{-1})	i_p(µA) theoretical	i_p(µA) experimental E6 polished	ΔEp E6 polished
1 mM $FcTMA^+$ Area: 1 mm^2 145-500-0045	500	4.85	4.86	332
	200	3.05	2.27	243
	100	2.15	2.13	197
	50	1.5	1.67	159
	20	0.95	1.11	128
	10	0.65	0.8	116
	5	0.48	0.06	104

Table 5.4 Summary of the current and peak separation for the 145-500-0045 single crystal intrinsic sample, H-terminated surface **A** (surface polished by E6 using a cast iron scaife as standard supplied), in 1 mM $FcTMA^+$ in 0.1 M KNO_3 at different scan rates.

For 0.1 mM and 1 mM $FcTMA^+$ the measured currents are in accord with what should be expected for a metal electrode using the Randles- Sevcik equation [28] to calculate the peak current at a macroelectrode where linear diffusion dominates for a reversible electron transfer process. However, the peak to peak separations in the cyclic voltammograms are considerably broader than what would be expected for reversible electron transfer kinetics [28], thus what is causing the peak broadening? The series resistance of the H-terminated diamond electrode was measured (section 5.5) to be $\leq$ 10 KΩ such that the *iR* drop is $\leq$ 10 mV for a current of 1 µA. Furthermore, using the capacitance determined from the SG-FET measurements of 2 µF/cm^2, an electrode active area of 1 mm^2 and a series resistance of 10 kΩ a time constant $\tau=RC$ of about 0.02 ms can be calculated. This is four orders of magnitude faster than even the fastest scan used in the cyclic voltammetry reported here, thus resistive or *RC*-limited effects can be ruled out as the origin of the peak broadening. The peak broadening thus appears to indicate that electron transfer is rate limited which is in accord with the results of other workers [16, 30, 36].

The CVs for 0.1 mM $Ru(NH_3)_6^{3+}$ can be interpreted in a similar fashion to the data for $FcTMA^+$. The current is close to that for metal electrodes, see Figure 5.13 and Tables 5.3 and 5.4 but the large peak to peak separations suggest that the electron transfer kinetics are slow. However, as the concentration of $Ru(NH_3)_6^{3+}$ is increased the waves broaden and the peak currents only increases slightly (i.e. by much less than the order of magnitude(s) increase in concentration). For the $Ru(NH_3)_6^{3+}$ couple, below the Fermi level of the diamond transfer doping would be expected to occur increasing the surface hole concentration above that for a IPI interface, see Figure 5.15.

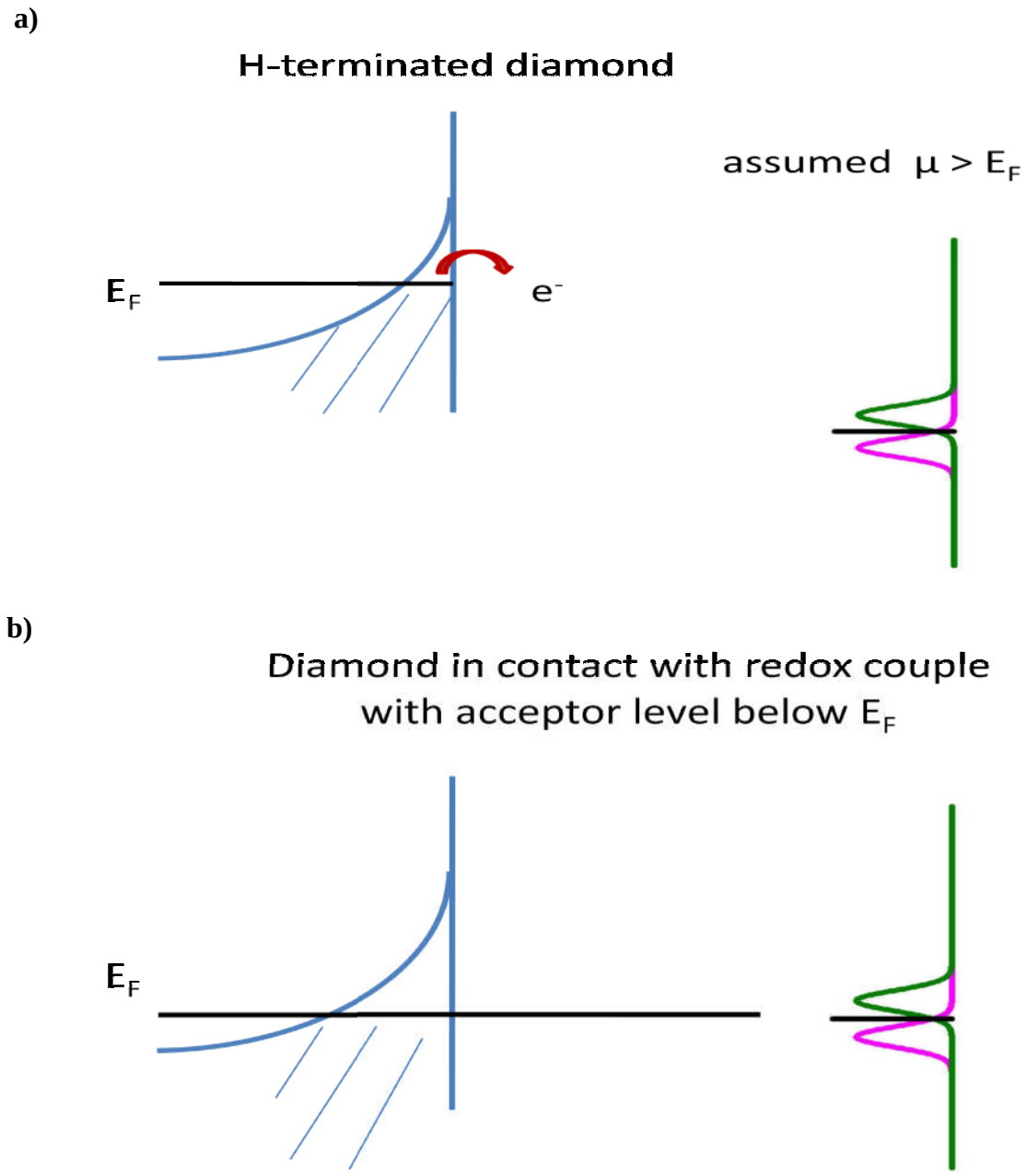

Figure 5.15 Transfer doping occurring between the H-terminated diamond and the redox couple with acceptor level below E_F.

The CVs confirm that this is not the case as in this situation $Ru(NH_3)_6^{3+}$ would behave like a metal electrode. However, if the couple is higher in energy than E_F, then assuming at rest the

concentration of $[Ru(NH_3)_6^{2+}]$ is zero no redox reaction would occur with an unbiased electrode. Applying a negative potential to the diamond electrode to drive electron transfer from the diamond to reduce $Ru(NH_3)_6^{3+} + e \rightarrow Ru(NH_3)_6^{2+}$ is perfectly feasible but applying a negative potential to the diamond reduces the conductivity, see section 5.6. At low concentration of $Ru(NH_3)_6^{3+}$ there are sufficient carriers in the near surface layer to sustain the redox reaction, however at higher concentration the demand for carriers is too great and effectively a large series resistance limits the electrode currents and pushes the wave separation out to large values, almost showing Ohmic behaviour at 5 mM. The $FcTMA^+$ couple shows rate limited electron transfer but the H-terminated intrinsic diamond surface is sufficiently conductive to support metal electrode like currents at redox couple concentrations up to 1mM.

The data presented here contradicts the report of Nebel [16], but is consistent with the current understanding of the electrical properties of the H-terminated intrinsic diamond.

5.7. Scanning electrochemical microscopy

Scanning electrochemical microscopy (SECM) was employed to investigate the surface conductivity and electrochemical behaviour of H-terminated intrinsic single crystal diamond. The technique was explained in Chapter 3, section 3.10 and the experimental set-up was detailed in Chapter 4, section 4.10.

The electrode reactions at UMEs are very well characterised and therefore in this configuration SECM can be used to extract one or more of the following parameters: the

surface conductivity, reaction kinetics at the diamond surface, the heterogeneity and stability of the surface.

Using different mediators, the H-terminated intrinsic single crystal diamond samples have been investigate at different potentials; varying the concentration of species in solution, the diamonds have been challenged at different rates. Both SG-TC and feedback modes were employed. As for the CVs, two mediators where used: $Ru(NH_3)_6^{3+}$ and $IrCl_6^{3-}$ (0.1 mM, 1 mM and 5 mM) to investigate these samples behaviour for both types of surfaces. While CVs give an overview of the overall behaviour of the samples, approach curves in SECM give an indication of the behaviour of an individual, very small area. A schematic representation of the mechanism for $Ru(NH_3)_6^{3+}$ and $IrCl_6^{3-}$ is presented in Figure 5.16.

a)

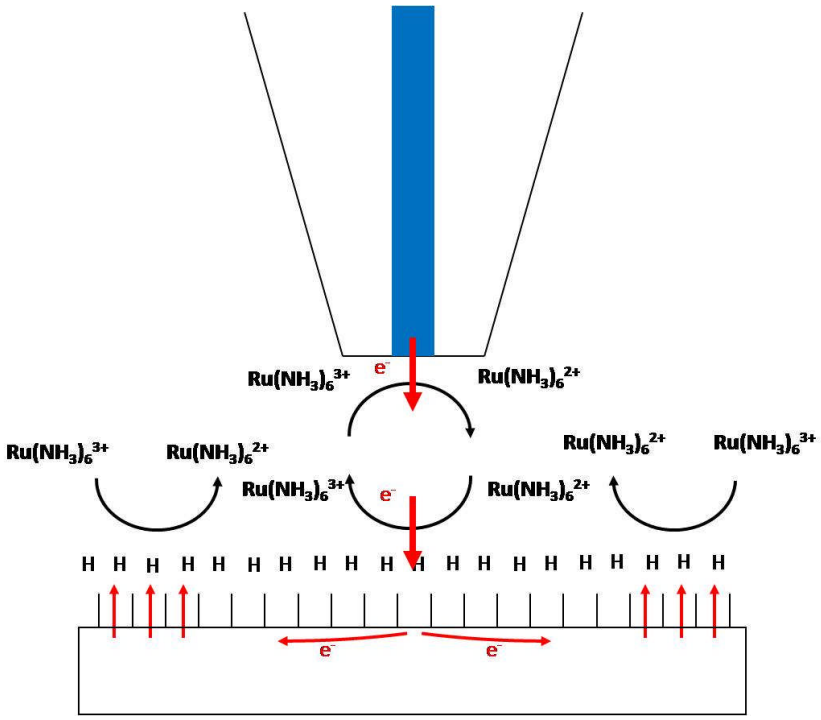

b)

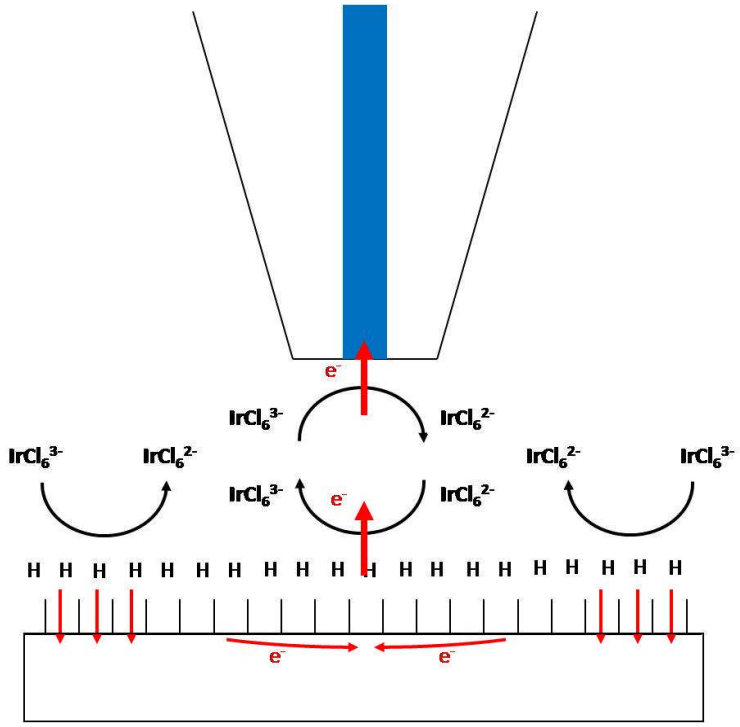

Figure 5.16 Schematic representation of the mechanism of a SECM experiment at a H-terminated single crystal diamond electrode for $Ru(NH_3)_6^{3+}$ and $IrCl_6^{3-}$.

Given the observation of quasi-reversible currents in the CVs for $FcTMA^+$ it is reasonable to predict that a couple such as $IrCl_6^{3-}$ ($E_{1/2}$ ~ 0.58 V vs. Ag/AgCl) should show positive-like feedback behaviour in SECM approach curves, as confirmed by our experiments, see Figure 5.17.

In general, the rate of the electrochemical reaction ($O + ne^- \rightarrow R$) can be controlled by applying a suitable potential to the substrate using a potentiostat. Alternatively, the potential of a conductive substrate (*e.g.* H-terminated intrinsic scCVD diamond) may be determined by the concentrations of redox species in solution. For example, if the solution contains mainly only the reduced form of the redox species, most of the substrate which is usually much larger than the tip, is in contact with a solution of R. According to Nernst equation:

$$E = E^0 + \frac{RT}{nF} ln \frac{c_o}{c_R} \quad (5.13)$$

the substrate in this case is poised at a potential much more negative than the standard potential of the mediator E^0, and reaction $O + ne^- \rightarrow R$ should be diffusion controlled [37].

However for exactly the same arguments invoked in section 5.6 it is expected that the H-terminated intrinsic diamond should behave like a metal for low concentrations of $Ru(NH_3)_6^{3+}$ (positive feedback) but become increasingly resistive when challenged with high concentrations. This was found to be the case, see Figure 5.18.

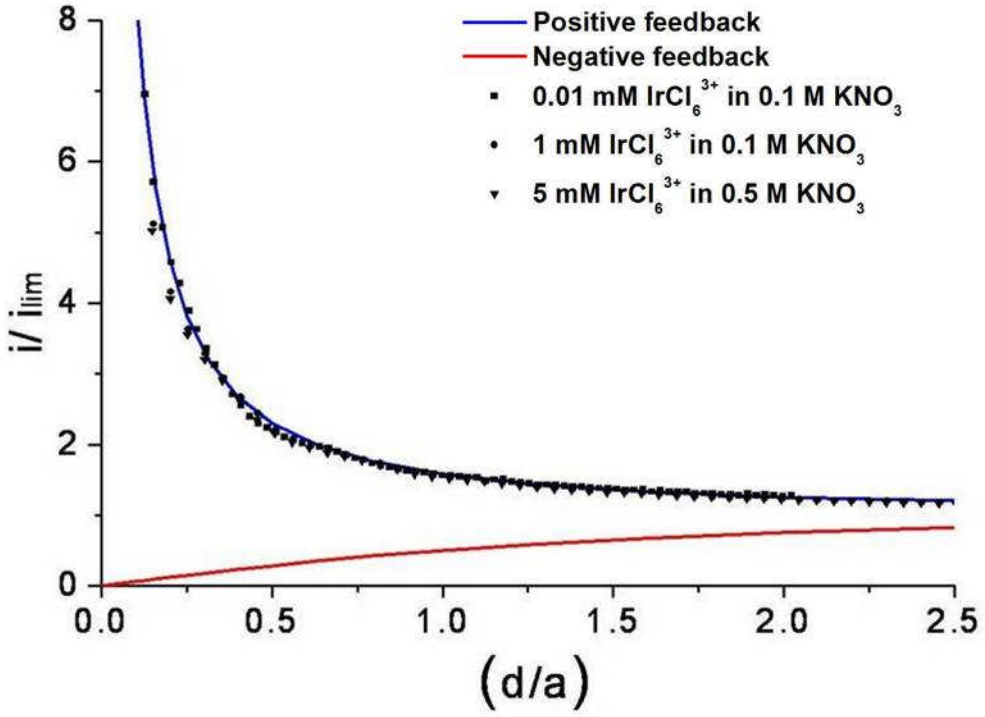

Figure 5.17 Approach curves on a H-terminated intrinsic single crystal diamond recorded in 0.01 mM, 1 mM and 5 mM $IrCl_6^{3-}$ in KNO_3.

Regardless of the concentration of species in solution the sample exhibits metal like behaviour *i.e.* conductive behaviour. The tip was held at 0.8 V while the substrate was not biased. The substrate is instead poised at a potential governed by the concentrations of the different forms of the redox couple in accordance with equation 5.13 (this will vary across the surface as the tip oxidises $IrCl_6^{3-}$ locally). This behaviour was observed for all the examined samples, regardless of their surface polish.

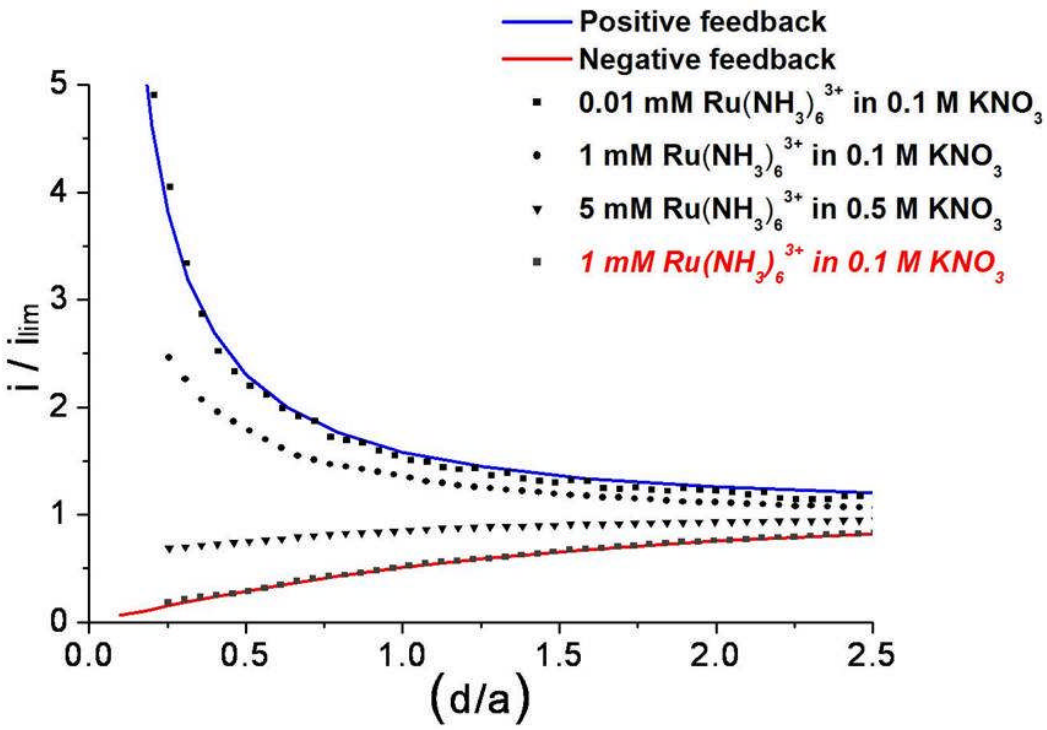

Figure 5.18 Approach curves on a H-terminated intrinsic single crystal diamond recorded in 0.01 mM, 1 mM and 5 mM $Ru(NH_3)_6^{3+}$ in KNO_3.

Figure 5.18 shows SECM experiments recorded in solutions containing 0.01 mM (■), 1 mM (●) and 5 mM $Ru(NH_3)_6^{3+}$ (▼) (using 0.1 M KNO_3 as supporting electrolyte) for hydrogen terminated intrinsic single crystal diamond. The UME was held at - 0.4 V so that the $Ru(NH_3)_6^{3+}$ was reduced at a diffusion-controlled rate. At 0.01 mM $Ru(NH_3)_6^{3+}$ the electrochemically active surface beneath the UME is able to oxidise the electrogenerated $Ru(NH_3)_6^{2+}$ and the experimental data follows the feedback curve for approach to a conducting surface. However, when the surface is challenged by greater concentrations of $Ru(NH_3)_6^{3+}$ the experimental data depart from the limiting theoretical curve for a good conductor. For oxygen terminated intrinsic single crystal diamond, with 1 mM $Ru(NH_3)_6^{3+}$ the experimental data (■) follow the theoretical curve for approach to an insulating surface.

In the case of $Ru(NH_3)_6^{3+}$, for low concentration of species in solution the sample exhibits metal like behaviour i.e. conductive behaviour. If we increase the concentration of species in solution, the conductive behaviour changes, moving towards negative feedback. In this case the tip was held at - 0.4 V while the substrate was not biased.

SECM can also be employed to map the reactivity of the substrate. 250 µm x 250 µm SECM feedback scans for the reduction of 5 mM $Ru(NH_3)_6^{3+}$ were recorded. The substrate was unbiased. The tip was help at a potential of - 0.45 V and at a distance of 6.75 µm away from the surface. All tip currents have been normalised with respect to the steady-state current, i_{lim}, for the reduction of $Ru(NH_3)_6^{3+}$ in the bulk solution. Initial studies suggest that the surface layer is homogeneously active, as demonstrated by the images presented in Figure 5.19. A region of ~ 25µm with low conductivity can also be identified. This is the position where 10 approach curves were continuously recorded and the H-termination of the single crystal diamond was intentionally damaged.

a)

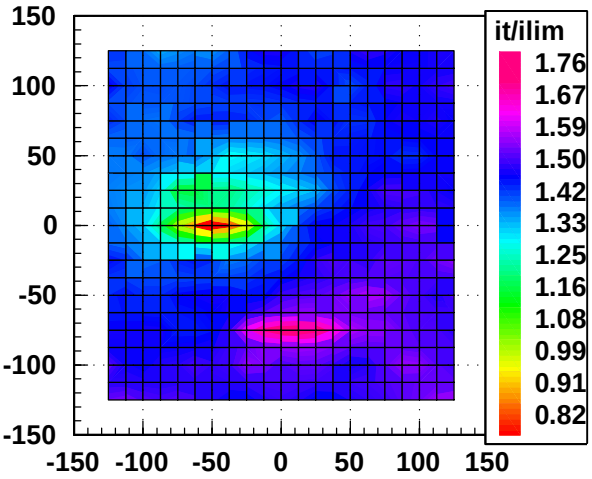

b)

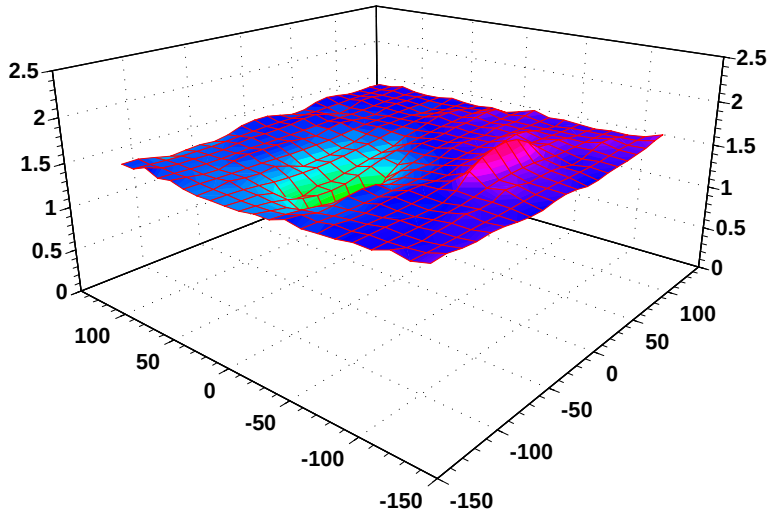

Figure 5.19 250 µm x 250 µm SECM feedback scans for the reduction of 5 mM $Ru(NH_3)_6^{3+}$. The substrate was unbiased. The tip was help at a potential of - 0.45V and at a distance of 6.75 µm away from the surface. All tip current have been normalised with respect to the steady-state current, i_{lim}, for the reduction of $Ru(NH_3)_6^{3+}$ in the bulk solution. The sample imaged was polished using a standard cast iron scaife by E6.

5.8. Theoretical modelling

As outlined in Chapter 3, section 3.10, SECM and the approach curves can be used to provide quantitative information about the kinetics of the electrode reaction and solution reactions. In this case, the kinetics of the electron transfer at the interface between the aqueous conductive layer of the H-terminated intrinsic sc CVD diamond and the electrolyte solutions can be regarded as a solid/liquid interface. The electrochemistry between solid/liquid interfaces has been studied extensively [38-40]. The very special case of totally irreversible substrate kinetics has been simulated by Bard et al.[40]. As mass transfer rates at small tip electrodes are high, measurements of fast reactions without interference of mass transfer are possible. The heterogeneous electron transfer rate constant was extracted by fitting the experimental SECM approach curves to the theory developed by Bard et al. [39-41]. In Bard's model, approach curves are described as follows:

$$I_T^k = I_S^k (1-I_T^{ins}/I_T^c) + I_T^{ins} \quad (5.14)$$

$$I_S^k = 0.78377/[L (1+1/\Lambda)] + [0.68 + 0.3315 \exp(-1.0672/L)]/[1 + F(L,\Lambda)] \quad (5.15)$$

where I_T^c, I_T^k and I_T^{ins} represent the normalised currents for diffusion controlled regeneration finite substrate kinetics, and insulating substrate (i.e. no mediator regeneration), respectively at a tip-substrate separation, L = d/a, I_S^k is the kinetically controlled substrate current; $\Lambda = k_f d/D$, where k_f is the apparent heterogeneous rate constant, D is the diffusion coefficient of the mediator; and $F(L,\Lambda) = (11 + 2.3\ \Lambda)/[\Lambda(110 - 40\ L)]$. These currents are normalised by the tip current at an infinite tip-substrate separation $i_{T,lim} = 4nFaDc_R$. The analytical approximation for I_T^c and I_T^{ins} are:

$$I_T^c = 0.78377/L + 0.3315 \exp(-1.0672/L) + 0.68 \quad (5.16)$$

$$I_T^{ins} = 1/(0.15 + 1.5358/L + 0.58 \exp(-1.14/L) + 0.0908 \exp[(L-6.3)/(1.017L)]) \quad (5.17)$$

Using this model the electron transfer kinetics of the approach curves recorded for $Ru(NH_3)_6^{3+}$ have been plotted against theoretical approach curves obtained for different values of k, see Figure 5.21. It can be seen that for 0.01 mM $Ru(NH_3)_6^{3+}$ k = 1, whereas for 1 mM $Ru(NH_3)_6^{3+}$ 0.05 < k < 0.01 and for 5 mM $Ru(NH_3)_6^{3+}$ 0.002 < k < 0.001. This observation is consistent with the remarks made while assessing the CV response. It should also be appreciate that the model is just a very simple approximation of the reactions taking place between the electrolyte solution and the H-terminated diamond. A more complex model, would obviously give a better fit.

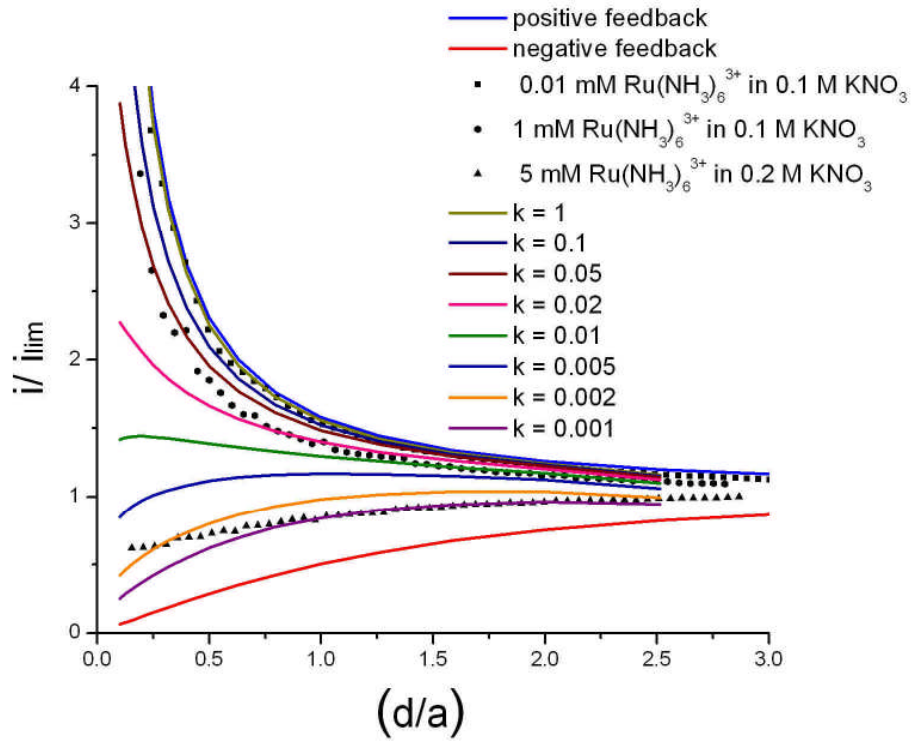

Figure 5.20 Approach curves of I_T^k for different values of k where k is the heterogeneous electron transfer rate constant (cms^{-1}). As the rate constant deceases, the extent of positive feedback decreases and the current approaches that of an inert, insulating surface. The experimental resulta recorded for 0.01 mM, 1 mM and 5 mM $Ru(NH_3)_6^{3+}$ are fitted to the theoretically obtained curves.

References:

[1] M. I. Landstrass, and K. V. Ravi, Applied Physics Letters **55**, 1391 (1989).
[2] M. I. Landstrass, and K. V. Ravi, Applied Physics Letters **55**, 975 (1989).
[3] F. Maier *et al.*, Physical Review Letters **85**, 3472 (2000).
[4] J. A. Garrido *et al.*, Applied Physics Letters **81**, 637 (2002).
[5] J. S. Foord *et al.*, Diamond and Related Materials **11**, 856 (2002).
[6] J. Ristein, M. Riedel, and L. Ley, Journal of the Electrochemical Society **151**, E315 (2004).
[7] www.e6.com.
[8] I. M. Watt, *The Principles and Practice of Electron Microscopy* (Cambridge University Press, 1997).
[9] J. Isberg *et al.*, Science **297**, 1670 (2002).
[10] G. Piantanida *et al.*, Journal of Applied Physics **89**, 8259 (2001).
[11] K. Tsugawa *et al.*, Diamond and Related Materials **8**, 927 (1999).
[12] A. Aleksov *et al.*, Diamond and Related Materials **11**, 382 (2002).
[13] H. Ishizaka *et al.*, Diamond and Related Materials **11**, 378 (2002).
[14] S. A. Grot *et al.*, Applied Physics Letters **58**, 1542 (1991).
[15] D. Takeuchi *et al.*, Physica Status Solidi A-Applied Research **186**, 269 (2001).
[16] C. E. Nebel *et al.*, Physica Status Solidi A-Applications and Materials Science **203**, 3273 (2006).
[17] M. Kasu *et al.*, Diamond and Related Materials **17**, 741 (2008).
[18] K. Ueda *et al.*, Diamond and Related Materials **15**, 1954 (2006).
[19] M. Kubovic *et al.*, Diamond and Related Materials **18**, 796 (2009).
[20] A. Aleksov *et al.*, Semiconductor Science and Technology **18**, S59 (2003).
[21] J. A. Garrido *et al.*, Journal of the American Chemical Society **130**, 4177 (2008).
[22] W. Y. Zhang, J. Ristein, and L. Ley, Physical Review E **78** (2008).
[23] H. Kawarada *et al.*, Physica Status Solidi A-Applied Research **185**, 79 (2001).
[24] H. Kawarada, Surface Science Reports **26**, 205 (1996).
[25] J. Ristein, W. Zhang, and L. Ley, Physical Review E **78** (2008).
[26] M. Dankerl *et al.*, Physica Status Solidi-Rapid Research Letters **2**, 31 (2008).
[27] C. E. Nebel *et al.*, Journal of Applied Physics **99** (2006).
[28] A. J. Bard, and L. R. Faulkner, *Electrochemical methods: Fundamentals and Applications* (John Wiley & Sons, INC., 2001).
[29] J. Seymour, *Electronic Devices and Components* (Longman Scientific and Technical, 1986).
[30] A. Chatterjee *et al.*, Physica Status Solidi a-Applied Research **199**, 49 (2003).
[31] A. R. Krauss *et al.*, Diamond and Related Materials **10**, 1952 (2001).
[32] Q. Y. Chen *et al.*, Journal of the Electrochemical Society **148**, E44 (2001).
[33] R. Ramesham, Sensors and Actuators B-Chemical **50**, 131 (1998).
[34] H. B. Martin, Argoitia, A., Angus, J. C., Anderson, A. B., Landau, U., Feldman, A., et al., , NIST Special Publication, US Dept of Commerce **885**, 91 (1995).
[35] H. B. Martin *et al.*, Journal of the Electrochemical Society **143**, L133 (1996).
[36] M. C. Granger *et al.*, Analytical Chemistry **72**, 3793 (2000).
[37] M. V. Mirkin, and B. R. Horrocks, Analytica Chimica Acta **406**, 119 (2000).
[38] A. J. Bard, and M. V. Mirkin, *Scanning Electrochemical Microscopy* (Marcel Dekker, INC., 2001).
[39] D. O. Wipf, and A. J. Bard, Journal of the Electrochemical Society **138**, 469 (1991).

[40] A. J. Bard *et al.*, Journal of Physical Chemistry **96**, 1861 (1992).
[41] A. J. Bard *et al.*, Scanned Probe Microscopy **241**, 235 (1992).

Chapter 6

Electrical and electrochemical characterisation of oxygen and hydrogen terminated moderately boron doped single crystal semiconducting diamond

The aim of this chapter is to investigate the electrical and electrochemical properties of oxygen and hydrogen terminated *moderately* boron doped ($< 10^{20}$ cm^{-3}) single crystal CVD diamond. The techniques used include PL imaging, AFM and SECM, bulk electrochemistry and Hall effect measurements. The nature of the electrical and electrochemical activity will be explored.

6.1. Introduction

It is well known that as-grown insulating CVD films can demonstrate surface conductivity without doping [1-3]. This surface conductivity is dependent on hydrogen termination of the surface (giving rise to a negative electron affinity) and the presence of a suitable absorbent which can act as a "transfer dopant" [4]. Hydrogen terminated surfaces are hydrophobic [5, 6]. Oxygen terminated surfaces have a large positive electron affinity, very low conductivity and are hydrophilic [7, 8]. Although electrochemistry with hydrogen terminated intrinsic single crystal diamond has been demonstrated (see Chapter 5) the results show that limited electron transfer kinetics is responsible for the distortion of the cyclic voltammograms and that only redox couples with chemical potentials below the top of the valence band can be studied using cyclic voltammetry [9].

Recognised as an insulating material, with resistivity of the order of 10^{18} Ωm [10], diamond is in fact a superior wide-band-gap semiconductor with a unique combination of properties (high breakdown voltage, high thermal conductivity, small dielectric constant, excellent radiation hardness). Bulk doping is achieved with boron (p-type) or phosphorus (n-type) in diamond produced by both CVD [11] or HPHT [12] synthesis as detailed in Chapter 2, section 2.1.

For many electrical and electrochemical applications, highly electrically conductive diamond is required and most research has focused on boron doped diamond. At low doping levels, due to the relatively large activation energy (ΔE_A= 0.37 eV [13]) for the boron acceptor, the carrier concentration is typically much less than the dopant concentration, at room temperature. In the [B] concentration range 3×10^{19} cm^{-3} to 3×10^{22} cm^{-3} hopping conduction contributes with the conductivity increasing dramatically above ~ 3×10^{20} cm^{-3}, at the metal-insulator transition. Here ΔE_A reduces to zero due to overlap of the acceptor band with the valence band resulting in metallic-like conduction [14].

In almost all electrochemical applications to date pBDD has been employed, because it is much easier to grow pBDD than scBDD. However, pBDD is a heterogeneous material [15, 16] presenting different crystallite morphologies with different boron uptake; with boron typically more readily incorporated (by a factor of 10) into (111) growth sectors than (100) [17] and possibly non diamond intergranular material if great care has not been taken during growth.

The application of a new generation of BDD electrodes based on single crystal material is foreseen. Single crystal CVD diamond homogeneously doped with boron is potentially advantageous for electrical and electrochemical application in that the boron uptake and metallic characteristics (if sufficiently highly doped) should be more uniform. However, as has been stated [18] homogeneous [B] doping in single crystal diamond is a challenge and will be discussed later.

The incorporation of [B] and [N] (a deep donor) is sector dependent. Changes in apparent conductivity could be due to changes in [B] or [N] incorporation (or both).

$$N_S^0 + B_S^0 \rightarrow N_S^+ + B_S^- \qquad (6.1)$$

For example increased [N] incorporation will increase the fraction of [B] which is compensated (equation 6.1) and decrease the electrical conductivity. Furthermore, great care has to be taken in preparing the substrate and conducting the CVD growth to minimise the formation of structural defects which lead to the inhomogeneous incorporation of impurities.

6.2. Moderately boron doped single crystal diamonds

The samples under investigation, 0372211- D(i) and 0372211- E(i), are single crystal boron doped diamonds, grown on a (100) oriented substrate using a microwave plasma CVD reactor. The boron doped diamond film was deposited on a substrate heated to temperatures in the range of 750- 950°C [19]. The boron dopant density was determined using SIMS measurements (spot size of 50 μm in diameter) and it was established to be in the range of $6 \times 10^{18} – 6 \times 10^{19}$ atoms cm^{-3} for both samples [19]. After growth poor quality material from around the edge of the sample and the substrate was removed by laser cutting and the sample was polished. The sample 0372211- D(i) was polished using a standard cast iron scaife. The

sample 0372211- E(i) was polished using a standard cast iron scaife, repolished using an experimental polish by Element Six Ltd. (precise details not revealed) and finally repolished using a standard cast iron scaife. Specific details on polishing can be found in Chapter 3, section 3.1 and Chapter 4, section 4.2. The oxygen and hydrogen terminated surfaces were prepared as described in Chapter 4, section 4.4. Electrical connection to the samples was established as detailed in Chapter 4, section 4.5 **d)**. For the electrical measurements presented in section 6.6., gold top contacts (0.8 mm x 0.8 mm wide with a separation of 1 mm between them) were deposited when the samples where H-terminated. The electrochemical experiments (sections 6.7 and 6.8) on the O-terminated surfaces were performed with the samples bottom contacted with titanium/gold.

6.3. Photoluminescence

Figures 6.1 and 6.2 show photoluminescence (PL) maps taken at room temperature (courtesy of Dr. Mark Newton) of the single crystal boron doped samples recorded using a Diamond View instrument [20]. The technique and the instrument were described in Chapter 4, section 4.3.

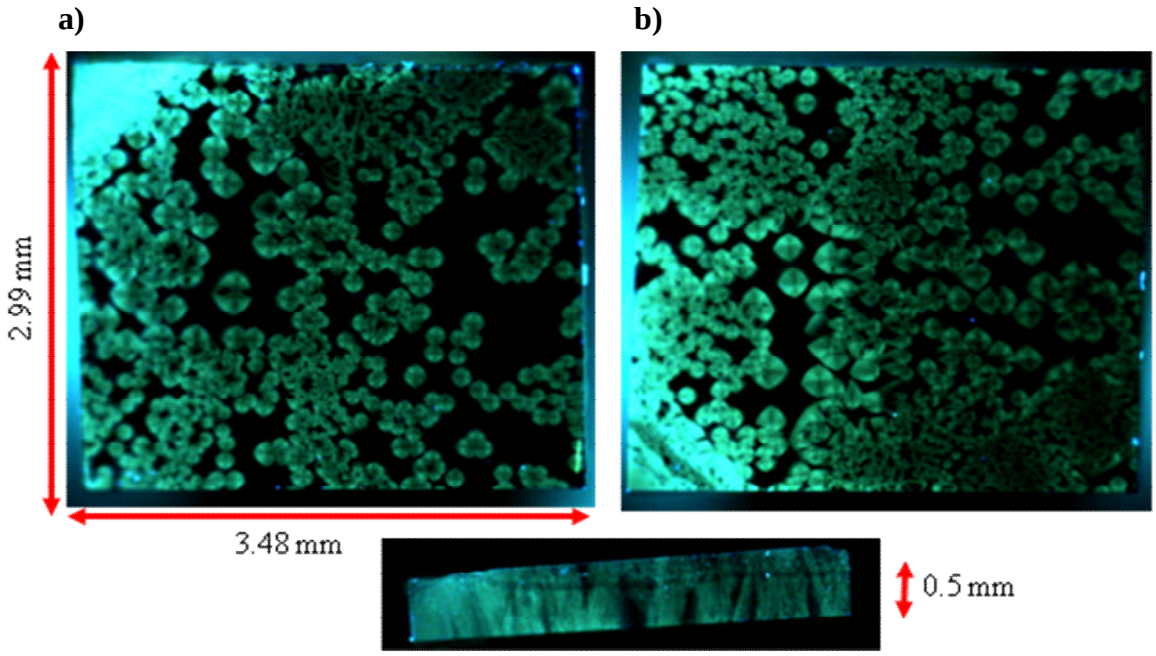

Figure 6.1 Room temperature Diamond View / Photoluminescence images of a single crystal boron doped diamond, 0372211- D(i), with a boron dopant density of $6 \times 10^{18} – 6 \times 10^{19}$ atoms cm^{-3} polished using a standard cast iron scaife. The images show the bottom (**a**), top (**b**) and side views of the diamond sample. Note that the bottom image (**a**) refers to the face closest to the substrate/ seed crystal, which has been removed.

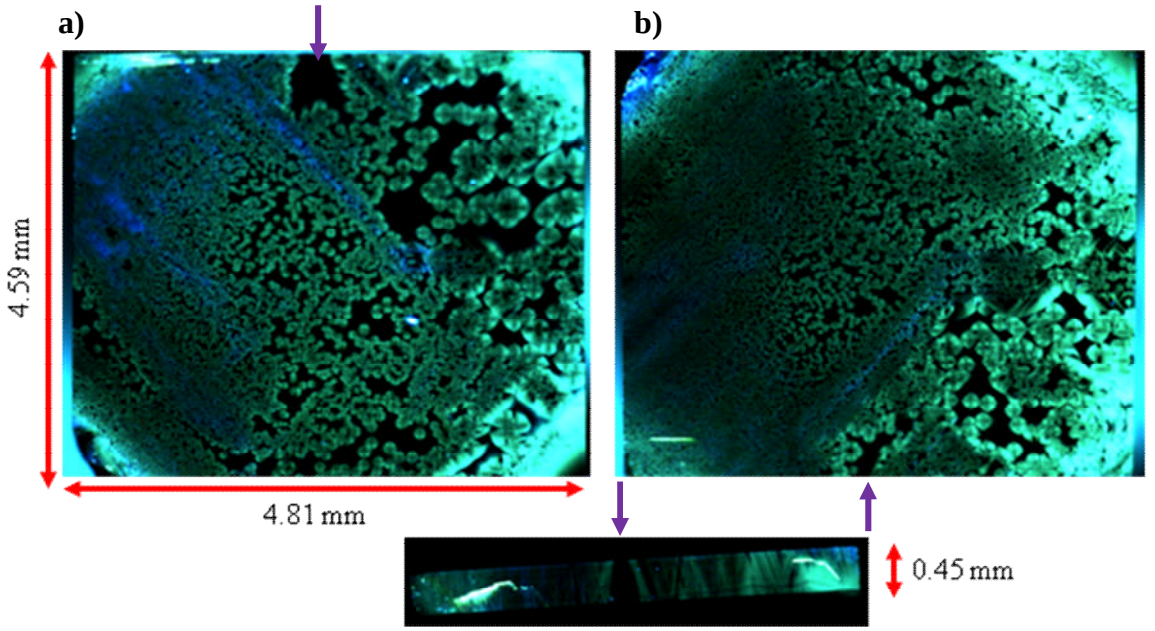

Figure 6.2 Room temperature Diamond View / Photoluminescence images of a single crystal boron doped diamond, 0372211- E(i), with a boron dopant density of $6 \times 10^{18} – 6 \times 10^{19}$ atoms cm^{-3}. The images show the bottom (**a**), top (**b**) and side views of the diamond sample. Note that the bottom image (**a**) refers to the face closest to the substrate/ seed crystal, which has been removed. The purple arrows point out a large pit free area at the bottom of the sample which gets narrower as the sample grows thicker.

All electrical and electrochemical experiments were performed on the side (**a**) (see Figures 6.1 and 6.2) for both samples, 0372211- D(i) and 0372211- E(i). The green luminescence observed in these samples originates from donor (presumed N_S^0) - acceptor (B_S^0) pair recombination. Details of such luminescence can be found in the literature [21]. The regions where no light is emitted from donor-acceptor pair recombination appear black on the PL map and indicate a region where $[B_S] \gg [N_S]$; a high concentration of [B] will quench emission. The light blue regions indicate strong emission from donor acceptor pair recombination. In such regions the concentrations of $[B_S]$ and $[N_S]$ are probably comparable and of order ≤ 10 ppm. For strong PL emission similar concentrations of boron and nitrogen are required. During the growth of the samples presented in Figure 6.1 and Figure 6.2 the surface became pitted and showed macrogrowth steps called risers, see Figure 6.3.

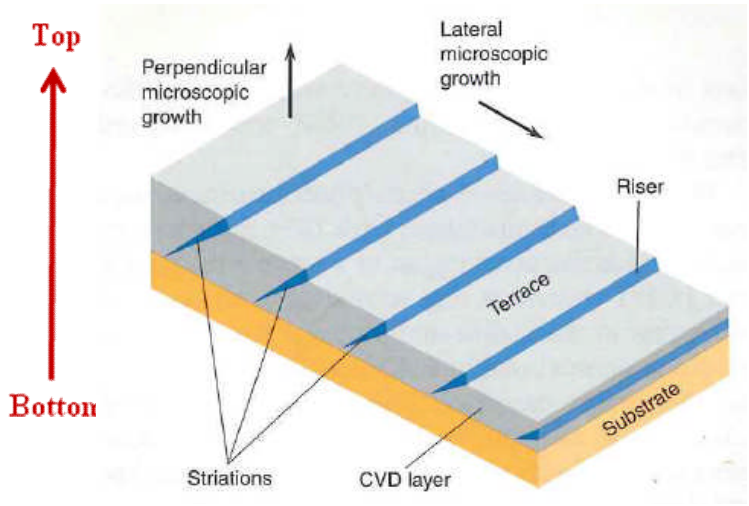

Figure 6.3 Diagram showing part of a CVD sc diamond (100) layer growth. It depicts the early development of striations caused by differential uptake of impurity-related defects on the rises and terraces of surface steps [22].

A diagram showing part of a CVD sc diamond (100) layer growth is presented in Figure 6.3; it illustrates the early development of striations caused by differential uptake of impurity-related defects on the rises and terraces of surface steps. It can be observed that the density of

pit features increases as the BDD grows up from the substrate. After growth the substrate and growth surface were polished flat and therefore the pits and steps were no longer directly visible. It is known that such pitting and/or steps can result when bundles of dislocations or individual dislocations break the growth surface because the strain associated with dislocations affects the local growth [22]. The heterogeneous uptake of boron across the sample occurs because there are both (100) terraces and angled surfaces (risers) on the growth surface. It has been reported in the literature that the incorporation of impurities (*e.g.* nitrogen) is greater on risers than on terraces and it is well known that boron and nitrogen are more readily incorporated on (111) than (110) crystallographic faces. The growth surface of nitrogen doped samples on (100) substrates invariably shows sequences of macroscopic growth steps with risers. This leads to striations in the sample which are easily observable by PL.

For single crystal CVD diamond samples lightly doped with boron ([B] in (100) sectors ranging from ppb to a few ppb) the crystal growth surface showed growth steps, shallow pits or combinations of both [22]. PL images showed that the luminescence properties (colour and intensity) of these steps and pits were different from those of adjacent regions where the surface was flat. In the samples studied here no striations are observed in the PL images but the images are dominated by luminescence from pits. For many of the pits clear geometric structure relating to differential impurity incorporation on different growth surfaces can be observed. Some of the pits appear to have had flat (001) bottoms with (possibly (111) and (110)) inclined surfaces. This is most likely a great over simplification referring to the sides of the pits as having low index crystallographic surfaces. This is probably not the case, they are simply inclined surfaces and there may well be a range of pit wall angles. Many different

pit like features and intersections between different faces of the pits can be seen in the images presented in Figure 6.1 and Figure 6.2. Figure 6.4 shows a schematic representation of a pit growing upwards from a (001) surface and Figure 6.5 illustrates a schematic representation of a pit with (111) sides on a (100) growth surface. It is assumed that the growth rate on the walls of the pit is lower than on the (100) surface.

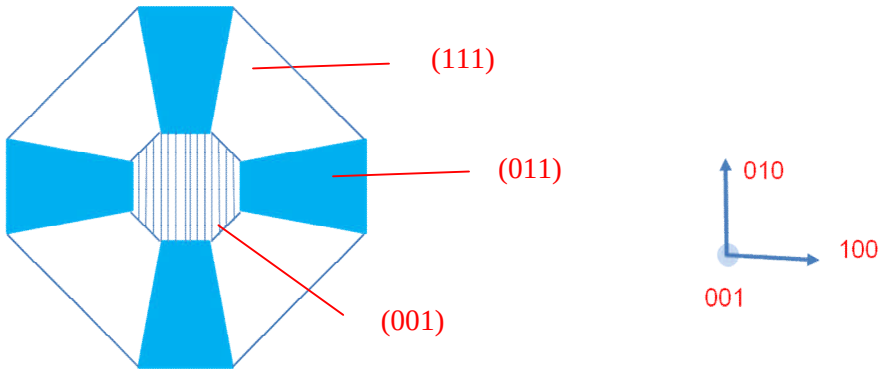

Figure 6.4 The structure of a pit growing upwards from a (001) surface, showing potential inclined (111) and (011) planes.

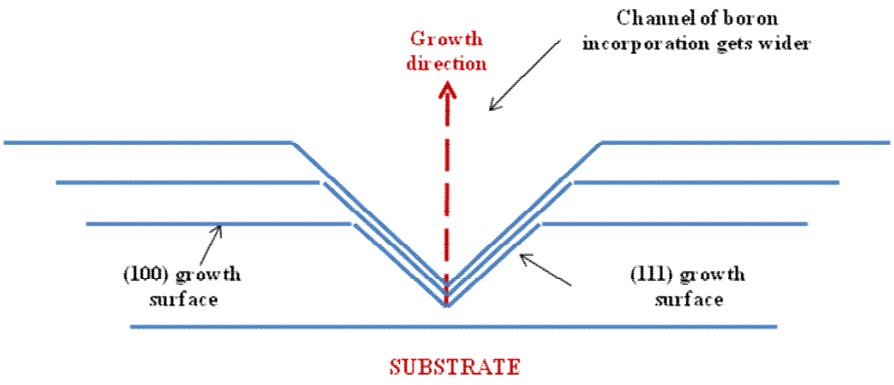

Figure 6.5 Illustration of a pit with (111) sides on a (100) growth surface. It is assumed that the growth rate on the walls of the pit is lower than that on the (100) surface.

If the growth rate on the inclined pit wall is slower than on the horizontal surface, then the size of the pit will increase as growth progresses, see Figure 6.5. Also new pits can be created while growth continues. Secondary ion mass spectroscopy (SIMS) indicates that the boron concentration was lower in the regions where growth had been in pits than where it had been on a flat (100) region [19]. Furthermore, the pit regions showed less absorption in the visible region of the spectrum from boron incorporated into the lattice [19]. Uncompensated boron gives rise to conductivity but substitutional nitrogen compensates the boron. The SIMS and optical absorption data shows that less boron is incorporated into diamond grown on the walls of the pits than on the (100) surface. The donor-acceptor pair luminescence shows that the pit wall diamond also contains significant concentrations of nitrogen. This is an intriguing observation as the pits have angled surfaces and would expect impurities incorporation to be higher in pits than in the bulk. However, for the two samples under investigation it can be stated that the incorporation of boron into the diamonds is lower on the pit walls than on the (100) surface and that a fraction of this boron is compensated by nitrogen. It appears that the growth temperature, chemistry and specifically the incorporation of boron and nitrogen is different in the pits than on an exposed surface. The measured lower conductivity, see section 6.4, from the regions where growth has been in pits is consistent with both SIMS and PL observations. However, as discussed in Chapter 7, Element Six Ltd. have also demonstrated the ability to dramatically reduce the density of the pit features.

6.4. Conductive atomic force microscopy

C-AFM [23, 24] is a powerful scanned microscopy technique, allowing the conductivity of a sample to be imaged at high spatial resolution. C-AFM was employed to study the local conductivity of samples 0372211- D(i) and 0372211- E(i). A home-made Pt AFM tip [25, 26]

was scanned in air, in contact with the sample with a fixed potential applied, allowing a detailed map of surface topography and conductivity to be obtained simultaneously. The lateral resolution of both images depends on the contact area between the Pt tip and the surface. Due to the toughness of the sample (diamond is the hardest material known to man) the tip size can wear with time. FE-SEM analysis of the C-AFM tips post imaging showed that the radius of curvature could be anywhere between 100 nm- 1 µm [27]. In addition to imaging, the tip was held in position over a feature of interest, *i.e.* a pit observed through photoluminescence and identified topographically using AFM, and local current-voltage characteristics measured.

Figure 6.6 shows 100 µm × 100 µm C-AFM height, (*a*), and conductivity, *(b*), images of the 0372211- E(i) single crystal boron doped sample after preparation with the experimental polish by Element Six Ltd. A potential of - 4 V was applied to the tip, with a 10 MΩ current limiting resistor in series. The height image demonstrated the low surface roughness (± 10 nm) after the polish. The boundary between the regions where the growth took place on an inclined pit wall or on the (001) surface of the BDD electrode and the surrounding undefected diamond were clear. Figure 6.6 exhibited clear heterogeneities in the conductivity of this BDD electrode, and these were seen to correlate with the location of different defects in the height image. It is well known that the incorporation of impurities such as nitrogen or boron can change the mechanical hardness of diamond. Local hardness can also be influenced by changes in the density of extended defects (*e.g.* dislocations) thus the height differences, on the polished surfaces, between the (001) grown material and that deposited on the inclined walls of the pits is not surprising.

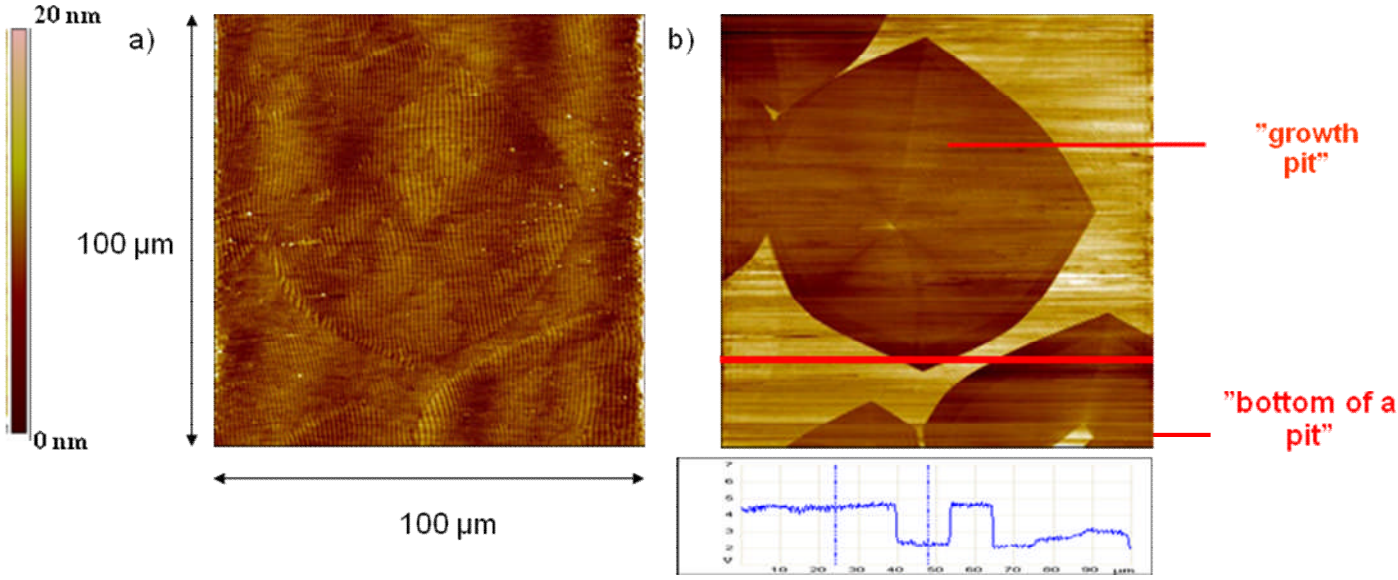

Figure 6.6 Simultaneously recorded (100 µm x 100 µm) a) height and b) C-AFM images of an oxygen terminated moderately doped (< 10^{19} cm^{-3}) single crystal CVD BDD, sample 0372211- E(i), recorded in air using an in house made Pt tip. The conductivity image in b) was taken at a tip potential of -4 V. Dark (light) regions correspond to low (high) current. The images were recorded on a surface polished using an experimental Element Six Ltd. method.

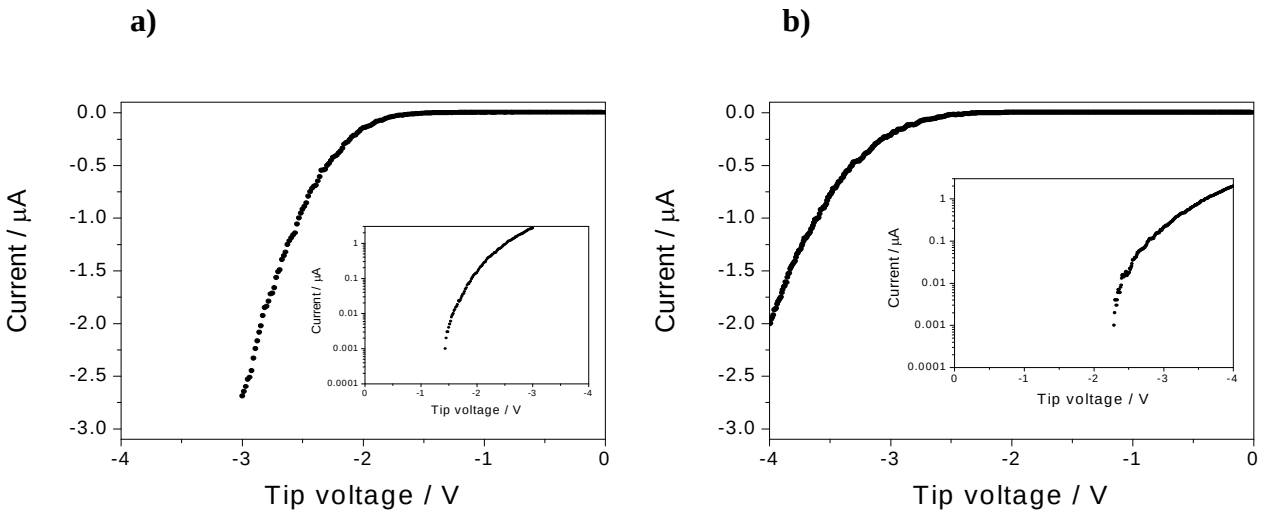

Figure 6.7 Current-voltage curves recorded in a) an undefected, high-conductivity region and b) a defected, low conductivity region of the 0372211- E(i) oxygen terminated sample, a single crystal CVD BDD, polished using an experimental Element Six Ltd. method.

Figure 6.7 shows I-V curves recorded in two regions of the single crystal CVD BDD sample. The curve presented in a) was recorded in an undefected region (identified topographically) with a high boron dopant density, while the curve in b) was recorded in a pitted region with lower boron dopant density. A dramatic change of the Schottky barrier between the tip and the diamond surface is observed. There was no current-limiting resistor present during these measurements.

6.5. Atomic force microscopy

The surface morphology was imaged in air using a Nanoscope E AFM (Digital Instruments, Santa Barbara, California) in conjunction with a Nanoscope IIIa controller. For these measurements, contact mode tips made of silicon nitride (Nanoprobes, Digital Intruments, California) were used.

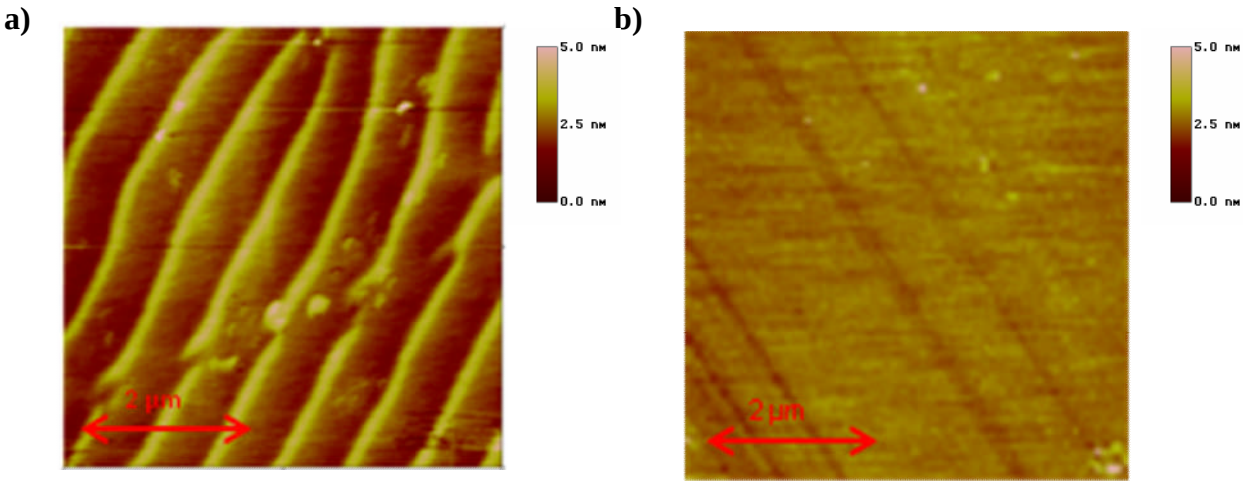

Figure 6.8 In air AFM images recorded on the oxygen terminated surface of a single crystal boron doped diamond with a boron dopant density of 6 x 10^{18} – 6 x 10^{19} atoms cm^{-3} **a)** after it was polished using an experimental Element Six Ltd. method and **b)** after it was repolished using a standard cast iron scaife (sample 0372211-E(i)).

The images (Figure 6.8) demonstrate the existence of clear topographical differences between surfaces polished using the experimental Element Six Ltd. method and the ones polished using a standard cast iron scaife. The polishing lines can be clearly identified for the surface polished using the experimental Element Six Ltd. method, while for the surface polished using a standard cast iron scaife the lines, though still present are less obvious. It is known that polishing can create subsurface damage in diamond; the manner in which polishing and hence polishing damage influences the electrical and electrochemical performance is quantified below.

6.6. Electrical characterisation

The graph presented in Figure 6.9 shows the variation of the resistivity of boron doped diamond at 300 K with boron doping levels. The data (■) was taken from reference [28], while data (●) was taken from reference [3].

In [B] doped diamond there is a general decreasing trend in mobility values with increasing carrier concentration. This relationship inevitably shows a large amount of scatter because the room temperature carrier concentration depends only on the compensation ratio N_A/N_D whereas the carrier scattering that determines the mobility includes contributions for both neutral and ionised impurities. Thus if [N] and [B] were both increasing by the same factor the room temperature carrier concentration would be unchanged but the mobility would certainly be lower.

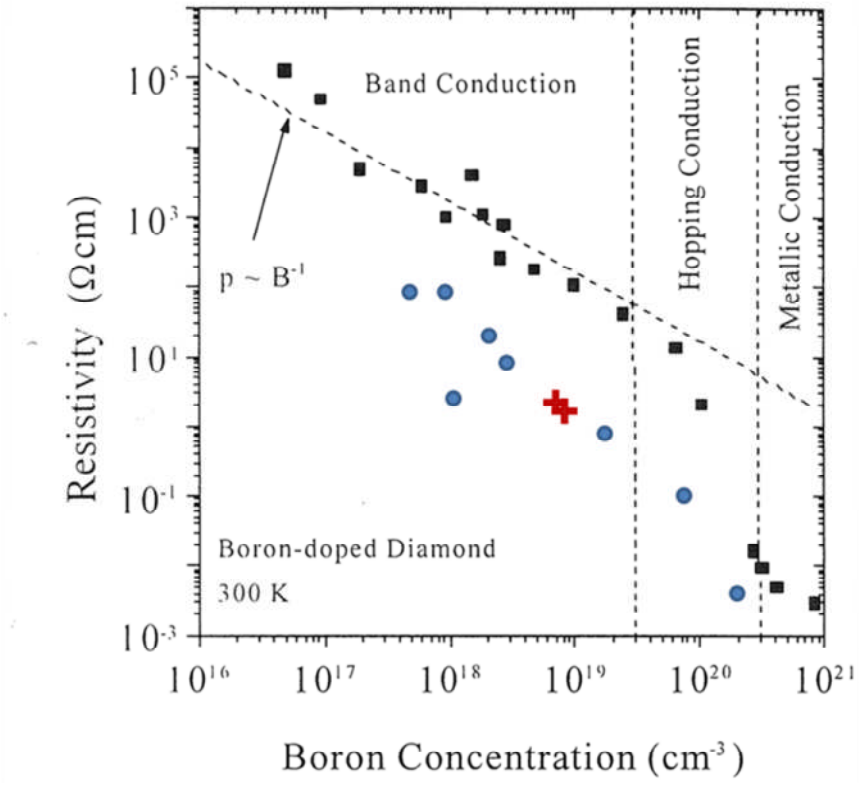

Figure 6.9 Values from the literature showing the variation of the resistivity of boron doped diamond at 300 K with boron doping levels [3, 28]. The red crosses represent the two samples discussed in this chapter.

If the boron concentration is smaller than 2 x 10^{19} cm^{-3} the resistivity is inversely proportional to the acceptor density, while in the range 2 x 10^{19} cm^{-3} to 3 x 10^{20} cm^{-3} hopping conduction dominates. Hopping conduction is unaffected by the mobility but depends on the wave function overlap which is proportional to $[B]^{-1/3}$ [29]. Metallic conduction is noticed for higher concentrations [28]. The red crosses represent the position of the two samples under investigation based on their electrical properties correlated with their boron concentration, information obtained through SIMS [19].

Resistivity and Hall effect measurements were performed in air while the samples were H-terminated. The set-up employed is described in Chapter 4, section 4.11. The sheet resistance values obtained experimentally are presented in Table 6.1.

Sample\Current	0372211- D(i) H terminated	0372211- E(i) H terminated
I= 4 µA	$R_S = 106 \pm 5\ \Omega$	$R_S = 113 \pm 6\ \Omega$
I= 100 µA	$R_S = 107 \pm 5\ \Omega$	$R_S = 114 \pm 6\ \Omega$
I= 500 µA	$R_S = 107 \pm 5\ \Omega$	$R_S = 114 \pm 6\ \Omega$

Table 6.1 Sheet resistance values obtained experimentally using the set-up described in Chapter 4, section 4.11 for the H-terminated 0372211-D (i) and 03772211- E (i) single crystal boron doped diamond samples.

While investigating the intrinsic single crystal diamonds, sheet resistance values of ~ 10^4 Ω were recorded. The sheet resistance values obtained experimentally for the 0372211- E(i) and 0372211- D(i) boron doped single crystal samples, confirm the fact that the active boron concentration in the two samples was in the range of 10^{19} cm^{-3} and that the samples conductivity comes as a result of the boron doping, not as a result of its H termination. The Hall measurements were recorded for I= 4 µA and using the formulas (3.8) and (3.10) from Chapter 3, section 3.4 mobilities of 8 ± 2 cm^2/Vs (for 0372211- D(i)) and 4 ± 2 cm^2/ Vs (for 0372211- E(i)) and carrier concentrations of 8 (± 0.8) x $10^{15}cm^{-3}$ (for 0372211- D(i)) and 1.5 (± 0.15) x 10^{16} cm^{-3} (for 0372211-E(i)) were obtained.

The number of holes *p* available for electrical conduction at room temperature T is given by [30]:

$$\frac{p(N_D + p)}{N_A - N_D - p} = \left(\frac{2\pi m kT}{h^2}\right)^{3/2} \exp\left(-\frac{E_A}{kT}\right) \qquad (6.2)$$

as long as the [B] concentration is sufficiently low to avoid impurity band conduction. From our work, by taking T= 293 K, E_A=0.37 eV, *p*= 1.5 x 10^{16} cm^{-3}, N_D=1.7 x 10^{17} cm^{-3} gives a value of N_A ~10^{19} cm^{-3}. The SIMS measurements give a boron concentration in the range 6 x 10^{18} – 6 x 10^{19} atoms cm^{-3}. It is assumed that the unintentionally doping with nitrogen (from N_2 in source gases) could produce donor concentrations of ~ 1ppm. Such donors will compensate boron reducing the fraction of electrically active boron. Thus this result is plausible and supports the assumption that the samples termination (hydrogen or oxygen) has no significant impact on the electrical transport measurements carried out (the results of which are characteristic of the bulk) apart for perhaps allowing the production of a better ohmic contact. The bulk electrical behaviour of the samples is in this case entirely due to their bulk boron doping.

The PL images presented in Figures 6.1 and 6.2 demonstrate that single crystal boron doped diamonds are not necessarily homogeneously doped. It is known that the incorporation efficiencies of boron (and nitrogen) vary significantly between different crystallographic growth surfaces [31] and that nitrogen, an omnipresent impurity in diamond, as a donor is able to compensate boron acceptors [32]. What is far less appreciated by the scientific community is the difficulty of growing thick (e.g. 0.5 mm) homogeneously doped sc diamond. It has been reported that for (100) boron doped single crystal diamond growth macroscopic steps, shallow pits or combinations of both are observed on the final growth surface [22]. The Diamond- View PL images presented here illustrate that growth has taken place differently on oriented surfaces. These data combined with the results of SIMS and optical absorption measurements clearly show that less boron is incorporated in the diamond grown up pit walls.

The edges of the samples 0372211- D(i) and 0372211- E(i) are parallel to [100] and [010] crystallographic directions (assuming growth direction parallel to [001]). It can be seen that many of the pits have a well determined morphology. A simple diagram, Figure 6.4., shows a possible pit structure where growth has taken place on inclined (111) and (110) faces. Comparison with Figures 6.1 and 6.2 shows many pits that exhibit bright luminescence from the inclined (111) facets and weak luminescence from the (110) sectors (dark cross shape feature in pit region). The bright luminescence is attributed to relatively low boron doping (consistent with the SIMS data) and relatively high nitrogen doping. These two impurities give rise to strong donor-acceptor pair recombination luminescence. The finding of low boron incorporation on the inclined pit walls is on first inspection surprising given the conventional wisdom that boron is more readily incorporated into (111) than (100) surfaces. However the finding is consistent with the growth CVD chemistry being different in a pit than on a flat surface. Several important parameters (in addition to the orientation) could be different (e.g. local temperature, hydrogen abstraction, etc.) for growth on the inclined pit walls compared to the flat surface, resulting in lower boron incorporation. The strong donor-acceptor pair luminescence shows that a significant fraction of the boron in the diamond grown on the pit walls is compensated by nitrogen. This observation is confirmed by the C-AFM studies which show that this material is significantly less conducting than the surrounding diamond. The heterogeneous nature of the doping and electrical properties must be considered when using these diamonds as electrodes. The bulk electrical measurements confirm that samples 0372211- D(i) and 0372211- E(i) are doped with ~ 10^{19} cm^{-3} boron. The low mobilities (~ 4- 8 cm^2/ Vs) and low resistivities (~5 Ωcm) are consistent with the boron doping. It is useful to note that Granger et al. [33] quote an in plane resistivity of ~ 0.01 Ωcm for polycrystalline diamond where the doping level was in the mid 10^{19} boron/cm^3 range.

6.7. Cyclic voltammetry

Voltammetric studies were used to investigate the nature of the electron transfer at the boron doped single crystal CVD diamond electrodes. The CVs give an indication of the average electron transfer surface activity of the scBDD. The measurements were recorded at room temperature using a three-electrode setup (CHI730A potentiostat, CH Instruments Inc.) controlled by a laptop computer, in a de-aerated stationary solution in the presence of a high concentration of an inert electrolyte (KNO_3). In these circumstances only the rate of diffusion of the electroactive species to the electrode surface needed to be considered as a possible mass transport mechanism. A chloridised Ag wire (Ag/AgCl) served as a reference electrode, while a platinum gauze served as a counter electrode.

The samples surface, O- and H-terminated, was prepared as detailed in Chapter 4, section 4.4 and the contacts were prepared as detailed in Chapter 4, section 4.5 **d)**. CVs were run at different sweep rates and in different mediators, to establish to what extent the samples showed characteristics of reversible electrochemistry. The electrolyte solution contained both $Ru(NH_3)_6^{3+}$ ($E_{1/2}$ ~ - 0.3 V) and $FcTMA^+$ ($E_{1/2}$ ~ 0.25 V) in equal concentrations. Scans of the single crystal boron doped samples were recorded in the scan range 0.5 to 0.005 Vs^{-1} with different redox mediator concentrations (in the range of 0.1 mM to 5 mM). The potential applied to the samples with respect to a Ag/AgCl reference electrode was cycled between 0 V and a maximum of - 0.7 V/ (0 V and a maximum of + 0.6 V) causing the reduction (oxidation) of $Ru(NH_3)_6^{3+}$ / ($FcTMA^+$), and back to 0 V allowing the redox active species to be oxidised (reduced) back to the original oxidation (reduction) state. The behaviour of these samples was analysed for both O- and H-terminations.

The Figures 6.10- 6.17 show CVs of the boron doped samples, 0372211- D(i) and 0372211- E(i), recorded for both mediators ($Ru(NH_3)_6^{3+}$ and $FcTMA^+$) and surfaces (hydrogen and oxygen), at concentrations of 0.1 mM and 1 mM. Tables 6.2- 6.5 show the theoretical peak current based on a reversible redox response, the experimentally obtained peak current and ΔEp. The two samples have been selected for investigations as they have different polishing history. However, in both cases, the final polish is a standard cast iron scaife polish.

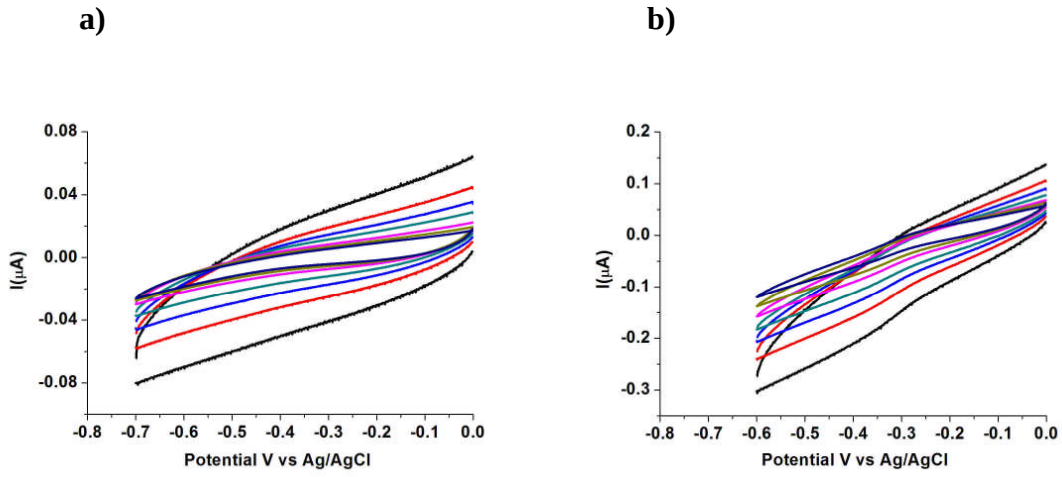

Figure 6.10 CVs in the scan rate range of 0.5 to 0.005 Vs^{-1} recorded in (a) 0.1 mM and (b) 1 mM **$Ru(NH_3)_6^{3+}$** (in the presence of $FcTMA^+$ of equal concentration) in 0.1 M KNO_3 on an O-terminated surface which was polished using a standard cast iron scaife (0372211- D(i)).

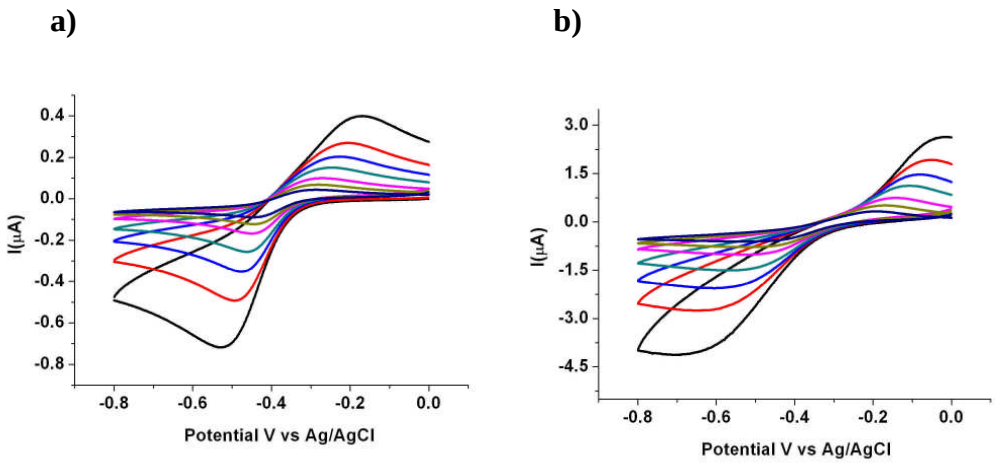

Figure 6.11 CVs in the scan rate range of 0.5 to 0.005 Vs^{-1} recorded in (a) 0.1 mM and (b) 1 mM $\mathbf{Ru(NH_3)_6^{3+}}$ (in the presence of $FcTMA^+$ of equal concentration) in 0.1 M KNO_3 on an H-terminated surface which was polished using a standard cast iron scaife (0372211- D(i)).

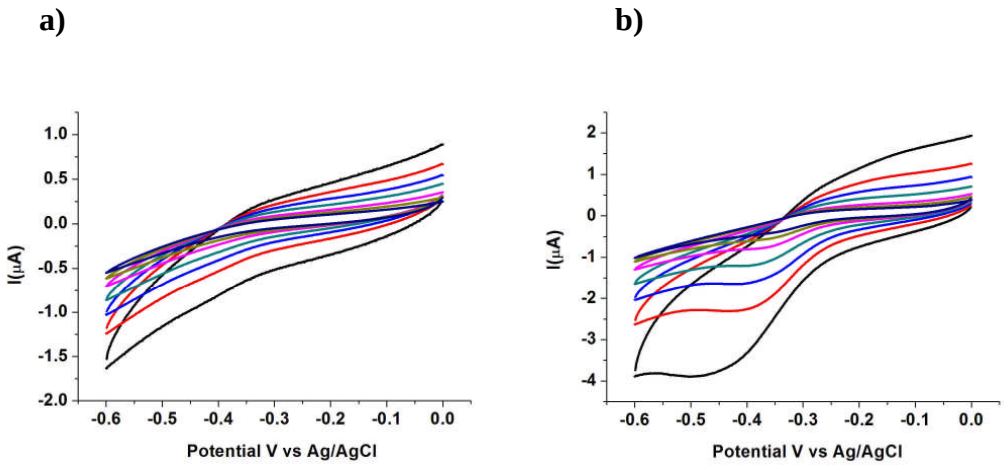

Figure 6.12 CVs in the scan rate range of 0.5 to 0.005 Vs^{-1} recorded in (a) 0.1 mM and (b) 1 mM $\mathbf{Ru(NH_3)_6^{3+}}$ (in the presence of $FcTMA^+$ of equal concentration) in 0.1 M KNO_3 on an O-terminated surface which was polished using a standard cast iron scaife/ using an experimental polish by E6/ repolished using a standard cast iron scaife (0372211- E(i)).

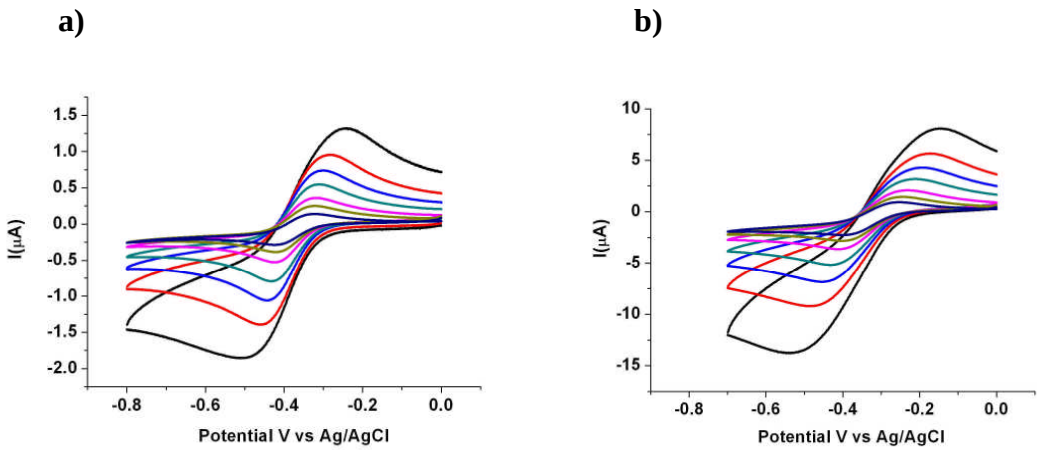

Figure 6.13 CVs in the scan rate range of 0.5 to 0.005 Vs^{-1} recorded in (a) 0.1 mM and (b) 1 mM **$Ru(NH_3)_6^{3+}$** (in the presence of $FcTMA^+$ of equal concentration) in 0.1 M KNO_3 on an H-terminated surface which was polished using a standard cast iron scaife/ using an experimental polish by E6/ repolished using a standard cast iron scaife (0372211- E(i))

Concentration/ mediator/area exposed	Scan Rate (mVs^{-1})	i_p(µA) theoretical	i_p(µA) experimental	ΔEp (mV)
0.1 mM $Ru(NH_3)_6^{3+}$ Area: 2 mm^2 H- terminated 0372211- D(i)	500	1.12	0.59	366
	200	0.71	0.44	278
	100	0.5	0.31	243
	50	0.35	0.23	212
	20	0.22	0.15	181
	10	0.15	0.11	162
	5	0.11	0.08	157

Table 6.2 Summary of the peak separation for the 0372211- D(i) sample, polished using a standard cast iron scaife, H-terminated, in 0.1 mM $Ru(NH_3)_6^{3+}$ in 0.1 M KNO_3 at different scan rates.

Concentration/ mediator/area exposed	Scan Rate (mVs^{-1})	i_p(µA) theoretical	i_p(µA) experimental	ΔEp (mV)
0.1 mM $Ru(NH_3)_6^{3+}$ Area: 4 mm^2 H terminated 0372211- E(i)	500	2.25	1.4	259
	200	1.42	1.29	174
	100	1	1	142
	50	0.7	0.7	123
	20	0.45	0.5	105
	10	0.31	0.35	99
	5	0.22	0.25	105

Table 6.3 Summary of the peak separation for the 0372211- E(i) sample, polished using a standard cast iron scaife/ using an experimental polish by E6/ repolished using a standard cast iron scaife, H-terminated, in 0.1 mM $Ru(NH_3)_6^{3+}$ in 0.1 M KNO_3 at different scan rates.

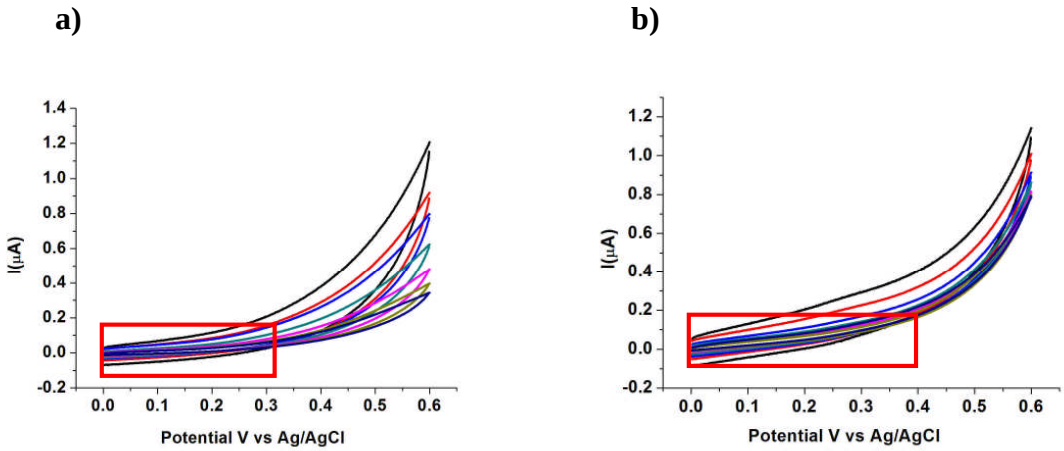

Figure 6.14 CVs in the scan rate range of 0.5 to 0.005 Vs^{-1} recorded in (a) 0.1 mM and (b)1 mM **FcTMA**$^{+}$ (in the presence of $Ru(NH_3)_6^{3+}$ of equal concentration) in KNO_3 on an O-terminated surface which was polished using a standard cast iron scaife (0372211- D(i)). The red boxes highlight the *x* axes used for the measurements recorded while the sample was H-terminated, see Figure 6.15.

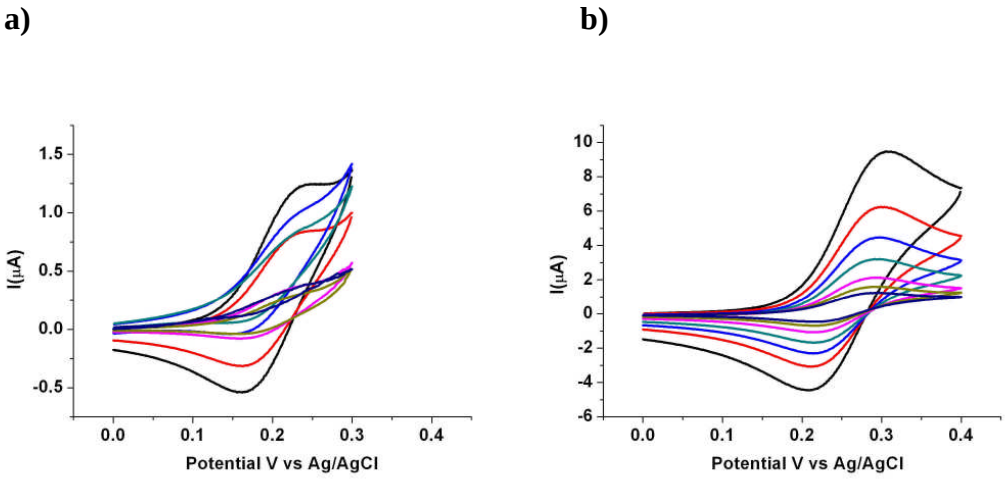

Figure 6.15 CVs in the scan rate range of 0.5 to 0.005 Vs^{-1} recorded in (a) 0.1 mM and (b) 1 mM **FcTMA**$^{+}$ (in the presence of $Ru(NH_3)_6^{3+}$ of equal concentration) in KNO_3 on an H-terminated surface which was polished using a standard cast iron scaife (0372211- D(i)).

Concentration/ mediator/area exposed	Scan Rate (mVs^{-1})	i_p(µA) theoretical	i_p(µA) experimental	ΔEp (mV)
1 mM $FcTMA^+$ Area: 2 mm^2 H terminated 0372211- D(i)	500	9.7	9.03	98
	200	6.1	5.9	88
	100	4.3	4.3	84
	50	3	3.1	84
	20	1.9	2	79
	10	1.3	1.4	86
	5	0.97	1	80

Table 6.4 Summary of the peak separation for the 0372211- D(i) sample, polished using a standard cast iron scaife, H-terminated, in 1 mM $FcTMA^+$ at different scan rates.

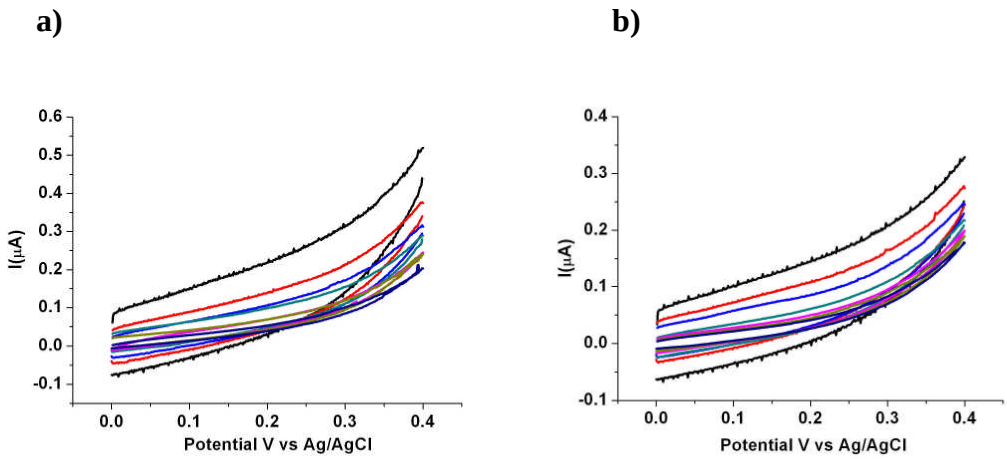

Figure 6.16 CVs in the scan rate range of 0.5 to 0.005 Vs^{-1} recorded in (a) 0.1 mM and (b) 1 mM **$FcTMA^+$** (in the presence of $Ru(NH_3)_6^{3+}$ of equal concentration) in KNO_3 on an O-terminated surface which was polished using a standard cast iron scaife/ using an experimental polish by E6/ repolished using a standard cast iron scaife (0372211- E(i)).

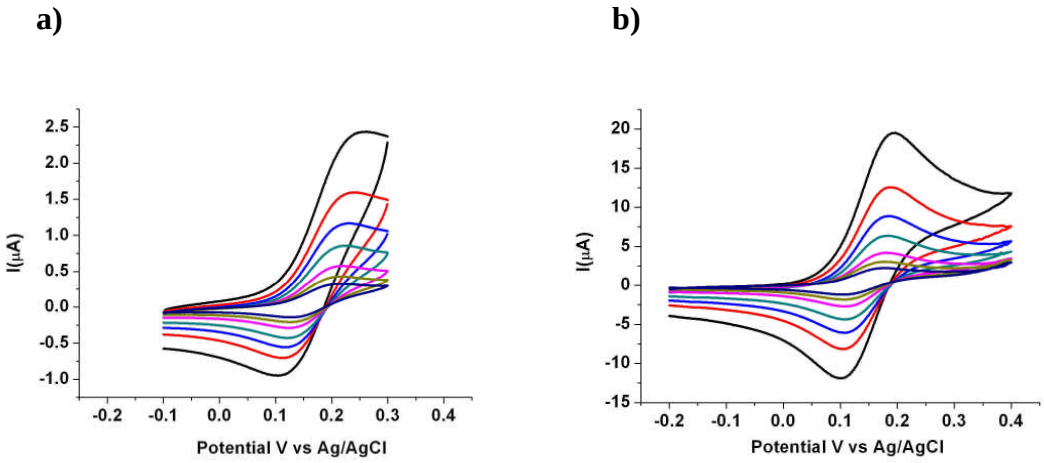

Figure 6.17 CVs recorded in the scan rate range of 0.5 to 0.005 Vs^{-1} in (a) 0.1 mM and (b) 1 mM **$FcTMA^+$** (in the presence of $Ru(NH_3)_6^{3+}$ of equal concentration) in 0.1 M KNO_3 on an H-terminated surface which was polished using a standard cast iron scaife/ using an experimental polish by E6/ repolished using a standard cast iron scaife (0372211- E(i)).

Concentration/ mediator/area exposed	Scan Rate (mVs^{-1})	i_p(μA) theoretical	i_p(μA) experimental	ΔEp (mV)
1 mM $FcTMA^+$ 4 mm^2 H terminated 0372211- E(i)	500	19.5	18.8	98
	200	12.3	12.1	85
	100	8.7	8.7	78
	50	6.1	6.2	78
	20	3.9	3.9	66
	10	2.7	2.8	73
	5	1.9	2	74

Table 6.5 Summary of the peak separation for the 0372211-E(i) sample, polished using a standard cast iron scaife/ using an experimental polish by E6/ repolished using a standard cast iron scaife, H-terminated, in 1 mM $FcTMA^+$ in 0.1 M KNO_3 at different scan rates.

Data for two couples $Ru(NH_3)_6^{3+}$ and $FcTMA^+$ are reported, see Figures 6.10- 6.17 and tables 6.2- 6.5. $Ru(NH_3)_6^{3+} + e^- \rightarrow Ru(NH_3)_6^{2+}$ involves a simple outer sphere electron transfer on most electrodes, and has been extensively studied on polycrystalline diamond [33, 34]. The electrode kinetics for $Ru(NH_3)_6^{3+}$ are relatively insensitive to surface microstructure, surface oxides, and adsorbed monolayers on sp^2 carbon electrodes [33]. The insensitivity of the rate of reaction to surface modification implies that electron transfer does not depend on an interaction with surface sites or other impurities [33]. Granger et al. [33] showed that for a $Ru(NH_3)_6^{3+}$ redox analyte concentration of 1 mM in a 1 M KCl supporting electrolyte at a scan rate of 100 mV/s a redox peak separation of $\Delta Ep = 74$ mV, and a peak oxidation current of 320 $\mu A/cm^2$ were recorded using a H-terminated polycrystalline boron doped electrode doped in the mid 10^{19} cm^{-3} boron. Granger et al. [33] report that ΔEp is largely unaffected by changing from a hydrogen to an oxygen surface termination for $Ru(NH_3)_6^{3+}$. This finding is somewhat surprising for a moderately doped BDD electrode given the change in electron affinity between oxygen and hydrogen terminated diamond.

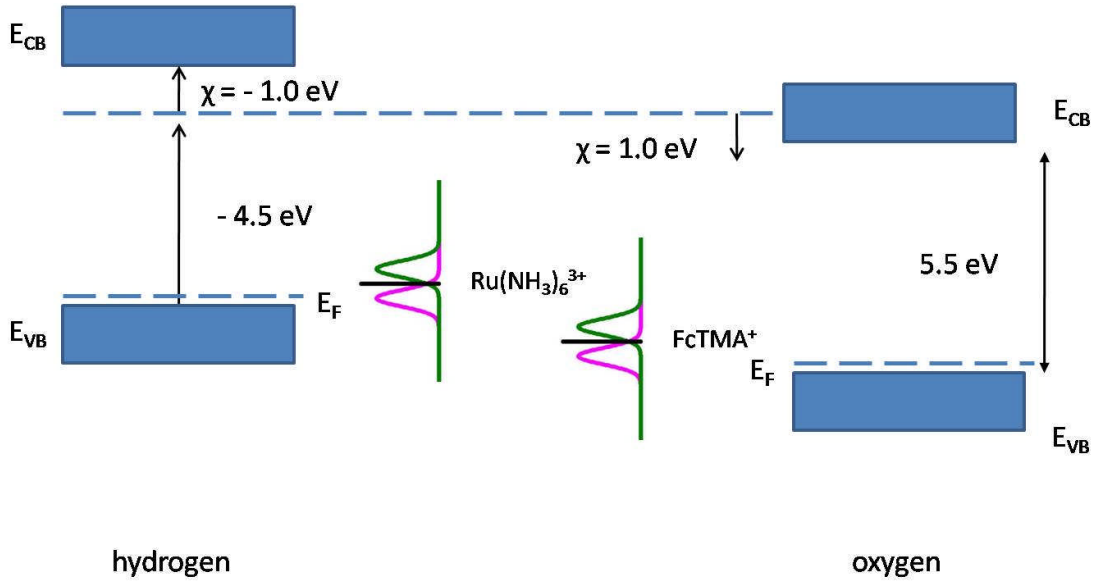

Figure 6.18 Schematic representation showing the position of the $Ru(NH_3)_6^{3+}$ and $FcTMA^+$ couples with respect to valence and conduction band for both oxygen and hydrogen terminated diamond.

Figure 6.18 shows the position of the $Ru(NH_3)_6^{3+}$ and $FcTMA^+$ couples for both oxygen and hydrogen terminated diamond. For an oxygenated surface the density of states near the formal potential of the $Ru(NH_3)_6^{3+}$ system is zero so no electrochemical activity is expected; for a hydrogenated surface the redox couple is sufficiently close such that there is a non zero density of states and electrochemistry is possible. Granger et al. [33] accepted that the formal potential for $Ru(NH_3)_6^{3+}$ lies within the band gap, and that the redox system is not expected to exchange charge with either valence or the conduction band. They invoked the presence of a sufficient density of electronic states in the band gap of the polycrystalline diamond at this potential to explain the nearly reversible response observed. This density of states must extend more than 1 eV above the top of the valence band to explain their results. The data reported here shows that there are no such states in the band gap of the sc BDD employed here.

Figures 6.10 and 6.12 show that there is little or no redox activity on samples 0372211- D(i) and 0372211- E(i) when O-terminated for $Ru(NH_3)_6^{3+}$. However, when H-terminated there is redox activity with this couple, see Figures 6.11 and 6.13. The peak currents for sample 0372211- E(i) at a concentration of 0.1 mM $Ru(NH_3)_6^{3+}$ are in reasonable accord with those expected for a metallic electrode (see Table 6.4). Sample 0372211- D(i) performs slightly less well (see Table 6.3), however as the concentration of the redox couple is increased the peak current in both samples scales approximately with the concentration. The peak separation, ΔEp, is considerably greater than that reported by Granger et al. [33] on polycrystalline boron doped diamond and increased more as the concentration of redox species was increased from 0.1 mM to 1 mM. This indicates that the electrode kinetics for

$Ru(NH_3)_6^{3+}$ are very sluggish on the H-terminated semiconducting boron doped sc diamond employed here; *iR* or *RC* effects can not be the cause for a large ΔEp.

The other couple studied here with cyclic voltammetry is $FcTMA^+$. It is expected that for O-terminated semiconducting boron doped single crystal diamond the formal potential falls within the band gap and no exchange of charge between the diamond and the redox couple is expected or observed. However, when the diamond is H-terminated, the formal potential is well positive of the valence band maximum. This means that charge exchange through the valence band is possible and as expected redox activity was observed. For concentrations of 1 mM $FcTMA^+$ the peak oxidation current is in good accord with the theoretical value on both samples and the value ΔEp at a scan rate of 100 mV/s is 81 ± 3mV, thus the reaction is close to reversible. As above we can rule out *iR* or *RC* effects.

The CV results for the two couples studied are consistent with the well-accepted Gerischer model [35] used to explain electron transfer at semiconducting electrodes. There is no need to invoke the presence of gap states to explain the results for $Ru(NH_3)_6^{3+}$. The data suggest that mid-gap states are not present in the semiconducting single crystal boron doped diamond electrodes studied here. Due to the gross inhomogeneities associated with the boron doping and conductivity of these scBDD semiconducting diamond samples, it is extremely difficult to apply the idealised model of the electron transfer. However, we observe quasi-reversible behaviour for $FcTMA^+$ on scBDD semiconducting H-terminated diamond, with electron transfer becoming more sluggish for $Ru(NH_3)_6^{3+}$. The new results invite re-evaluation of the results of Granger *et al.* [33] on what was described as high quality H-terminated polycrystalline BDD film. The most plausible explanation is: 1) in the polycrystalline BDD

there are regions with very high boron doping where the diamond is metallic and these regions dominate the electrochemical response or 2) mid band gap states associated with grain boundaries and other defects in the polycrystalline films dominate the electrochemical response, not the diamond itself.

The samples studied here are mechanically polished rather than as grown and one should worry about the introduction of surface and subsurface damage (diamond is very brittle) which adversely influences the electronic properties. The samples discussed in this chapter have different polishing histories; the experiments carried out and presented here show that regardless of their history, if finally polished using the same technique, the samples show similar behaviour. No thorough studies were carried out on the intermediate stages of the surface polishing.

6.8. Scanning electrochemical microscopy

The significant differences in behaviour observed for these samples in different mediators and for different functionalised surfaces deserved further investigation, thus SECM was employed to examine their electrochemical activity. The technique was explained in Chapter 3, section 3.10 and the experimental set-up was detailed in Chapter 4, section 4.10. The measurements were recorded in various areas across the sample. Both SG-TC and feedback modes were employed. As for the CVs measurements described above, two mediators were used: $Ru(NH_3)_6^{3+}$ ($E_{1/2}$~ -0.3 V) and $FcTMA^+$ ($E_{1/2}$~ 0.25 V) (0.1 mM, 1 mM and 5 mM) in the same electrolyte solution in equal concentrations. While CVs give an overview of the overall behaviour of the samples, approach curves in SECM offer an alternative approach to examining the electron transport properties of the surface with a spatial resolution governed by the diameter of the electrode employed [36]. Since the samples 0372211- D(i) and 0372211- E(i) exhibited similar behaviour, hereafter only the approach curves for 0372211- E(i) will be presented.

For 0372211- E(i), polished using a standard cast iron scaife/ using an experimental polish by E6/ repolished using a standard cast iron scaife, O-terminated, the approach curve behaviour for both $Ru(NH_3)_6^{3+}$ and $FcTMA^+$, tip reduction and oxidation respectively is presented in Figures 6.19 and 6.20. Regardless of the concentration of species in solution (i.e. 0.1 mM, 1 mM or 5 mM) the substrate showed negative feedback behaviour.

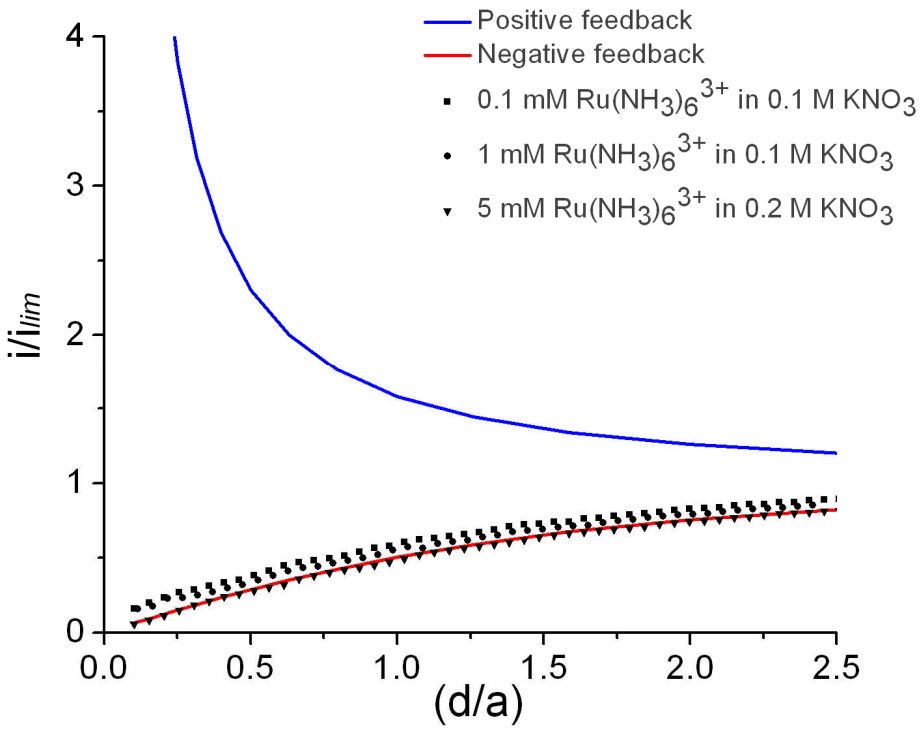

Figure 6.19 Approach curves on an O-terminated boron doped single crystal diamond, with a boron dopant density of 6 x 10^{18} – 6 x 10^{19} atoms cm^{-3}, recorded in 0.1 mM, 1 mM and 5 mM $Ru(NH_3)_6^{3+}$ in KNO_3 (0372211- E(i)). The same behaviour was observed regardless if the substrate was i) unbiased or ii) biased at 0 V.

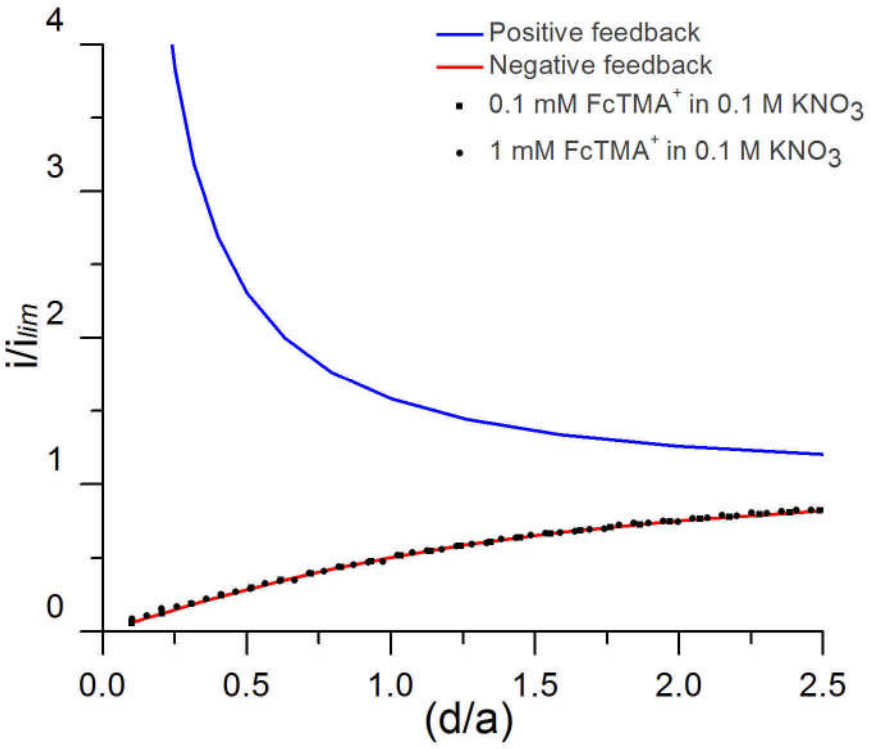

Figure 6.20 Approach curves on an O-terminated boron doped single crystal diamond, with a boron dopant density of 6 x 10^{18} – 6 x 10^{19} atoms cm^{-3}, recorded in 0.1 mM and 1 mM $FcTMA^+$ in KNO_3 (0372211- E(i)). The same behaviour was observed regardless if the substrate was i) unbiased and ii) biased at 0 V.

For both $Ru(NH_3)_6^{3+}$ and $FcTMA^+$ the surface behaves like a perfect insulator regardless of the concentration of species in solution, in agreement with the CV data. The experiments were performed many times at various locations across the sample; the same behaviour was observed each time.

The same sample was examined in both mediators while H-terminated. When H-terminated, the sample exhibited conductive behaviour for low concentration of mediator in solution,

while slowly moving away from this state by increasing the concentration. These characteristics were observed regardless of the mediator in solution, see Figures 6.21, 6.22 and 6.23.

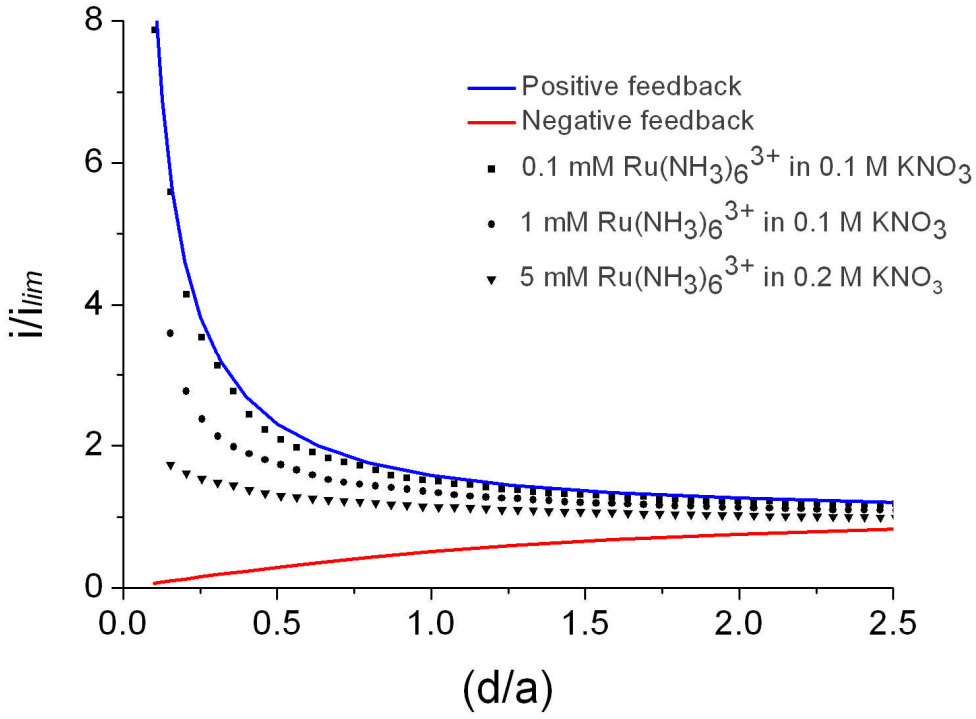

Figure 6.21 Approach curves on an H-terminated boron doped single crystal diamond, with a boron dopant density of 6 x 10^{18} – 6 x 10^{19} atoms cm^{-3}, recorded in 0.1 mM, 1 mM and 5 mM $Ru(NH_3)_6^{3+}$ in KNO_3 (0372211- E(i)). The substrate was biased at 0V.

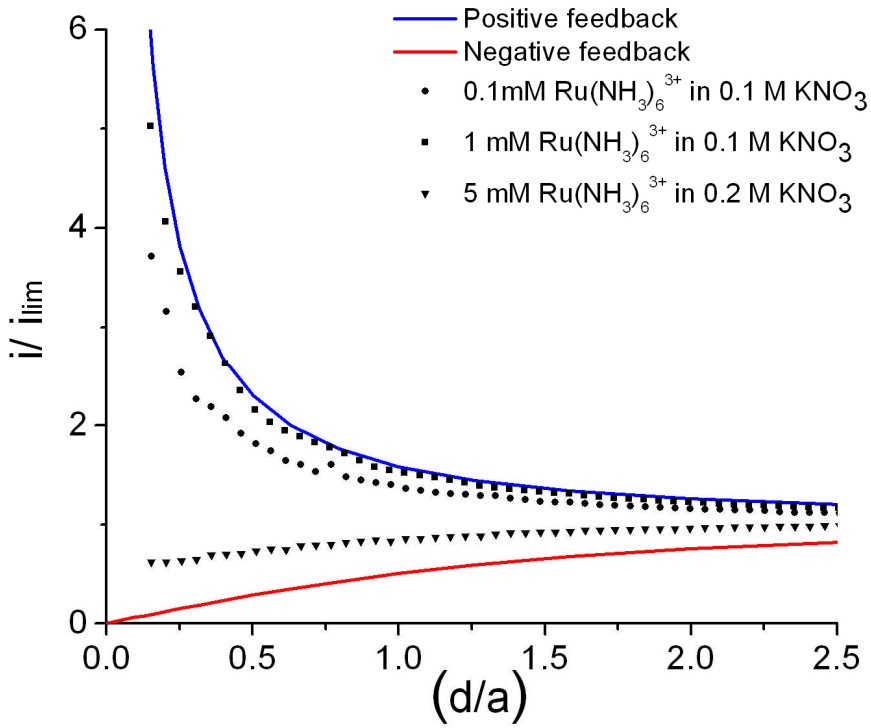

Figure 6.22 Approach curves on an H-terminated boron doped single crystal diamond, with a boron dopant density of 6 x 10^{18} – 6 x 10^{19} atoms cm^{-3} , recorded in 0.1 mM, 1 mM and 5 mM $Ru(NH_3)_6^{3+}$ in KNO_3 (0372211- E(i)). The substrate was unbiased.

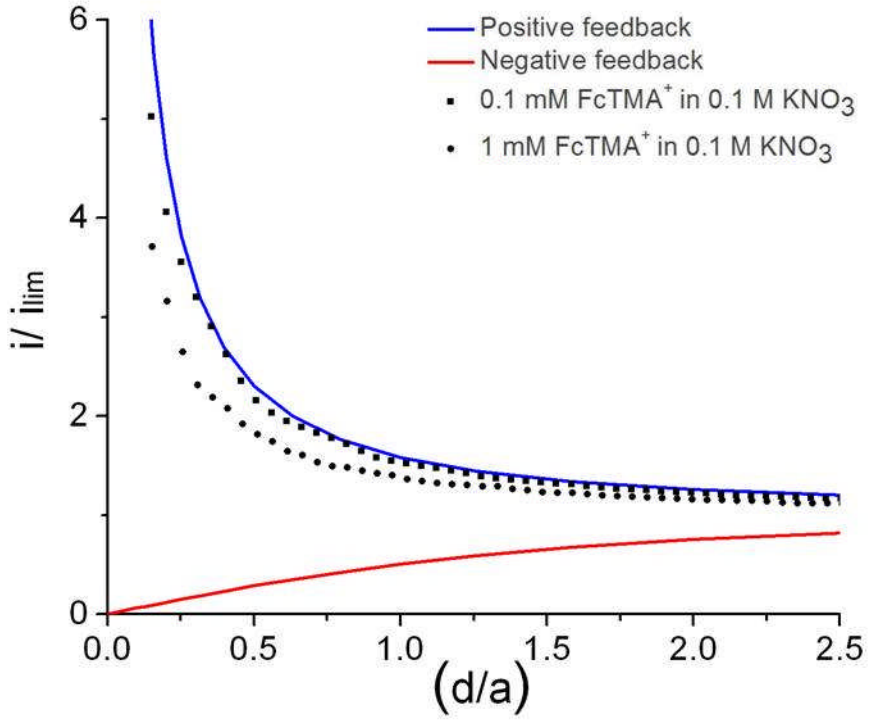

Figure 6.23 Approach curves on an H-terminated boron doped single crystal diamond, with a boron dopant density of 6 x 10^{18} – 6 x 10^{19} atoms cm^{-3}, recorded in 0.1 mM and 1 mM $FcTMA^+$ in KNO_3 (0372211- E(i)). The same behaviour was observed regardless if the substrate was i) unbiased and ii) biased at 0 V.

When H-terminated the sc semiconducting boron doped diamond is active for both redox couples. Both $Ru(NH_3)_6^{3+}$ and $FcTMA^+$ exhibit positive feedback at 0.1 mM concentration; the feedback gets increasingly less positive as the concentration of redox species is increased. Such a result is entirely in accord with the expected density of electronic states near the formal potential of each redox system. The electrochemical reaction taking place on the substrate is the reverse as to the one occurring during the CV measurements for both $Ru(NH_3)_6^{3+}$ and $FcTMA^+$. The chemical potential of $FcTMA^+$ is well below the top of the VB

whereas $Ru(NH_3)_6^{3+}$ is near the top where the density of states is low. Thus as the electrode is increasingly challenged the feedback decreases.

With SECM being a versatile technique which can also provide localised electrochemical topographical information, SECM electrochemical imaging was attempted on sample 0372211- E(i). A 25 μm Pt UME was scanned typically at a rate of 20 μm s^{-1} in a series of unidirectional scans (line separation of 20 μm) with a scan size of 500 μm x 500 μm or 250 μm x 250 μm; the electrolyte solutions were thoroughly de-aerated with nitrogen before measurements were made. The distance at which the scans were recorded, was set by carrying out an approach curve in feedback mode in order to determine the point of tip-substrate contact. It has to be noted that this is the distance at the centre of the scan.

Using $FcTMA^+$ as the redox couple the activity of the sc semiconducting H-terminated diamond surface appears to be relatively uniform with the feedback current typically varying less than 30% (Figure 6.26). Additionally, it has to be mentioned that placing the sample perfectly flat during an experiment is extremely difficult. However using $Ru(NH_3)_6^{3+}$ as the redox couple variation of activity of ~75% were observed (Figure 6.24). Once again this is consistent with the $Ru(NH_3)_6^{3+}$ being very sensitive to the variation in the density of states close to the top of the VB. Unfortunately it is not known precisely on the image shown in Figure 6.25 where the SECM image was recorded. However it can be seen that the features indicating low activity regions (Figure 6.24) in the SECM image are of approximately the correct dimensions (~ 25 μm) so they could be related to the pits evidentiated in the PL image, Figure 6.25. The active spots (Figure 6.24) are most likely areas without defects where the active boron concentration is higher compared with the rest of the surrounding

material. The white box in Figure 6.25 highlights a region where images similar to the one presented in Figure 6.26 could have been recorded.

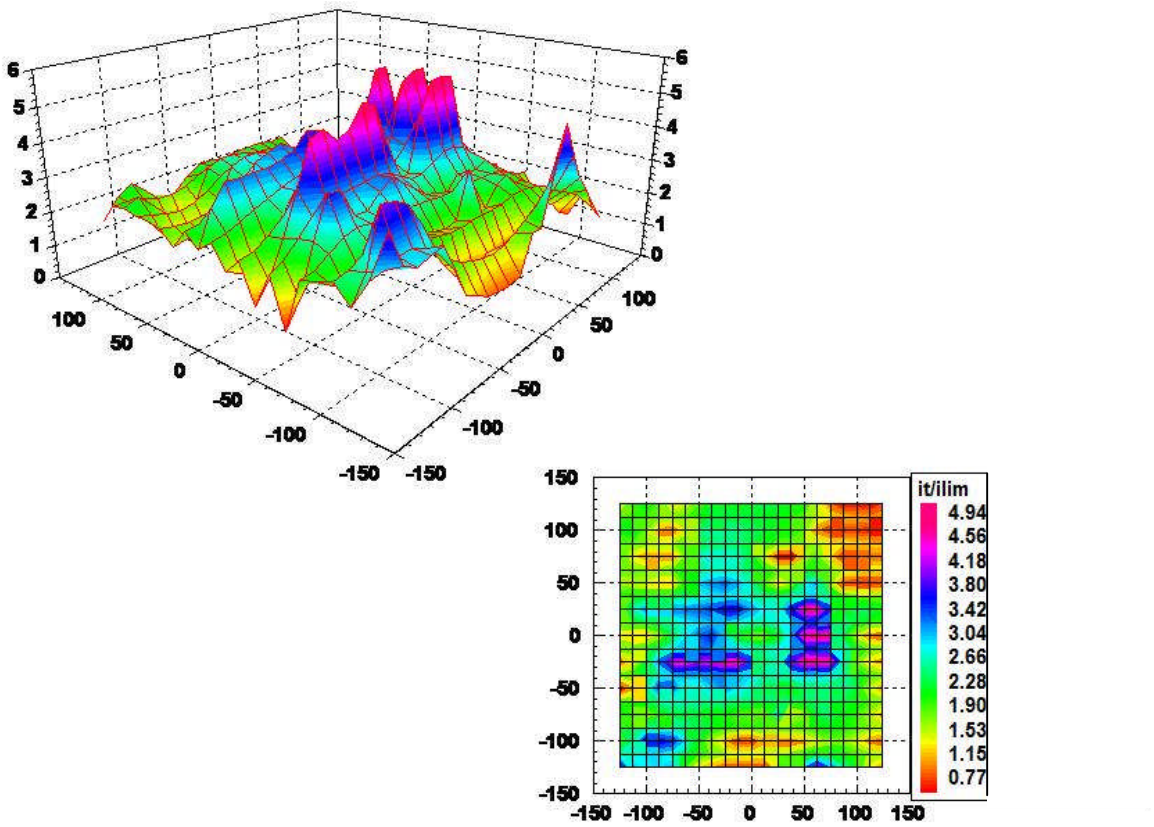

Figure 6.24 250 µm × 250 µm SECM image recorded for 5 mM $Ru(NH_3)_6^{3+}$ in 0.2 M KNO_3 at the surface of the scBDD. The substrate was held at 0 V, whilst the 25 µm diameter Pt UME tip was maintained at - 0.5 V. A tip-substrate separation of *ca*. 5.20 µm was employed during imaging. The sample 0372211- E(i) was H-terminated.

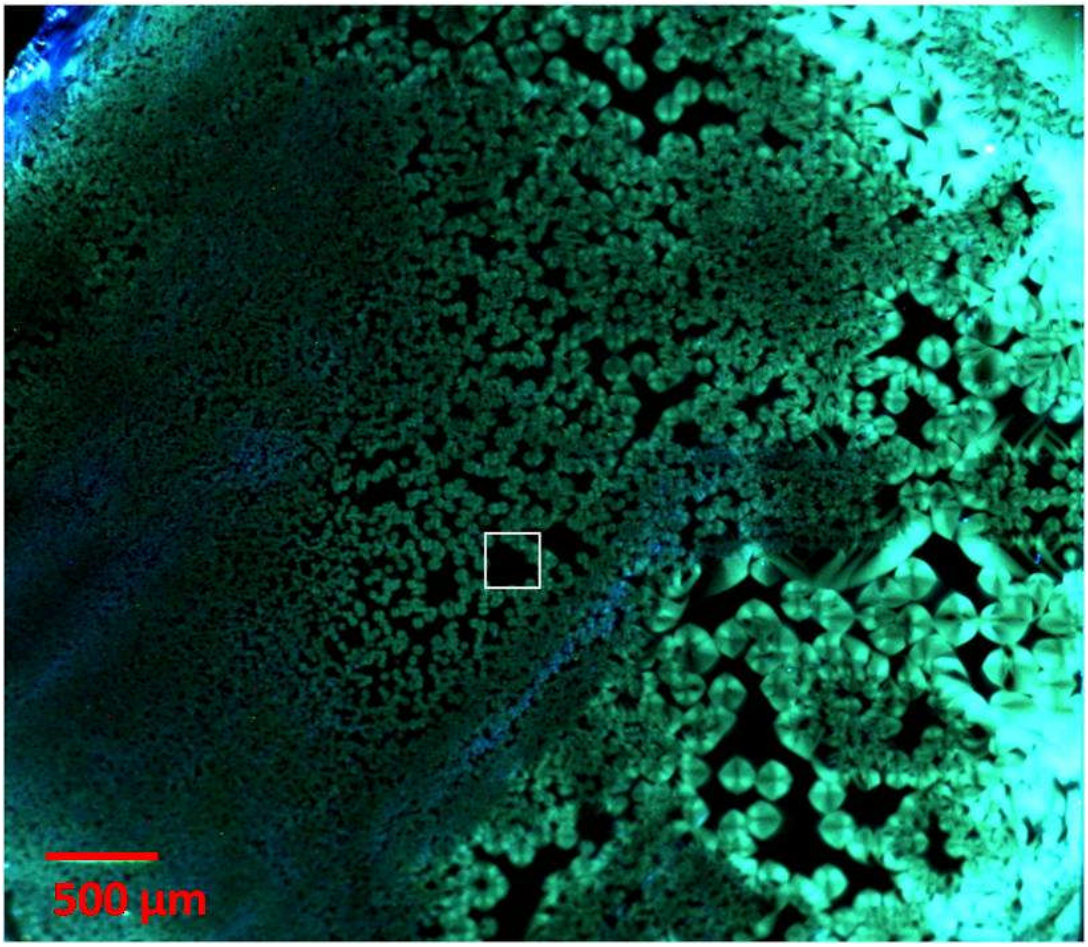

Figure 6.25 Diamond View image of the single crystal diamond 0372211- E(i), with the white box indicating the possible position of the scan shown in Figure 6.26.

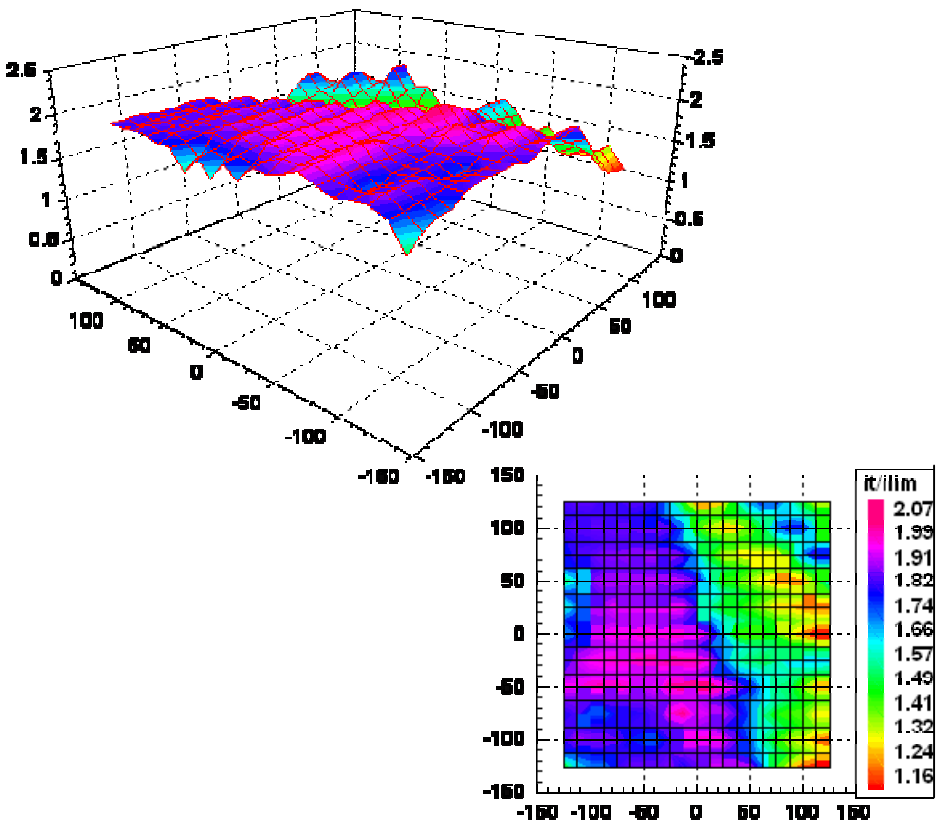

Figure 6.26 250 µm × 250 µm SECM image recorded for 1 mM $FcTMA^+$ in 0.1 M KNO_3 at the surface of the scBDD. The substrate was held at 0 V, whilst the 25 µm diameter Pt UME tip was maintained at 0.5 V. A tip-substrate separation of *ca*. 6.25 µm was employed during imaging. The sample 0372211- E(i) was H-terminated.

References:

[1] M. I. Landstrass, and K. V. Ravi, Applied Physics Letters **55**, 1391 (1989).
[2] M. I. Landstrass, and K. V. Ravi, Applied Physics Letters **55**, 975 (1989).
[3] T. H. Borst, and O. Weis, Physica Status Solidi a-Applied Research **154**, 423 (1996).
[4] J. Ristein, M. Riedel, and L. Ley, Journal of the Electrochemical Society **151**, E315 (2004).
[5] I. Yagi *et al.*, Journal of Electroanalytical Chemistry **473**, 173 (1999).
[6] Y. Kaibara *et al.*, Diamond and Related Materials **12**, 560 (2003).
[7] J. Ristein *et al.*, Physica Status Solidi a-Applied Research **181**, 65 (2000).
[8] J. Ristein, Applied Physics a-Materials Science & Processing **82**, 377 (2006).
[9] A. Chatterjee *et al.*, Physica Status Solidi a-Applied Research **199**, 49 (2003).
[10] H. O. Pierson, *Handbook of Carbon, Graphite, Diamond and Fullerenes - Properties, Processing and applications* New Jersey, 1993).
[11] N. Fujimori, H. Nakahata, and T. Imai, Japanese Journal of Applied Physics Part 1-Regular Papers Short Notes & Review Papers **29**, 824 (1990).
[12] G. Braunstein, and R. Kalish, Journal of Applied Physics **54**, 2106 (1983).
[13] A. T. Collins, Lightowlers, E. C. , Physical Review **171** (1968).
[14] C. Nebel, and J. Ristein, *Thin- film diamond II* (Elsevier Academic Press, 2003), Vol. 77.
[15] A. L. Colley *et al.*, Analytical Chemistry **78**, 2539 (2006).
[16] N. R. Wilson *et al.*, Journal of Physical Chemistry B **110**, 5639 (2006).
[17] K. Ushizawa *et al.*, Diamond and Related Materials **7**, 1719 (1998).
[18] G. A. Scarsbrook *et al.*, (Patent WO03052174A2, 2003).
[19] P. Martineau, (Personal Communication, 2008).
[20] C. M. Welbourn, M. A. Cooper, and P. M. Spear, Gems & Gemology, 156 (1996).
[21] K. Wantanabe *et al.*, Diamond and Related Materials **6**, 99 (1997).
[22] P. M. Martineau *et al.*, Gems & Gemology **40**, 2 (2004).
[23] A. Kulik *et al.*, Forces in Scanning Probe Methods **286**, 119 (1995).
[24] T. W. Kelley, E. L. Granstrom, and C. D. Frisbie, Advanced Materials **11**, 261 (1999).
[25] J. V. Macpherson, J. P. G. de Mussy, and J. L. Delplancke, Electrochemical and Solid State Letters **4**, E33 (2001).
[26] C. J. Boxley *et al.*, Journal of Physical Chemistry B **107**, 9677 (2003).
[27] D. P. Burt *et al.*, Langmuir **24**, 12867 (2008).
[28] M. H. Nazare, and A. J. Neves, *Properties, Growth and Applications of Diamond* (INSPEC, London, 2001), Vol. 26.
[29] M. H. Nazare, and A. J. Neves, **26** (2001).
[30] A. T. Collins, and A. W. Williams, Journal of Physics Part C Solid State Physics **4**, 1789 (1971).
[31] R. Samlenski *et al.*, Diamond and Related Materials **5**, 947 (1996).
[32] R. Locher *et al.*, Diamond and Related Materials **4**, 678 (1995).
[33] M. C. Granger *et al.*, Analytical Chemistry **72**, 3793 (2000).
[34] M. C. Granger, and G. M. Swain, Journal of the Electrochemical Society **146**, 4551 (1999).
[35] R. Memming, *Semiconductor Electrochemistry* (Wiley - VCH, 2001).
[36] A. J. Bard, and M. V. Mirkin, *Scanning Electrochemical Microscopy* (Marcel Dekker, INC., 2001).

Chapter 7

Electrical and electrochemical characterisation of heavily doped (>10^{20} cm^{-3} boron) oxygen and hydrogen terminated single crystal diamond

This chapter aims to investigate the electrical and electrochemical behaviour of heavily doped (> 10^{20} cm^{-3} boron) oxygen and hydrogen terminated single crystal diamonds. FE-SEM, SECM, bulk electrochemistry, Hall effect measurements and white-light interferometry (WLI) will be employed. The nature of the electrical and electrochemical activity will be analysed.

7.1. Introduction

As outlined in Chapter 2, section 2.2, boron can be incorporated into diamond [1] and dopes holes into a shallow acceptor level close to the top of the valence band. Electrical transport studies showed that at low boron concentrations (10^{17}- 10^{19} cm^{-3}) diamond behaves like a semiconductor with E_A~ 0.37 eV [2-6], while when the boron concentration increases (10^{20} cm^{-3}) the activation energy decreases [4, 5] and for concentrations higher than ~ 5 x 10^{20} cm^{-3} diamond exhibits metal-like conduction [3-6]. Boron incorporates on substitutional bonding sites of the lattice where it behaves like an electronic acceptor. Due to the larger covalent radius of boron (0.88 Å) compared with that of carbon (0.77 Å) the introduction of substitutional boron into the diamond leads to an expansion of the lattice parameter [7]. Hydrogen can also be found in diamond and can passivate boron acceptors as well as other defects. The metal to insulator transition is a result of the boron-related hydrogenic states with a Bohr radius $a_H = \varepsilon a_0/m^*$, which overlap when n_B reaches n_c with $a_H n_c^{1/3} = 0.26$ as seen

in various other materials. Taking ε = 5.7 for diamond and m* = 0.74 for the holes, the Bohr radius a_H is estimated at 0.35 nm in agreement with values based on the acceptor excited states [7]. This estimates agree with experimental data where 3.4 x 10^{20} cm^{-3} < n_c < 5.5 x 10^{20} cm^{-3} [8]. At low temperatures heavily boron doped metallic diamond undergoes a normal superconducting phase transition i.e. the resistivity drops to zero [7]. The precise details of the mechanism are still under debate.

For advanced electrical and electrochemical application the use of single crystal heavily boron doped diamond is envisaged, but as mentioned in Chapter 2, section 2.1 and section 2.2, growing homogeneous and heavily boron doped single crystal diamond is not straight forward. Chapter 6, section 6.3 discusses some of the structural/ morphological defects that might appear during single crystal diamond synthesis and their influence on the uptake of boron. Silva et al. [9] discuss how the morphology of single crystal diamond evolves during the synthesis of thick layers from which free standing boron doped electrodes can be fabricated. The variation in boron uptake on different crystallographic oriented substrates is well documented in the literature [10, 11].

7.2. Heavily boron doped single crystal diamond

The sample under investigation, 0572389/1 (6.16 mm x 5.66 mm x 0.17 mm), is a single crystal boron doped diamond, grown on a (100) oriented diamond substrate using a microwave plasma CVD reactor. The boron dopant density was determined using SIMS measurements (spot size of 50 µm in diameter) and it was established to be ~3.4 x 10^{20} boron atoms cm^{-3}. The sample was not polished after growth. The oxygen and hydrogen surfaces were prepared as described in Chapter 4, section 4.4. As the sample was still on the substrate,

all electrical and electrochemical measurements were performed with the sample top contacted regardless if O- or H-terminated, see Chapter 4, section 4.5 **d)**.

7.3. Photoluminescence

The sample did not exhibit any contrast in PL imaging using the Diamond-View instrument described in Chapter 4, section 4.3. As already outlined in Chapter 6, section 6.3 the regions where no light is emitted from donor acceptor pair recombination appear black on the PL map and indicate a region where $[B_S] \gg [N_S]$; a high concentration of [B] quenching emission.

7.4. Field Emission-Scanning Electron Microscopy (FE-SEM)

To investigate the sample's morphology FE-SEM was employed. Its principles are outlined in Chapter 4, section 4.13. In Chapter 2, section 2.1, some of the factors that influence the diamond growth, such as the substrate's preparation and temperature, the source gas composition and pressure, etc. have been discussed. Diamond's surface morphology has been shown to depend on the methane concentration; the morphology changed periodically with time in such a way that a microcrystalline phase and a faceted phase appeared alternately [12]. Structural variations observed on the 0572389/1 sample, are presented in Figure 7.1. The red boxes on the left hand side images, (i) and (iii), are a guide to the eye, highlighting the position of the zoomed in images on the right hand side, (ii) and (iv).

i) ii)

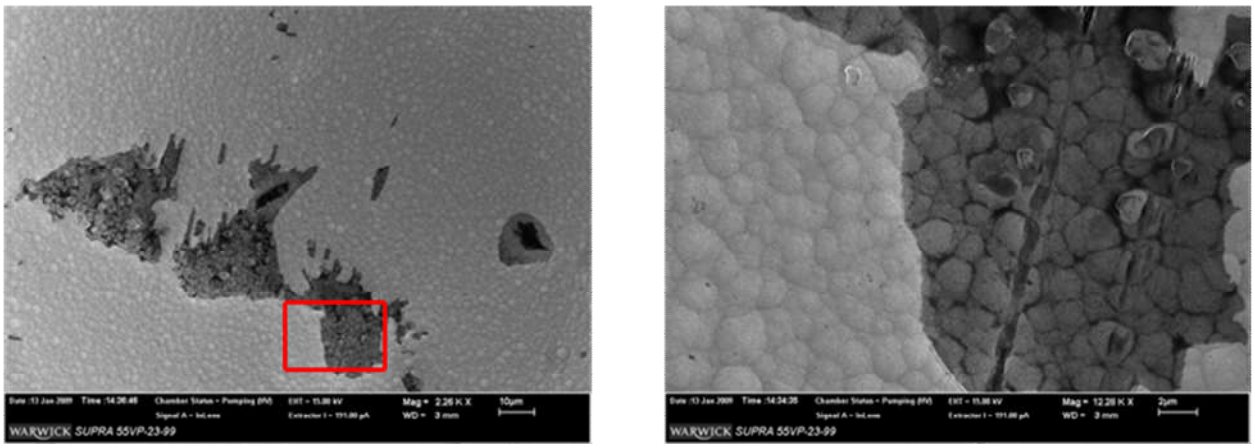

iii) iv)

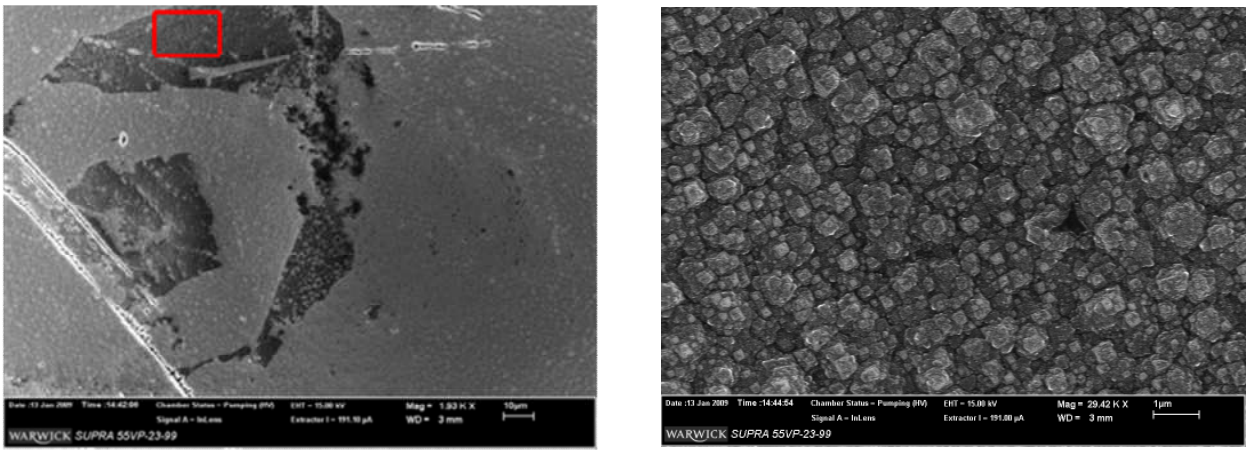

Figure 7.1 FE-SEM images showing different structural variations of the surface of 0572389/1, a single crystal highly boron doped diamond. The red boxes on the left hand side images, (i) and (iii), are a guide to the eye, highlighting the position of the zoomed in images on the right hand side, (ii) and (iv).

7.5. White Light Interferometry (WLI)

The surface roughness of the single crystal boron doped sample was analysed using scanning white-light interferometry. Noncontact optical profilometry using white light interferometry is a quick and reliable method of measuring the surface roughness. The technique involves scanning the sample in the *z* direction in non contact mode using white light and measuring

the visibility of the interference fringes at each pixel in the image [13]. Figure 7.2 shows a schematic representation of the instrument.

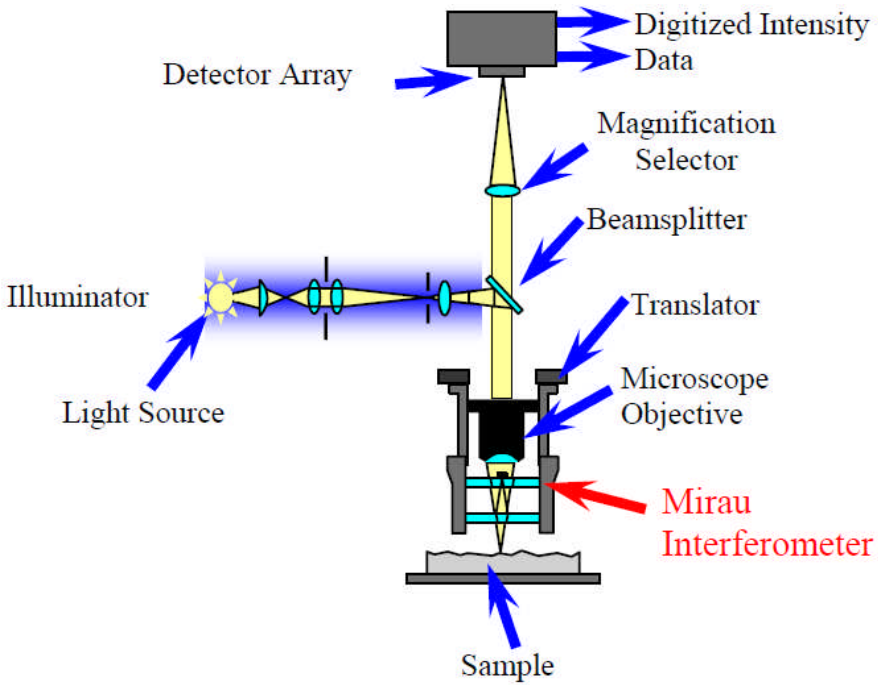

Figure 7.2 Schematic of an interference microscope used for measurement of fine surface structures, highlighting the Mirau interferometer, the microscope objective, the beamsplitter, the magnification selector and the light source [14].

During a scan, light from the source is divided into two beams by a beamsplitter; one will go to the Mirau interferometer (a white-light interferometer consisting of a microscope objective, a semitransparent mirror and a reference mirror) and the other to the surface of the sample. The two beams are reflected back to the beam splitter and combined to create interference fringes, which are recorded by a charge–coupled device (CCD) camera. The interference pattern gives information on the surface profile; the resulting constructive fringes along the scanning axis give the height of the surface at that point and their variation along the surface gives information about variation on the surface roughness. This technique is quick and because it measures topographical features via wave interference, subnanometer

resolution with step heights as 0.1 nm becomes possible. The lateral spatial resolution is of 150 nm, while long working distances as great as 10000 µm can be achieved [15].

For this study, the sample was coated with ~10 nm Au using the Moorfield sputter/evaporator. A white-light interferometer (WYKO NT-2000, Surface Profiler, WYKO Systems) was employed. Large areas of the sample showed a consistent morphology with a surface roughness Ra ~ 0.4 µm, however regions could be sometimes seen where the growth morphology was significantly different (see Figure 7.1). A typical image of the surface of the single crystal boron doped diamond, 0572389/1, with the associated profiles showing such regions is presented in Figure 7.3; these regions are typically ~2 µm below the larger area's growth surface.

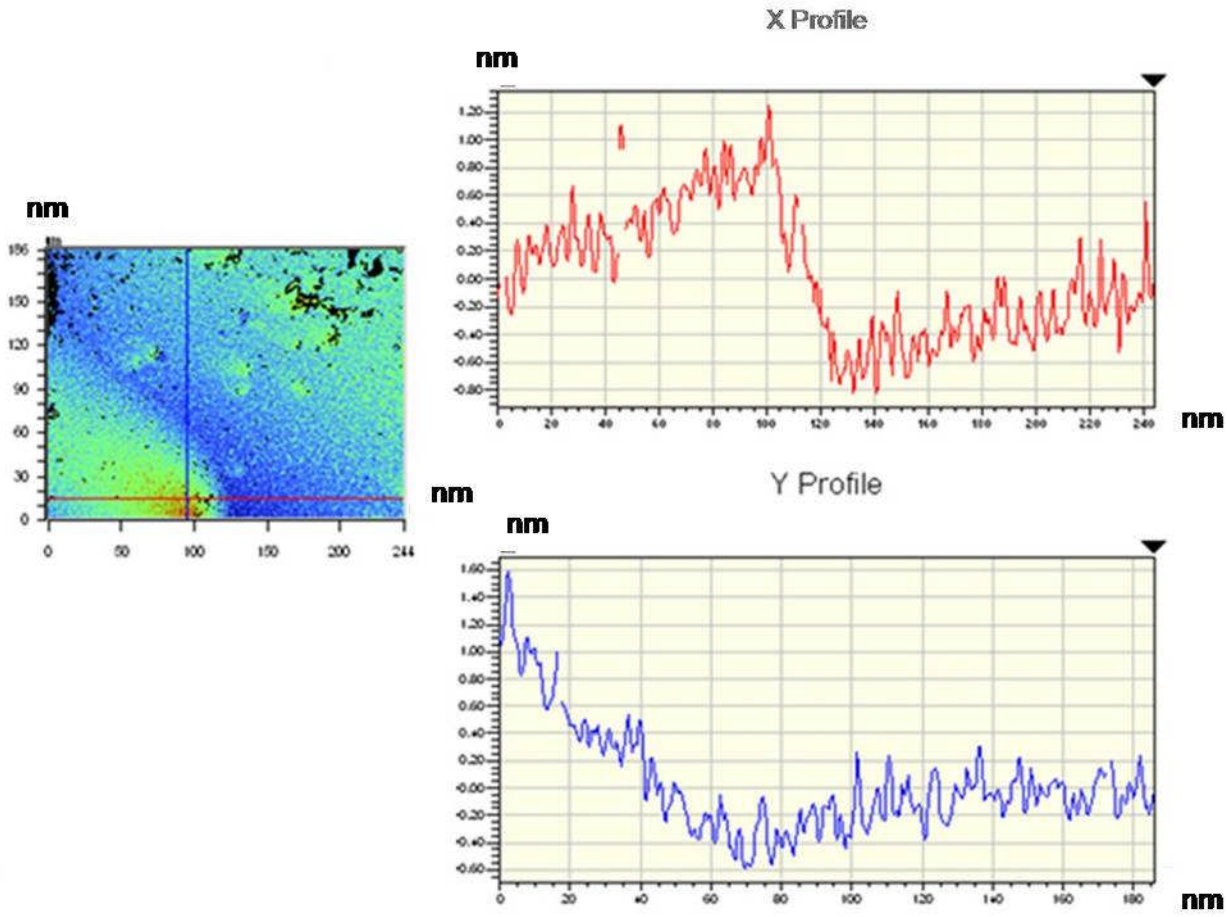

Figure 7.3 Interferometry image and profiles of 0572389/1, an unpolished single crystal boron doped diamond, showing variations in height on the surface of the sample; differences as high as ~2 µm can be observed.

7.6. Electrical characterisation

Gold contacts, 0.8 mm x 0.8 mm wide with a separation of 1 mm between them, were deposited and in air resistivity and Hall effect measurements were carried out. Their principle is detailed in Chapter 3, section 3.4 and the set-up's description can be found in Chapter 4, section 4.11. The sheet resistance values obtained experimentally are summarised in Table 7.1.

Current	Sample 0572389/1 H terminated
I= 3 µA	R_s= 1 ± 0.2 Ω
I= 8 µA	R_s= 1 ± 0.2 Ω
I= 100 µA	R_s= 1 ± 0.2 Ω

Table 7.1 Sheet resistance values obtained experimentally using the set-up described in Chapter 4, section 4.11 for the H terminated 0572389/1 single crystal boron doped diamond sample.

The sheet resistance values obtained experimentally confirm the fact that the active boron concentration in this sample was higher than 10^{20} cm^{-3} and that the sample's conductivity is a result of the boron concentration, not a result of its H termination.

For 0572389/1 the Hall measurements were carried out when I= 3 µA. Using the formula (3.8) and (3.10) from Chapter 3, section 3.4, mobilities of 1 (± 0.3) cm^2/Vs and carrier concentrations of 2.5 (± 0.2) x 10^{20} cm^{-3} were obtained.

Data from the literature, showing the variation of the resistivity of boron doped diamond at 300 K with the boron doping levels is presented in Figure 7.4. The red cross represents the position of the sample under investigation based on its electrical properties correlated with its

boron concentration, information obtained through SIMS. The data (■) was taken from reference [16], while data (●) was taken from reference [5].

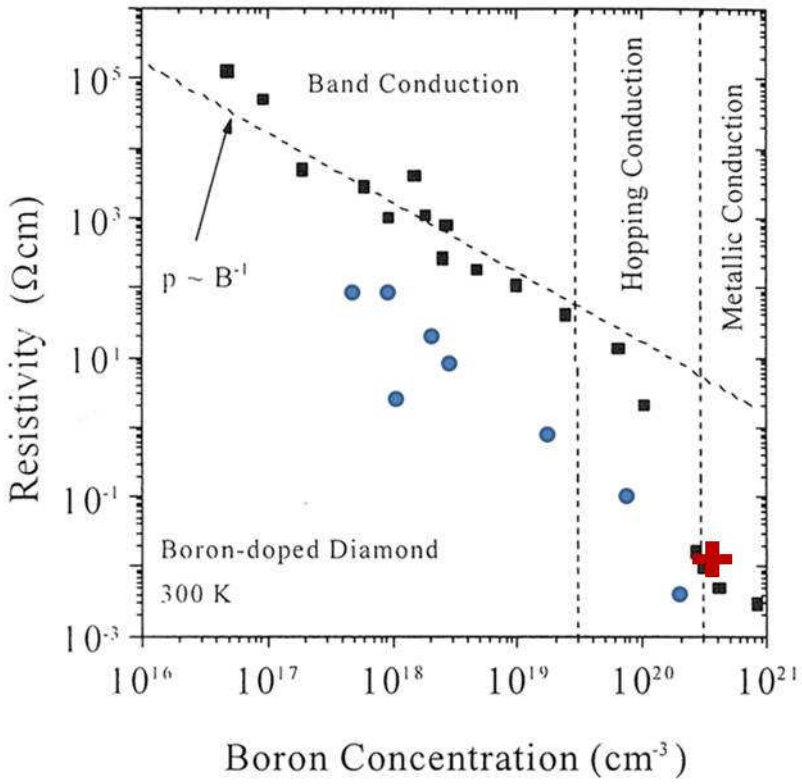

Figure 7.4 Collection of values from the literature showing the variation of the resistivity of boron doped diamond at 300 K with boron doping levels [5, 16]. The red cross represents the sample discussed in this chapter.

7.7. Cyclic voltammetry

Its principles have been outlined in Chapter 3, section 3.8 and the equipment employed was presented in Chapter 4, section 4.9. The measurements were taken at room temperature using a three-electrode setup (CHI730A potentiostat, CH Instruments Inc.) controlled by a laptop computer, in a de-aerated stationary solution in the presence of a high concentration of an inert electrolyte (KNO_3). A platinum gauze counter electrode was employed, with a chloridised Ag wire (Ag/AgCl) as a reference electrode and the diamond sample as the working electrode. The sample's surface, O- or H-terminated, was prepared as detailed in

Chapter 4, section 4.4 and the contacts were prepared as detailed in Chapter 4, section 4.5 **d)**. Cyclic voltammograms were recorded for the reduction/ oxidation of $Ru(NH_3)_6^{3+}$ / $FcTMA^+$ (in KNO_3) at the scBDD electrode sample (0572389/1). Both mediators were present in the electrolyte solution in equal concentrations.

The Figures 7.5- 7.8 show CVs of the sc heavily boron doped diamond sample, recorded for both mediators ($Ru(NH_3)_6^{3+}$ and $FcTMA^+$) and surfaces (hydrogen and oxygen), at concentrations of 0.1 mM, 1 mM and 5 mM. Tables 7.2- 7.6 show the theoretical peak current based on a reversible electrode response, the experimentally obtained peak current and ΔEp.

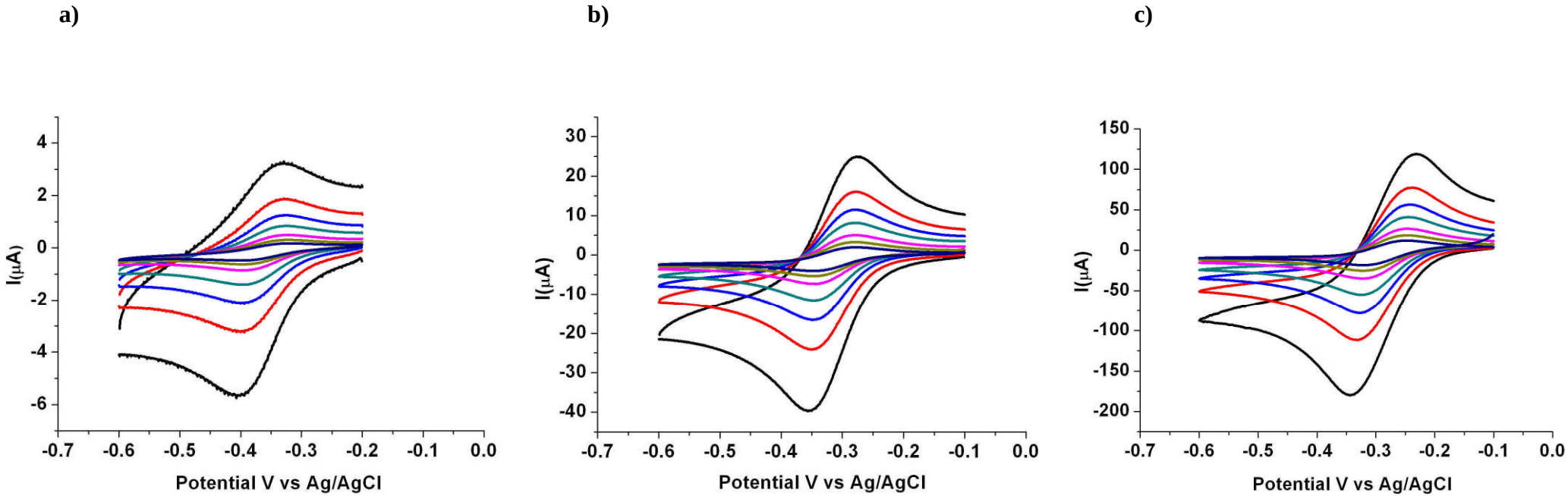

Figure 7.5 CVs in the scan rate range of 0.5 to 0.005 Vs^{-1} recorded in (a) 0.1 mM, (b) 1 mM and (c) 5 mM $Ru(NH_3)_6^{3+}$ (in the presence of $FcTMA^+$ of equal concentration) in KNO_3 (0.1 M for (a) and (b) and 0.2 M for (c)) on an O-terminated surface which was not polished (0572389/1 scbdd sample with a boron dopant density of 3.4 x 10^{20} atoms cm^{-3}).

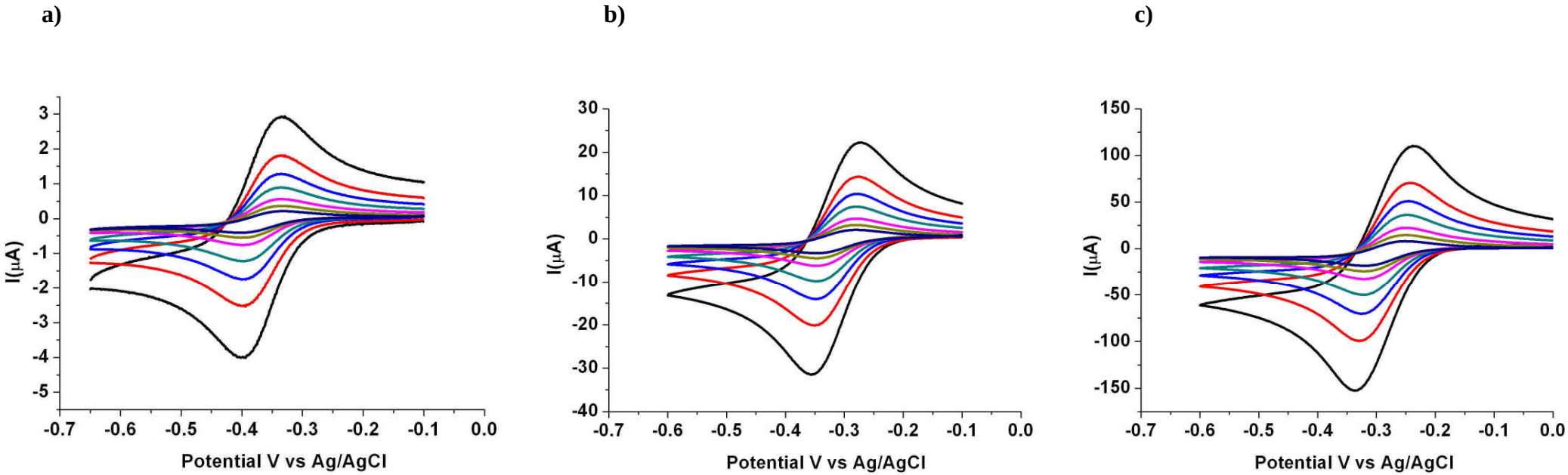

Figure 7.6 CVs in the scan rate range of 0.5 to 0.005 Vs^{-1} recorded in (a) 0.1 mM, (b) 1 mM and (c) 5 mM $Ru(NH_3)_6^{3+}$ (in the presence of $FcTMA^+$ of equal concentration) in KNO_3 (0.1 M for (a) and (b) and 0.2 M for (c)) on an H-terminated surface which was not polished (0572389/1 scbdd sample with a boron dopant density of 3.4 x 10^{20} atoms cm^{-3}).

Concentration/ mediator/area exposed	Scan Rate (mVs^{-1})	i_p(µA) theoretical	i_p(µA) experimental O terminated	i_p(µA) experimental H terminated	ΔEp O terminated	ΔEp H terminated
0.1 mM $Ru(NH_3)_6^{3+}$ Area: 4.7 mm^2 0572389/1	500	2.8	3.55	3.77	78	65
	200	1.78	2.05	2.39	65	65
	100	1.26	1.35	1.67	65	58
	50	0.89	0.89	1.17	65	59
	20	0.56	0.47	0.73	79	66
	10	0.39	0.31	0.52	79	66
	5	0.28	0.23	0.38	79	66

Table 7.2 Summary of the peak separation for the 0572389/1 sample, O- and H-terminated, in 0.1 mM $Ru(NH_3)_6^{3+}$ in 0.1 M KNO_3 at different scan rates.

Concentration/ mediator/area exposed	Scan Rate (mVs^{-1})	i_p(µA) theoretical	i_p(µA) experimental O terminated	i_p(µA) experimental H terminated	ΔEp O terminated	ΔEp H terminated
1 mM $Ru(NH_3)_6^{3+}$ Area: 4.7 mm^2 0572389/1	500	28	34.85	31.23	85	85
	200	17.8	21.49	19.89	71	71
	100	12.6	14.99	14.03	71	71
	50	8.9	10.26	9.66	71	71
	20	5.6	6.28	5.86	73	73
	10	3.9	4.47	4.1	73	66
	5	2.8	3.28	2.95	73	73

Table 7.3 Summary of the peak separation for the 0572389/1 sample, O- and H-terminated, in 1 mM $Ru(NH_3)_6^{3+}$ in 0.1 M KNO_3 at different scan rates.

Concentration/ mediator/area exposed	Scan Rate (mVs^{-1})	i_p(µA) theoretical	i_p(µA) experimental O terminated	i_p(µA) experimental H terminated	ΔEp O terminated	ΔEp H terminated
5 mM $Ru(NH_3)_6^{3+}$ Area: 4.7 mm^2 0572389/1	500	140	163.3	153.8	111	98
	200	89	104.6	99.4	91	85
	100	63	74.55	71.01	84	78
	50	44.5	52.05	50.15	79	78
	20	28	31.15	32.01	79	67
	10	19.5	21.38	23.47	79	67
	5	14	11.03	17.53	79	66

Table 7.4 Summary of the peak separation for the 0572389/1 sample, O- and H-terminated, in 5 mM $Ru(NH_3)_6^{3+}$ in 0.1 M KNO_3 at different scan rates.

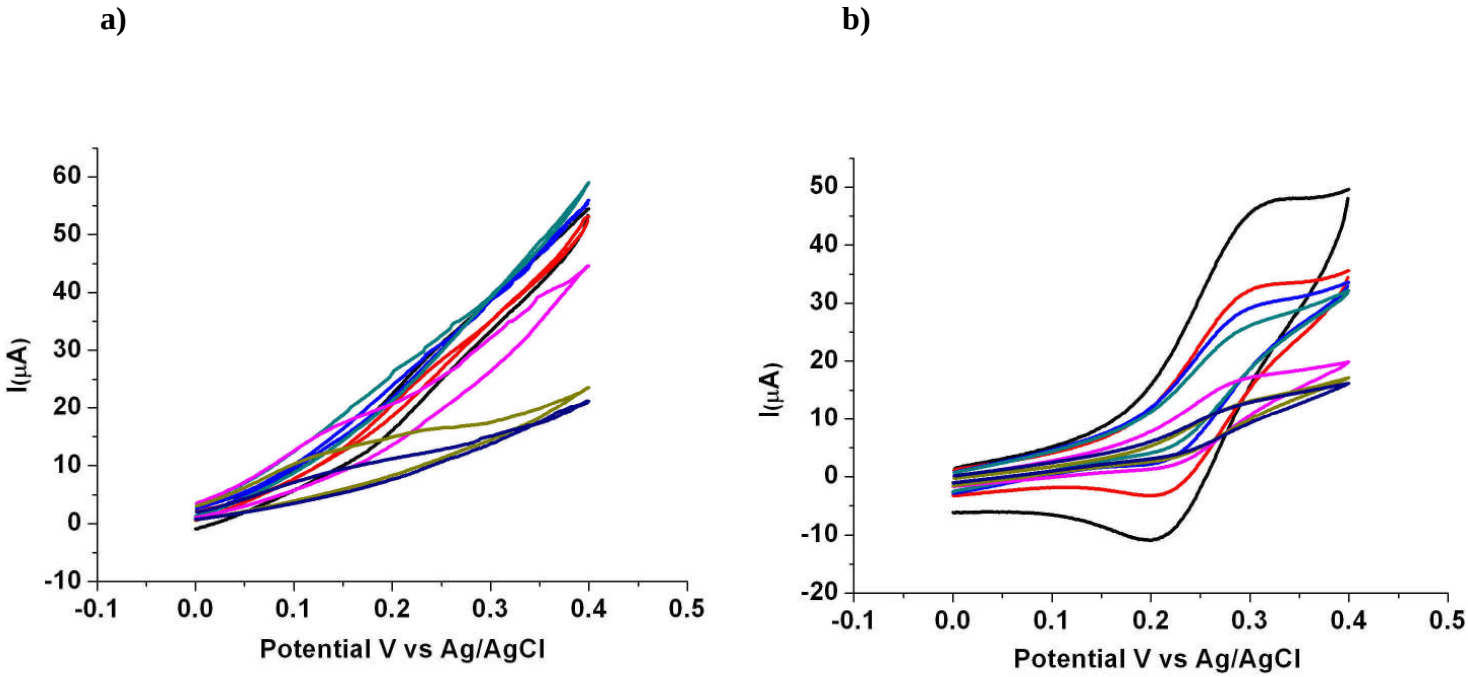

Figure 7.7 CVs in the scan rate range of 0.5 to 0.005 Vs^{-1} recorded in (a) 0.1 mM and (b) 1 mM $FcTMA^+$ (in the presence of $Ru(NH_3)_6^{3+}$) in 0.1 M KNO_3 on an O-terminated surface which was not polished (0572389/1 scBDD sample with a boron dopant density of 3.4 x 10^{20} atoms cm^{-3}).

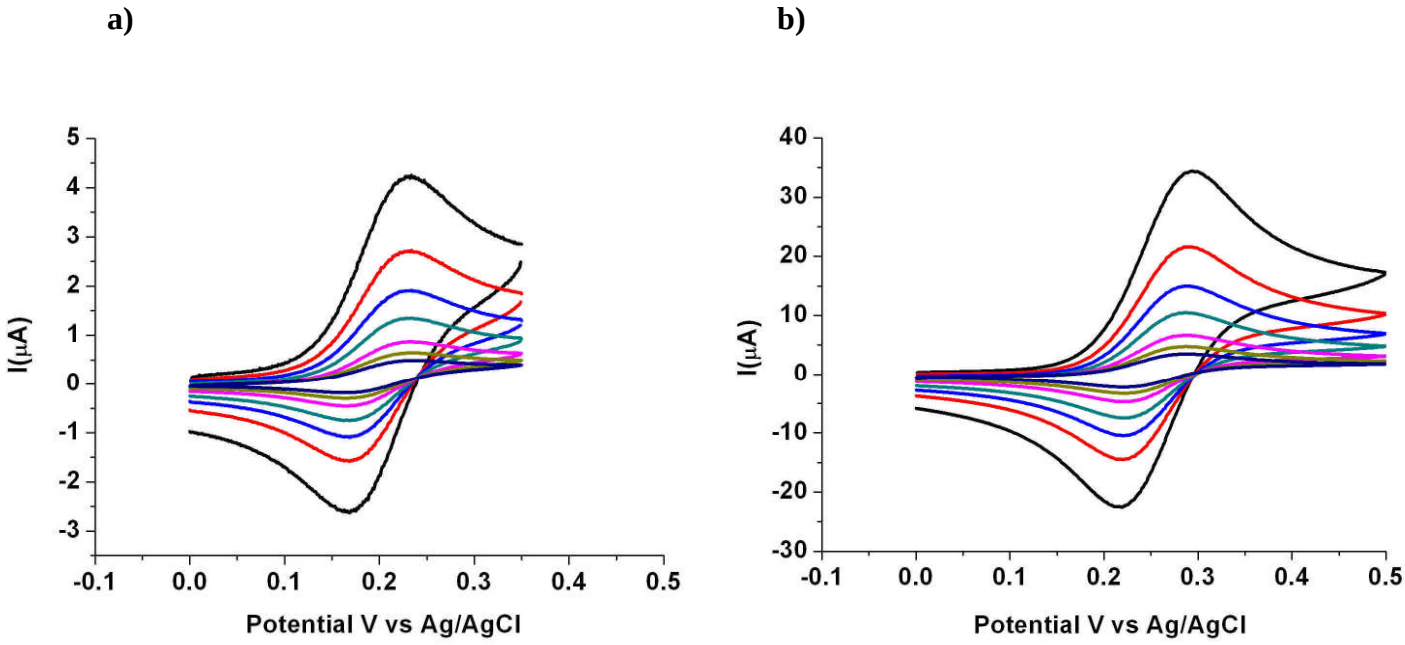

Figure 7.8 CVs in the scan rate range of 0.5 to 0.005 Vs^{-1} recorded in (a) 0.1 mM and (b) 1 mM $FcTMA^+$ (in the presence of $Ru(NH_3)_6^{3+}$) in 0.1 M KNO_3 on an H-terminated surface which was not polished (0572389/1 scBDD sample with a boron dopant density of 3.4 x 10^{20} atoms cm^{-3}).

Concentration/ mediator/area exposed	Scan Rate (mVs^{-1})	i_p(μA) theoretical	i_p(μA) experimental H terminated	ΔEp H terminated
0.1 mM $FcTMA^+$ Area: 4.7 mm^2 0572389/1	500	2.44	3.69	65
	200	1.54	2.36	65
	100	1.09	1.68	65
	50	0.77	1.2	65
	20	0.48	0.74	66
	10	0.34	0.52	73
	5	0.24	0.37	73

Table 7.5 Summary of the peak separation for the 0572389/1 sample, H-terminated, in 0.1 mM $FcTMA^+$ in 0.1 M KNO_3 at different scan rates.

Concentration/ mediator/area exposed	Scan Rate (mVs^{-1})	i_p(μA) theoretical	i_p(μA) experimental H terminated	ΔEp H terminated	ΔEp O terminated
1 mM $FcTMA^+$	500	24.4	33.17	75	118
Area: 4.7 mm^2	200	15.4	21.06	72	104
0572389/1	100	10.9	14.73	65	98
	50	7.7	10.29	65	87
	20	4.8	6.4	67	90
	10	3.4	4.5	66	84
	5	2.4	3.2	67	81

Table 7.6 Summary of the peak separation for the 0572389/1 sample, H-terminated, in 1 mM $FcTMA^+$ in 0.1 M KNO_3 at different scan rates.

The diamond electrode exhibited low background current and quasi-reversible behaviour for the $Ru(NH_3)_6^{3+}$ ($E_{1/2}$~ -0.3 V) couple regardless of the surface termination, see Tables 7.2, 7.3 and 7.4 for ΔEp. Typical CVs for the O- and H-terminated surface are shown in Figure 7.5 and 7.6 respectively, at scan rates of 5, 10, 20, 50, 100, 200 and 500 mVs^{-1}. For quasi-reversible systems the current is controlled by both the charge transfer rate and the mass transport. Another factor that has to be taken into consideration is the electrode kinetics. For the 0572389/1 diamond sample, both the shape and the peak to peak separation suggest that the electrode kinetics are much faster than the rate of the diffusion. The values of the current measured experimentally (for both O- and H-terminations) are in good agreement with the theoretical values, suggesting that the entire area is electrochemically active. In 0.1 mM $Ru(NH_3)_6^{3+}$ at a scan rate of 100 mV/s ΔEp = 65 mV (O-terminated) and ΔEp = 58 mV (H-terminated), therefore it can be stated than when H-terminated at 100 mV/s the diamond electrode behaves like a reversible electrode. This type of electrode has shown stability over time, as long as the potential was not pushed above 1.6 V (diamond potential window), when the H-termination can be destroyed. The fact that the current values measured experimentally are higher (~10 %) than the theoretical calculated one can be attributed to the fact that the

sample is as grown and rough, therefore a larger area than the one actually measured is exposed to the solution. For example a 10% increase of the estimated area (due to the roughness of the sample) will result in an increase of 10% in the experimental current recorded, see Tables 7.2- 7.3.

The sample was also analysed in $FcTMA^+$ ($E_{1/2}$~ 0.25 V). While H-terminated the sample exhibited quasi-reversible behaviour, see Figure 7.8. The experimental and theoretical current's values for the sample 0572389/1 are in good agreement, see Table 7.5 and 7.6 suggesting that the entire area is electrochemically active for this mediator also. While the sample is H-terminated and examined in $FcTMA^+$ both the CVs shape and the peak to peak separation suggest that its kinetics are faster than the rate of diffusion. When O-terminated, the scBDD electrode exhibits a high background current; its origins have not been clearly identified and this topic requires further investigation. However, it has to be noted that when O-terminated the sample is hydrophilic and when H-terminated hydrophobic. Changing the wetability of the surface and/ or unidentified surface contamination could adversely affect the electrochemical response. Surface oxygen species are expected to modify the electrochemical properties of diamond electrodes, because oxygen-containing functionalities that are formed on various types of carbon electrodes, for example glassy carbon and highly oriented pyrolytic graphite are known to change the electron transfer kinetics for certain redox species [17-19]. Nevertheless, in 1 mM $FcTMA^+$ quasi-reversible behaviour can be observed. At a scan rate of 100 mV/s ΔEp = 98 mV (O-terminated) and ΔEp = 65 mV (H-terminated), therefore it is obvious that the electrode kinetics are sluggish for the O-terminated diamond.

In general diamond electrochemistry studies reported in the literature have employed boron doped polycrystalline material, even if nanocrystalline material can also be used [20, 21]. The investigations presented here on the heavily boron doped as grown single crystal diamond electrode show a similar behaviour to the ones reported in the literature on polycrystalline material [19, 22-24]. For example, although $IrCl_6^{3-}$ - $e^- \rightarrow IrCl_6^{2-}$ is classified as an outer-sphere system, which is not affected by surface oxides, as well as $Ru(NH_3)_6^{3+}$ + $e^- \rightarrow Ru(NH_3)_6^{2+}$ at glassy carbon, at diamond electrodes, this redox couple is classified as a member of the group that is sensitive to oxygen termination [19]. $FcTMA^+$ - $e^- \rightarrow FcTMA^{2+}$, unsurprisingly, shows a similar behaviour to $IrCl_6^{3-}$. On the other hand, $Ru(NH_3)_6^{3+}$ is not sensitive to the presence of oxygen either at diamond or glassy carbon [19], as demonstrated also by our observations. Swain and Granger [23] have investigated the electrochemistry of several couples at the polycrystalline, boron-doped diamond electrodes before and after anodic polarization and hydrogen plasma treatment. For $Ru(NH_3)_6^{3+}$ they showed that the ΔEp= 70 mV (scan rate 100 mV/s), is unaffected by the treatment. Yagi et al. [19] analysed the electrochemical selectivity for different redox systems at O-terminated diamond electrodes and as-grown H-terminated electrodes. The apparent surface conductivity did not change, but the electrochemical responses of some redox couples became remarkably different; the peak to peak separations for the O-terminated diamond electrodes were much larger compared to those for the as-grown electrodes. For 0.5 mM $Ru(NH_3)_6^{3+}$ they showed that ΔEp was 117 mV and 135 mV, at a scan rate of 100 mV/s, for as-grown and 1 min O_2 plasma treated diamond. The values reported in literature for ΔEp vary between 70 mV -135 mV. The values obtained in the studies presented here are always at the low end of this range.

7.8. Scanning electrochemical microscopy (SECM)

SECM (see Chapter 3, section 3.10) experiments were carried out using a 25 μm diameter Pt disc UME (fabrication described in Chapter 4, section 4.7; RG = 10) as the tip in both SG-TC and feedback mode. The electrolyte solution had both $Ru(NH_3)_6^{3+}$ and $FcTMA^+$ in equal concentrations. Typical approach curves recorded these mediators for both H- and O-terminated surfaces are presented below, see Figures 7.9- 7.12. The approach curves were recorded for two situations: i) substrate unbiased and ii) substrate biased at 0 V.

The approach curves show clear differences between the O- and H-terminated surface. When H-terminated, the sample exhibits positive feedback, therefore metal-like behaviour regardless of the mediator or concentration of species in solution. This behaviour is in good agreement with the observations made while running CVs. For O-terminated surfaces the sample exhibits identical conductive behaviour for varying concentrations, with a similar departure from the positive feedback for both $Ru(NH_3)_6^{3+}$ and $FcTMA^+$. This suggests that the electrode kinetics are slower for the O-terminate surface than for the H-terminated one. Using Bard's theory on approach curves, model described in Chapter 5, section 5.8, a k can be extracted. For both mediators and regardless of the concentration, when O-terminated $0.05 < k < 0.01$, as can be seen in Figure 7.13. For image clarity only the experimental approach curve obtained for 1 m M $Ru(NH_3)_6^{3+}$ was fitted to the theoretically obtained ones.

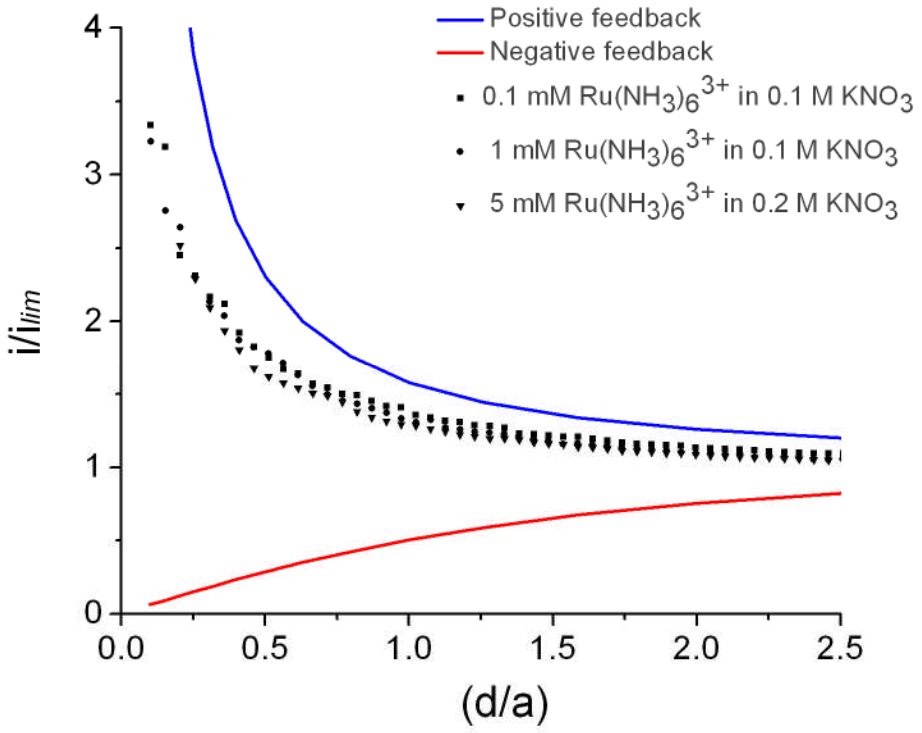

Figure 7.9 Approach curves on an O-terminated boron doped single crystal diamond, with a boron dopant density of 3.4 x 10^{20} atoms cm^{-3}, recorded in 0.1 mM, 1 mM and 5 mM $Ru(NH_3)_6^{3+}$ in KNO_3 (0572389/1). The same behaviour was observed for both biased and unbiased substrate situations. If biased, the substrate was held at 0 V and the tip was held at -0.5 V.

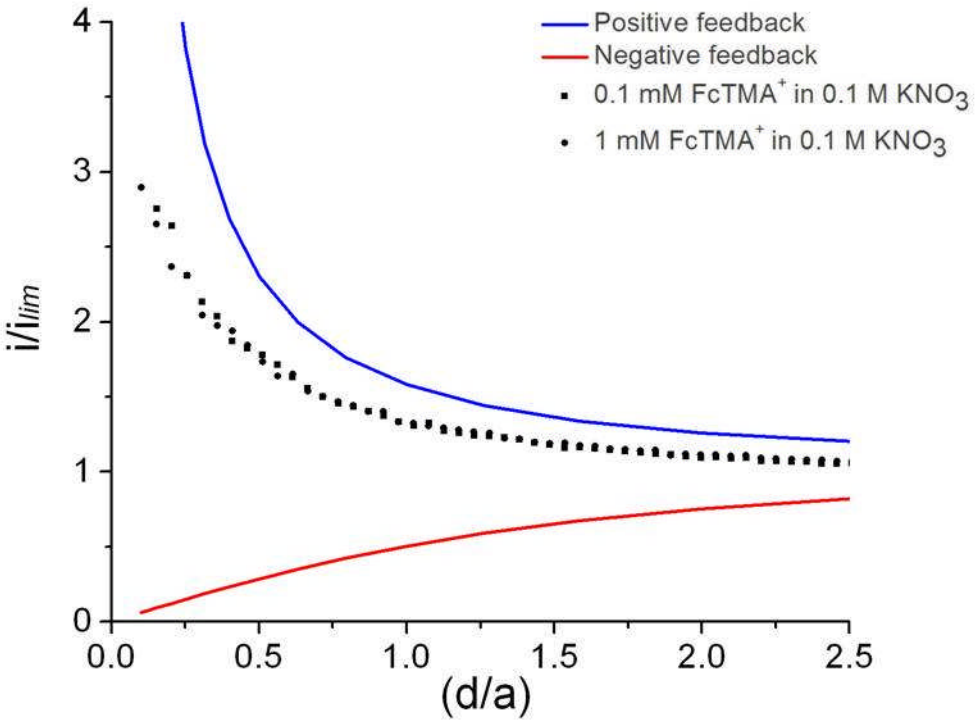

Figure 7.10 Approach curves on an O-terminated boron doped single crystal diamond, with a boron dopant density of 3.4 x 10^{20} atoms cm^{-3}, recorded in 0.1 mM and 1 mM $FcTMA^+$ in KNO_3 (0572389/1). The same behaviour was observed for both biased and unbiased substrate situations. If biased, the substrate was held at 0 V and the tip was held at 0.5 V.

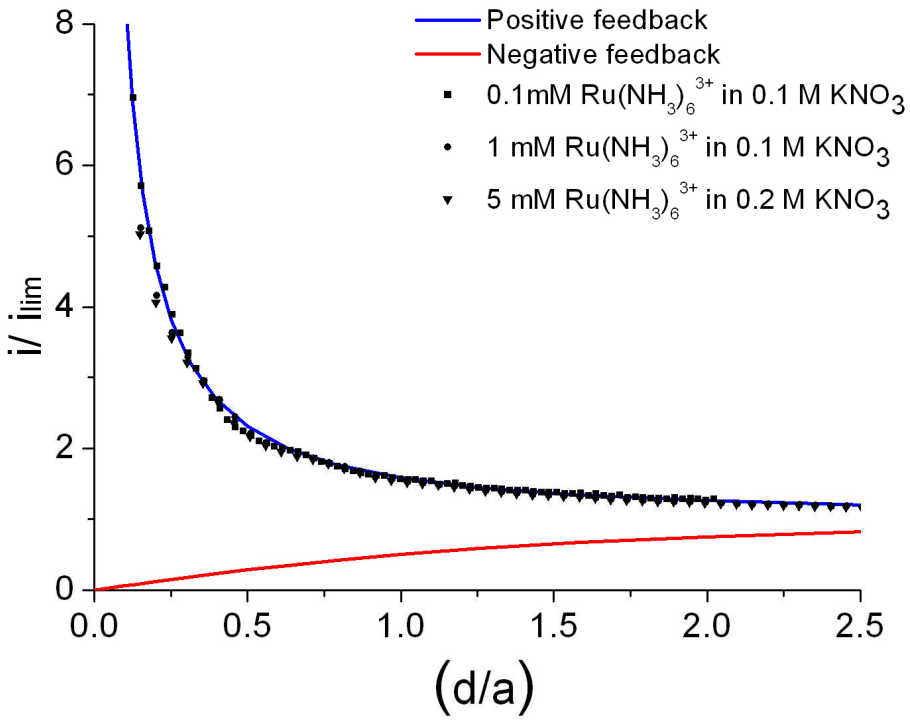

Figure 7.11 Approach curves on an H-terminated boron doped single crystal diamond, with a boron dopant density of 3.4 x 10^{20} atoms cm^{-3}, recorded in 0.1 mM, 1 mM and 5 mM $Ru(NH_3)_6^{3+}$ in KNO_3 (0572389/1). The same behaviour was observed for both biased and unbiased substrate situations. If biased, the substrate was held at 0 V and the tip was held at -0.5 V.

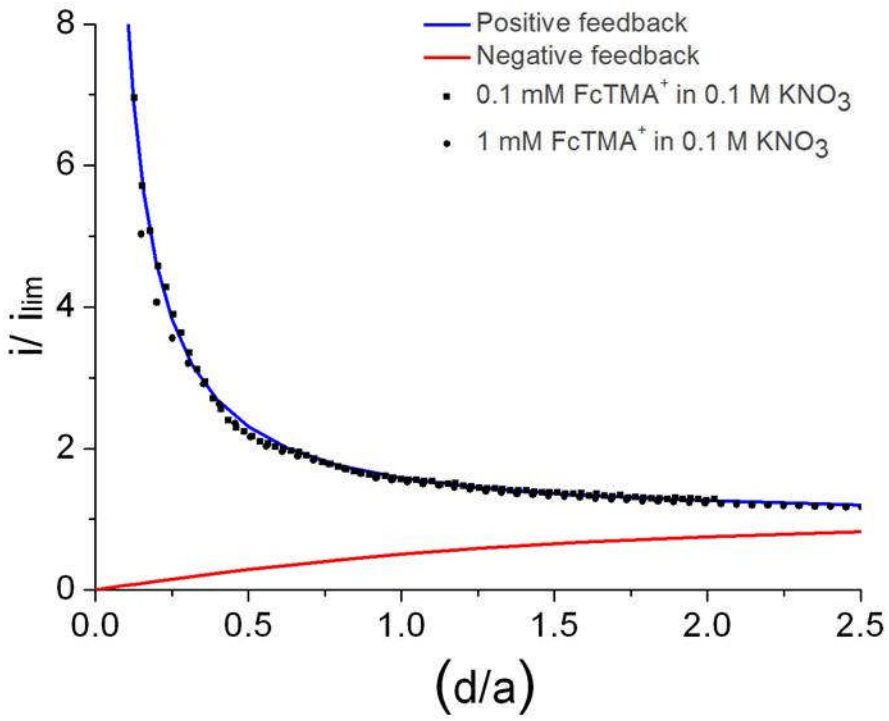

Figure 7.12 Approach curves on an H-terminated boron doped single crystal diamond, with a boron dopant density of 3.4 x 10^{20} atoms cm^{-3}, recorded in 0.1 mM and 1 mM $FcTMA^+$ in KNO_3 (0572389/1). The same behaviour was observed for both biased and unbiased substrate situations. If biased, the substrate was held at 0 V and the tip was held at 0.5 V.

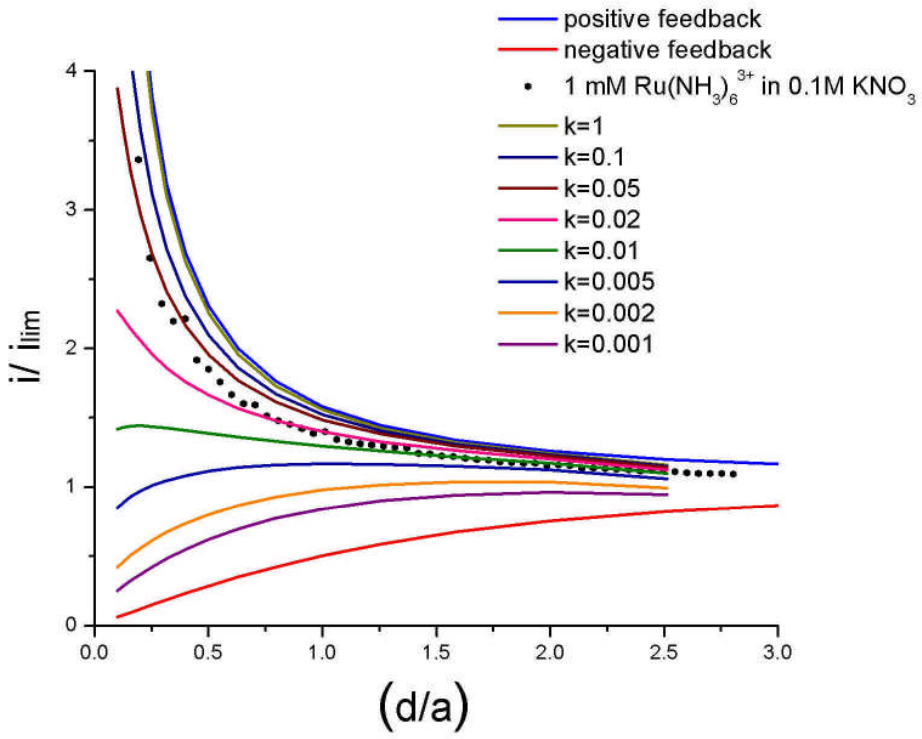

Figure 7.13 Theoretical approach curves for different values of k, where k is the heterogeneous electron transfer rate constant (cms^{-1}). As the rate constant deceases, the extent of positive feedback decreases and the current approaches that of an inert, insulating surface. The experimental result recorded for 1 mM $Ru(NH_3)_6^{3+}$ while the sample was O-terminated was fitted to the theoretically obtained curves.

SECM was employed to image areas of the scBDD with holding the tip at a reasonable tip-substrate separation to minimising the risk of tip crash. The SECM instrumentation is described in section 4.10, Chapter 4. It was typically operated in substrate generation-tip collection (SG-TC) or feedback mode at a rate of 20 μm s^{-1} in a series of unidirectional line scans (line separation 20 μm) with a scan size of 500 μm x 500 μm or 250 μm x 250 μm and a tip-substrate separation less than 10 μm. This distance was set by recording approach curves and utilising the feedback response to determine the absolute tip-substrate separation.

Various studies reported in the literature [25-27] employed SECM to map the electrochemical activity of polycrystalline diamond and diamond arrays. Figure 7.14 shows 250 μm x 250 μm scans recorded in 1 mM $Ru(NH_3)_6^{3+}$ in 0.1 M KNO_3 while the scBDD was O-terminated. The substrate was a) unbiased and b) biased. The tip was held at -0.5 V at a distance of a) 4.80 μm and b) 5 μm away. All tip current have been normalised with respect to the steady-state current, i_{lim}, for the reduction of $Ru(NH_3)_6^{3+}$ in the bulk solution. Firstly it should be noted that the scans show that the entire surface is active. On a metal, if there is diffusion limited turnover between the tip and the surface, a positive feedback current of ~4 would be expected. Therefore it can be stated that some regions of the sample present metal-like behaviour. Additionally it has to be mentioned that the electrochemical activity of the sample shows that this has not been perfectly flat during imagining. The scan started at the centre of the image and as this point was used as reference for the tip-substrate separation it is known that this distance was 4.8 μm; as such d/a ~ 0.4. Looking at the Figure 7.9 which shows the approach curves on the O-terminated surface it is easy to establish that i_t/i_{lim} ~ 2 fact which can be corroborated with the SECM scans shown in Figure 7.14. However if we take the highest point of the current for the SECM image which is i_t/i_{lim} ~ 4 and relate this point to

the Figure 7.9 showing the approach curves on the O-terminated scBDD it can be observed that d/a ~ 0.1, therefore the tip substrate distance in this case is distance 1.25 µm. Following the same logic, at the lower end when i_t/i_{lim} ~ 1.6, d/a ~0.6, so the tip substrate separation in this case is 7.5 µm. Using this analyses it can be concluded that the entire sample is electrochemically active (observation in agreement with the CVs), but there is a slope of ~ 6 µm.

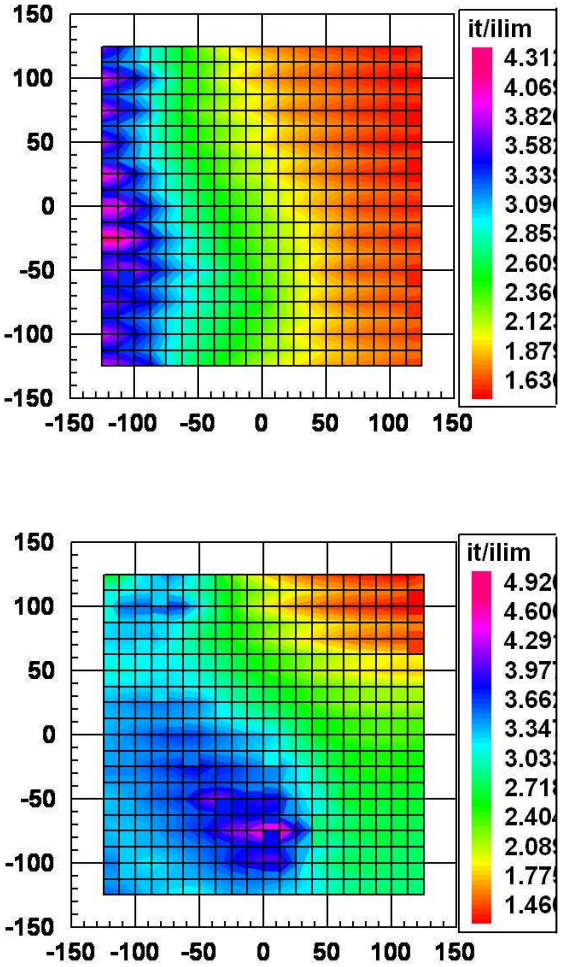

Figure 7.14 250 µm x 250 µm SECM images recorded in 1 mM $Ru(NH_3)_6^{3+}$ in 0.1 M KNO_3. The substrate was a) unbiased and b) biased. The tip was held at -0.5 V at a distance of a) 4.80µm and b) 5µm away. All tip current have been normalised with respect to the steady-state current, i_{lim}, for the reduction of $Ru(NH_3)_6^{2+}$ in the bulk solution. The sample was a scBDD with a boron dopant density of 3.4 x 10^{20} atoms cm^{-3}(0572389/1 –O terminated).

References:

[1] P. W. May, Philosophical Transactions of the Royal Society of London Series a-Mathematical Physical and Engineering Sciences **358**, 473 (2000).
[2] A. W. Williams, Lightowl.Ec, and A. T. Collins, Journal of Physics Part C Solid State Physics **3**, 1727 (1970).
[3] A. S. Vishnevskii *et al.*, Soviet Physics Semiconductors-Ussr **15**, 659 (1981).
[4] M. Werner *et al.*, Applied Physics Letters **64**, 595 (1994).
[5] T. H. Borst, and O. Weis, Physica Status Solidi a-Applied Research **154**, 423 (1996).
[6] R. J. Zhang, S. T. Lee, and Y. W. Lam, Diamond and Related Materials **5**, 1288 (1996).
[7] E. Bustarret *et al.*, Philosophical Transactions of the Royal Society a-Mathematical Physical and Engineering Sciences **366**, 267 (2008).
[8] K. Winzer, D. Bogdanov, and C. Wild, Physica C-Superconductivity and Its Applications **432**, 65 (2005).
[9] F. Silva *et al.*, Diamond and Related Materials **17**, 1067 (2008).
[10] R. Locher *et al.*, Diamond and Related Materials **4**, 678 (1995).
[11] R. Samlenski *et al.*, Diamond and Related Materials **5**, 947 (1996).
[12] K. Kobashi *et al.*, Journal of Vacuum Science & Technology a-Vacuum Surfaces and Films **6**, 1816 (1988).
[13] S. Kuwamura, and I. Yamaguchi, Applied Optics **36**, 4473 (1997).
[14] www.optics.arizona.edu/jcwyant/pdf.
[15] D. E. Haas *et al.*, Journal of Materials Science Letters **20**, 1763 (2001).
[16] M. H. Nazare, and A. J. Neves, *Properties, Growth and Applications of Diamond* (INSPEC, London, 2001), Vol. 26.
[17] K. Kinoshita, *Carbon: Electrchemical and Physicochemical Properties* (Wiley, NY, 1988).
[18] A. J. Bard, Mirkin, M. V., Fan, R. F., *Electroanalytical Chemistry* (Marcel Dekker, 1994).
[19] I. Yagi *et al.*, Journal of Electroanalytical Chemistry **473**, 173 (1999).
[20] L. C. Hian *et al.*, Journal of the Electrochemical Society **150**, E59 (2003).
[21] Q. Y. Chen *et al.*, Journal of the Electrochemical Society **148**, E44 (2001).
[22] M. C. Granger *et al.*, Analytical Chemistry **72**, 3793 (2000).
[23] M. C. Granger, and G. M. Swain, Journal of the Electrochemical Society **146**, 4551 (1999).
[24] A. Chatterjee *et al.*, Physica Status Solidi a-Applied Research **199**, 49 (2003).
[25] N. R. Wilson *et al.*, Journal of Physical Chemistry B **110**, 5639 (2006).
[26] A. L. Colley *et al.*, Analytical Chemistry **78**, 2539 (2006).
[27] A. K. Neufeld, and A. P. O'Mullane, Journal of Solid State Electrochemistry **10**, 808 (2006).

Chapter 8
Summary and further work

It this thesis a combination of high resolution imaging (PL, AFM, C-AFM, FE-SEM), electrical (FET, Hall effect) and electrochemical (CV, SECM) techniques have been employed to study the electrical and electrochemical properties of (H- and O-terminated) single crystal intrinsic and boron doped diamond. The samples used were all grown by E6 using CVD of diamond on a (100) substrate. The material varied from intrinsic single crystal diamond with [N] < 1 ppm and [B] < 0.05 ppm to moderately doped (< 10^{20} cm^{-3} boron) semiconducting diamond and heavily doped (> 10^{20} cm^{-3} boron) superconducting diamond. Considerable attention was paid to the effect of H- and O- surface terminations. In addition to the investigations carried out into the properties of different types of materials, initial research was conducted into the effect of different mechanical surface preparations on the electrical and electrochemical behaviour of single crystal intrinsic and boron doped diamond.

In Chapter 5 studies conducted on the electrical and electrochemical properties of H-terminated intrinsic single crystal diamond were presented. Three types of surfaces were analysed: a surface polished by E6 using a cast iron scaife (standard polish), a surface polished at Warwick using a cast iron scaife (Warwick polish) and a lapped surface (Ra < 250 nm) prepared by E6. The results obtain for the in air electrical measurements showed that the polished surfaces have similar properties (mobility, hole sheet density, sheet resistance). For the lapped surface the hole sheet density proved to be higher and the mobility lower; this is probably a consequence of surface roughness (increased area) and surface/subsurface damage reducing mobility. The electrical measurements performed in solution and the SG-FET measurements were explained modelling the diamond/solution interface as an ideally

polarisable interface. In accord with the observations made by Garrido et al.[1] and Zhang et al.[2, 3] it has been demonstrated that while in air the transfer doping model proposed by Maier et al. [4] can be successfully applied to explain the surface conductivity of H-terminated diamonds. In aqueous solutions the polarization charge density on the diamond must be considered. The data presented here shows that for the polished surfaces, in solution, the carrier sheet density increases linearly with the gate potential (until ~ 450 mV) as would be expected for an ideal polarisable interface and constant carrier mobility. The hole mobility has also been proven to depend on the gate potential. The lapped surface showed that the mobility is gate potential independent with a large scatter of the sheet carrier concentrations. A non uniform surface potential could perhaps explain the observed behaviour. Electrochemistry of single crystal H-terminated electrodes with well defined redox couples ($Ru(NH_3)_6^{3+}$ and $FcTMA^+$) with chemical potentials close to the energy level of the maximum of the valence band has been demonstrated. The CVs are quasi-reversible for both couples at low concentrations, with a relatively slow electron transfer rate constant rather than *iR* or *RC* effects responsible for the large peak separation. The peak currents for $Ru(NH_3)_6^{3+}$ do not scale with increasing mediator concentration, indicating that the limited density of states near the top of the valence band limits the Faradaic current. Initial SECM experiments indicate that the surface is homogeneously active, but can be easily damaged.

Chapter 6 presented investigations carried out onto the electrical and electrochemical properties of O- and H-terminated moderately boron doped ($< 10^{20}$ cm^{-3}) semiconducting diamond. Even if thought as a homogeneous material, since it is a single crystal diamond, PL imaging and C-AFM have highlighted regions with different boron uptake and so different conductivity. Therefore great care has to be taken when investigating this type of material. Two samples 0372211- E(i) and 0372211- D(i) have been investigated. Electrical

measurements were performed in air. Their results support the assumption that the samples termination (O- or H-) does not have any influence on the measurements of bulk conductivity. The samples showed similar behaviour and the calculated carrier concentration was in the correct range in accord with the doping level determined by SIMS; similar behaviour was observed also during the electrochemical experiments. A very different electrochemical response was obtained when the samples' surfaces were O- or H-terminated. Little or no redox activity was observed when the samples were O-terminated; at low mediator concentrations quasi-reversible behaviour was observed for $Ru(NH_3)_6^{3+}$ and $FcTMA^+$ couples when the samples were H-terminated. The peak to peak separations are considerably larger for $Ru(NH_3)_6^{3+}$ than for $FcTMA^+$ indicating a slower effective electron transfer rate. The peak currents in the CVs scaled as expected with increasing mediator concentration between 0.1 mM and 1 mM for both couples. The position of the two couples with respect to the valence and conduction band for both O- and H-terminated scBDD clearly explains the lack of redox activity for the oxygen terminated surface.

Chapter 7 reported studies of the electrical and electrochemical properties of O- and H-terminated highly doped ($> 10^{20}$ cm^{-3} boron) metallic single crystal diamond. All experiments were performed on the as-grown surface. The carrier concentration calculated from the data obtained in the electrical measurements performed in air is in good agreement with the boron concentration determined by SIMS. The sample is metallic and the surface termination O- or H- does not influence the bulk conductivity. The electrochemical data were recorded for both O- and H-terminated surfaces. When O-terminated, the sample showed a large background current for CVs run with $FcTMA^+$; its origin has not been clearly identified. If H-terminated, the sample showed low background current, quasi-reversible behaviour with fast electron transfer. For $Ru(NH_3)_6^{3+}$ the metallic scBDD (O- or H-terminated) showed quasi-reversible

behaviour with fast electron transfer kinetics. The SECM images showed that the electrochemical activity of the sample was uniform, the differences in the feedback current being attributed to surface roughness.

Neither H-terminated intrinsic diamond nor H-terminated boron doped semiconducting diamond do not make robust reversible electrodes for analytical applications. However, the metallic single crystal BDD is much more attractive, especially if the boron doping density can be increased such that reversible behaviour is achieved for O-termination. Such electrodes will be the topic of future research.

References:

[1] J. A. Garrido *et al.*, Journal of the American Chemical Society **130**, 4177 (2008).
[2] J. Ristein, W. Zhang, and L. Ley, Physical Review E **78** (2008).
[3] W. Y. Zhang, J. Ristein, and L. Ley, Physical Review E **78** (2008).
[4] F. Maier *et al.*, Physical Review Letters **85**, 3472 (2000).